



THÈSE / UNIVERSITÉ DE RENNES 1
sous le sceau de l'Université Européenne de Bretagne

pour le grade de

DOCTEUR DE L'UNIVERSITÉ DE RENNES 1

Mention : Traitement de signal et télécommunications

Ecole doctorale MATISSE

présentée par

Mario MARTINIS

Préparée à l'unité de recherche (UMR CNRS 6164, IETR)
Institute d'Electronique et de Télécommunications de Rennes
Université de Rennes 1

**Développement et
caractérisation de
métamatériaux pour
applications en cavité.
Application à la
conception d'antennes
compactes.**

**Thèse soutenue à l'Université de Rennes 1
le 13 Novembre 2014**

devant le jury composé de :

Christophe DELAVEAUD

CEA-Leti Grenoble / *rapporteur*

Thierry MONEDIERE

Professeur, Université de Limoges / *rapporteur*

Robert STARAJ

Professeur, Université de Nice-Sophia Antipolis /
examineur

Armin SCHNEIDER

ISL / *examineur*

Kouroch MAHDJOUBI

Professeur, Université de Rennes 1 / *Directeur de thèse*

Ronan SAULEAU

Professeur, Université de Rennes 1 / *co-directeur de
thèse*

Loïc BERNARD

ISL / *examineur / co-encadrant*

Sylvain COLLARDEY

Université de Rennes 1 / *examineur / co-encadrant*

ACKNOWLEDGMENTS

First of all, I would like to express my profound gratitude to my thesis supervisors, Professor Kourosh MAHDJOUBI, Professor Ronan SAULEAU, Dr. Sylvain COLLARDEY and Dr. Loïc BERNARD for their support and guidance. Thank you very much for your patience, advices, suggestions, your valuable time, and for encouraging me throughout the three years of thesis.

Furthermore, I would like to thank both of my reviewers (Dr. Christophe DELAVEAUD and Professor Thierry MONEDIERE) for accepting my thesis work. Many thanks also to all the members of my jury, (Professor Robert STARAJ, Armin SCHNEIDER) for their presence. I deeply appreciate your evaluation and valuable comments.

I would like to acknowledge the kindness, support and hard work put in by the technicians at ISL, Mr. Christophe BISSEL, Mr. Olivier LITSCHIG, and Mr. Francois WEBER). Without their help, it would not have been possible for me to complete my work in time. My thanks to Dr. Laurent Le COQ for helping me in carrying out the measurements at IETR, and Dr. Loïc BERNARD for helping me in carrying out the measurements at ISL. Also, many thanks to Dr. Guido VALERIO for his help and sharing his valuable research work time in discussions with me.

I would also like to thank all my colleagues at IETR and ISL, for their warm welcome and their support. The ambience at the cafeteria and outings, made my stay at IETR, very pleasant and unforgettable. Finally, I would like to acknowledge the Region Bretagne and ISL, for their financial support.

Table des matières / Table of contents:

Développement et caractérisation de métamatériaux pour applications en cavité. Application à la conception d'antennes compactes.	I
Résumé	II
Introduction	III
Les objectifs généraux de la thèse	V
Les objectifs pratiques spécifiques	V
Antennes cavités simples ouvertes	V
Antennes patch en cavité	VIII
Modèle expliquant la relation bande passante-permittivité	X
Modèle expliquant le phénomène de bosse de la bande passante	XI
Limite de Q_{\min} pour l'antenne patch en cavité	XII
Modèle pour des antennes en cavité atteignant bande passante maximale	XIII
Nouvelles antennes atteignant la limite prévue	XIV
Conception physique du condensateur à l'ouverture	XIV
Conception d'une nouvelle antenne en cavité	XV
Avantages de la nouvelle conception	XVI
Antennes fabriquées et résultats de mesure	XVI
Sujets additionnels	XIX
Potentiel des matériaux magnétiques pour des antennes en cavité	XIX
Applications pour des tailles de cavités proches de la demie-longueur d'onde	XX
Applications pour la construction d'un réseau d'antennes compact	XXI
Conclusion	XXII

Development and characterization of metamaterials in cavities. Applications to the design of compact antennas....i

Abstract	iii
General introduction	iv
Chapter 1. Theoretical background and state of the art	1-1
1.1. Introduction to bounds on small antennas	1-1
1.1.1. What are small antennas	1-1
1.1.2. Spherical mode expansion approach and the Chu bound	1-2
1.1.3. Scattering approach and the Gustafsson bound	1-8
1.2. Introduction to microstrip antennas.....	1-12
1.2.1. Basic operation of microstrip antennas.....	1-12
1.2.2. Miniaturization techniques	1-14
1.2.3. Bandwidth enhancement techniques.....	1-18
1.3. Introduction to cavity antennas	1-25
1.3.1. Transmission line model of small open ended cavity antennas	1-26
1.3.2. Microstrip antennas in cavities with examples	1-34
1.4. Introduction to metamaterials and applications to antennas.....	1-38
1.4.1. General Concepts of metamaterials (MTMs)	1-38
1.4.2. Use of metamaterials in antenna size reduction and bandwidth	1-39
1.4.3. Use of metamaterials in antenna miniaturization	1-41
1.4.4. Use of metamaterials in antenna bandwidth enhancement	1-48
1.4.5. Challenges and future trends of metamaterials.....	1-51
1.5. Conclusion of Chapter 1.....	1-52
Chapter 2. Bandwidth of patch antennas in small cavities	2-53
2.1. On the restriction to single patch configuration	2-53
2.1.1. Simulation procedure for single patch antennas in cavities.....	2-54
2.1.2. Optimization goal	2-56
2.2. Bandwidth behavior of patch antennas in square cavities	2-56
2.2.1. Simulation results	2-58
2.2.2. Effect of the cavity aperture size:	2-60
2.2.3. Effect of cavity height:	2-60
2.2.4. Effect of substrate permittivity:.....	2-61
2.2.5. Effect of the ground plane	2-61
2.3. Bandwidth behavior patch antennas in circular cavities.....	2-61
2.3.1. Simulation results	2-62
2.4. Proposed model for patch antennas in cavities.....	2-64

2.5. Measurement results.....	2-67
2.6. Conclusion of chapter 2.....	2-69
Chapter 3. Bound on Q and bandwidth for cavity antennas	3-70
3.1. Motivation for a precise bound	3-70
3.2. Scattering approach applied to cavity antennas.....	3-71
3.2.1. Restriction to broadside radiation pattern.....	3-72
3.2.2. Formulation of the scattering problem	3-72
3.3. Applying the scattering approach to specific geometries	3-75
3.3.1. Bound on bandwidth for rectangular cavities	3-75
3.3.2. Bound on bandwidth for circular cavities.....	3-81
3.3.3. Comparison with patch antennas	3-84
3.4. On objects inside the cavity	3-86
3.5. A “quick and dirty” derivation of the bound.....	3-87
3.6. Conclusion of Chapter 3.....	3-88
Chapter 4. Bandwidth improvement using metamaterial concepts	4-89
4.1. Transmission Line model for cavity antennas achieving the bound.....	4-89
4.1.1. Introduction of parasitic capacitance at the aperture	4-90
4.1.2. Comparison with Gustafsson’s bound	4-91
4.1.3. Extension to finite ground plane antennas.....	4-92
4.2. From model to reality.....	4-93
4.2.1. Physical design of the capacitor at the aperture.....	4-93
4.2.2. Antenna excitation.....	4-94
4.2.3. What is new?	4-95
4.3. Cavity antennas reaching the bound on bandwidth.....	4-95
4.3.1. Design of a square cavity antenna	4-95
4.3.2. Design of a Circular cavity antenna.....	4-98
4.3.3. Measurement results.....	4-102
4.4. Achieving circular polarization with cavity antennas	4-104
4.5. Conclusion of Chapter 4.....	4-107
Chapter 5. Applications and potentials of the new design	5-109
5.1. Applications to projectile design and miniaturization.....	5-109
5.1.1. Ability to use lower cost materials	5-109
5.1.2. Ability to manufacture smaller cavity antennas	5-110
5.1.3. Other characteristics	5-112
5.1.4. Measurement results.....	5-112
5.2. Applications to cavity sizes close to half the wavelength	5-114
5.2.1. Broadband cavity antennas.....	5-114

5.2.2.	Comparison with stacked patches.....	5-116
5.3.	Potentials of magnetic materials for cavity antennas	5-117
5.3.1.	Modifying the bound with perfect magnetic conductors inside the cavity	5-118
5.3.2.	On the impossibility of achieving the bound with AMC metasurfaces.	5-119
5.3.3.	Modifying the bound with ideal magnetic material inside the cavity.....	5-120
5.3.4.	On the impossibility of achieving the bound with SRR type metamaterials	5-121
5.3.5.	Modifying aperture admittance	5-122
5.4.	Applications for building compact antenna arrays.....	5-122
5.5.	Conclusion of Chapter 5.....	5-123
Conclusion.....		5-125
APPENDIX A.	Definitions of Q factor and bandwidth	127
APPENDIX B.	Scattering theory useful definitions	132
APPENDIX C.	Calculation of the aperture admittance for a rectangular aperture.	134
APPENDIX D.	Calculation of the aperture admittance for a circular aperture.	139
APPENDIX E.	A more intuitive introduction to counterintuitive meta-materials	145
APPENDIX F.	Publications related to the thesis	147
References		148

*Développement et caractérisation de métamatériaux
pour applications en cavité. Application à la
conception d'antennes compactes.*

Résumé

Cette thèse présente de nouveaux développements pour de petites antennes en cavité. L'objectif principal de la thèse est l'analyse de la performance de la bande passante de ces antennes pour des tailles d'ouverture qui sont petites par rapport à la longueur d'onde en espace libre. Des cavités de formes rectangulaires et circulaires intégrées dans un plan de masse infini et dans des plans de masse de dimensions latérales finies sont examinées en détail. Jusqu'à présent, dans la littérature, le choix pour ces antennes en cavités porte sur des antennes imprimées microruban. L'objet de la thèse est de déterminer si les performances d'antennes en cavité de petite taille peuvent être améliorées et comment. A cet effet, la limite supérieure de la bande passante pour cette configuration particulière en cavité est étudiée théoriquement. Il est conclu que les antennes microruban intégrées dans une cavité, en fait, n'atteignent pas la limite de la bande passante, ce qui est l'un des principaux résultats de la thèse. Les antennes intégrées dans une cavité avec un plan de masse infini ou fini sont ensuite analysées à l'aide de plusieurs modèles de ligne de transmission simples. Le deuxième résultat clé de la thèse est une démonstration qu'un modèle de ligne de transmission spécifique et original correspond à des antennes qui peuvent atteindre la limite de la bande passante. Ce modèle de ligne de transmission constitue la base d'une nouvelle conception de l'antenne en cavité. Enfin, le résultat le plus important de la thèse est une conception physique pratique de nouvelles antennes en cavité capables d'atteindre la bande passante maximale possible. En outre, plusieurs autres sujets sont abordés; une comparaison avec des structures à base d'éléments empilés en termes de bande passante, de facilité de fabrication et de coût; l'extension de la limite grâce à l'inclusion de matériaux magnétiques idéaux et conducteurs magnétiques; l'utilisation de la nouvelle structure d'antenne pour la constitution d'un réseau d'antennes compact; les avantages de la nouvelle structure pour la réalisation d'antennes en cavité de tailles vraiment petites pour lesquelles la conception classique précédente ne permet pas la constitution d'antennes.

Dans cette thèse, nous étudions spécifiquement des cavités avec des ouvertures plus petites que $0.5 \lambda_0$ et les conditions pour obtenir la bande passante maximale possible. Des cavités rectangulaire (carré) et circulaire présentant des tailles d'ouverture de $0.15 \lambda_0$, $0.245 \lambda_0$, $0.3 \lambda_0$, et $0.37 \lambda_0$ sont choisis pour notre étude et sont considérés comme des "exemples de tailles d'ouverture" dans la suite du document. A des fins de conception, de simulation et de comparaison de toutes les antennes, une fréquence de fonctionnement de 2,3 GHz est choisie comme la résonance souhaitée pour ces antennes.

Introduction

La motivation de ce travail de doctorat est décrit creux à la Fig. 1, où plusieurs exemples de projectiles fabriqués/instrumentés à l'Institut franco-allemand de Recherches de Saint-Louis (ISL) sont présentés. Ici, une antenne est intégrée sur le culot du projectile pour une transmission de données (télémétrie). La bande de fréquence pour cette transmission est fixée à 2,3 GHz (longueur d'onde en espace libre ($\lambda_0 = 130.4$ mm)). Jusqu'à présent, les lignes directrices de conception reposaient sur des antennes classiques en technologie micro-ruban, c'est à dire une surface métallique conductrice ou "patch" placée sur un substrat diélectrique et excitée par une sonde, constituée par un câble coaxial qui est soudé au patch à la bonne position pour rendre l'antenne opérationnelle à 2,3 GHz.

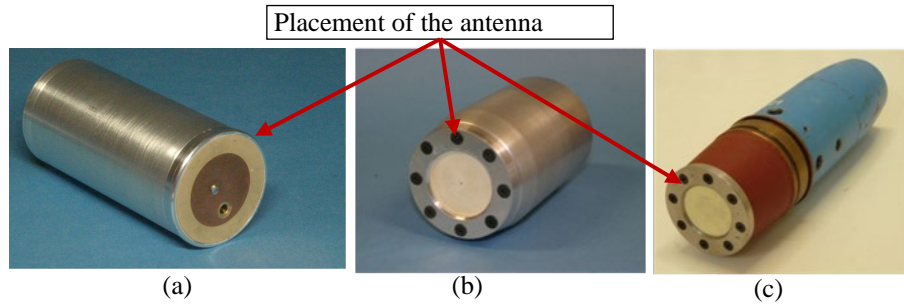


Fig. 1 Exemple de structures de l'ISL utilisant des antennes patchs placées dans une cavité. (a) un projectile avec une antenne patch à polarisation circulaire [1]. (b) et (c) projectiles avec des antennes intégrées au culot.

Des exemples de conception d'antennes micro-ruban en cavités sont également représentés à la Fig. 2. La géométrie cylindrique est plus intéressante pour les applications de l'ISL alors qu'une géométrie rectangulaire présente plus d'intérêt pour les études théoriques, où l'analyse est généralement plus simple.

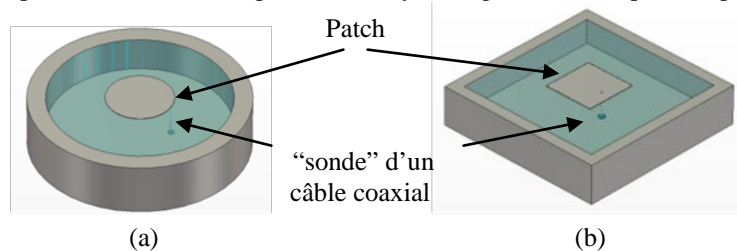


Fig. 2 Exemples typiques d'antennes patch en cavité (a) rectangulaire et (b) circulaire, considérées dans cette étude.

La principale conséquence de l'intégration de l'antenne à l'intérieur d'une cavité est la réduction de la bande passante disponible. En outre, la réduction de la taille (volume) de la cavité par rapport à la longueur d'onde d'espace libre réduit également considérablement la largeur de bande. Ce problème est illustré à la Fig. 3.

Quand une antenne est beaucoup plus petite que la longueur d'onde à la résonance, la largeur de bande est délimitée par des lois physiques et devient très étroite. Ainsi l'étude de la limite de la bande passante pour les antennes en cavité est d'une importance primordiale dans cette thèse.

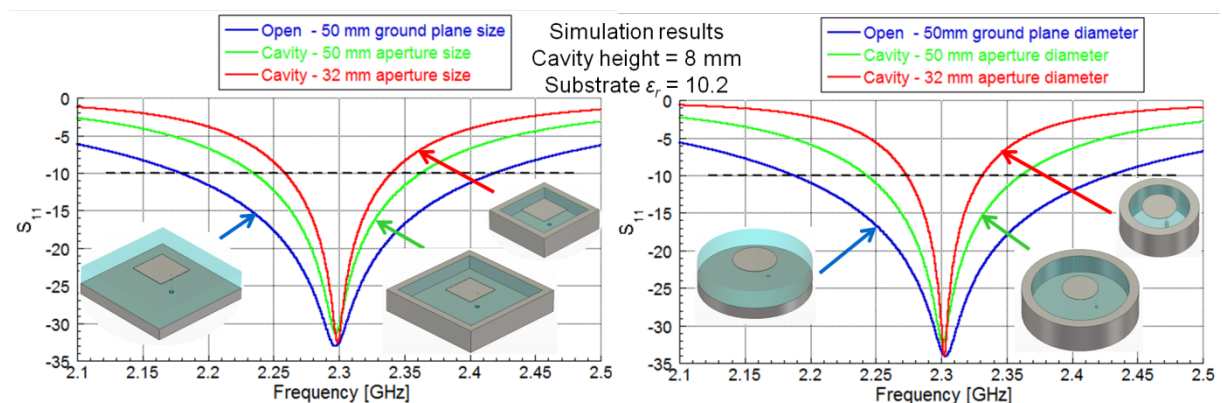


Fig. 3 Démonstration de la problématique principale de cette thèse : réduction de la bande passante avec la présence de la cavité et en particulier avec une petite taille de cette cavité. (a) Exemple d'une géométrie circulaire, et (b) d'une géométrie rectangulaire.

Les métamatériaux sont un sujet de recherche prometteur dans divers domaines, et en particulier dans l'électromagnétisme pour les applications de circuits (filtres, déphaseurs, etc) ou pour des applications de rayonnement (antennes, diffraction, dissimulation). Il s'agit de matériaux avancés, incluant de petits éléments (devant la longueur d'onde) et offrant dans des bandes de fréquence spécifiques, des propriétés particulières, qui sont différentes de celles des mêmes matériaux à leur état naturel. Parmi les différents avantages potentiels de métamatériaux rapportés dans la littérature se trouvent la miniaturisation des antennes, l'élargissement de la bande passante et la réduction du couplage mutuel dans un réseau d'antennes. Les métamatériaux semblent être une solution potentielle à l'amélioration de la bande passante de petites antennes. Néanmoins, les structures conçues jusqu'à maintenant ont été relativement larges et considérées dans un environnement ouvert, c'est-à-dire sans parois métalliques placés sur les côtés de l'antenne, comme dans le cas d'une cavité. Ici, les avantages de concepts de métamatériaux sur la bande passante des antennes sont étudiés dans un environnement cavité.

Dans la présentation des résultats de cette thèse, nous avons décidé de plusieurs paramètres pour faciliter la comparaison. Le paramètre le plus important, à des fins de conception, de simulation et de comparaison de la bande passante de toutes les antennes, est la fréquence de fonctionnement de 2,3 GHz comme résonance souhaitée, ce qui correspond à une longueur d'onde en espace libre $\lambda_0 = 130.4$ mm et au nombre d'onde $k = 2\pi/\lambda_0 = 48.2$. Pour des cavités rectangulaires, nous avons choisi de nous concentrer sur le cas de l'ouverture carrée où l'ouverture de la cavité est prise à 20 mm, 32 mm, 40 mm et 48 mm. Dans le cas de la cavité circulaire, le diamètre d de l'ouverture est choisi pour être de 20 mm, 32 mm, 40 mm et 50 mm. Il est également courant d'exprimer la taille électrique de l'antenne en fonction de (kr) where r est le rayon de la sphère la plus petite intégrant l'antenne. Ces dimensions sont résumées dans le Tableau 1 et seront appelés "*exemple de tailles d'ouverture*" dans la suite du texte.

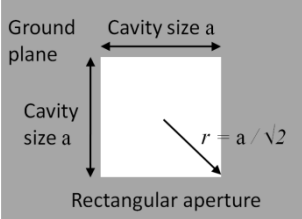
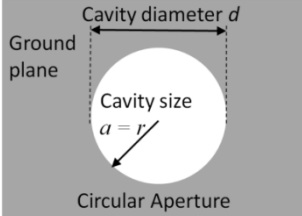
	Exemples de taille d'ouverture: cavité carré			
	Size a	$a [\lambda_0]$	Radius r	(kr)
	20 mm	0.153	14.142 mm	0.679
	32 mm	0.245	22.627 mm	1.086
	40 mm	0.307	28.284 mm	1.358
	48 mm	0.368	33.941 mm	1.629
	Exemples de taille d'ouverture: cavité circulaire			
	Diameter d	$d [\lambda_0]$	Radius $r = a$	(ka)
	20 mm	0.153	10 mm	0.480
	32 mm	0.245	16 mm	0.768
	40 mm	0.307	20 mm	0.960
	50 mm	0.383	25 mm	1.200

Tableau 1 Comparaison des ouvertures rectangulaires et circulaires.

A l'ISL, les matériaux diélectriques antennes disponibles et utilisés pour la fabrication des antennes sont des matériaux Rogers de permittivité relative 3,66, 6,15 et 10,2, soit Rogers 4350, Rogers 3006, et Rogers 3010 respectivement. Il a donc été décidé d'utiliser ces valeurs de permittivité dans nos analyses et simulations. Un résumé est donné dans le Tableau 2.

Material	Permittivity	$\tan \delta$
Air	1	0
Polypropylene	2.26	0.002
Rogers 4530	3.66	0.004
Rogers 3006	6.15	0.002
Rogers 3010	10.2	0.0023

Tableau 2 Récapitulatif des propriétés électriques des matériaux considérés dans cette thèse

Des simulations numériques ont été réalisées avec le logiciel commercial, CST Microwave Studio. L'une des premières conclusions des simulations de conception d'antenne classique concerne l'utilisation des résonances multiples pour l'amélioration de la bande passante ; par exemple, des patches empilés (stacked patches), plusieurs patches parasites et d'autres géométries (complexes) sont utilisés pour introduire deux ou plus de résonances proches afin d'élargir la bande passante. Cependant, nous avons constaté que lorsque de telles structures sont placées dans un petit volume de cavité, le couplage entre les résonateurs est trop serré et l'effet désiré devient

impossible. La conclusion est que, dans une très petite cavité le mieux que nous pouvons faire est d'étudier une antenne à résonance unique et les conditions pour atteindre une bande passante maximale possible (de manière équivalente: le facteur Q minimum possible).

Les objectifs généraux de la thèse

Basé sur la problématique de petites antennes en cavité, l'objectif principal de cette thèse est de répondre aux questions suivantes:

- Quelle est la bande passante théorique maximale possible d'une antenne dans une cavité?
- Des concepts inspirés de métamatériaux peuvent ils apporter des avantages pour la bande passante et la réduction de la taille par rapport à la conception classique de l'antenne patch?
- Est-il possible de concevoir et de fabriquer des antennes dans de très petites cavités avec une bande passante suffisante pour des applications spécifiques?
- Existe-t-il des avantages pour un réseau compact d'antennes en termes de réduction de la taille, d'amélioration de la bande passante et de réduction de couplage mutuel inter-élément ?

Les objectifs pratiques spécifiques

Du point de vue pratique, les objectifs sont de concevoir, simuler et analyser des antennes patch compactes dans des petites cavités avec les restrictions suivantes:

- diamètre circulaire de la cavité: 20mm ($0.15 \lambda_0$), 32mm ($0.245 \lambda_0$), 40mm ($0.3 \lambda_0$), and 50mm ($0.38 \lambda_0$).
- Epaisseur maximale de l'antenne: jusqu'à 20mm ($0.15 \lambda_0$).
- Fréquence de fonctionnement 2.3 GHz
- Les matériaux diélectriques à être utilisés: Polypropylène ($\epsilon_r = 2.26$) Rogers 3.66, Rogers 6.15 and Rogers 10.2
- Diagramme de rayonnement identique à celui d'un patch, c'est-à-dire vers le demi-espace au-dessus de l'élément rayonnant
- Fabrication et mesure d'antennes

Antennes cavités simples ouvertes

Nous commençons par montrer comment analyser la forme la plus simple d'une antenne cavité, à savoir des cavités ouvertes à une extrémité et sans métallisation sur cette surface. Dans sa thèse de doctorat, Cohen [53] a donné une analyse approfondie de petites antennes en cavité rectangulaire. Pour plus de simplicité, l'étude a été réalisée pour une géométrie rectangulaire dans un plan de masse infini. Nous reproduisons ici les principaux résultats, car ils seront d'une grande importance dans le reste de la thèse.

Considérons une cavité rectangulaire enterré dans un plan de masse infini et rempli avec un matériau homogène de permittivité ϵ_r et de perméabilité $\mu_r = 1$ comme le montre la Fig. 4. La cavité peut être considérée comme un guide d'onde en court-circuit et ouvert vers un demi-espace. Celui-ci peut être modélisé par une ligne de transmission ayant un court-circuit sur un côté et une charge à l'autre côté (correspondant à l'ouverture).

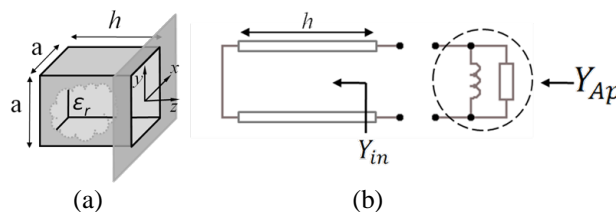


Fig. 4 (a) A square cavity in an infinite ground plane and (b) the corresponding transmission line model.

On suppose que le mode TE_{10} est dominant dans le guide d'ondes rectangulaire. La constante de propagation dans un guide d'onde rectangulaire est $k_{TE}^2 = \epsilon_r k^2 - k_c^2$ où $k^2 = \omega^2 \mu_0 \epsilon_0$ est le nombre d'onde, et $k_c = \pi/a$ est

le nombre d'onde de coupure pour le mode TE_{10} . L'admittance caractéristique pour les modes TE est $Y_{TE} = k_{TE}/\omega\mu = k_{TE}/k\eta_0$ et donc l'admittance d'entrée Y^C dans un guide d'onde court-circuité (cavité) est

$$Y^C(k) = Y_{TE} \frac{Y_{TE} + jY_T \tan(k_{TE}h)}{Y_T + jY_{TE} \tan(k_{TE}h)} = -j \frac{k_{TE}}{k\eta_0} \cot(k_{TE}h), \quad (1)$$

où $Y_T = \infty$ l'admission de court-circuit. Pour plusieurs valeurs de permittivité relative, l'admittance d'entrée est tracée en fonction de la hauteur h à la Fig. 5. Pour des cavités courtes, l'admittance d'entrée est inductive (négative).

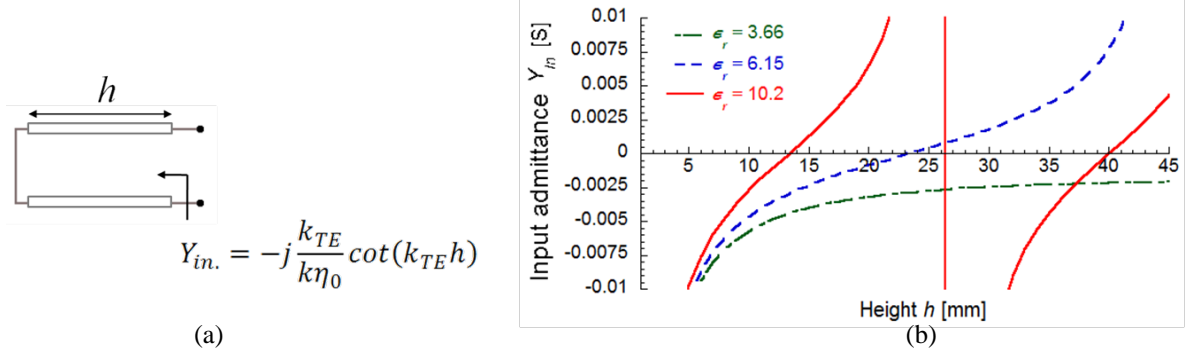


Fig. 5 (a) le modèle de ligne de transmission d'un guide d'onde en court-circuit qui représente la cavité. (b) Exemples d'admittance d'entrée dans un guide d'onde carré court-circuit de taille $0.245 \lambda_0$ à la fréquence $f = 2.3$ GHz ($k = 48.2$) lorsque le volume est homogène rempli de permittivité relative de 3.66, 6.15 et 10.2.

D'autre part, l'extrémité ouverte de la structure est modélisée par l'admittance d'ouverture Y^{Ap} . Cette admittance peut être calculée analytiquement, en utilisant l'approche dans le domaine spectral. Le calcul complet figure en **Annexe C** pour le mode TE_{mn} général. Nous n'écrivons ici que l'expression finale pour le mode TE_{10}

$$Y^{Ap}(k) = G^{Ap} + jB^{Ap} = \frac{ab}{8k\eta_0} \iint_{\mathbb{R}^2} \frac{k^2 - k_x^2}{\sqrt{k^2 - k_x^2 - k_z^2}} \left(\frac{\cos\left(\frac{k_x a}{2}\right) \text{sinc}\left(\frac{k_y b}{2}\right)}{\left(\frac{\pi}{2}\right)^2 - \left(\frac{k_x a}{2}\right)^2} \right)^2 dk_x dk_y. \quad (2)$$

L'intégrale dans (1.56) doit être calculée numériquement pour chaque valeur de k . Toutefois, le résultat de Y^{Ap} pour l'ouverture carrée ($a = b$) a été donné par Cohen dans [53] sous la forme d'une série de Taylor,

$$\begin{aligned} G^{Ap}(x) &= g^0 x^2 + g^1 x^4 + g^2 x^6 \dots, \\ B^{Ap}(x) &= b^0 x^{-1} + b^1 x + b^1 x^3 + \dots, \end{aligned} \quad (3)$$

Avec $x = a/\lambda_0 = ka/(2\pi)$. L'admittance d'ouverture est représentée sur la Fig. 6 où l'admission pour les exemples de tailles étudiées dans cette thèse est également notée. En fait, dans tous les cas, l'admission est négatif (inductive).

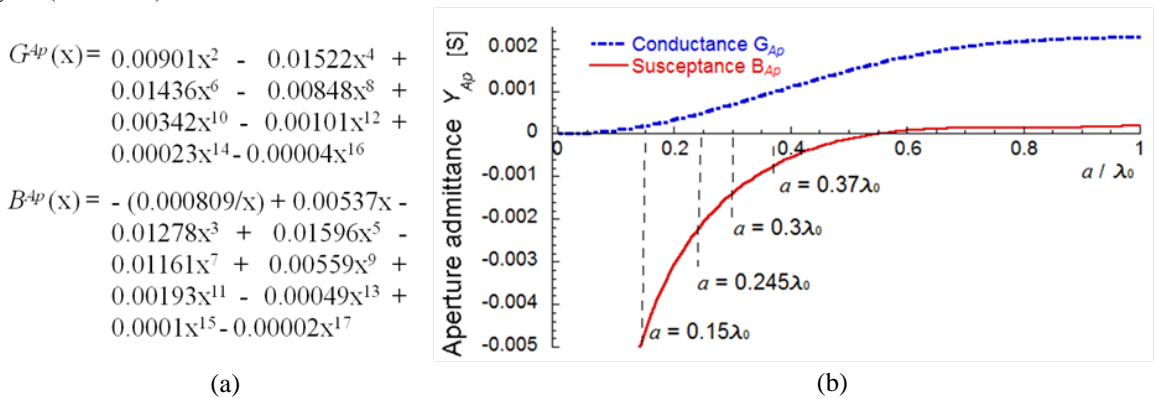


Fig. 6 Admittance d'ouverture Y^{Ap} pour le mode TE_{10} donné par (1.56) ou (1.57). Voir l'annexe C pour la dérivation. (a) approximation polynomiale donnée en termes de $x = a/\lambda_0 = ka/(2\pi)$ (b) un tracé de la partie réelle et imaginaire de Y^{Ap} en fonction de la taille de la cavité. Notez que pour les exemples de tailles d'ouverture la susceptance est inductive.

Sans sources, le système de la Fig. 4(b) oscille lorsque les réactances dans le circuit s'annulent, soit :

$$jB^{Ap}(k) - j\frac{k_{TE}}{k\eta_0}\cot(k_{TE}h) = 0, \quad (4)$$

Où B^{Ap} est la susceptance d'ouverture, $k_{TE}^2 = \epsilon_r k^2 - k_c^2$ avec $k^2 = \omega^2 \mu_0 \epsilon_0$, $k_c = \pi/a$, a est le côté d'une ouverture carrée et h la hauteur de la cavité. Notez que nous avons transformé la géométrie vers un modèle 1D qui est facile à analyser. Il ya deux variables dans (4) à savoir la hauteur h et la permittivité ϵ_r . Pour obtenir la résonance, l'un ou l'autre peut être ajusté. Ici, il est plus utile de traiter ϵ_r en fonction de la hauteur h , donc l'équation (4) est utilisée pour obtenir la permittivité ϵ_r nécessaire pour une hauteur h donnée de la cavité.

Une fois que la hauteur de résonance est connue, on peut calculer le facteur de qualité d'une telle antenne à l'aide des formules définies dans (A 22) de l'annexe A

$$Q_{Ant.} = \frac{\omega_0}{2G^{Ap}(\omega_0)} \left| \frac{\partial Y(\omega)}{\partial \omega} \right|_{\omega=\omega_0} = \frac{k_{0r}}{2G^{Ap}(k_{0r})} \left| \frac{\partial Y(k)}{\partial k} \right|_{k=k_{0r}}, \quad (5)$$

Où ω_0 est la fréquence de résonance, et de façon équivalente, k_{0r} nombre d'onde de résonance, $Y = Y^C + Y^{Ap}$ est l'admittance totale du circuit, soit la somme des admittances de l'ouverture et du guide d'onde, donnée par

$$Y(k) = G^{Ap}(k) + jB^{Ap}(k) - j\frac{k_{TE}}{k\eta_0}\cot(k_{TE}h). \quad (6)$$

En outre, nous sommes intéressés par la bande passante relative d'adaptation, définie en Annexe A et qui est calculée directement à partir du facteur Q comme

$$FBW = \frac{2\sqrt{\beta}}{Q}, \quad \beta = \frac{\alpha}{1-\alpha}, \quad \alpha = |\Gamma_0(\omega)|^2 \quad (7)$$

où $\Gamma_0(\omega)$ est le coefficient de réflexion. Comme pour les applications antennes, la largeur de bande pour un coefficient de réflexion inférieur à -10 dB est souvent l'objectif souhaité, on obtient l'expression de la bande passante suivante en considérant la valeur de $\alpha = 0.1$:

$$FBW_{-10dB} = \frac{2}{3Q_{Ant.}}. \quad (8)$$

En utilisant les relations (4), (5) et (8), on peut prédire analytiquement la bande passante des antennes en cavité. Les prévisions pour les exemples de tailles d'ouverture dans le cas rectangulaire sont présentées à la Fig. 7.

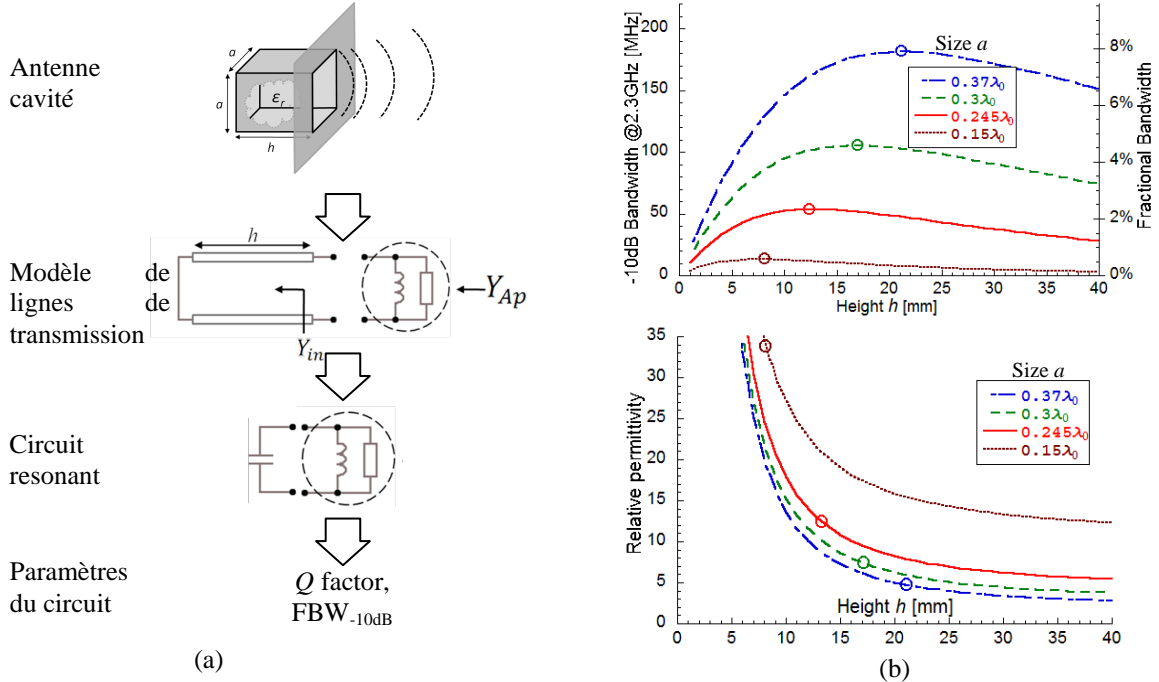


Fig. 7 Le comportement de la bande passante des antennes en cavité rectangulaire pour l'exemple des tailles d'ouverture. (a) Synthèse de la façon dont l'antenne est analysé. (b) bande passante par rapport à la hauteur de la cavité, avec une permittivité correspondant pour chacune des valeurs de hauteur. Les cercles sur les courbes indiquent la largeur de bande maximale pouvant être atteinte pour une taille donnée.

Il existe des combinaisons optimales de valeurs de hauteur-permittivité pour une taille d'ouverture spécifique qui va donner une bande passante maximale (Q minimum). Dans [53] Cohen a utilisé la technique d'optimisation mathématique des multiplicateurs de Lagrange et donné une formule approximative pour le Q minimum d'antennes en cavité lorsque $(a/\lambda_0) < 0.35$, soit

$$Q_{min}^{square} (Cohen) \cong 0.424 \left(\frac{a}{\lambda_0} \right)^{-3}, \quad (9)$$

où a est la dimension de l'ouverture carrée, λ_0 la longueur d'onde en espace libre. La dépendance cubique révèle une ressemblance avec la formule de limite Chu bien connu. A des fins de comparaison de la relation (9) avec la limite de Chu, on peut introduire r comme étant le rayon de la plus petite sphère qui entoure l'ouverture de la cavité. La valeur de r pour une ouverture carrée est la moitié de la diagonale du carré donnée par $r = a/\sqrt{2}$. Nous pouvons ré-écrire la validité de l'expression $(a/\lambda_0) < 0.35$ sous la forme $ka < 2.2 \Leftrightarrow kr < 1.55$ et re-exprimer (9) comme

$$Q_{min}^{square} (Cohen) \cong \frac{105.17}{(ka)^3} = \frac{37.18}{(kr)^3} \quad (10)$$

Sous la forme (10), il est évident que la prédiction pour les très petites cavités est beaucoup plus grande d'un facteur d'environ 37 par rapport à la limite de Chu. A noter que ni la permittivité ni la hauteur n'entrent dans la formule explicite, car il est supposé que pour chaque taille d'ouverture les valeurs optimales de h et ϵ_r sont utilisés.

En utilisant une analyse similaire, l'auteur a étendu les résultats de Cohen à des cavités circulaires et à des cavités circulaires dans un plan de masse de dimensions latérales finies. Un résumé de tous les résultats est présenté dans le Tableau 3.

Type de cavité	Carré	Circulaire
Plan de masse infini	$Q_{min}^{square} \cong \frac{37.18}{(kr)^3}$	$Q_{min}^{circular} = \frac{19.75}{(ka)^3}$
Plan de masse fini	$Q_{min}^{square} \approx \frac{29.3}{(kr)^3}$	$Q_{min}^{circular} \approx \frac{17.5}{(ka)^3}$

Tableau 3 Résumé des résultats théoriques pour des antennes cavités simples ouvertes indéterminée. $r = a/\sqrt{2}$ où a est le rayon d'une ouverture circulaire, et a est le côté d'une ouverture carrée.

Antennes patch en cavité

Contrairement à une antenne patch classique alimentée par sonde sans cavité, lorsque la sonde est dans une petite cavité, les murs agissent comme un bouclier et aident à établir un mode TEM. La cavité et la sonde se comportent comme un câble coaxial dont l'âme est excentrée, avec une impédance caractéristique qui est différente de 50 Ohms. La mise en place du mode TEM à l'intérieur de la cavité est une raison majeure expliquant la possibilité d'augmenter la hauteur au-delà de ce qui est possible pour des antennes patch classiques.

En outre, une antenne patch classique alimentée par sonde excite seulement son mode fondamentale (TM_{010}). Toutefois, pour les substrats épais, la cavité représente une petite partie d'un guide d'onde de sorte que le patch excite aussi le mode TE_{10} fondamental du guide d'onde de forme rectangulaire (carré). Ce fait est crucial dans l'explication des résultats présentés. Le "mode de guide d'ondes" nous permet d'augmenter la hauteur plus que possible pour des antennes patch classiques. Il est également responsable de l'évolution progressive des dimensions de l'antenne patch dans une cavité comme vu dans l'exemple détaillé des Fig. 8(c) et Fig. 9(b).

Des simulations détaillées d'antennes patch dans des cavités carrés et circulaires pour les exemples de tailles ont été réalisées. Toutefois, sur les Fig. 8 et Fig. 9 nous ne présentons que les exemples les plus illustratifs qui montrent tous les aspects intéressants de ces antennes. Il ya plusieurs détails importants que nous souhaitons souligner:

Tout d'abord, sur la Fig. 8(a) le résultat pour une antenne cavité simple ouverte de géométrie carrée est présenté. Nous nous concentrons sur la bande passante pour des permittivités spécifiques ($\epsilon_r = 3.66, 6.15$ et 10.2). Une antenne cavité nécessite une combinaison spécifique de valeurs de hauteur et de permittivité, donc un seul point représente une antenne cavité simple ouverte. A noter que pour $\epsilon_r = 3.66$ le guide d'ondes est sous sa fréquence de coupure et antenne cavité simple ouverte n'est pas possible. Pour une cavité circulaire, sur la Fig. 9,

les points indiquant les antennes de la cavité sont immédiatement combinés avec les résultats des simulations de l'antenne patch.

Deuxièmement, sur les figures Fig. 8(b) et Fig. 9(a), nous voyons les résultats de simulation pour une antenne patch à l'intérieur d'une cavité. Les principales différences par rapport à l'antenne cavité simple ouverte sont que, au lieu d'un seul point pour une permittivité spécifique, nous avons maintenant une courbe pour chaque valeur de permittivité. Fait important, les points indiquant les antennes cavité simples ouvertes apparaissent à la fin de la courbe de bande passante pour les antennes patch. Comme il n'y a pas de point pour une antenne cavité remplie de $\epsilon_r = 3.66$ la courbe de l'antenne patch correspondant peut effectivement se prolonger indéfiniment, mais il a été décidé de ne présenter que les résultats jusqu'à une hauteur de 40 mm.

Troisièmement, sur les figures Fig. 8(c) et Fig. 9(b) des représentations des antennes simulées (et optimisées) pour différentes hauteurs sont présentées. Cela montre que la taille du patch est réduite lorsque la hauteur h de la cavité est augmentée. En fait, pour les cas $\epsilon_r = 6.15$ et 10.2 la taille se réduit à zéro (et est inadaptable), et donc l'antenne se transforme en une antenne cavité simple ouverte. Pour le cas $\epsilon_r = 3.66$ la taille se réduit mais au-dessus d'une certaine hauteur de cavité elle reste à une valeur relativement constante.

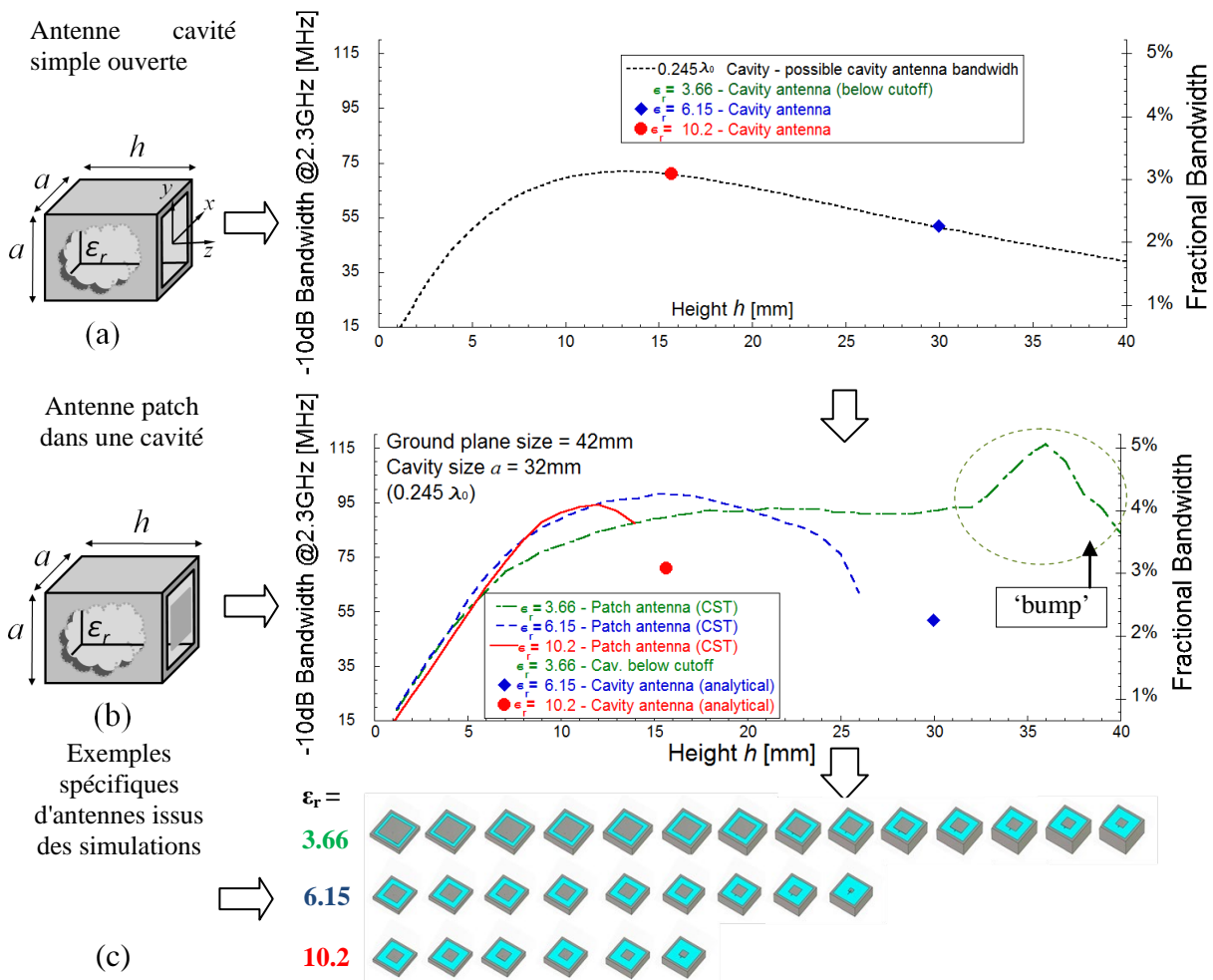


Fig. 8 Exemple détaillé d'une ouverture de cavité de $0.245 \times 0.245 \lambda_0$ dans un plan de masse fini. (a) prédiction d'analyse de la bande passante d'une antenne cavité simple ouverte. La courbe indique un comportement de la bande passante générale qui dépend de ϵ_r , et les points indiquent des cas particuliers lorsque le volume est rempli avec $\epsilon_r = 3.66, 6.15$ et 10.2 . (b) Les résultats de simulation pour la bande passante à 10dB d'antennes patch en cavité, ainsi que les points pour le cas de l'antenne cavité simple ouverte. (c) géométries d'antennes réelles issues de CST. En raison du manque d'espace, les images CST sont présentées pour des incréments de hauteur $\Delta h = 2$ mm.

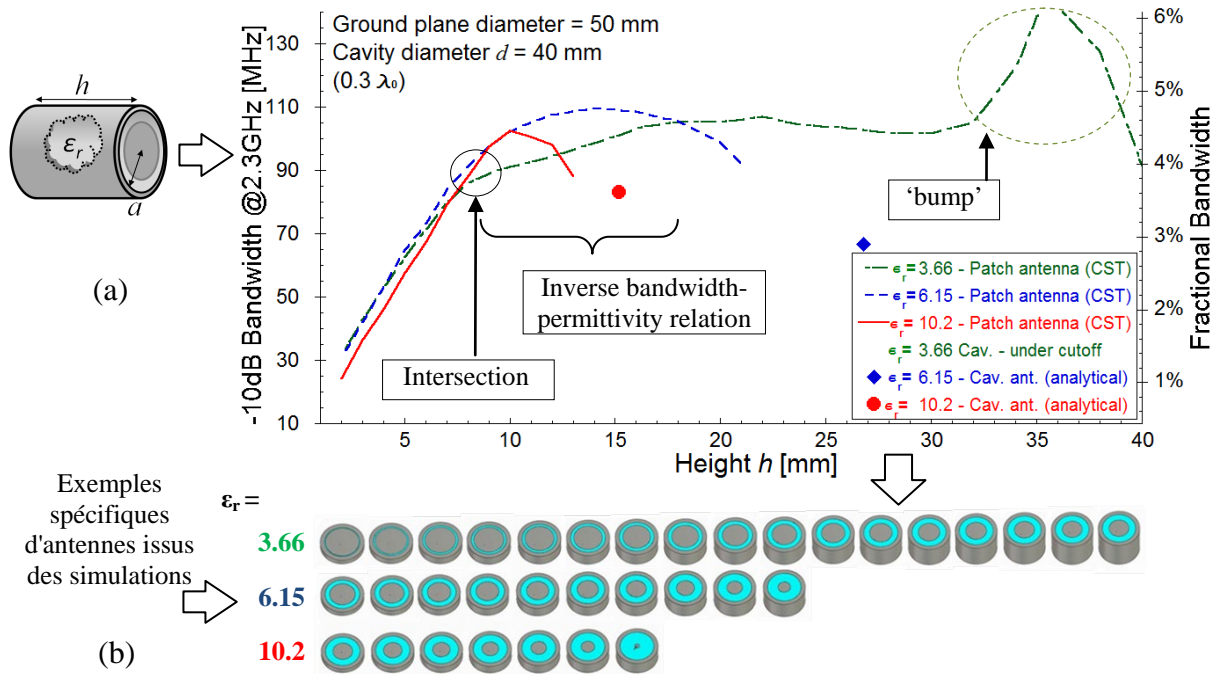


Fig. 9 Exemple détaillé d'une ouverture de cavité de diamètre $0.3 \lambda_0$ dans un plan de masse fini. (a) Les résultats de simulation pour la bande passante à -10dB d'antennes patch dans une cavité, ainsi que les points pour le cas de l'antenne cavité simple ouverte. (b) géométries d'antennes réelles issues de CST. En raison du manque d'espace, les images CST sont présentées pour des incréments de hauteur $\Delta h = 2$ mm.

Il ya plusieurs observations sur le comportement de la bande passante qui peuvent être faites sur la base des résultats de simulation :

- Pour les très petites cavités les meilleurs résultats sont obtenus avec la plus haute permittivité
- Pour des cavités fines, le comportement de l'antenne patch classique peut être observé (une permittivité plus élevée conduit à une bande passante réduite)
- Pour des cavités épaisses des phénomènes inhabituels peuvent se produire :
 - dépendance inverse de la largeur de bande avec la permittivité pour des cavités épaisses
 - "bosses" inhabituels sur les courbes de bande passante pour certains cas de grande hauteur de la cavité.
- Pour toutes les tailles de cavité, la bande passante est plus élevée dans le cas du plan de masse fini.

Modèle expliquant la relation bande passante-permittivité

Lorsque le substrat est épais, un patch peut exciter le mode TE fondamental de la cavité. Par rapport à l'ouverture d'une antenne cavité simple ouverte, un patch localisé à l'ouverture va changer l'admittance d'ouverture. Le modèle complet est une simple modification du modèle d'antenne cavité simple ouverte et est représentée sur la Fig. 10.

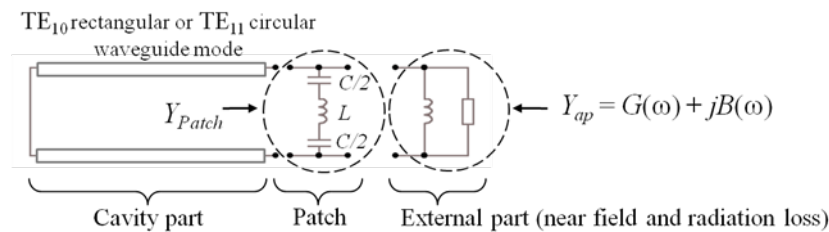


Fig. 10 Modèle de ligne de transmission d'une cavité avec un patch à l'ouverture. Le patch est modélisée par un circuit résonnant série en parallèle à l'admittance de l'ouverture. Notons que le modèle est raisonnable pour les cavités épaisses avec une ouverture de taille inférieure à la moitié de la longueur d'onde en espace libre.

La condition de résonance pour le modèle de la Fig. 10 peut s'écrire

$$jB^{Ap} - j\frac{k_{TE}}{k\eta_0}\cot(k_{TE}h) + \frac{1}{j\omega C + j\omega L} = 0, \quad (11)$$

Où k_{TE} et B^{Ap} dépendent du type de cavité particulier à l'étude. C'est une équation avec trop de variables, à savoir la hauteur h , la permittivité relative ϵ_r , la capacité C , et l'inductance L . Ici, nous voulons simplement utiliser le modèle proposé pour expliquer les phénomènes observés dans nos résultats de simulation et nous allons essayer de deviner la valeur de L .

Example: prenons L comme un simple paramètre. Nous montrons un exemple de prédiction de la bande passante en fonction de la hauteur à la Fig. 11 pour une cavité rectangulaire de taille 32 mm et pour plusieurs valeurs de L . Pour des cavités fines le modèle ne prédit évidemment pas le comportement correct car le mode TM_{010} n'est pas modélisé; pour les cavités épaisses le comportement peut être considéré comme présentant des similitudes avec les résultats de la simulation.

Le modèle est capable de prédire l'inversion de dépendance de la bande passante avec permittivité. L'ampleur de ce phénomène, ainsi que la bande passante maximale, dépendent de la valeur de l'inductance L . Pour les faibles valeurs d'inductance, le phénomène disparaît et la largeur de bande maximale est beaucoup plus élevée. C'est la conclusion la plus importante tirée de ce modèle.

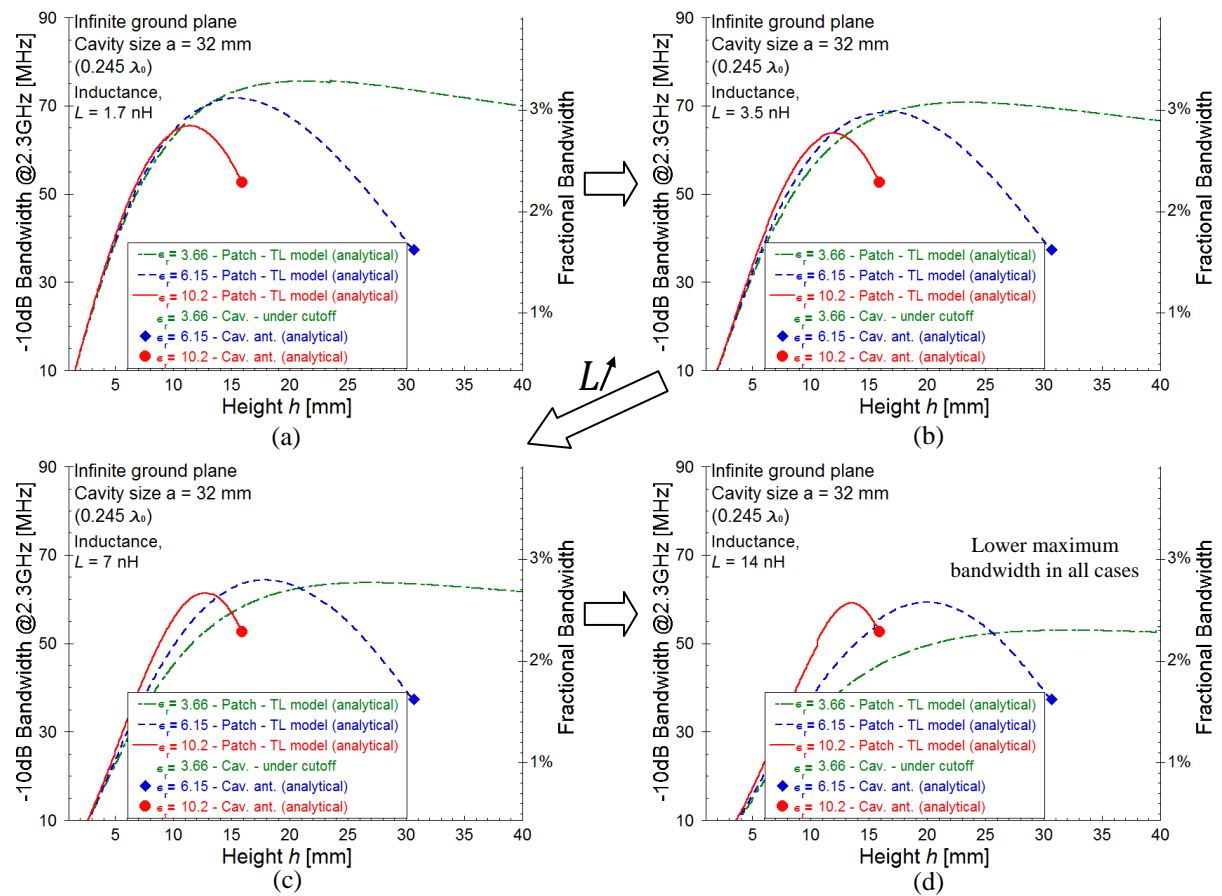


Fig. 11 Le comportement de la bande passante prédite avec l'augmentation de l'inductance du circuit oscillant série (a) $L = 1.7$ nH (b) $L = 3.5$ nH (c) $L = 7$ nH (d) $L = 14$ nH

Modèle expliquant le phénomène de bosse de la bande passante

Le modèle proposé à la Fig. 10 ne peut pas tenir compte des "bosses" dans les courbes de bande passante dans les cas de cavités fonctionnant en dessous de la fréquence de coupure. Pour remédier à cet inconvénient, nous avons besoin de modéliser aussi la partie alimentation de l'antenne. La sonde et la cavité circulaire forment un câble coaxial dont l'âme est excentré et supportant un mode TEM coaxial. Tel que présenté à la Fig. 12, une ligne de transmission supplémentaire de la même longueur que la hauteur de la cavité est ajoutée en parallèle à l'un des condensateurs dans le modèle. Les valeurs des deux condensateurs dans le modèle est maintenant différent, désigné par $C1$ et $C2$ (la valeur du condensateur $C2$ avec la ligne ajoutée étant beaucoup plus grande).

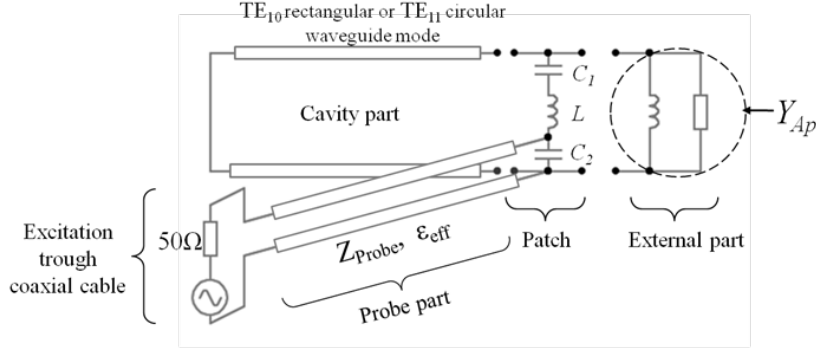


Fig. 12 Modèle incluant la partie alimentation de l'antenne ; le câble coaxial 50 Ohm venant au fond de la cavité et l'âme centrale se trouvant dans la cavité forment une seconde partie de ligne coaxial. Le guide d'onde et la sonde ont la même longueur h .

La Fig. 13 présente la bande passante calculée en utilisant le modèle de la Fig. 12. En comparant à la Fig. 11(c) la différence constatée est la «bosse» dans le cas de la cavité remplie avec une permittivité de 3.66 (en dessous de la fréquence de coupure).

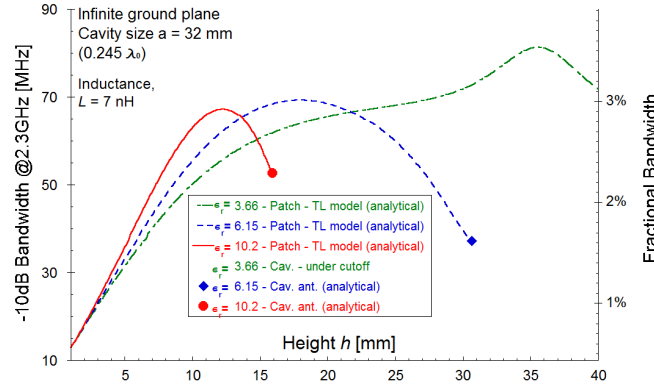


Fig. 13 Prédictions analytiques qualitatives en utilisant le modèle en Fig. 12. La valeur de l'inductance L a été estimée à 7nH dans les trois cas de valeurs de permittivité.

Limite de Q_{min} pour l'antennepatch en cavité cavité

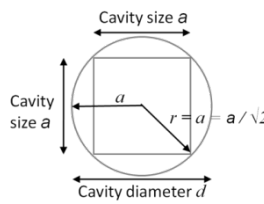
La limite de Gustafsson [26] sur le facteur Q minimum possible d'une antenne à polarisation linéaire est donnée comme suit :

$$Q_{min} = \frac{2 \pi D}{\eta k_0^3 \gamma}, \quad (12)$$

où k est le nombre d'onde en espace libre et D de la directivité de l'antenne. η représente le rapport de la puissance absorbée à la somme des puissances absorbées et dispersées, appelé efficacité d'absorption. Pour des antennes bien adaptées à diffusion minimales, on peut prendre $\eta = 0.5$, et nous allons assumer cette valeur tout au long de la thèse. Enfin, γ est la polarisabilité totale de l'antenne de réception considérée comme un objet de diffusion.

Le principal avantage de la nouvelle limite est qu'elle est valable pour des géométries quelconques. Nous avons été en mesure de l'appliquer au problème de cavités dans un plan de masse infini. Dans cette thèse, la polarisabilité géométries de cavité carrés et circulaires sont dérivées analytiquement. Sur la base de la dérivation, de nouvelles limites de telles antennes ont été trouvés. Les résultats ont été résumés dans le

Tableau 4 ci-dessous (avec l'hypothèse d'une très grande hauteur de la cavité pour simplifier la formule).



Comparaison des facteurs Q	Carré	Circulaire
Limite de Chu (general)	$Q = \frac{1}{(kr)^3} + \frac{1}{(kr)}$	$Q = \frac{1}{(ka)^3} + \frac{1}{(ka)}$
Limite de Gustafsson (Plan de masse fini)	$Q = \frac{20.78}{(kr)^3} + \frac{1.78}{(kr)}, h \gg$	$Q = \frac{10.88}{(ka)^3} + \frac{1.53}{(ka)}, h \gg$

Tableau 4 Résumé des résultats théoriques de la borne sur le Q minimum pour les antennes de la cavité. . $r = a/\sqrt{2}$ où a est le rayon d'une ouverture circulaire, et a est le côté du carré.

Sur la base de la limite de Q, on peut obtenir une prédiction de la largeur de bande maximale possible en utilisant (8) Les résultats pour les cavités carrés et circulaires sont donnés à la Fig. 14.

Une conclusion importante de ces prévisions est que les antennes patch ne parviennent pas à la bande passante prédite. Un nouveau type d'antenne est nécessaire pour atteindre la limite.

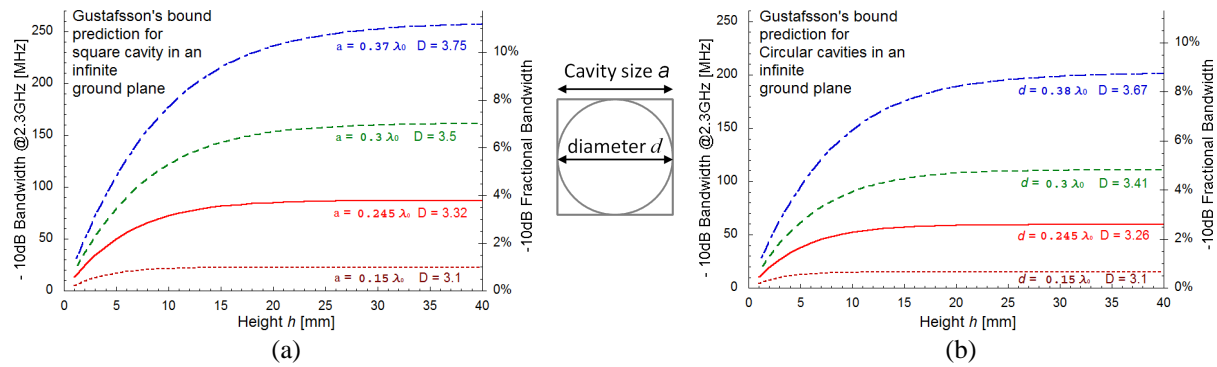


Fig. 14 Comparaison des résultats de bande passante maximale prédit ene fonction de la hauteur, basé sur la limite de Gustafsson pour des cavités (a) carré et (b) circulaire.

Modèle pour des antennes en cavité atteignant bande passante maximale

Ici, nous présentons un modèle d'une antenne qui peut atteindre la bande passante maximale prévue. Par rapport à de simples cavités ouvertes, un condensateur supplémentaire est introduit au niveau de l'ouverture, comme illustré à la Fig. 15.

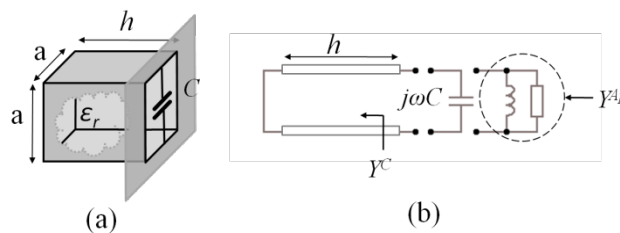


Fig. 15 (a) Nouvelle antenne en cavité avec la capacité parasite à l'ouverture, et (b) son modèle de ligne de transmission.

Nous supposons que le condensateur ne perturbe pas trop le champ ce qui exclut un élément localisé qui concentrerait le champ dans un très petit volume. Le condensateur doit être une surface idéale à impédance réactive.

A partir de ce modèle, la condition de résonance est à présent donnée par

$$jB_{Ap}(k) - j \frac{k_{TE}}{k \eta_0} \cot(k_{TE} h) + j c_0 k C = 0, \quad (13)$$

où tout est écrit en termes de nombre d'onde k, avec c₀ la vitesse de la lumière. La condition de résonance est maintenant une équation à trois variables, h, C, et εᵣ. Cependant, εᵣ peut être une constante et fixé à la meilleure valeur. Ceci nous permet de considérer la capacité C comme une fonction de la hauteur h.

Exemple: les prévisions de bande passante basées sur le modèle de la Fig. 15 sont montrées à la Fig. 16 pour un plan de masse infini et une cavité rectangulaire 32mm. La Fig. 16 peut être directement comparés à la Fig. 11. On peut voir que des résultats optimaux (maximaux) sont obtenus pour $\epsilon_r = 1$.

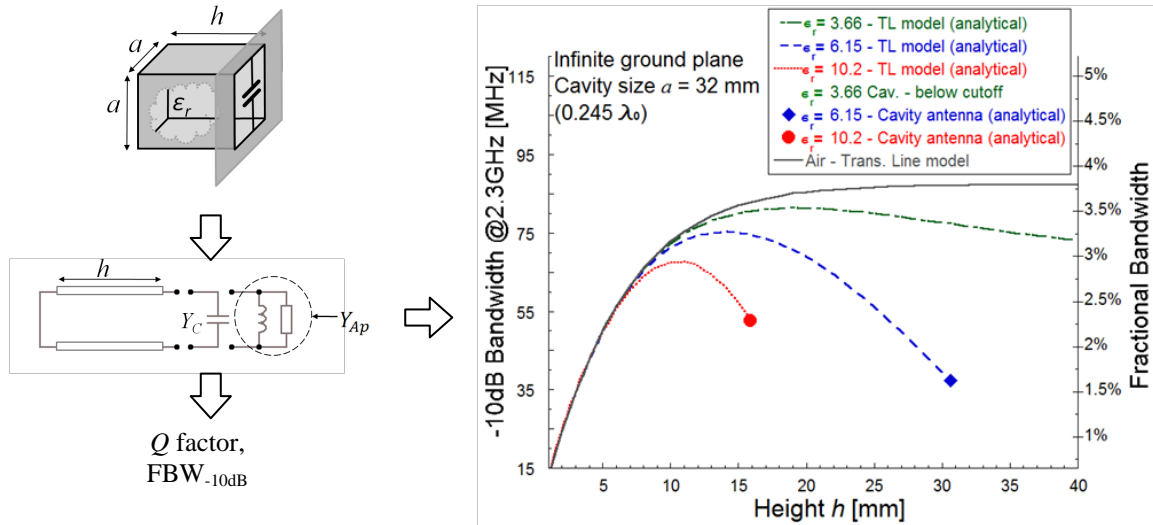


Fig. 16 Les résultats calculés pour une cavité carrée ($a = 32$ mm) à l'aide du modèle de ligne de transmission. Les points représentent l'antenne cavité simple ouverte. La courbe grise pleine correspond à pour une cavité remplie d'air et se révèle le meilleur des cas.

Fait important, le modèle de ligne de transmission peut être étendue à des cavités dans un plan de masse fini. La seule différence par rapport au cas du plan de masse infini se trouve dans l'admittance d'ouverture, qui peut être obtenue grâce à la simulation. Une comparaison des résultats pour le Q minimal obtenue en utilisant le modèle de ligne de transmission est donnée dans le Tableau 5.

Comparaison des facteurs Q	Carré	Circulaire
Limite de Gustafsson (Plan de masse infini)	$Q = \frac{20.78}{(kr)^3} + \frac{1.78}{(kr)}, h \gg$	$Q = \frac{10.88}{(ka)^3} + \frac{1.53}{(ka)}, h \gg$
Limite approximative Pour un plan de masse fini	$Q \approx \frac{14.3}{(kr)^3} + \frac{2.4}{(kr)}, h \gg$	$Q \approx \frac{8.25}{(ka)^3} + \frac{2.5}{(ka)}, h \gg$

Tableau 5 Résumé des résultats théoriques pour le facteur de qualité minimum sur la base du modèle de ligne de transmission de la Fig. 15. $r = a/\sqrt{2}$ où a est le rayon d'une ouverture circulaire, et a est le côté du carré.

Nouvelles antennes atteignant la limite prévue

Conception physique du condensateur à l'ouverture

En disposant plusieurs petits patches au lieu d'un seul grand conduit à une diminution de l'inductance et à la capacité souhaitée "pure" à l'ouverture (sans partie réelle). L'évolution de ce processus est illustrée à la Fig. 17 pour les ouvertures circulaires et rectangulaires.

La conclusion de notre étude à partir de simulations est une estimation approximative que des éléments plus petits qu'environ $1/13 \lambda_0$ sont nécessaires pour approcher correctement le condensateur à l'ouverture, représentée à la Fig. 17. Par conséquent, les éléments satisfont aux critères des métamatériaux (taille de l'élément $< 1/10 \lambda_0$). La structure peut donc être appelée une metasurface.

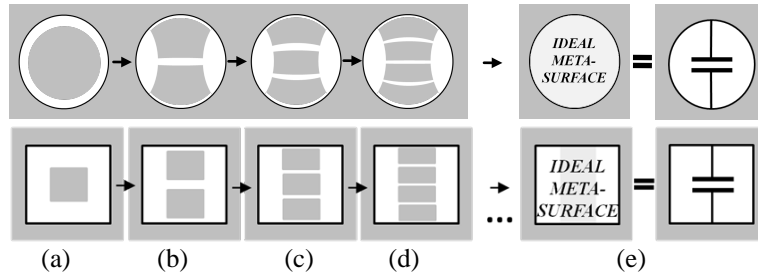


Fig. 17 Conceptions possibles d'éléments micro-ruban à l'ouverture d'une cavité carrée. (a) un seul patch - utilisé jusqu'à présent dans la littérature, (b) deux éléments, (c) trois éléments, premier concept à donner une assez bonne approximation d'une capacité pure à l'ouverture, (d) quatre éléments, (e) cas idéal d'une capacité pure à l'ouverture.

Conception d'une nouvelle antenne en cavité

Sur la Fig. 18 est représentée une conception d'antennes schématique répondant aux besoins pratiques. L'écart g entre les éléments est ajusté pour atteindre la valeur idéale de la capacité. L'écart entre la paroi de la cavité et le premier élément de la metasurface est $g/2$. La présence de colle avec une épaisseur gt dans cet écart peut sensiblement affecter les performances. La colle modifie l'effet capacitif global de la metasurface en raison de sa valeur de permittivité différente et introduit des pertes supplémentaires (élevées). Il est donc souhaitable de rendre les intervalles entre les éléments de la metasurface et la paroi le plus large possible, afin de réduire relativement l'effet de la colle. Cela peut être fait en utilisant un substrat de permittivité élevée sur lequel est gravée la metasurface et en utilisant plusieurs couches de métallisation pour augmenter la capacité.

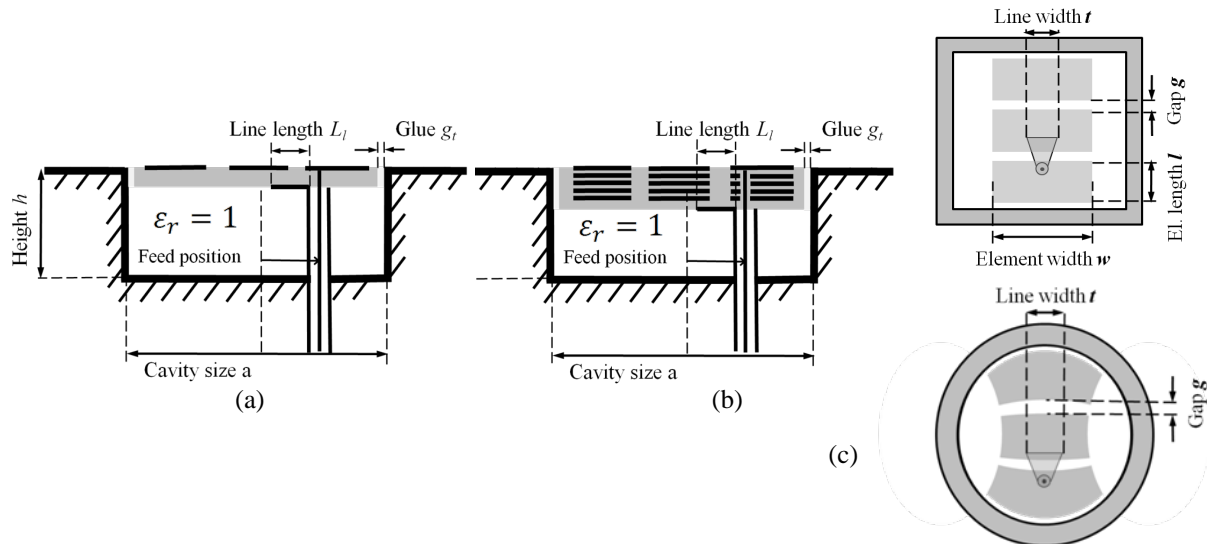


Fig. 18 Exemple schématique d'une conception pratique à des fins de fabrication. La seule couche de substrat à l'ouverture présente une permittivité $\epsilon_r \gg 1$, dans notre travail, $\epsilon_r = 10.2$ a été choisi. (a) Vue de côté d'une conception simple couche. (b) Vue de côté d'une conception multicouche nécessaire pour de très petites tailles de la cavité. (c) Vue du dessus.

Une Metasurface avec plusieurs couches de métallisation, illustré à la Fig. 18(b), constituera effectivement un condensateur "épais" et augmentera la capacité. Cependant, la conception de plusieurs couches doit être évitée si possible. Seul dans le case de très petites cavités, où un grand effet capacitif est nécessaire, nous sommes obligés de considérer cette option.

L'excitation est réalisée avec un câble coaxial s'étendant presque jusqu'à l'ouverture et avec l'âme central s'étendant jusqu'au bord de l'élément supérieur de la metasurface. Une courte ligne de transmission est ajoutée au niveau de la gaine extérieure du câble coaxial, qui est capacitivement couplée au bord du second élément de la metasurface. En outre, il a été constaté que le rétrécissement en triangle (tapering) de cette ligne de transmission peut donner des résultats légèrement meilleurs. La largeur w des éléments métalliques affecte également les performances de la bande passante. Des éléments plus larges forcent le champ électrique à l'ouverture à être plus uniforme plutôt qu'une distribution sinusoïdale, ce qui conduit à des performances légèrement supérieures. Cependant, avec des éléments de metasurface plus larges, l'écart entre les éléments doit être réduit. Finalement, une largeur de la moitié de la taille de la cavité a été jugée adaptée.

Des exemples de résultats de simulation avec la nouvelle conception proposée de l'antenne sont présentés à la Fig. 19 pour une cavité de 32 x 32 mm. Pour le cas du plan de masse infini à la Fig. 19(a), la limite a été atteinte avec une conception à trois éléments. Dans le cas du plan de masse fini à la Fig. 19(b), la prédiction est approximative car elle ne prend pas en compte le changement de plan de masse lorsque la hauteur augmente. En raison de ce problème, il y a un léger décalage entre théorie et simulations.

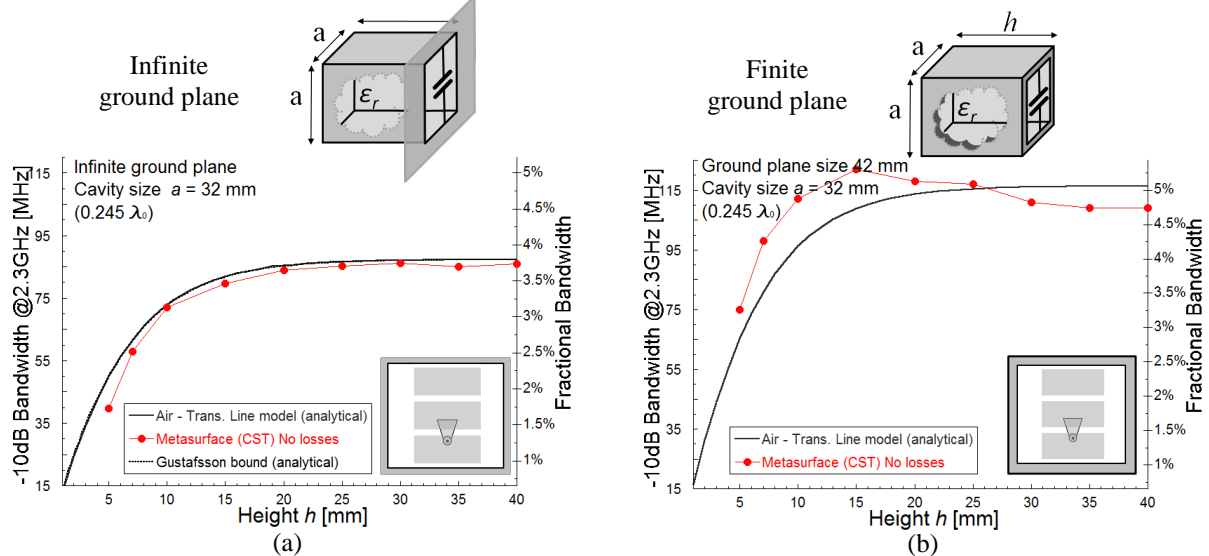


Fig. 19 Comparaison des résultats de la simulation d'une conception de metasurface avec les prédictions d'analyse du modèle de ligne de transmission et avec la limite de Gustafsson. (a) plan de masse infini et (B) plan de masse fini

Avantages de la nouvelle conception

Tout d'abord, la nouvelle conception de metasurface permet de créer des antennes en cavité atteignant la bande passante maximale prédite. Cette bande passante est plus élevée que précédemment avec des antennes patch. En outre, par rapport aux antennes patch, la directivité et le gain de ces antennes ne sont pas affectés. Deuxièmement, la nouvelle conception permet de créer de très petites antennes en cavité. Par exemple, dans le passé à l'ISL, les antennes patch ne pouvaient pas être fabriquées dans des cavités circulaires de diamètre inférieur à 22 mm (avec une permittivité maximale de 10). Cependant, de petites antennes basées sur les metasurfaces en cavité ont été fabriquées avec succès et qualifiées pour être opérationnelles (voir les résultats des mesures ci-dessous). Ces deux aspects sont une grande amélioration par rapport aux modèles précédents. En ce qui concerne les projectiles, cela ouvre des possibilités pour l'instrumentation de petits projectiles et l'instrumentation de projectiles avec des antennes dont la bande passante offerte est plus large ce qui permet de transmettre plus d'informations et ce qui permet également une plus grande tolérance dans le processus de fabrication. En outre, il est intéressant de noter que les matériaux utilisés présentent de faible permittivité. Ces matériaux sont généralement beaucoup moins chers. Le matériau idéal en termes de permittivité est l'air; il ne présente que très peu de pertes et est gratuit. Toutefois, à des fins mécaniques le volume doit être rempli avec un matériau dur qui peut résister à des forces élevées (accélérations très importantes lors d'un coup de canon). Un matériau qui convient à ces exigences mécaniques est le polypropylène avec une permittivité $\epsilon_r = 2.26$ et une tangente de pertes $\delta = 0.002$. Dans l'antenne proprement dite, la métallisation est gravée sur une couche de matériau Rogers coûteux, mais l'épaisseur de cette couche est faible et le reste du volume est rempli avec du polypropylène moins coûteux. Le coût total des antennes devrait donc être inférieur à celui d'antennes patchs en cavités. En conclusion, sur la base de tous ces exemples, on peut dire que de nouvelles possibilités ont été apportées par l'introduction du concept à base de metasurface.

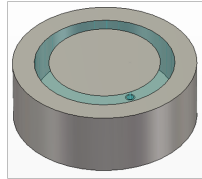
Antennes fabriquées et résultats de mesure

Des prototypes d'antennes en cavité avec un patch ou une metasurface ayant des ouvertures de 32 mm ($0.245 \lambda_0$), 20 mm ($0.15 \lambda_0$) et 16 mm ($0.12 \lambda_0$) ont été fabriqués à l'Institut franco-allemand de Recherches de Saint-Louis (ISL) pour confirmer la faisabilité de ces antennes; la conception, ainsi que les résultats de mesure sont présentés à la Fig. 20 et sont résumés dans le Tableau 6.

Résultats expérimentaux pour les cavités circulaires dans un plan de masse fini			
Dimensions d'ouverture	Patch	Metasurface	Commentaires
32 mm	60 MHz	90 MHz	Elargissement 50%
20 mm	non réalisable	21 MHz	Nouvelle faisabilité
16 mm	non réalisable	22 MHz	

Tableau 6 Résumé des largeurs de bande mesurées pour des cavités circulaires.

Ouverture de 32 mm

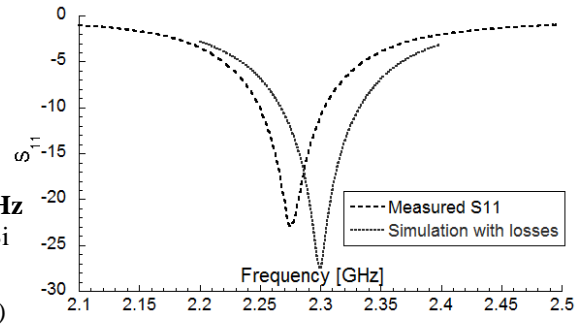


$\epsilon_r = 6.15$

Sim. BW = 64 MHz
 Sim. Directivity = 4.71dBi
 Sim. Relised gain = 4.5dBi

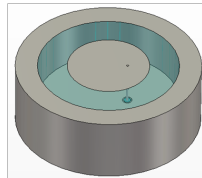


Mes. BW = 52 MHz
 Mes. gain \approx 3.9 dBi



(a)

Ouverture de 32 mm

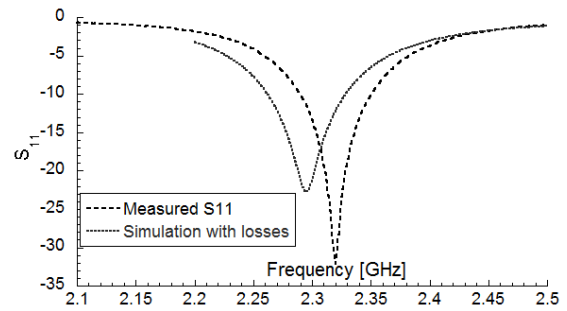


$\epsilon_r = 10.2$

Sim. BW = 64 MHz
 Sim. Directivity = 4.71dBi
 Sim. Relised gain = 4.5dBi

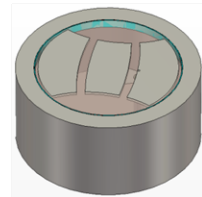


Mes. BW = 60 MHz
 Mes. gain \approx 4.2 dBi



(b)

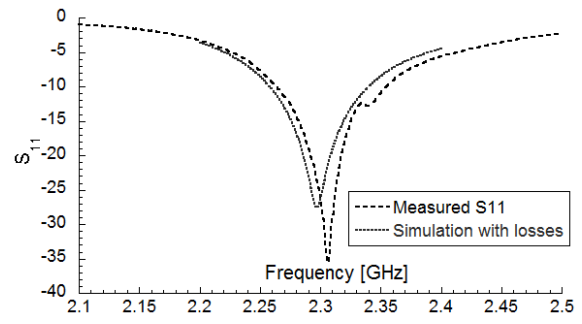
Ouverture de 32 mm



Sim. BW = 77 MHz
 Sim. Directivity = 4.71dBi
 Sim. Relised gain = 4.5dBi

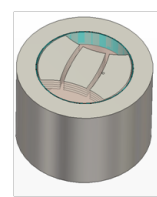


Mes. BW = 90 MHz
 Mes. gain \approx 3.9dBi



(c)

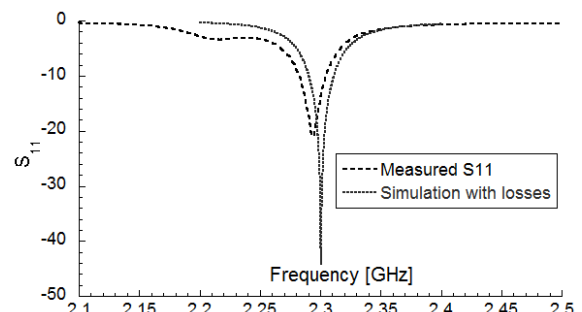
Ouverture de 20 mm



Sim. BW \approx 20 MHz
 Sim. Directivity = 3.69 dBi
 Sim. Realized gain = 0.8 dBi

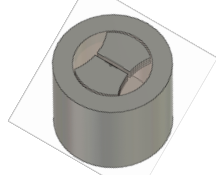


Mes. BW \approx 21 MHz
 Mes. gain = -1 dBi

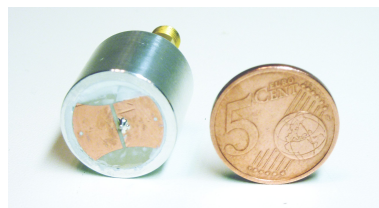


(d)

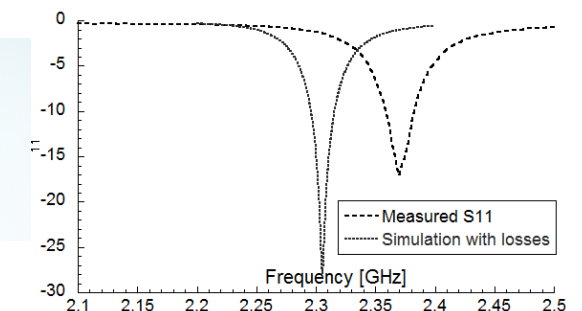
Ouverture de 16 mm



Sim. BW \approx 19.8 MHz
 Sim. Directivity = 3.28 dBi
 Sim. Realized gain = -3 dBi



Mes. BW \approx 22MHz
 Mes. gain = -5.5 dBi



(e)

Fig. 20 Prototypes mesurés: (a) Cavité de diameter 32 mm rempli avec $\epsilon_r = 6.15$ et un patch l'ouverture. (b) Cavité de diameter 32 mm rempli avec $\epsilon_r = 10.2$ et un patch l'ouverture. (c) Cavité de diameter 32 mm rempli avec $\epsilon_r = 1$ (excepté le substrat supérieur sur lequel est gravé la métasurface) et une métasurface à 3 éléments à l'ouverture. (c) Cavité de diameter 20 mm rempli avec $\epsilon_r = 1$ (excepté pour les substrats avec métallisation et une métasurface à 2 éléments à l'ouverture. (c) Cavité de diameter 16 mm rempli avec $\epsilon_r = 1$ (excepté pour les substrats avec métallisation et une métasurface à 2 éléments à l'ouverture.

Sujets additionnels

Potentiel des matériaux magnétiques pour des antennes en cavité

Les matériaux magnétiques et conducteurs peuvent améliorer de manière significative la limite de la bande passante. De l'avis de l'auteur, cette analyse n'est qu'une lecture intéressante pour l'instant, mais pourrait devenir important à l'avenir avec les progrès de la nano-technologie.

Nous supposons un matériau ou un conducteur magnétique idéal, ce qui signifie pas de dépendance à la fréquence et des valeurs arbitraires, pour obtenir le "cas du meilleur résultat."

Les conducteurs magnétiques parfaits (PMC) ne se trouvent pas dans la nature. Cependant, lorsqu'on les suppose placés sur les parois de la cavité comme à la Fig. 21, la propagation à l'intérieur du guide d'ondes n'est pas évanescence et la distribution du champ à l'ouverture change. La limite résultante est beaucoup plus faible que le cas de la cavité carré régulière.

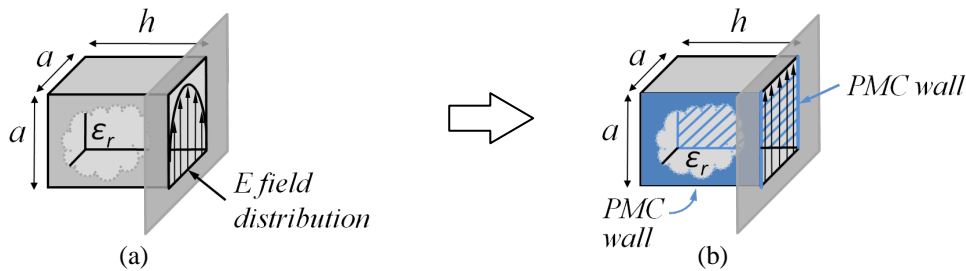


Fig. 21 (a) Cavité métallique carré régulière avec une distribution de champ TE_{10} à (b) Cavité carré avec des conducteurs magnétiques parfaits sur deux parois, rendant la distribution du champ à l'ouverture et à l'intérieur du guide d'onde uniforme.

Si le volume de la cavité est remplie d'un matériau magnétique à haute perméabilité idéale (voir Fig. 22) la limite sur le Q minimum est également plus faible. Comme l'énergie électromagnétique à l'intérieur du guide d'ondes (cavité) est évanescence dans le cas standard (sans PMC), l'effet de la cavité diminue pour de grandes épaisseurs h . L'introduction d'un matériau magnétique rend la constante de décroissance plus grande et l'énergie décroît rapidement avec l'augmentation de h . En outre, l'admittance inductive dans le guide d'onde devient petite et finalement se rapproche de l'admittance d'un circuit ouvert (zéro). Dans ce cas, l'antenne est essentiellement modélisée par un circuit résonnant parallèle pour lequel (voir *Annexe A*) on a $Q = 1/(\omega_0 GL)$, ainsi une plus grande inductance diminue Q . Ceci est visuellement représenté à la Fig. 23.

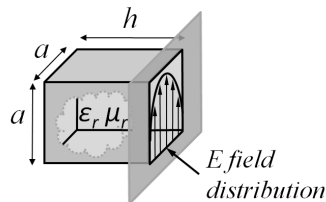


Fig. 22 Cavité métallique carrée avec une distribution de champ de TE_{10} à l'ouverture remplie d'un matériau magnéto-diélectrique.

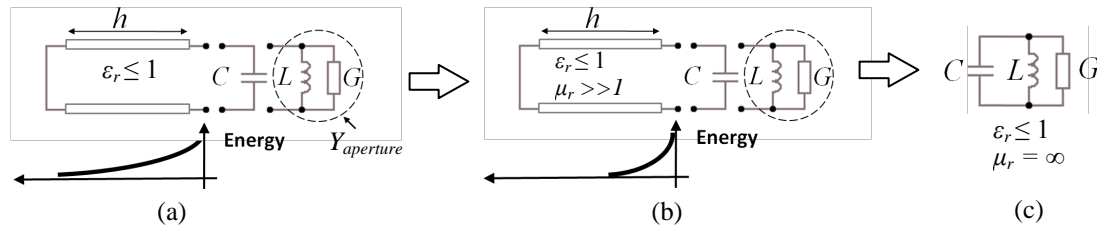


Fig. 23 Croquis du modèle d'une cavité antenne montrant l'énergie en décroissance à l'intérieur de la cavité pour (a) un matériau diélectrique à faible permittivité; (b) pour un matériau magnétique à haute perméabilité; (c) pour un matériau avec une perméabilité infinie lorsque le modèle peut être réduite à un simple circuit résonnant parallèle.

Les limites théoriques pour des cavités remplies de matériaux magnétiques ou conducteurs magnétiques sont résumées dans le Tableau 7.

Comparaison des facteurs Q	Carré	Circulaire	Comment
- un matériau magnétique (plan de masse infini)	$Q = \frac{7.87}{(kr)^3} + \frac{0.67}{(kr)}, \mu_r \gg 1$	$Q = \frac{4.28}{(ka)^3} + \frac{0.6}{(ka)}, \mu_r \gg 1$	Peut-être réalisables dans les basses fréquences ou dans l'avenir avec les progrès de la nanotechnologie
- avec conducteur magnétique (plan de masse infini)	$Q = \frac{2.97}{(kr)^3} + \frac{0.29}{(kr)}, h \gg \lambda$	Pas clair	Probablement pas possible car il n'existe pas de conducteurs magnétiques naturels

Tableau 7 Résumé des résultats théoriques sur la borne du facteur Q minimum pour des cavités remplies avec des matériaux magnétiques ou des conducteurs magnétiques. $r = a/\sqrt{2}$ où a est le rayon d'une ouverture circulaire, et h est le côté du carré

Applications pour des tailles de cavités proches de la demie-longueur d'onde

Nous donnons ici deux brefs exemples des possibilités avec un metasurface dans une cavité dont la taille est très proches de $0.5 \lambda_0$ à 2.3 GHz. Nous démontrons qu'ils peuvent être utilisés pour créer des antennes à large bande et même dépasser la bande passante de patchs empilés, ce qui en fait une conception supérieure, même pour de grandes cavités. La raison de cela? Il existe une deuxième résonance à une fréquence plus élevée due uniquement à la taille de la cavité étant comparable à $0.5 \lambda_0$. La seconde résonance est une conséquence du comportement de l'admittance d'ouverture pour une taille d'ouverture au-dessus de $a/\lambda_0 > 0.5$, où la partie réelle est grande et la partie imaginaire est proche de zéro. Un exemple de comparaison entre les patchs empilés et la structure à base de metasurface est représenté à la Fig. 24. La metasurface présente une bande passante plus large et est plus simple à réaliser. Elle n'utilise qu'une seule couche de substrat tandis que les patchs empilés en requierent deux. En outre, des matériaux de permittivité faible sont nécessaires, ce qui rend la conception de metasurface moins cher dans la pratique.

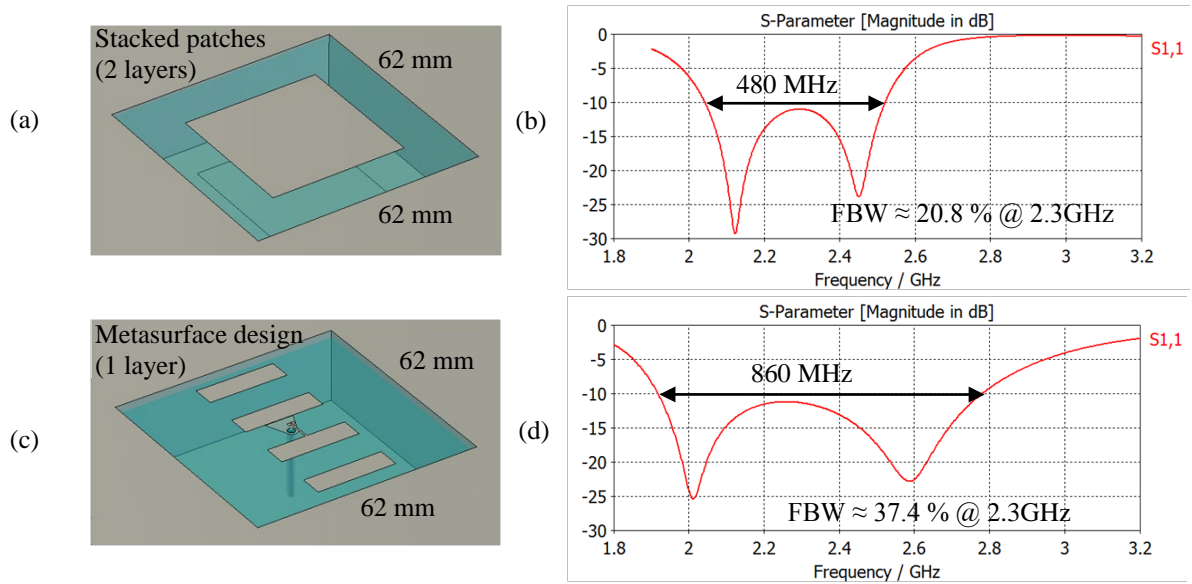


Fig. 24 La comparaison entre les patches empilés et une métasurface dans une cavité rectangulaire de dimensions $62 \times 62 \times 20$ mm soit $0.475 \times 0.475 \times 0.15 \lambda_0$ à 2.3 GHz incorporés dans un plan de masse infini. (a) Vue en perspective des patches empilés. (b) paramètre simulé S_{11} pour les patches empilés. (c) Vue en perspective d'un élément métasurface de 4 éléments de largeur 24 mm. (d) paramètre simulé S_{11} pour la métasurface.

Applications pour la construction d'un réseau d'antennes compact

La détection de l'arrivée (DOA) est une méthode de détermination de la direction de propagation d'une onde incidente de haute fréquence sur un réseau d'antennes. Dans la perspective de créer un système compact de DOA (taille $d = 0.15 \lambda_0$) de système d'arrivée, nous avons étudié un réseau de quatre éléments (le reste de ce projet est actuellement en cours à l'ISL). Nous donnons ici un bref exemple d'une conception possible de réseau compact. La configuration d'antenne est donnée à la Fig. 25. Le diamètre du plan de masse n'est que de $0.46 \lambda_0$ et les quatre antennes ont une cavité de diamètre $0.15 \lambda_0$. Chaque élément est mis en rotation de 90 degrés par rapport à son voisin. Parce que les éléments eux-mêmes sont polarisés linéairement cette rotation met les éléments dans des positions orthogonales et minimise le couplage mutuel entre antennes. Cependant, les éléments 1 et 3 (ainsi que de 2 et 4) de la Fig. 25(a) sont malheureusement orientées dans le même sens, ce qui entraîne un couplage relativement élevé (10 dB), comme on le voit à la Fig. 25(b). La bande passante de chaque élément reste pratiquement la même que pour l'antenne unitaire en cavité (dans le cas présent environ 14,4 MHz). De plus, cette conception est capable de donner une polarisation circulaire moyennant un circuit de distribution adapté.

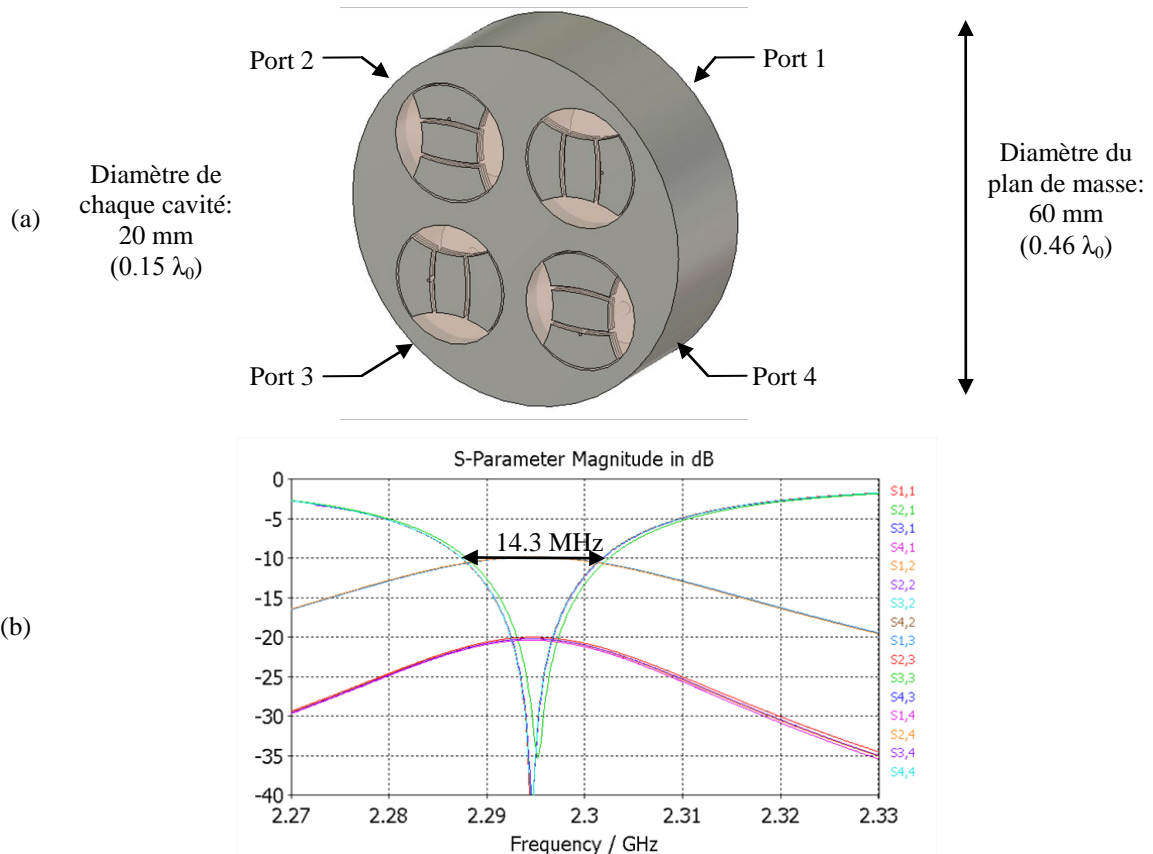


Fig. 25 (a) Géométrie du réseau d'antenne compacte pour l'application DOA. (b) les paramètres de diffusion simulés montrant la bande passante approximative de chaque antenne est environ 14 MHz et le couplage entre les antennes en diagonale de -10 dB.

Conclusion

Le but de ce travail était d'étudier des antennes en cavité compactes et électriquement petites. La question principale était : est-il possible d'utiliser des concepts de métamatériaux pour développer des antennes plus petites en cavité et en même temps augmenter leurs performances en bande passante par rapport aux types d'antenne en cavité utilisés aujourd'hui. Heureusement, la réponse à ces questions est affirmative. Cette thèse a étudié les antennes en cavité de trois façons: en théorie, par une analyse rigoureuse des limites de ces antennes; numériquement, par la réalisation de nombreuses simulations pour confirmer la théorie ou découvrir de nouveaux effets; et expérimentalement, par la fabrication de prototypes basés sur la théorie et les simulations numériques. De cette façon, le sujet des antennes en cavité a été complètement exploré et a été développée avec l'introduction d'un nouveau type d'antenne en cavité. Le nouveau type d'antenne peut être qualifié «inspiré des métamatériaux» en raison de l'utilisation d'une metasurface à l'ouverture de la cavité. Il est important à deux égards: il est capable d'atteindre la limite théorique de Q pour les petites antennes, et il peut être rendu très faible dans la pratique; ces deux aspects sont une grande amélioration par rapport aux types d'antennes utilisés dans la littérature à ce jour.

*Development and characterization of metamaterials
in cavities. Applications to the design of compact
antennas*

Abstract

This thesis presents new developments in cavity type antennas. Cavities of rectangular and circular shapes in an infinite and finite ground plane are investigated in detail. The main objective of the thesis is the bandwidth performance analysis of antennas in cavities with aperture sizes which are small compared to the free space wavelength. So far in the literature, microstrip patch antennas were the antenna of choice for cavity type antennas; their aperture sizes being about half the free space wavelength. Here we give a thorough investigation of the performance of patch antennas in very small cavities, showing dependence on aperture size, cavity depth and substrate permittivity. However, the intention of the thesis is to determine if cavity type antennas can be improved and how, or do patch antennas still present the best choice in terms of bandwidth performance and ease of fabrication. To this end, the bound on bandwidth for cavity antennas is investigated theoretically. The bound on Q factor and corresponding maximum bandwidth for rectangular and circular cavities is derived analytically in the case of an infinite ground plane using the scattering approach. It is demonstrated that patch antennas, in fact, do not reach the bound for cavity antennas, which is one of the key results of the thesis. Unfortunately, the scattering approach is not extendable to finite sized cavities. Infinite and finite sized ground plane cavity antennas are further analyzed using several simple transmission line models. The second key result of the thesis is a demonstration that a special transmission line model corresponds to antennas that reach the bound Q and predicted maximum bandwidth. This special transmission line model is then the basis to a new design of cavity antennas. Importantly, the transmission line model is indeed extendable to finite sized ground planes. A new micro-strip antenna design is suggested, that falls into a category of metasurface antennas. Finally, the practical physical design, including the excitation, of a new type of small cavity antennas capable of reaching the predicted maximum bandwidth is presented. Additionally, we show measurement results from several prototypes of such antennas which can be considered as a meta-surface inspired antenna.

Furthermore, we explore several additional topics; A comparison with stacked patches design in terms of bandwidth, ease of fabrication, and cost; The extension of the bound on bandwidth with the inclusion of ideal magnetic materials and magnetic conductors; The new antenna design use in constructing a compact antenna array with superior bandwidth compared to classical design; The benefits of the new design for constructing small cavity antennas not feasible with the classical design.

In this thesis we specifically study cavities with apertures smaller than $0.5 \lambda_0$ and the conditions to achieve the maximum possible bandwidth. Rectangular (square) and circular aperture sizes with sides of $0.15 \lambda_0$, $0.245 \lambda_0$, $0.3 \lambda_0$, and $0.37 \lambda_0$ are chosen for our investigation and are referred to as “*example aperture sizes*” in the text. For purposes of design, simulations and bandwidth comparison of all antennas, an operation frequency of 2.3 GHz is chosen as the desired resonance for antennas in cavities of example aperture sizes.

General introduction

HISTORY

This three year PhD thesis on small size cavity antennas was conducted at IETR (Institute d'Electronique et de telecommunications de Rennes) for a period of two years. These two years were concentrated on mainly theoretical and numerical investigations of cavity antennas under the supervision of Professors Ronan SAULEAU, Kourosh MAHDJoubi and Sylvain COLLARDEY from IETR. The last, third year was conducted at ISL (Institut franco-allemand de recherches de Saint-Louis) under the supervision of Loic BERNARD where the emphasis was on building working prototypes of antennas and publishing the results. The project was co-financed by the Région Bretagne ARED program, and ISL.

CONTEXT AND OBJECTIVES OF THE STUDY

Interest in this Ph.D. work can be described through Figure 1 where several example projectiles manufactured at ISL are shown. On the bottom of the projectile is an integrated antenna for transmission of telemetry data. Frequency band for this transmission is fixed at 2.3 GHz (free space wavelength $\lambda_0 = 130.4$ mm). So far, manufactured antennas used microstrip technology and followed classical design guidelines for microstrip patch antennas i.e. a metallic surface or "patch" placed on a dielectric substrate and excited by a wire (probe) from a coaxial cable which is soldered to the patch at the right position as to make the antenna operational at 2.3 GHz.

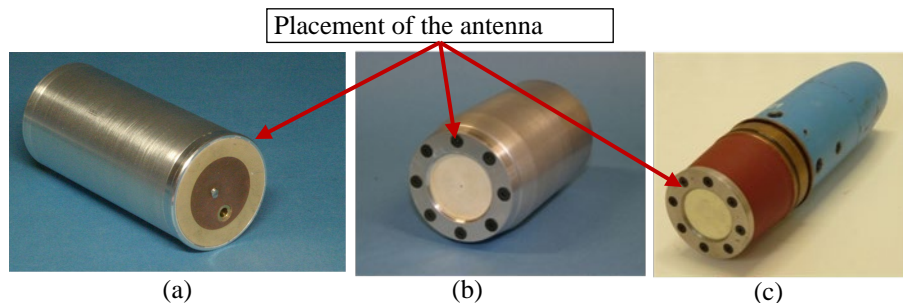


Figure 1 Example structures from ISL that use antennas placed in a cavity. (a) A projectile with a visible circularly polarized patch antenna; studied in [1]. (b) and (c) are projectiles with hidden antennas at the bottom; used in past experiments at ISL.

Examples of patch antenna design in cavities are also shown in Figure 2. Cylindrical geometry is of more interest for applications and a rectangular geometry is of more interest for theoretical investigations, because the analysis is usually simpler.

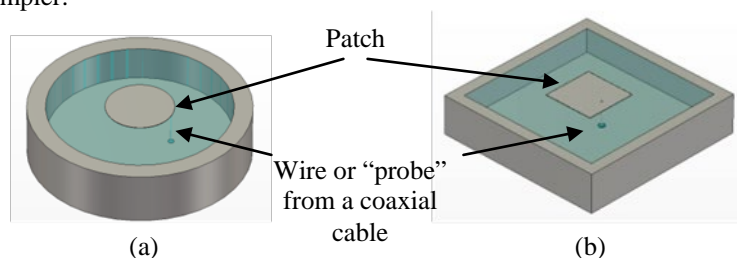


Figure 2 Typical examples of patch antennas in a cavity of (a) circular and (b) rectangular geometry investigated in this work.

In general, applications may concern integrating an antenna onto a specific platform of small size, like a projectile; this in turn may require antenna miniaturization and placement in a small metallic cavity for mechanical, thermal or other reasons, while the antenna should retain good bandwidth characteristics. Larger bandwidth is desirable for any cavity dimension because of two reasons: First, today the communication systems need more and more bandwidth. Second, the manufacturing process. Manufacturing is never as perfect as numerical simulations. In practice, the dimensions of the antenna can never be as exact as in a simulation and as a result the resonance frequency can shift. Having larger bandwidth gives a higher tolerance to the manufacturing process.

If the frequency of operation is always fixed, but the application requires small cavity antennas of various sizes, then we are brought to the main problematic and concern of this Ph.D. The main consequence of antenna integration inside a typical cavity is the reduction of available bandwidth. Furthermore, reducing the size

(volume) of the cavity compared to the free space wavelength dramatically reduces the bandwidth. This problematic is depicted in Figure 3.

In essence, when an antenna is made much smaller than its operating wavelength, its bandwidth is bounded by physical laws and it becomes very narrow. Thus the investigation of the bound on bandwidth for cavity antennas is of primary importance and a major contribution of this thesis.

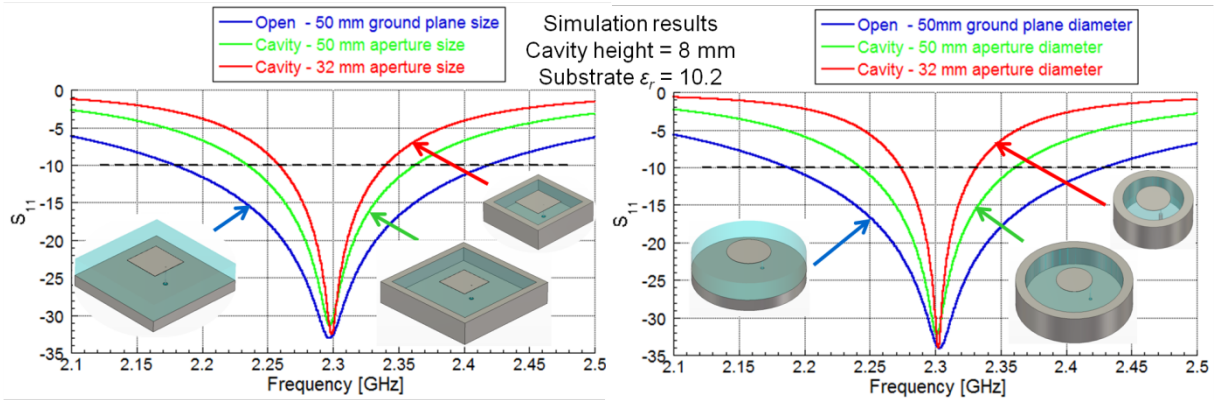
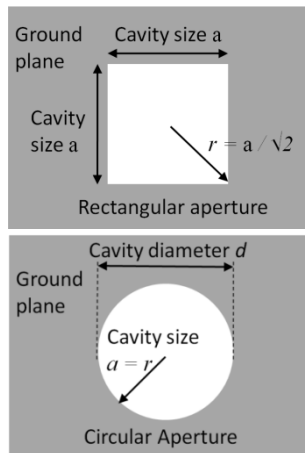


Figure 3 Demonstration of the main problematic in this thesis. Reduction of bandwidth with cavity enclosure, especially with small cavity size. (a) Example for a circular geometry, and (b) rectangular geometry.

Metamaterials are a promising research topic in various domains, and in particular in electromagnetism for circuit applications (filters, phase-shifters, etc.) or for radiating applications (antennas, diffraction, cloaking). They are engineered materials, constituted of small elements (in regards to the wavelength) and offering in specific frequency bands, particular properties, which are different from the ones of natural materials. Among the various potential benefits of metamaterials reported in literature are: the antenna miniaturization, bandwidth enhancement and reduction of the mutual coupling in an antenna array. Metamaterials seem to be a potential solution to the bandwidth enhancement of small antennas. Nevertheless, the designed structures up to now have been relatively large and considered in an open environment; no metallic walls are placed on the antenna lateral sides, as in the case of a cavity. Here, the benefits for bandwidth of metamaterial concepts are investigated in a cavity environment.

In the presentation of the results of this thesis, we have decided upon several parameters for easier comparing of all the different bandwidth behaviors for the antennas investigated. The most important parameter, for purposes of design, simulations and bandwidth comparison of all antennas, is the operation frequency of 2.3 GHz as the desired resonance, making the free space wavelength $\lambda_0 = 130.4$ mm and the corresponding wave-number $k = 2\pi/\lambda_0 = 48.2$. For rectangular cavities we chose to concentrate on the square aperture case where the cavity aperture size a for our investigation is taken to be 20 mm, 32 mm, 40 mm and 48 mm. In the case of circular cavity case, the diameter of the aperture d is chosen to be 20 mm, 32 mm, 40 mm and 50 mm. It is also common to express the electrical size of the antenna in terms of (kr) where r is the radius of the smallest circumscribing sphere. These sizes are summarized in Table 1 and will be referred to as “*example aperture sizes*” in the further text.



<i>Example aperture sizes: Square cavity</i>			
Size a	a [λ_0]	Radius r	(kr)
20 mm	0.153	14.142 mm	0.679
32 mm	0.245	22.627 mm	1.086
40 mm	0.307	28.284 mm	1.358
48 mm	0.368	33.941 mm	1.629

<i>Example aperture sizes: Circular cavity</i>			
Diameter d	d [λ_0]	Radius $r = a$	(ka)
20 mm	0.153	10 mm	0.480
32 mm	0.245	16 mm	0.768
40 mm	0.307	20 mm	0.960
50 mm	0.383	25 mm	1.200

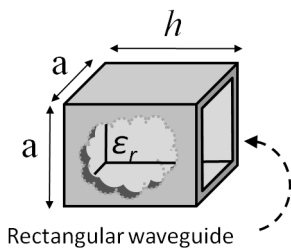
Table 1 Comparison of square and circular apertures.

At ISL, the available dielectric materials antenna manufacturing antennas are Rogers materials of relative permittivity 3.66, 6.15, and 10.2, i.e. Rogers 4350, Rogers 3006, and Rogers 3010 respectively. The durability and mechanical properties of these materials, when placed inside the cavity, were already well tested in the past. It was thus decided to use these permittivity values in our analysis and simulations. A summary of material properties is given in Table 2.

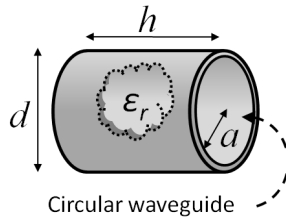
Material	Permittivity	$\tan \delta$
Air	1	0
Polypropylene	2.26	0.002 [2]
Rogers 4350	3.66	0.0037 [3]
Rogers 3006	6.15	0.002 [3]
Rogers 3010	10.2	0.0023 [3]

Table 2 Summary of electrical properties for materials used in this thesis. Values are obtained from references [2]-[3].

It will be useful in the following chapters to consider the cavity volume as a portion of a waveguide. An important parameter of any waveguide is its cut-off frequency f_c for the lowest, fundamental mode. f_c depends on the relative permittivity filling the volume and the geometry of the cross section (square and circular in our case). In regard to the Rogers substrates mentioned above, and the example cavity aperture sizes, we give the cut-off frequencies f_c in Table 3. As operating frequency for studies in this thesis was chosen to be 2.3 GHz, the light red color in Table 3 indicates if the cavity-waveguide is below cut-off, $f_c < 2.3$, and light green if it is above cut-off, $f_c > 2.3$. This feature of antenna's cavity part will prove to be of significant importance throughout the thesis.



Cut-off frequencies f_c for a square waveguide TE ₀₁ mode [GHz]					
Size a	Permittivity ϵ_r :	1	3.66	6.15	10.2
20 mm		7.49	3.92	3.02	2.35
32 mm		4.68	2.45	1.89	1.47
40 mm		3.75	1.96	1.51	1.17
48 mm		3.12	1.63	1.26	0.98



Cut-off frequencies f_c for a circular waveguide TE ₁₁ mode [GHz]					
Diameter d	Permittivity ϵ_r :	1	3.66	6.15	10.2
20 mm		8.79	4.59	3.54	2.75
32 mm		5.49	2.87	2.21	1.72
40 mm		4.39	2.3	1.77	1.38
50 mm		3.51	1.84	1.42	1.10

Table 3 Comparison of cut-off frequencies for square and circular waveguides filled with permittivity 1, 3.66, 6.15, and 10.2. Green color indicates the waveguide is above cut-off at 2.3 GHz, and red color that it is below cut-off.

Numerical simulations in this thesis consisted in investigating the state of the art in compact low profile antennas and in characterizing metamaterial types adapted to reduced-size structures and bandwidth enhancement in a cavity environment. In all cases, simulations were performed using commercial software for numerical electromagnetism, CST Microwave studio. For resonant antenna simulations the Frequency Domain solver was used, and for scattering simulations the Time Domain solver was used.

One of the first conclusion using simulations of classical antenna design concerned the use of multiple resonances for bandwidth enhancement. Traditionally, the use of multiple resonances; for example, stacked patches, multiple parasitic patches and various other (complicated) geometries are used to introduce two or more close by resonances which can effectively broaden the bandwidth. However, we found that when such structures are placed in a small cavity volume, the coupling between resonators becomes too tight and the desired effect becomes impossible. The conclusion is that in a very small cavity the best we can do is to study a single resonance antenna and conditions to achieve maximum possible bandwidth (equivalently: minimum possible Q factor).

GENERAL OBJECTIVES:

Based on the problematic of small cavity antennas, the main objective of this Ph.D. is to answer the following questions:

- What is the maximum possible theoretical bandwidth of any antenna in a cavity?
- Can metamaterial inspired designs bring benefits for bandwidth and size reduction compared to classical patch antenna design?
- Is it possible to design and manufacture antennas in very small cavities with sufficient bandwidth for applications?
- Are there benefits for a compact array design?

SPECIFIC, PRACTICAL OBJECTIVES:

From a practical perspective the objectives are to design, simulate and analyze compact patch antennas in small cavities with following restrictions:

- Circular cavity diameter: 20 mm ($0.15 \lambda_0$) 32 mm ($0.245 \lambda_0$), 40 mm ($0.3 \lambda_0$), and 50 mm ($0.38 \lambda_0$).
- Thickness of antenna: up to 20 mm ($0.15 \lambda_0$).
- Operating frequency at 2.3 GHz
- Dielectric materials to be used: Polypropylene ($\epsilon_r = 2.26$), Rogers 4350 ($\epsilon_r = 3.66$), Rogers 3006 ($\epsilon_r = 6.15$), and Rogers 3010 ($\epsilon_r = 10.2$).
- Patch like (broadside) radiation pattern
- Fabrication and measurement of antennas

OUTLINE OF THE THESIS

Chapter 1 introduces the reader to the theoretical background necessary for following the thesis, and state of the art examples in microstrip antenna technology that is of particular interest for this thesis. Topics presented in Chapter 1 are merged together in later chapters. Section 1.1 of this chapter consists of a brief introduction to the classical approach to analyzing small antennas using spherical mode expansion (Chu bound) and a contemporary approach using scattering theory (Gustafsson bound). Section 1.2 is an introduction to the basics of microstrip patch antennas without the cavity environment and state of the art in miniaturization, bandwidth enhancement techniques from the literature. Section 1.3 is an introduction to the basics of cavity antennas and research made on microstrip patch antennas in the cavity environment in the literature. Section 1.4 consists of the introduction to metamaterials which includes general definitions, and a survey of different types of metamaterials that might be useful in engineering problems with microstrip antennas for miniaturization and bandwidth enhancement.

Chapter 2 merges the subject of microstrip antennas and the subject of cavity antennas in a systematic investigation patch antennas in small cavities, i.e. cavities with apertures smaller than half the free space wavelength at the operating frequency. Section 2.1 summarizes the possibility of applying the miniaturization and bandwidth enhancement techniques in a cavity environment and motivates the investigation of only the classical single patch design. Studies have been made on rectangular and circular shaped cavities in an infinite and a finite ground plane for several example aperture sizes and substrate materials. Section 2.2 shows and discusses simulation results for single patch antennas in rectangular cavities. Section 2.3 shows simulation results for single patch antennas in circular cavities. In Section 2.4, several transmission line models are also presented to describe and explain the phenomena seen in simulation results. Section 2.5 presents measurements of several prototypes manufactured at ISL.

Chapter 3 unveils a new derivation of the bound on minimum Q for the case of cavity antennas of rectangular and circular shapes. Section 3.1 discusses the inadequacy of the Chu bound for cavity antenna and motivates the need for considering the Gustafsson bound. Section 3.2 describes how the more general, scattering approach can be applied to cavities in infinite ground planes and gives an exact formulation of the problem. Section 3.3 uses the presented formulation to derive precise bounds for rectangular and circular cavity shapes respectively. Section 3.4 discusses the validity of the newfound bound in the presence of antennas or objects inside the cavity. Finally, Section 3.5 gives an alternative way of arriving at the same bound giving, perhaps, more insight into the whole matter.

Chapter 4 is the central chapter of the thesis, discussing the realization of a new cavity antenna type capable of reaching predicted maximum bandwidth. The chapter effectively merges the subjects of cavities, microstrip technology and metamaterial concepts. Section 4.1 introduces a new transmission line model for cavity antennas and demonstrates the equivalence between the model and Gustafsson's bound. Section 4.2 uses the conclusion from the transmission line model to arrive at a new physical design of a cavity antenna that can reach the bandwidth predicted by the transmission line model. Section 4.3 discusses simulation results of the new antenna

design for square and circular shapes and shows measurement results. Section 4.4 expands the new design concept to include the possibility of circular polarization.

Chapter 5 expands the topics presented in previous chapters by discussing new applications and further potential of the presented theory in the future. Section 5.1 presents the novel possibility of manufacturing electrically small cavity antennas still coming close to the bound on bandwidth. The emphasis is on antennas smaller than previously possible with classical patch antenna design. Section 5.2 briefly explores the other end of the problem; cavity antennas that are not electrically small and the question: how does the new, metasurface design compare to classical designs with increased bandwidth. Section 5.3 is purely theoretical, exploring the potential of magnetic conductors and magnetic materials for improving the bound on Q . Section 5.4 briefly shows the application of small cavity antennas in creating a compact antenna array.

Chapter 1.

Theoretical background and state of the art

The intention of this chapter is to introduce the reader to the theoretical background necessary for following the thesis, and show state of the art examples in small microstrip antennas.

Section 1.1 of this chapter consists of a brief introduction to the classical approach to analyzing small antennas using spherical mode expansion (Chu bound) and a contemporary approach using scattering theory (Gustafsson bound).

Section 1.2 is an introduction to the basics of microstrip patch antennas without the cavity environment and state of the art in miniaturization, bandwidth enhancement and from the literature. In some examples the author included his own simulation results for purposes of better comparison with other results in the later chapters.

Section 1.3 is an introduction to the basics of cavity antennas; most importantly to the theory of small cavity antennas developed by 1950s. Since this theory is of great importance as the basis for thesis, the theory is immediately expanded with some new results obtained by the author. Furthermore, a literature review of research made on microstrip patch antennas in a cavity is presented.

Section 1.4 consists of the introduction to metamaterials which includes general definitions, and a survey of different types of metamaterials that might be useful in engineering problems with microstrip antennas for miniaturization and bandwidth enhancement.

1.1. Introduction to bounds on small antennas.

In this Section we first present the theoretical background and developments to obtain gain, Q factor and bandwidth limitations with respect to the size of the antenna. For the definition of the Q factor and the discussion on the link between the Q factor and the bandwidth, which is no trivial matter, the reader is referred to *Appendix A*. The classical approaches to obtain the physical limits of antennas, based on spherical wave expansions, will be summarized, their results compared, and contrasted to a newer method, based on the scattering approach. For definitions of scattering parameters and important theorems used in the scattering approach, the reader is referred to *Appendix B*.

1.1.1. What are small antennas

Miniaturization in the semiconductor technologies has been progressing at an exponential level for decades. This trend towards smaller, lightweight, electronics with increasingly more functionalities has of course also put the pressure on antenna designers to provide smaller antennas. However, in opposition to electronic chips, the size of the antenna for a given application is not mainly related to the technology used, but is determined by the laws of physics. The antenna size with respect to the free space wavelength λ_0 is the parameter which will have the preponderant influence on the radiation characteristics. This is easily understood considering that an antenna is a device transforming a guided wave into a radiated wave and vice versa. To perform this transformation efficiently, the size should be of the order of half a wavelength ($\lambda_0/2$) or larger. Antennas can of course be made smaller, but at the expense of their bandwidth and radiation performances.

Finding an explicit relation between the electrical size of an antenna and its potential radiation performances has been a goal of antenna engineers since the early radio days. The pioneering work started by Wheeler [1], and Chu [5], and continued by many others [6]-[30] Their theoretical developments and results are still used by antenna engineers to estimate the potentials of an antenna.

Definition of small antennas: Usually, the electrical size or volume of the small antenna is defined by the value of ka , where k is the free-space wave-number $2\pi/\lambda_0$, and a is the radius of an imaginary sphere circumscribing the maximum dimension of the antenna, seen in Figure 4. Wheeler [1] suggests defining an electrically small antenna as an antenna which can be enclosed in a sphere which is smaller than a radian-length, thus $1/2\pi$ wavelengths. Wheeler's statement that the small antenna is one occupying a small fraction of the radian-sphere has led to the commonly accepted electrical size limit for an electrically small antenna being $ka < 1$. Examination of Wheeler's work reveals that he describe the small antenna as having a *maximum* dimension less than the radian length, $1/2\pi$. From the definition of a in Figure 4 being one-half the antenna's maximum

dimension, this defines a value of $ka = 0.5$ as the electrical size limit for the electrically small antenna. You could argue that this lower value of ka simply makes the definition of an electrically small antenna more stringent. However, examining the impedance properties of a number of electrically small wire antennas, it becomes evident that many small antennas exhibit similar behavior near the $ka = 0.5$ limit. For this reason, the definition of an antenna being electrically small is taken to be one where $ka \leq 0.5$ [31].

Additionally, the radian-sphere can, for an antenna smaller than this size, be interpreted as the limit between the near and the far field of the antenna [32].

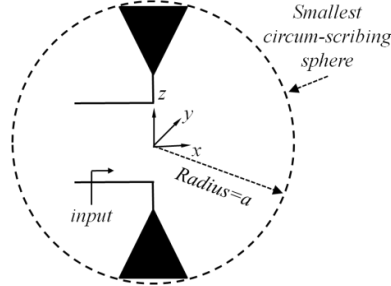


Figure 4 Smallest circumscribing sphere enclosing the antenna of maximum dimension $2a$. It is also known as the Chu sphere, of radius “ a ” centered about the origin.

1.1.2. Spherical mode expansion approach and the Chu bound

Most works dedicated to the study of the physical limitation of electrically small antennas base their analysis at some step on the expansion of the electromagnetic fields in spherical wave functions. The purpose of this section is to summarize this approach, introduced by Chu in [5] in order to contrast it with a newer, scattering approach.

In spherical coordinates the scalar Helmholtz equation $\nabla^2 \psi + k^2 \psi = 0$, has a solution for free space boundary conditions in terms of modes given by [33]

$$\psi_{mn} = h_n^{(2)}(kr) P_n^m(\cos\theta) \cos(m\phi), \quad (1.1)$$

where $h_n^{(2)}(kr) = j_n^{(2)}(kr) - j_n^{(1)}(kr)$ is the spherical Hankel function of the second kind, $j_n^{(2)}(kr)$ is the spherical Bessel function of the first kind, $n_n^{(2)}$ is the spherical Bessel function of the second kind, $P_n^m(\cos\theta)$ are the associated Legendre functions of the first kind. The spherical Bessel and Hankel functions are related to the ordinary Bessel and Hankel functions as $b_n(kr) = \sqrt{\pi/2kr} B_{n+1/2}(kr)$. From the scalar wave function we can obtain the magnetic and vector potentials \mathbf{A} and \mathbf{F} as [33]

$$\mathbf{A} = \mathbf{r}\psi^a, \mathbf{F} = \mathbf{r}\psi^f \quad (1.2)$$

where \mathbf{r} is the radius vector $\mathbf{r} = \hat{r}r$ from the origin, and ψ^s are the solutions to the Helmholtz equation. Therefore, introducing the modified spherical Bessel functions $\tilde{B}_n(kr) = kr b_n(kr) = \sqrt{\pi kr/2} B_{n+1/2}(kr)$ we obtain:

$$\begin{aligned} (A_r)_{mn} &= A_{mn} \tilde{H}_n^{(2)}(kr) P_n^m(\cos\theta) \cos(m\phi), \\ (F_r)_{mn} &= F_{mn} \tilde{H}_n^{(2)}(kr) P_n^m(\cos\theta) \cos(m\phi). \end{aligned} \quad (1.3)$$

From these expressions, the electromagnetic field components are readily obtained from:

$$\begin{aligned} E_r &= \frac{1}{j\omega\epsilon} \left(\frac{\partial^2}{\partial r^2} + k^2 \right) A_r & H_r &= \frac{1}{j\omega\mu} \left(\frac{\partial^2}{\partial r^2} + k^2 \right) F_r \\ E_\theta &= -\frac{1}{r \sin\theta} \frac{\partial F_r}{\partial \phi} + \frac{1}{j\omega\epsilon} \frac{\partial^2 A_r}{\partial r \partial \theta}, & H_\theta &= -\frac{1}{r \sin\theta} \frac{\partial A_r}{\partial \phi} + \frac{1}{j\omega\epsilon} \frac{\partial^2 F_r}{\partial r \partial \theta} \\ E_\phi &= \frac{1}{r} \frac{\partial F_r}{\partial \phi} + \frac{1}{j\omega\epsilon r \sin\theta} \frac{\partial^2 A_r}{\partial r \partial \phi} & H_\phi &= \frac{1}{r} \frac{\partial A_r}{\partial \phi} + \frac{1}{j\omega\epsilon r \sin\theta} \frac{\partial^2 F_r}{\partial r \partial \phi} \end{aligned} \quad (1.4)$$

These fields can be thought of as “modes of free space” [33]. There exists a set of modes which are Transverse Magnetic (TM) to the radial direction and Transverse Electric to r (TE). If we consider the outward traveling waves, the TM modes are generated by functions $(A_r)_{mn}$ in (1.3) while $(F_r)_{mn}$ are taken to be zero. Similarly, the TE modes are generated by functions $(F_r)_{mn}$ while $(A_r)_{mn}$ are taken to be zero. The wave impedance of these modes will be given by

$$(Z_+^{TM})_{mn} = \frac{(E_\theta^{TM})_{mn}^+}{(H_\phi^{TM})_{mn}^+}, \quad (Z_+^{TE})_{mn} = \frac{(E_\theta^{TE})_{mn}^+}{(H_\phi^{TE})_{mn}^+} \quad (1.5)$$

Where the subscript + denotes an outward travelling wave. Inserting the functions (1.3) into (1.4) to obtain the fields and using (1.5) we get

$$(Z_+^{TM})_{mn} = j\eta_0 \frac{\check{H}_n^{(2)}(kr)}{\check{H}_n^{(2)}(kr)}, \quad (Z_+^{TE})_{mn} = -j\eta_0 \frac{\check{H}_n^{(2)}(kr)}{\check{H}_n^{(2)}(kr)}, \quad (1.6)$$

where $\eta_0 = \sqrt{\mu/\varepsilon}$ denotes the free space impedance. The wave impedance is independent of m . Starting from the expression (1.6) for the impedances of spherical waves and using the recurrence formula for the modified Henkel's functions, $b_n(kr) = (2n-1)/(kr) b_{n-1}(kr) - b_{n-2}(kr)$ and $b'_n(kr) = b_{n-1}(kr) - (n+1)/(kr)b_n(kr)$, Chu [5] obtained the following expressions for the mode impedances:

$$Z_{+r}^{TM} = \frac{n\eta_0}{jkr} + \frac{\eta_0}{\frac{2n-1}{jkr} + \frac{1}{\frac{2n-3}{jkr} + \frac{1}{\frac{3}{jkr} + \frac{1}{jkr+1}}}}, \quad Y_{+r}^{TE} = -\frac{n}{jkr\eta_0} + \frac{1/\eta_0}{\frac{2n-1}{jkr} + \frac{1}{\frac{2n-3}{jkr} + \frac{1}{\frac{3}{jkr} + \frac{1}{jkr+1}}}} \quad (1.7)$$

Chu recognized the similarity of these expressions with the transfer function of a Cauer network from filter theory. If we consider the TM case, then the first term represents a capacitor value $C_1 = \varepsilon r/n$ in series with the remainder, formed by an inductor in parallel in series with the remainder, and so on. The last term, η_0 is a termination resistor. Thus, the expression of equation (1.7) for Z_{+r}^{TM} can be represented as a high pass filter for each mode excited by the antenna, see Figure 5(a), from which it follows directly that the largest possible bandwidth is obtained for an antenna exciting only the TM_{01} spherical mode. Indeed, all higher modes will only add to the reactive energy stored in the filter, and thus enhance the Q factor. Analogously, in the case of TE waves, we obtain the ladder network in Figure 5(b).

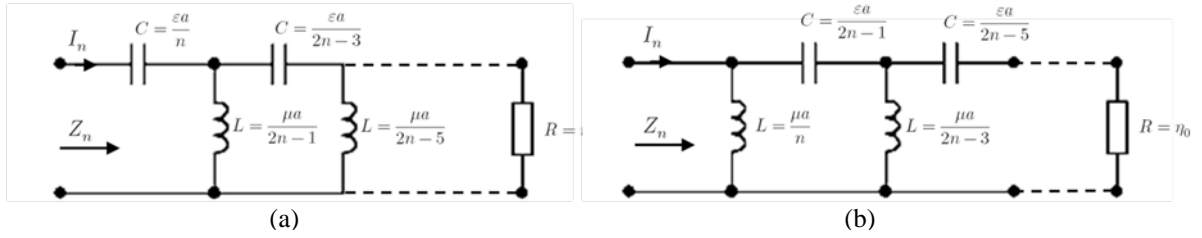


Figure 5 (a) TM circuit (b) TE circuit network

Let us now consider a simple linearly polarized antenna, for example, an electric dipole. A small electrical dipole will excite only the TM_{01} mode, and we consider the radius r to be the size of a circumscribing sphere a , $r = a$. The equivalent ladder network becomes very simple.

$$Z_{+r}^{TM} = \frac{1}{j\omega a \varepsilon} + \frac{1}{\frac{1}{j\omega a \mu} + \frac{1}{\eta_0}} = \eta_0 \left\{ \frac{1}{jka} + \frac{1}{\frac{1}{jka} + 1} \right\} = \eta_0 \left\{ \underbrace{\frac{1}{jka}}_C + \underbrace{\frac{jka}{1 + (ka)^2}}_L + \underbrace{\frac{(ka)^2}{1 + (ka)^2}}_R \right\}, \quad (1.8)$$

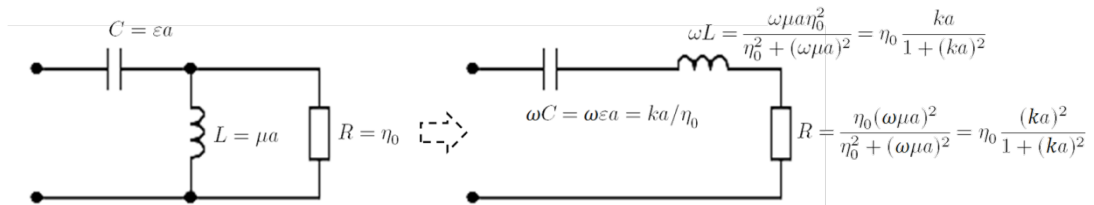


Figure 6 Transformation of the TM_{01} network into a series resonant circuit

To calculate the Q factor of such a circuit we use the definition (A.1) from **Appendix A** that involves the stored and the dissipated energy in the circuit. It is important to realize, since we are interested in electrically small antennas in free space, the energy stored around the antenna is dominantly electric. To make the system resonant

we can imagine a lossless inductor is added. Therefore the resonance arises quite differently from one dependent upon antenna arm length. Since at resonance the time-average values of electric and magnetic energy are equal, we must take the peak value of the stored energy to be twice the time-average stored electric energy. Using (A.6) we have for the total electric energy stored in the circuit

$$W_e^S = \frac{1}{4}|V|^2 C = \frac{1}{4} \frac{|I|^2}{\omega^2 C} = \frac{|I|^2 \eta_0}{4\omega ka}. \quad (1.9)$$

The power dissipated in the resistor is

$$P_R^S = \frac{1}{2}|I|^2 R = \frac{1}{2}|I|^2 \eta_0 \frac{(ka)^2}{1 + (ka)^2}. \quad (1.10)$$

Inserting (1.9) and (1.10) into the (A.1) we have the Chu limit

$$Q_{Chu} = \frac{2\omega W_e^S}{P_R^S} = \frac{1}{(ka)^3} + \frac{1}{ka}. \quad (1.11)$$

The same considerations can be made for a small magnetic loop, which will excite the TE₁₀ mode. We have thus obtained Chu's classical result, stating that the minimum quality factor of a linearly polarized antenna is given by (1.11).

Historical note: Rather than evaluate Q separately for each modal equivalent circuit, Chu stated that the work involved would be “tedious” and sought approximate values that were easier to calculate. Chu approximated the equivalent circuit as a series RLC circuit, and wrote the relationships between the input reactance and reactive elements L and C

$$X_n = \left(\omega L_n - \frac{1}{\omega C_n} \right) \text{ and } \frac{dX_n}{d\omega} = \frac{1}{\omega} \left(\omega L_n + \frac{1}{\omega C_n} \right), \quad (1.12)$$

Solving for the values of the elements as a function of the reactance, and with R_n being the real part of the input impedance gives:

$$C_n = \frac{2}{\omega^2} \left(\frac{dX_n}{d\omega} - \frac{X_n}{\omega} \right)^{-1}; \quad L_n = \frac{1}{2} \left(\frac{dX_n}{d\omega} + \frac{X_n}{\omega} \right); \quad R_n = \left| (ka) h_n^{(2)}(ka) \right|^{-2} \quad (1.13)$$

As an example, we will show the result for the TM₀₁ mode. Combining the above for $n=1$ shows that

$$R_1 = \frac{(ka)^2}{1 + (ka)^2}, \quad C_1 = \frac{(ka)(1 + (ka)^2)}{\eta_0 \omega (1 + 2(ka)^2)} \quad (1.14)$$

Using (1.9) and (1.10), we get the approximate Q :

$$Q_{Chu, approx} = \frac{1}{(ka)^3} \frac{1 + 2(ka)^2}{(1 + (ka)^2)}, \quad (1.15)$$

Note that formula (1.15), nor the exact formula (1.11), which both appear often in literature, did not appear explicitly in the original Chu paper [5].

Following Chu's pioneering work, several authors, like Collin et al [6], Fante [7], Fano [8] or McLean [10] proposed rigorous methods to obtain the smallest possible quality factor of antenna without having to use circuit analogy, but based on field considerations only. We will briefly summarize the method proposed by McLean here, as it is rigorous, very intuitive and easily understood.

Again, we need to compute the radiated power and the energy stored in the reactive field. McLean did this for $n = 1$ in [10], without Hankel functions while Collin [6], extended it for $n = 1, 2, 3, \dots$. The problem is solved in the following steps:

- The field due to an antenna is expanded in spherical waves
- Total energy due to traveling waves and reactive fields are calculated.
- The radiated energy is obtained from the far field components, showing a $1/r$ dependency.
- The non propagating reactive energy is obtained by subtracting the radiated energy from the total energy.

If we apply this method to the case of a short electric dipole of length l and supporting a current I , oriented along the z -axis, we can write for the vector potential in (1.3) for the first mode

$$(A_r)_{01} = -\cos \theta e^{-jkr} \left(1 - \frac{j}{kr}\right), \quad (1.16)$$

From (1.4) We obtain for the field components

$$\begin{aligned} H_\phi &= \sin \theta e^{-jkr} \left(\frac{j}{kr^2} - \frac{1}{r}\right), \\ E_\theta &= \frac{1}{j\omega\epsilon} \sin \theta e^{-jkr} \left(-\frac{1}{r^2} - \frac{jk}{r} + \frac{j}{kr^3}\right), \\ E_r &= \frac{2}{\omega\epsilon} \cos \theta e^{-jkr} \left(\frac{j}{r^2} + \frac{1}{kr^3}\right). \end{aligned} \quad (1.17)$$

The field components are taken as root mean square (RMS) values. In this case the total electric energy density w_e is larger than the magnetic energy density w_m , and is given by

$$\begin{aligned} w_e &= \frac{1}{2} \epsilon \vec{\mathbf{E}} \cdot \vec{\mathbf{E}}^* = \frac{1}{2} \epsilon (|E_\theta|^2 + |E_r|^2) \\ &= \frac{\eta_0}{2\omega} \left[\sin^2 \theta \left(\frac{1}{k^3 r^6} - \frac{1}{kr^4} + \frac{k}{r^2}\right) + 4 \cos^2 \theta \left(\frac{1}{k^3 r^6} + \frac{1}{kr^4}\right) \right] \\ w_m &= \frac{1}{2} \mu \vec{\mathbf{H}} \cdot \vec{\mathbf{H}}^* = \frac{1}{2} \mu |H_\phi|^2 = \frac{1}{2} \mu \sin^2 \theta \left(\frac{1}{k^2 r^4} + \frac{1}{r^2}\right). \end{aligned} \quad (1.18)$$

Now consider the electric- energy density associated with the traveling wave; that is, the energy calculated from the field components which produce radiated power. This can be called the propagating energy, w_e^{rad} . This energy density is computed using only the radiation fields

$$\begin{aligned} H_\phi^{rad} &= -\sin \theta \frac{e^{-jkr}}{r}, \\ E_\theta^{rad} &= -\eta_0 \sin \theta \frac{e^{-jkr}}{r}, \\ w_e^{rad} &= \frac{1}{2} \epsilon |E_\theta^{rad}|^2 = \frac{\eta_0}{r^2} \sin^2 \theta \end{aligned} \quad (1.19)$$

The stored (non-propagating) energy density is given by the difference of the total energy density with the radiated (propagating) energy density:

$$w_e^{np} = w_e - w_e^{rad} = \frac{\eta_0}{2\omega} \left[\sin^2 \theta \left(\frac{1}{k^3 r^6} - \frac{1}{kr^4}\right) + 4 \cos^2 \theta \left(\frac{1}{k^3 r^6} + \frac{1}{kr^4}\right) \right]. \quad (1.20)$$

The total stored energy is now obtained by integrating (1.20) over the entire space, except for the sphere of radius a enclosing the antenna:

$$W_e^{np} = \int_0^{2\pi} \int_0^\pi \int_a^\infty w_e^{np} r^2 \sin \theta dr d\theta d\phi = \frac{4\pi\eta_0}{3\omega} \left[\frac{1}{(ka)^3} + \frac{1}{ka} \right]. \quad (1.21)$$

The total radiated power may be determined by integrating the real part of the pointing vector over a spherical surface of any radius

$$P_{rad} = \int_0^{2\pi} \int_0^\pi \text{Re}(\mathbf{E} \times \mathbf{H}^*) \cdot \hat{\mathbf{r}} r^2 \sin \theta dr d\theta d\phi = \frac{8\pi}{3} \eta_0, \quad (1.22)$$

Giving the quality factor

$$Q = \frac{2\omega W_e^{np}}{P_{rad}} = \frac{1}{(ka)^3} + \frac{1}{ka}. \quad (1.23)$$

This is, as expected, exactly the same result as the one obtained by Chu for the smallest possible Q for a linear antenna (without approximation). Following the same principle for a circularly polarized antenna constructed using the TE_{01} and TM_{01} modes excited with a phase shift of $\pi/2$, McLean obtains [10]

$$Q = \frac{1}{2} \left[\frac{1}{(ka)^3} + \frac{2}{ka} \right]. \quad (1.24)$$

We note that an inherent assumption in the analysis so far is that the fields inside the sphere of radius a are zero. However, any antenna that is contained within a sphere of radius a will have additional energy storage within the enclosing sphere and will consequently have a higher Q . In fact, many electrically small antennas

have a Q that is considerably larger than Chu's lower bound. In order to complete the derivation of the new lower bound on antenna Q , the effects of energy stored within the sphere of radius a were also considered. In two recent papers, Thal [11]-[12] reevaluated the Q of TE_{n1} and TM_{n1} modes by assuming that the antenna consisted of a suitable current sheet on the surface of the sphere of radius a . This allowed the modes excited in the interior of the sphere to be included in the energy storage and hence led to larger values for the minimum achievable Q . The work was based on the use of continued fraction expansions for the mode impedances in both the internal and external regions. Thal extended the circuit analysis of Chu by developing a ladder network that included the energy inside the enclosing sphere. Hansen and Collin [13] extended the exact formulation in terms of spherical modes. The result is a quotient of spherical Bessel and Hankel functions. Numerical values are shown in Table 1.1, and as expected these agree with those published by Thal.

ka	Chu- Q (TM or TE)	Thal- Q (TM)	Thal- Q (TE)
0.1	1010.0	1506.0	3030.0
0.15	302.96	448.51	908.90
0.2	130.00	190.58	390.00
0.25	68.000	98.506	204.00
0.30	40.370	57.684	121.11
0.35	26.181	36.850	78.540
0.40	18.125	25.111	54.380
0.45	13.196	17.991	39.590
0.50	10.000	13.421	30.004

Table 4 New Q values based on the energy inside and outside the smallest circumscribing sphere of radius a .

Unlike the Chu- Q case, the new formulas do not have Q expressed as a two or three-term formula. This was remedied by Hansen and Collin [13] who performed a fitting to the exact values for both the TM_{10} and TE_{10} modes for two terms. The TM coefficients were close to 0.707 and 1.5, so these were used; TE coefficients were close to 3. We thus write

$$\begin{aligned} TM_{10}: Q_{Thal} &= \frac{1.5}{(ka)^3} + \frac{1}{\sqrt{2}ka}, \\ TE_{10}: Q_{Thal} &= \frac{3}{(ka)^3} + \frac{3}{ka}. \end{aligned} \quad (1.25)$$

Thal also considered the relationship between gain, Q , and the energy inside the Chu sphere, and concluded that these quantities are not independent of one another [14].

Example 1: As mentioned, many electrically small antennas do not reach the desired lower limit on Q . However, there are a few examples of approaching the limit closely. In 2005 the Q of Best's [15] spherical helix antenna was found to be nearly identical to the minimum Q_{New} limit found by Thal, given in (1.25). The spherical helix resonator, shown in Figure 7(a), excites the TM_{10} spherical mode; Stuart *et al.* [16] reported an alternative version, i.e. a capped dipole resonator shown in Figure 7(b), also having exciting the TM_{10} mode and having a $1.5Q_{Thal}$. In [17] Best also gave an antenna design shown in Figure 7(c) exciting the TE_{10} mode and approaching the Q_{Thal} .

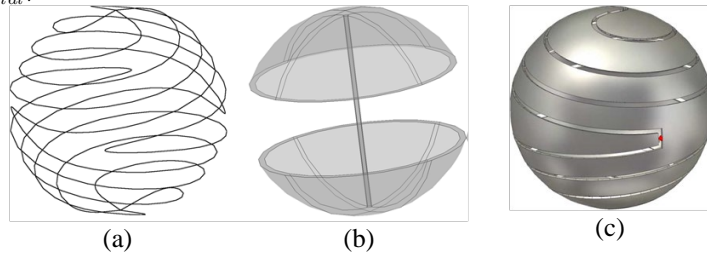


Figure 7 (a) 4-arm Folded spherical helix resonator. (b) Spherical capped dipole resonator. Each of these two resonators acts as an electric dipole (excites the TM_{10} mode) and can be designed to be electrically small with a Q -factor near 1.5 times the Chu limit. (c) Depiction of the 2-arm folded slot spherical helix magnetic dipole (excites the TE_{10} mode).

Example 2: Later, in 2010 Stuart and Yaghjian [18] also studied how to approach the lower bounds on Q for electrically small dipole or monopole antennas based upon the high permeability shells as indicated by Figure 8. It was reported that the magnetic polarization currents induced in the thin shell of magnetic material are able to reduce the internal stored energy leading to a lower Q compared with conventional designs. In the case of the spherical electric dipole antenna, a sufficiently large value of permeability enables the Q to be reduced to a value that is only $1.11Q_{Chu}$. However, up to now there are still no antennas implemented in reality using these

conceptions to the knowledge of the authors. The practical challenge of implementing these designs is in the development of low-loss uniform materials with high magnetic permeability. Nevertheless, research along this line still provides a valuable direction to achieve high-performance electrically small antennas.

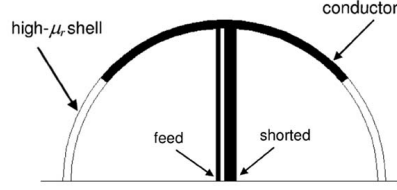


Figure 8 (a) Antenna element based upon a half-sphere of ENG material placed at the termination of a coaxial transmission line, and (b) cross section of the spherical capped monopole antenna on a large ground plane. A thin, high- μ shell is used to complete the sphere [18].

LIMITATIONS ON GAIN.

The limitations on the gain of an electrically small antenna are based on considerations somewhat different than the limitations on Q , in the sense that gain is not limited per se. Indeed, it would be more correct to speak about a limit on gain bandwidth product (as we will see later) or on a practical limit on the gain. This latter approach was proposed by Harrington in his classic paper [19], here we will show only the important results.

Harrington expanded on the work of Chu, but followed Chu's approximate method to obtain the Q 's of TE_{n1} and TM_{n1} modes. Harrington has shown that the maximum gain of an antenna, obtained by using only a finite number of TE_{n1} and TM_{n1} modes, was given by

$$G_{max} = \sum_{n=1}^N (2n + 1) = N^2 + 2N \quad (1.26)$$

Where n is the mode number and N is the highest considered mode. If there was no constraint on the mode amplitudes, an arbitrarily large gain would theoretically be possible. However, high-order modes are very difficult to excite because their wave impedances (wave admittances for the TE_{n0} modes) are very large. The modes of order $n > kr$ are rapidly cut off and are not naturally present in the field of an antenna of radius a . Modes of order $n > kr$ will increase heavily the stored reactive energy, but have no impact on radiated power. Thus for a practical antenna, a natural limit for the gain, when $n > kr$ is given by

$$G_{max} = (ka)^2 + 2(ka). \quad (1.27)$$

An antenna could in theory have larger gain, but at the cost of a very narrow bandwidth. This is the case in the so called super-directive antennas. For lossless electrically small antennas in free space, the maximal achievable gain for a meaningful bandwidth is thus $G_{max} = 2 = 3\text{dB}$.

Going back to the impedance of the first mode, we see that as the electrical dimension of the antenna becomes smaller, the mode impedance becomes more reactive. This means that for very small lossless antennas, the above mentioned gain will be reached on a very limited bandwidth. If dielectric or conductive losses are present, this will severely reduce the antenna's efficiency.

All above results have been obtained for TM modes, as they were derived for a small electric dipole. Similar results are obtained for a small magnetic dipole. If an electric and magnetic dipole are present at the same time, different limits on quality factor and gain are obtained depending on the relative orientation and phase of the dipoles. Recently Pozar [20] proposed a very useful summary of these results. The basic configurations for the two dipoles are given in Figure 9, while the summary from [20] is reproduced in Table 5.

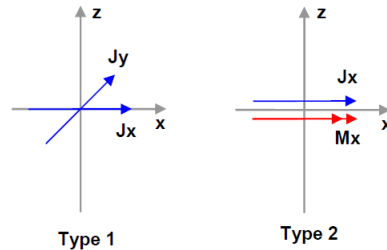


Figure 9 Equivalent elementary dipole sources for two types of circular polarization. Type 1 uses two orthogonal electric (or magnetic) dipoles with 90° phasing. Type 2 uses collinear electric and magnetic dipoles. Examples of Type 1 circularly polarized antennas include crossed dipoles, crossed slots, turnstile antennas, and square (or circular) microstrip patches with feeds that excite two orthogonal modes. Type 2 circularly polarized small antennas generally involve structures that can be modeled as a superposition of collinear electric and magnetic dipole moments, such as dipole/loop antennas, monopole/slot antennas, loop/monopole antennas, short helix antennas, and the spherical helix antenna [20].

Sources	Polarization	Pattern	Max Gain	Min Q
J_z (or J_x , or J_y)	LP-1	Omni	1.5	Q_0
M_z (or M_x , or M_y)	LP-1	Omni	1.5	Q_0
$J_z \pm M_z$	LP-2	Omni	1.5	$Q_0/2$
$J_z \pm M_y$	LP-2	Directional	3	$Q_0/2$
$J_z \pm j M_z$	CP-2	Omni	1.5	$Q_0/2$
$J_z \pm j M_y$	LP-2	Bi-directional	1.5	$Q_0/2$
$J_x \pm j J_y$	CP-1	Bi-directional	1.5	Q_0
$M_x \pm j M_y$	CP-1	Bi-directional	1.5	Q_0
$J_x \pm j J_y$ and $M_x \pm j M_y$	CP-2	Directional	3	$Q_0/2$

 Table 5 Maximum gain and minimum q for various combinations of elementary sources. $Q_0 = 1/(ka)^3$

With the increased demand for electrically small antennas induced by the boom in wireless communications, the work to their limitations has received new interest starting in the early nineties, with several aims: refine the limitations by taking into account dispersive materials [21], lossy materials, [22] and [23] and materials having negative permittivity or permeability [24]. The next section will specifically investigate the limitations taking into account the antenna's shape factor.

1.1.3. Scattering approach and the Gustafsson bound

So far, spherical wave functions were used to represent the radiation outside the Chu sphere. In contrast, recent publications [25]-[30] considered a different approach to analyzing small antennas. As already noted by, Thal, and others, Chu's approach may not be suitable for practical antennas. Gustafsson *et.al.* proceeded to instead use the scattering properties of small particles (i.e. their polarizability dyads) to extract the minimum Q , gain, and bandwidth of small antennas. The new bound on Q is derived in the following steps:

- Scattering is represented in the low frequency limit to define the polarizabilities of an object
- Optical theorem is used to connect the polarizabilities with the extinction cross section over all frequencies
- Integral of the extinction cross section is approximated and shown to involve a product of gain and bandwidth

Consider a plane wave $\mathbf{E}^{\text{inc}} = E_0^+ e^{-jkr}$ incident on an object (antenna) and is scattered by it. For any antenna, the scattered electric field \mathbf{E}^{S} in the forward direction $\hat{\mathbf{k}}$ from an object, expressed by

$$\mathbf{E}^{\text{S}}(k, \mathbf{r}) = E_0^+ \frac{e^{-jkr}}{r} \underline{\mathbf{S}}(k, \hat{\mathbf{k}}) \cdot \hat{\mathbf{p}}_e + \mathcal{O}(r^{-2}) \quad \text{as } r \rightarrow \infty \quad (1.28)$$

where $\underline{\mathbf{S}}(k, \hat{\mathbf{k}})$ is the forward scattering dyadic, $\hat{\mathbf{p}}_e$ is the electric polarization and E_0^+ is the amplitude of the incident electric field. What is of particular interest is to look at the low frequency (long wavelength) asymptotic of the scattering [34]

$$\underline{\mathbf{S}}(k, \hat{\mathbf{k}}) \cdot \hat{\mathbf{p}}_e = \frac{k^2}{4\pi} (\hat{\mathbf{p}}_e^* \cdot \underline{\gamma}_e \cdot \hat{\mathbf{p}}_e + \hat{\mathbf{p}}_m^* \cdot \underline{\gamma}_m \cdot \hat{\mathbf{p}}_m) + \mathcal{O}(k^3), \quad (1.29)$$

where $\hat{\mathbf{p}}_m = \hat{\mathbf{k}} \times \hat{\mathbf{p}}_e$ represents the magnetic polarization of the incident wave. $\underline{\gamma}_e$ and $\underline{\gamma}_m$ are the electric and magnetic polarizability dyadics of the target. They allow determining the induced electric and magnetic dipole moments $\mathbf{p} = \varepsilon_0 \underline{\gamma}_e \hat{\mathbf{p}}_e E_0$ and $\mathbf{m} = \mu_0 \underline{\gamma}_m \hat{\mathbf{p}}_m H_0$ when the target is immersed in a uniform electrostatic or magnetostatic field of amplitude E_0 and H_0 respectively. Relation (1.29) together with (1.28) is in fact similar to the far field of infinitesimal electric and magnetic dipoles. This is reasonable because in the long wavelength limit all antennas are electrically small. From (1.29) it is useful to define a quantity ϱ called the extinction volume as

$$\varrho(k) = \frac{\hat{\mathbf{p}}_e^* \cdot \underline{\mathbf{S}}(k, \hat{\mathbf{k}}) \cdot \hat{\mathbf{p}}_e}{k^2}. \quad (1.30)$$

This is a well defined quantity for $k \rightarrow 0$, purely by the polarizabilities of the scattering object, as can be seen

immediately by dividing (1.29) with k^2 and making the limit. We thus define $\varrho(0)$ to be

$$\varrho(0) = \frac{1}{4\pi} (\hat{\mathbf{p}}_e^* \cdot \underline{\gamma}_e \cdot \hat{\mathbf{p}}_e + \hat{\mathbf{p}}_m^* \cdot \underline{\gamma}_m \cdot \hat{\mathbf{p}}_m), \quad (1.31)$$

Next, we invoke the forward scattering theorem or optical theorem. For a derivation of the theorem and necessary definitions, see **Appendix B**. The forward scattering theorem is a remarkable relation [35] which states

$$\sigma_{ext}(k) = \frac{4\pi}{k} \text{Im} \{ \hat{\mathbf{p}}_e^* \cdot \underline{\mathbf{S}}(k, \hat{\mathbf{k}}) \cdot \hat{\mathbf{p}}_e \} = 4\pi k \text{Im} \{ \varrho(k) \} \quad (1.32)$$

Where σ_{ext} is the total cross section of a scatterer representing the total power loss from the incident wave due to the scattering σ_s and absorption σ_a of a wave by the scatterer, i.e. $\sigma_{ext} = \sigma_s + \sigma_a$. The loss is related to the imaginary part of the scattering amplitude in the forward direction.

The following step is a stunning connection between the total (extinction) cross section $\sigma_{ext}(k)$ and the static extinction volume $\varrho(0)$ defined by the polarizabilities. The idea is to use the Cauchy integral theorem that relates an integral over a closed loop in the complex planes to the residue at the poles in the plane. Thus to get $\varrho(0)$ one could use a function $\varrho(k)/k$ that has a pole at $k = 0$. Gustafsson *et. al.* in [26] concluded that since the elements of $\underline{\mathbf{S}}(k, \hat{\mathbf{k}})$ are holomorphic in k for $\text{Im}\{k\} > 0$, it follows that also $\varrho(k)$ is a holomorphic function in the upper half plane. They thus write the Cauchy integral theorem with respect to the curve in Figure 10. as

$$2\pi j \varrho(0) = \oint \frac{\varrho(k)}{k} dk \quad (1.33)$$

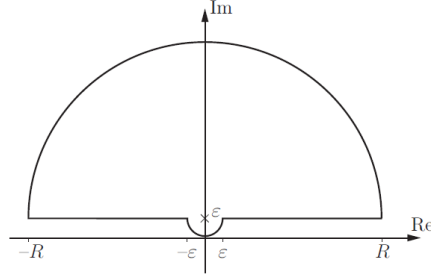


Figure 10 Integration contour in the complex k plane used in

The integral (1.33) has to be carefully evaluated for each part of the contour. Noting that on the large semicircle we let $k = Re^{j\varphi}$ and on the small semicircle around the pole we let $k = \epsilon e^{j\varphi}$ and letting $R \rightarrow \infty$, $\epsilon \rightarrow 0$, we can write

$$\varrho(0) = \frac{1}{2\pi j} \underbrace{\int_0^\pi \frac{\varrho(\epsilon e^{j\varphi})}{\epsilon e^{j\varphi}} j\epsilon e^{j\varphi} d\varphi}_{\pi \varrho(0)} + \underbrace{\frac{1}{2\pi j} \int_\pi^0 \frac{\varrho(Re^{j\varphi})}{Re^{j\varphi}} jRe^{j\varphi} d\varphi}_0 + \frac{1}{2\pi j} \int_{\epsilon < |k| < R} \frac{\varrho(k)}{k} dk. \quad (1.34)$$

The last term in (1.34) can be rewritten using the optical theorem (1.32) as

$$\frac{1}{2\pi j} \int_{-\infty}^{\infty} \frac{\varrho(k)}{k} dk = \frac{-1}{2\pi} \int_{-\infty}^{\infty} \frac{\text{Im}\{\varrho(k)\}}{k} dk = \frac{-1}{8\pi^2} \int_{-\infty}^{\infty} \frac{\sigma_{ext}(k)}{k^2} dk = \frac{1}{8\pi^3} \int_0^\infty \sigma_{ext}(\lambda) d\lambda. \quad (1.35)$$

Inserting (1.36) back into (1.35) gives finally

$$\varrho(0) = \frac{1}{2} \varrho(0) + \frac{1}{8\pi^3} \int_0^\infty \sigma_{ext}(\lambda) d\lambda. \quad (1.36)$$

Since $\varrho(0)$ is defined with the polarizabilities by (1.30) and (1.29) we obtain useful relation

$$\int_0^\infty \sigma_{ext}(\lambda) d\lambda = \pi^2 (\hat{\mathbf{p}}_e^* \cdot \underline{\gamma}_e \cdot \hat{\mathbf{p}}_e + \hat{\mathbf{p}}_m^* \cdot \underline{\gamma}_m \cdot \hat{\mathbf{p}}_m). \quad (1.37)$$

Remarkably, we see from (1.37) that there is a fundamental connection between the polarizability, the static response, of an object (its dipole moments) and broadband scattering from it, a dynamic quantity which includes absorption and scattering properties of the object. The relation can be also used in the cases when the polarizability cannot be obtained analytically but numerical simulations of broadband radar cross sections are possible. However, we will use (1.37) to bound the scattering ability of an object, i.e. its bandwidth.

Recall that directivity D depends on the electric polarization $\hat{\mathbf{p}}_e$ as well as the incident direction $\hat{\mathbf{k}}$. In the present case of no ohmic losses, the partial gain G coincides with the partial directivity D .

Since the extinction cross section is composed from two parts, namely scattering and absorption cross section, in fact, $\sigma_{ext} > \sigma_a$ and we can write $\sigma_{ext} = \sigma_a / \eta$, where we have introduced the notion of absorption efficiency $0 < \eta < 1$. For most antennas at resonance $\eta \leq 1/2$, but exceptions from this rule of thumb exist. In particular, minimum scattering antennas can be defined by $\eta = 1/2$. We can now also write the left hand side of (1.37) as

$$\int_0^\infty \sigma_{ext}(\lambda) d\lambda = \frac{1}{\tilde{\eta}} \int_0^\infty \sigma_a(\lambda) d\lambda, \quad (1.38)$$

where constant $\tilde{\eta}$ is bounded from above by the absorption efficiency via $\tilde{\eta} < \sup_\lambda \eta$, and it provides a broadband generalization of the absorption efficiency.

Effective area or absorption cross section is connected to gain, directivity via

$$\sigma_a = \frac{\lambda^2}{4\pi} D = \frac{\pi}{k^2} D. \quad (1.39)$$

Under the assumption of N non-interfering resonances characterized by the real valued wave numbers k_n , Gustafsson *et al.* [26] give a model for the absorption cross section as

$$\sigma_a(k) = 2\pi \sum_{n=1}^N \varrho_n \frac{Q_n k_n}{1 + \frac{Q_n^2}{4} \left(\frac{k}{k_n} - \frac{k_n}{k} \right)^2}, \quad (1.40)$$

Where k is assumed real valued and ϱ_n are positive weight functions satisfying $\sum \varrho_n = \varrho(0)$. Here, the Q factor of the resonance at k_n is denoted by Q_n , and for $Q \gg 1$, the associated relative half-power bandwidth is $B \approx 2/Q_n$. For the resonance model (1.40) one can argue that Q_n coincides with the corresponding antenna Q -factor when the relative bandwidth $2/Q_n$ is based on the half power threshold. In the case of strongly interfering resonances, the model either has to be modified or another estimate has to be used. The absorption cross section is the imaginary part, $\sigma_a(k) = 4\pi k \text{Im}(\varrho_n)$, of the function

$$\varrho_a(k) = \sum_{n=1}^N \varrho_n \frac{jQ_n k_n / (2k)}{1 + j \frac{Q_n}{2} \left(\frac{k}{k_n} - \frac{k_n}{k} \right)}, \quad (1.41)$$

for real valued k . The function $\varrho_a(k)$ is holomorphic for $\text{Im}(k) > 0$ and has a symmetrically distributed pair of poles for $\text{Im}(k) > 0$. The integrated absorption cross section is

$$\frac{1}{4\pi^2} \int_{-\infty}^{\infty} \frac{\sigma_a(k)}{k^2} dk = \varrho_a(0) = \tilde{\eta} \varrho(0) \leq \varrho(0), \quad (1.42)$$

where $\varrho(0)$ is the static limit defined in (1.31). For antennas with a dominant first resonance at $k = k_1$, it follows from (ono za bandwidth 3.1 u gusta) and (gore) that the partial realized gain satisfies

$$(1 - |\Gamma|^2)G = \frac{k^2 \sigma_a}{\pi} \leq \varrho(0) \frac{Q k_1}{1 + \frac{Q^2}{4} \left(\frac{k}{k_1} - \frac{k_1}{k} \right)^2}, \quad (1.43)$$

Where $\varrho_n \leq \varrho(0)$ has been used. The right hand side of () reaches a maximum value $\varrho(0) 2k_1^3 Q / (1 - Q^{-2})$ at $k_0 = k_1 (1 - 2Q^{-2})^{-1/2}$ or $k_0 = k_1 + O(Q^{-2})$ as $Q \rightarrow \infty$. Hence, k_0 is a good approximation to k_1 if $Q \gg 1$. For a loss-less antenna which is perfectly matched at $k = k_0$, the partial realized gain $(1 - |\Gamma|^2)G$ coincides with the partial directivity D . Under this assumption, (1.44) yields

$$\frac{D}{Q} \leq \frac{\varrho(0) 2k_1^3}{(1 - Q^{-2})}, \quad (1.44)$$

Which can further be estimated from above as

$$\frac{D}{Q} \leq \frac{k^3}{2\pi} (\hat{\mathbf{p}}_e^* \cdot \underline{\gamma}_e \cdot \hat{\mathbf{p}}_e + \hat{\mathbf{p}}_m^* \cdot \underline{\gamma}_m \cdot \hat{\mathbf{p}}_m), \quad (1.45)$$

which can be transformed into a bound for Q , given by

$$Q = \frac{2\pi D}{\tilde{\eta}k^3 (\hat{\mathbf{p}}_e^* \cdot \underline{\gamma}_e \cdot \hat{\mathbf{p}}_e + \hat{\mathbf{p}}_m^* \cdot \underline{\gamma}_m \cdot \hat{\mathbf{p}}_m)}. \quad (1.46)$$

By defining the total polarizability $\gamma = (\hat{\mathbf{p}}_e^* \cdot \underline{\gamma}_e \cdot \hat{\mathbf{p}}_e + \hat{\mathbf{p}}_m^* \cdot \underline{\gamma}_m \cdot \hat{\mathbf{p}}_m)$ we can write (1.46) compactly as

$$Q = \frac{2\pi D}{\tilde{\eta}k^3 \gamma}. \quad (1.47)$$

We have thus derived the expression for the Q factor of a scattering object i.e. and antenna based on its static, polarizability parameters. To consider (1.46) as a bound on Q we just have to consider the polarizabilities of object made from perfect electric (PEC) or magnetic (PMC) conductors that do not allow fields inside the objects. If the fields within the volume are zero, just like the case of the Chu sphere, we obtain the bound, i.e. limit on the Q factor for such a volume.

Example: Considering now an antenna being perfectly electric conducting (PEC) in free space, it follows that $\underline{\gamma}_m = 0$ and only $\underline{\gamma}_e$ is of concern. In the case of linear polarization the total polarizability γ reduces to just one electric polarizability γ_e . Additionally, we can normalize the polarizability and write $\gamma_e = 4\pi a^3 \gamma_e^{norm}$, where a is the radius of the Chu sphere, and γ_e^{norm} is given in Figure 11 for several antenna geometries (scatterers). Further, since the directivity D of the single mode radiating small antennas ($ka \ll 0.5$ (like the Hertzian dipole) is $D = 1.5$, it follows from (1.46) that

$$Q = \frac{1.5}{(ka)^3 \gamma_e^{norm}}, \quad (1.48)$$

With γ_e^{norm} given in Figure 11. For a spherical volume (Chu sphere), for $ka \ll 0.5$, when $D = 1.5$ and $\tilde{\eta} = 0.5$, since $\gamma_e^{norm} = 1$, from (1.50) we have

$$Q_{Sphere, Gustafsson} = \frac{1.5}{(ka)^3}, \quad (1.49)$$

This is, in fact, identical to Thal's antenna supporting a single TM_{10} mode given in (1.25) when $ka \ll 0.5$. We also note that Gustafsson's (1.49) is thus identical to the Q values obtained by Best [22] for a N -turn arm spherical helix. An example is given in Figure 12 for four arm elongated helix antenna with height/width = 2/3. The number of turns is adjusted to adjust the resonance and generate the data.

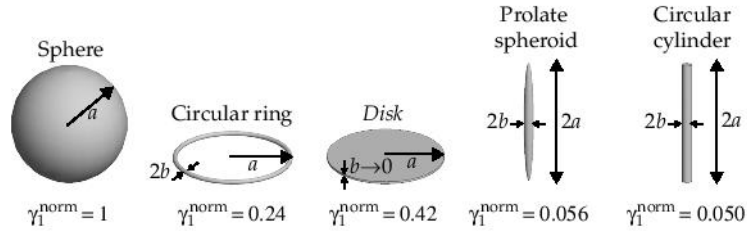


Figure 11 Normalized γ_e^{norm} eigenvalues for several small antenna geometries with $b/a = 10^{-3}$ for the circular ring, prolate spheroid, and circular cylinder. Taken from [36].

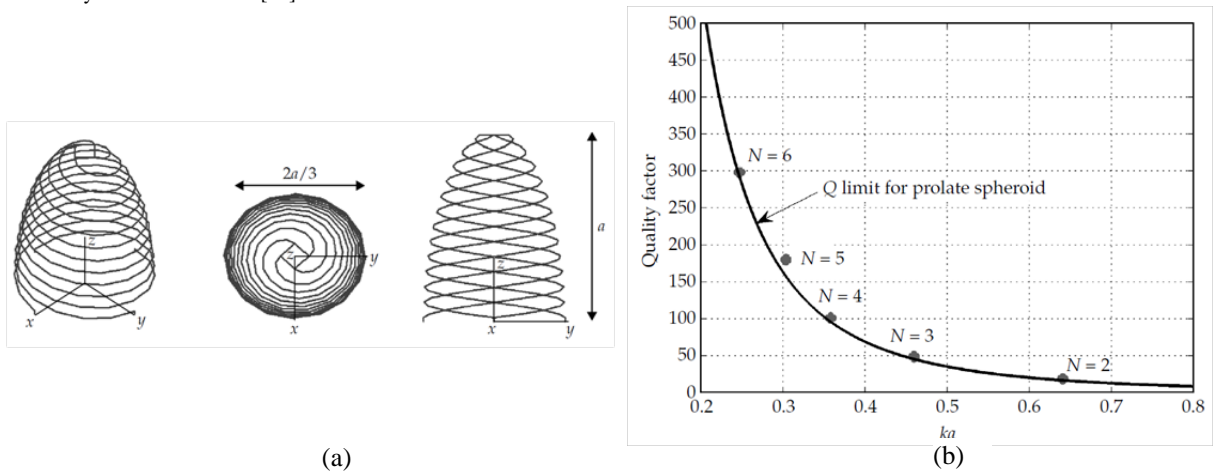


Figure 12 (a) Three turn four arm elongated helix antenna with height/width = 2/3 (b) Gustafsson Q limit for a prolate spheroid with width to height ratio 2/3 along with measured N -turn four arm elongated helix Q . Taken from [36].

In conclusion, Gustafsson’s bound combines directivity and Q into a single bound and shows the tradeoff between them directly, unlike the spherical mode expansion technique. Additionally, there are no assumptions of an a priori volume, like a sphere. Applying the scattering approach to a sphere leads to realistic predictions for the minimum Q factor, confirmed by the spiral helical type of antennas introduced by Best [22]. Compared to the spherical mode expansion approach the mathematical difficulty in the scattering approach is the ability to analytically derive the object’s polarizability. However, a major improvement in this regard is that the polarizability γ can also be estimated numerically using broadband scattering simulations and using (1.37). Knowledge of the antenna’s absorption characteristics are, however, necessary to use the Gustafsson bound.

In the recent years Gustafsson *et. al.* also introduced new methods of obtaining minimum Q factor based on the optimum currents approach, which is currently outside the scope of this thesis.

1.2. Introduction to microstrip antennas

In this section we restrict ourselves to **pin fed** compact microstrip design or **rectangular** and **circular** shape, shown in Figure 13, because it is believed to be of greater importance for the end application.

There are two basic analytical approaches to pin fed patch antennas. The *transmission-line model* and the *cavity model* that will be shown in order to explain the basic operation of patch antennas. The chapter will concentrate on miniaturization and bandwidth enhancement techniques.

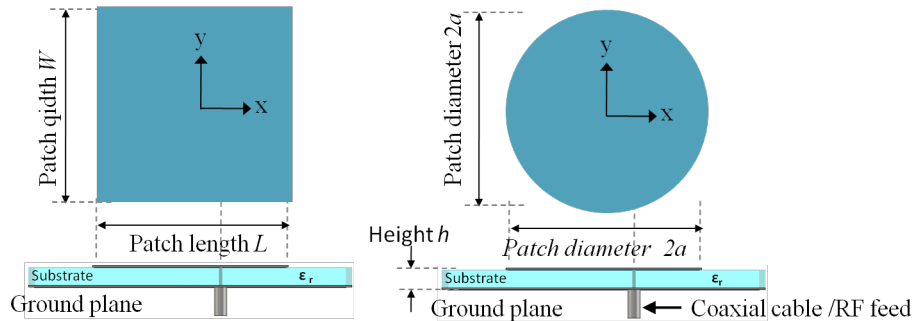


Figure 13 (a) Rectangular microstrip patch antenna and (b) circular microstrip patch antenna.

Microstrip antennas are used in high-performance aircraft, spacecraft, satellite, and missile applications, and commercial applications, such as mobile radio and wireless communications where size, weight, cost, performance, ease of installation, and aerodynamic properties and low profile are constraints.

Microstrip antennas have following advantages: they are low profile, light weight, conformable to planar and non-planar surfaces, simple and inexpensive to manufacture using modern printed-circuit technology, mechanically robust when mounted on rigid surfaces, and when the particular patch shape and mode are selected, they are very versatile in terms of resonant frequency, polarization, pattern, and impedance. They are amendable to mass production, easily integrated with microwave integrated circuits and are conveniently integrated into array. These advantages contributed to the success of the microstrip antenna.

Microstrip antennas also have some limitations compared to conventional microwave antennas: narrow bandwidth which is typically only a fraction of a percent or at most a few percent and associated tolerance problems with resonance frequency, low efficiency, poor polarization purity, poor scan performance, spurious feed radiation, somewhat lower gain ($< 6\text{dBi}$), large ohmic loss in the feed line of arrays, excitation of surface waves [37].

1.2.1. Basic operation of microstrip antennas

At first glance it might seem surprising that a microstrip antenna can operate very well at all, since it consists of a horizontal electric surface current (corresponding to the patch current) suspended (via the substrate) a short distance above a ground plane. Basic image theory predicts that such a current will not radiate very well. However, the microstrip patch and the ground plane together form a resonant cavity (filled with the substrate material). The cavity is lossy, due not only to the material (conductor and dielectric) loss, but also to the (desirable) radiation into space from its edges.

The fields within the dielectric substrate (between the patch and the ground plane) can be found by treating that region as a cavity bounded by electric conductors (above and below it) and by magnetic walls (to simulate an open circuit) along the perimeter of the patch. This is an approximate model, which in principle leads to a reactive input impedance (of zero or infinite value of resonance), and it does not radiate any power. However, assuming that the actual fields are approximate to those generated by such a model, the resonance frequency can

be calculated and a microstrip antenna can be understood as an array of two *radiating* narrow apertures (slots). In the case of rectangular geometry, each of width W and height h , separated by a distance L .

In this so-called *cavity model*, the patch acts as resonant cavity with an electric field perpendicular to the patch, that is, along the z -direction in Figure 14(a). The magnetic field has a vanishing tangential component at the four edges of the patch. Due to these boundary conditions, the lowest possible cavity mode is a transverse magnetic TM_{010} mode. The fields of the lowest resonant mode (assuming $L > W$) are given by

$$\begin{aligned} \mathbf{E} &= -\hat{\mathbf{z}}E_0 \sin\left(\frac{\pi}{L}x\right) & -\frac{L}{2} \leq x \leq \frac{L}{2} \\ \mathbf{H} &= -\hat{\mathbf{y}}H_0 \cos\left(\frac{\pi}{L}x\right) & -\frac{W}{2} \leq y \leq \frac{W}{2} \end{aligned} \quad \text{for} \quad (1.50)$$

where $H_0 = -jE_0/\eta_0$. We have placed the origin at the middle of the patch. It can be verified that (1.50) satisfy Maxwell's equations and the boundary conditions, that is, $\mathbf{H} = \mathbf{0}$ at $x = \pm L/2$ provided the resonant frequency is:

$$\omega = \frac{\pi c}{L} \Rightarrow \boxed{(f_r)_{010} = 0.5 \frac{c}{L} = 0.5 \frac{c_0}{L\sqrt{\epsilon_r}}}, \quad (1.51)$$

where $c = c_0/\sqrt{\epsilon_r}$, $\eta = \eta_0/\sqrt{\epsilon_r}$, and ϵ_r is the relative permittivity of the dielectric substrate. It follows that the resonant microstrip length will be half-wavelength. The length L is usually increased by an amount $\Delta L \approx h$ because, in reality, the (fringing) fields extend slightly beyond the imagined edge of the cavity and effectively prolong the patch size. The fringing fields, shown in Figure 14(b), are the actual cause of radiation.

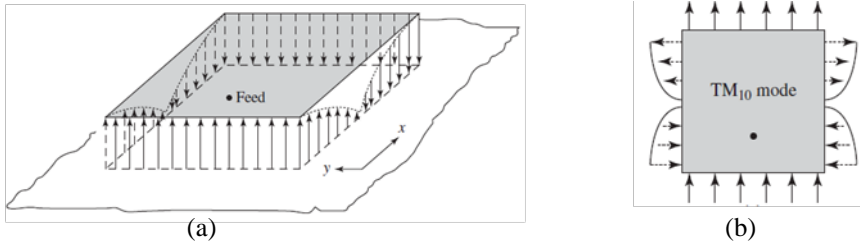


Figure 14 (a) Cavity model of a rectangular patch antenna and (b) the fringing fields that extend beyond the cavity in reality. Taken from [37]

For a circular the electric field of the lowest resonant mode is given by [31]

$$\mathbf{E} = \hat{\mathbf{z}}E_0 \frac{J_1\left(\frac{p'_{11}\rho}{a}\right)}{J_1(p'_{11})}, \quad \text{for} \quad 0 < \rho < a \quad (1.52)$$

where p'_{11} is the first zero of the Bessel function $J_1(x)$, and a is the physical radius of the circular patch. The usual mode of operation is the TM_{110} mode with $p'_{11} = 1.8418$. This mode has a broadside pattern the lowest resonance frequency given by.

$$\boxed{(f_r)_{110} = \frac{p'_{11}c}{2\pi a_e \sqrt{\epsilon_r}}}, \quad (1.53)$$

where instead of the patch radius a , we used the effective patch radius a_e , due to the (fringing) fields extending slightly beyond the imagined cavity. a_e is given by an empirical formula

$$a_e = a \left\{ 1 + \frac{2h}{\pi a \epsilon_r} \left[\ln\left(\frac{\pi a}{2h}\right) + 1.17726 \right] \right\}^{1/2}, \quad (1.54)$$

These formulas can also be used to calculate the needed patch size for a desired resonant frequency but are only approximate.

An alternative, approach to describe patch antennas is the *transmission line model*. For a rectangular or square patch, its radiation is basically generated from fringing fields at its two edges, as shown in Figure 15(a). Patch radiation is similar to radiation from two narrow slots separated by the patch length L , as mentioned in the cavity model. When operating at its fundamental mode, the patch is essentially a $\frac{1}{2} \lambda_g$ -long microstrip transmission line and can be represented by an equivalent transmission line model. The transmission line seems open ended at each end, however there is a capacitive effect and radiation loss, both created by the fringing fields. Thus the microstrip radiator can be characterized by two slots separated by a transmission line, where each slot is represented by a parallel circuit of conductance (G) and susceptance (B). The complete patch

antenna can be represented by the equivalent network shown in Figure 15(b). The feeding pin is connected at a position where the imaginary parts of the transformed admittances from the transmission line edges cancel out.

This transmission-line model is simple, intuitively appealing, and computationally fast, but it suffers from limited accuracy. For example, this model lacks the radiation from the non-radiating edges of the patch, and it has no mutual coupling between the two radiating slots, it lacks the flexibility and generalization of analyzing other patch shapes. Nevertheless, it does shed some physical insight into the operation of the antenna.

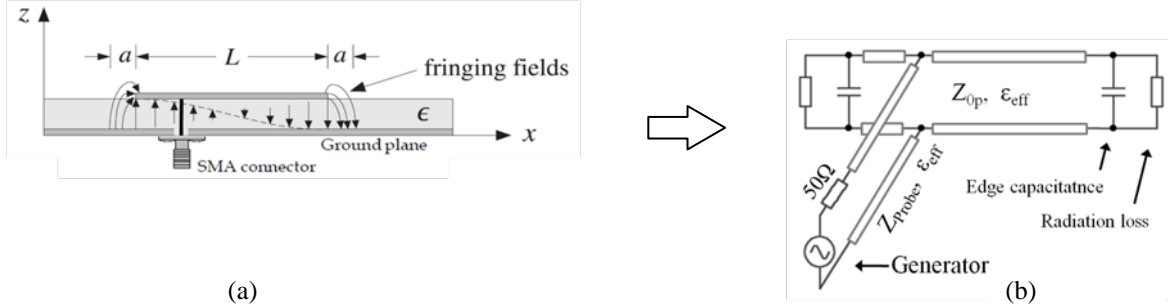


Figure 15 (a) Microstrip patch radiation source represented by two equivalent slots. (b) Equivalent circuit of a microstrip patch element.

The characteristic impedance of the patch transmission line Z_{0p} and its effective permittivity ϵ_r can be calculated using very accurate, but cumbersome empirical formulas one can find in [38]. The feed pin can also contribute to radiation, thus it introduces additional loss, but more importantly, it introduces unwanted inductive reactance. A precise analysis of the feeding pin impedance was done in [39]. Effective capacitance and radiation loss are also described by empirical formulas only, and can be found in [40]. Writing out all these formulas is avoided as they will not be used in this thesis.

1.2.2. Miniaturization techniques

Here we discuss the miniaturization techniques for pin fed classical patch antennas and show specific examples. The material loading example shows simulation results created by the author while other examples are taken from the literature.

A. MATERIAL LOADING

For a rectangular patch we can transform (1.51) to state $L = 0.5c_0 / ((f_r)_{010} \sqrt{\epsilon_r})$, where we immediately see that for a fixed resonance frequency $(f_r)_{010}$ length L , i.e. patch size, is inversely proportional to the square root of the substrate permittivity. The simplest miniaturization technique is thus an increase of permittivity.

Example: A demonstration of this miniaturization technique is visible Figure 16 for a rectangular patch over an infinite ground plane and substrates of different permittivity's. The exact size and miniaturization factor are given in Table 6 for several substrate height values.

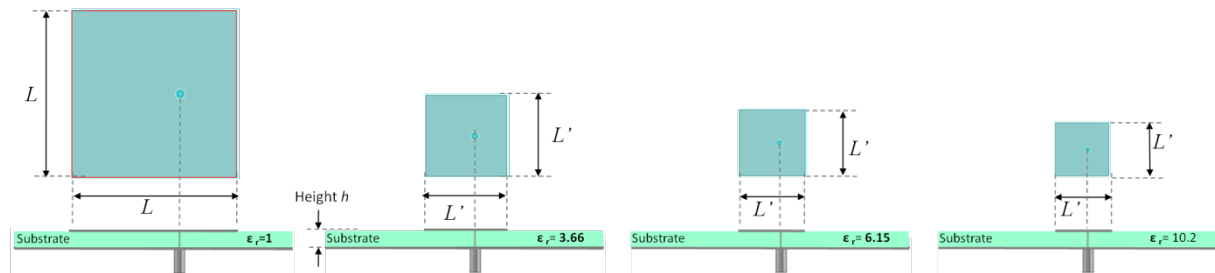


Figure 16 Comparison of size of a pin-fed rectangular patch over infinite substrate of relative permittivity 1, 3.66, 6.15 and 10.2. In each case, size is adjusted for a resonance at 2.3GHz.

Substrate height h	1 mm		3 mm		6 mm	
Permittivity ϵ_r	Patch size and miniaturization factor		Patch size and miniaturization factor		Patch size and miniaturization factor	
1	62.14 mm	1.00	59.21 mm	1.00	57.99 mm	1.00
3.66	33.35 mm	1.86	32.03 mm	1.85	30.94 mm	1.87
6.15	25.85 mm	2.40	24.70 mm	2.40	22.94 mm	2.53
10.2	20.13 mm	3.09	19.00 mm	3.12	17.06 mm	3.40

Table 6 Exact patch size in [mm] for three different heights of the substrate and the corresponding miniaturization factor for each permittivity.

B. SHORTING PIN

Based on the cavity-model approximation, the fundamental or first resonant frequency of the rectangular patch in Figure 17(a) without a shorting pin is determined from formula $(f_r)_{010} = 0.5c_0/L\sqrt{\epsilon_r}$ for the TM_{010} mode. The rectangular microstrip antenna is usually operated as a half-wavelength antenna. When a shorting wall is used at the edge of the patch, the null-voltage point that was at the center of the rectangular patch (operated at the TM_{010} mode) is shifted to the patch edge, and the first resonant frequency occurs close to, or at about $0.5(f_r)_{010}$. In this case, the shorted microstrip antenna is operated as a quarter-wavelength antenna, a 50% decrease in size. Compared to shoring wall, a shorting-pin-loaded rectangular microstrip antenna is operated with a resonant length less than one quarter-wavelength and a greater reduced antenna size than for the case with a shorting wall can be obtained.

Example: Figure 17(a) shows the configurations of shorted rectangular and circular microstrip antennas with a shorting pin. When there is a shorting pin placed at $x = -L/2, y = 0$, (center of the patch edge) and the feed position is chosen on the centerline (x axis), the first resonant frequency occurs at about $0.38(f_r)_{010}$ [42].

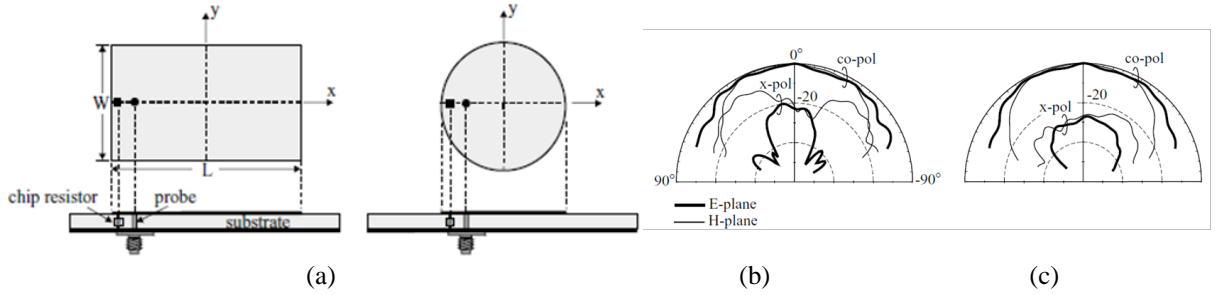


Figure 17 Geometries of compact (a) rectangular, and circular microstrip antennas with shorting-pin loading. (b) Typical measured radiation patterns in E- and H-plane at resonance of (a) shorted and (b) conventional microstrip antennas. Pictures taken from [42], and the original paper [43].

Similar behavior is true also for a circular patch, with the shorting-pin-loading technique, the antenna size reduction is mainly due to the shifting of the null-voltage point at the center of the circular patch (operated at the TM_{110} mode) to the patch edge, which makes the shorted patches resonate at a much lower frequency. The reduction in the patch size is limited by the distance between the null-voltage point in the patch and the patch edge. The radiation patterns for the compact and conventional microstrip antennas are plotted in Figure 17(b) and (c). It is observed that the component of cross-polarization radiation is increased due to the shorting-pin loading, especially for H-plane ($y-z$ plane) radiation. However, for E-plane ($x-z$ plane) radiation, the cross-polarization radiation is still below -20 dB. Note that, due to the antenna size reduction, a decrease in the antenna gain and bandwidth is expected.

C. MEANDERED PATCH

This kind of miniaturization technique is achieved mainly by loading several meandering slits at the non-radiating edges of a rectangular patch or at the boundary of a rectangular or circular patch. The narrow slots meander the patch, which increases the effective electrical length of the patch.

Example: Figure 18 shows the geometry of a short-circuited, meandered circular microstrip antenna. The circular patch is short-circuited at the edge with a shorting pin, and three narrow slots of the same length l and width w are cut in the patch. The shorting pin also makes the circular patch resonate at a much lower frequency compared with a conventional circular patch of the same size. Based on the above design concept, short-circuited circular microstrip antennas with different slot lengths were constructed. The circular patch has a radius R of 7.5 mm, and a shorting pin of radius $r_s = 0.4$ mm is placed near the patch edge at $d_s = 6.5$ mm. The patch substrate has a relative permittivity $\epsilon_r = 4.4$ and thickness $h = 1.6$ mm. Figure 18(b) shows the measured resonant frequency against the slot length in the short-circuited circular patch. Results clearly indicate that, with increasing slot length, the resonant frequency of the meandered patch decreases. It is also found that the slot width has relatively little effect on the resonant frequency.

From the results for the case of $l = R$, a circular patch of radius 7.5 mm has a resonant frequency of 1652 MHz. For a conventional circular patch antenna (without a shorting pin and slots in the patch) to be operated at 1652 MHz, the radius of the circular patch needs to be about 25.2 mm (with the same substrate material). That is, the patch size is reduced to about 9% compared with the conventional circular patch of the same operating frequency. The impedance bandwidth determined from a 10-dB return loss is found to be about 1.6%, which is

less than that (1.9%) of a conventional circular microstrip antenna at the same operating frequency. This reduction in the antenna bandwidth is expected due to the reduced antenna size.

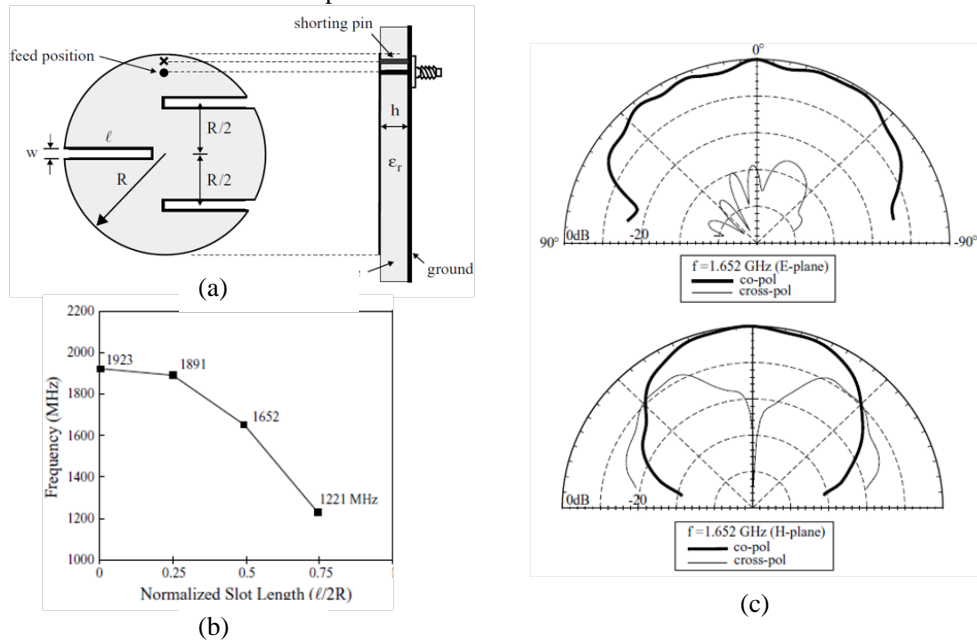


Figure 18 (a) Geometry of a meandered circular microstrip antenna with a shorting pin. (b) Measured resonant frequency against slot length ℓ in the circular patch; $R = 7.5$ mm (c) Measured E- and H-plane radiation patterns at resonance for an antenna with $\ell = R$. Taken from [44].

It is seen in Figure 18(c) that the radiation patterns remain broadside. However, probably owing to the increasing of the patch surface current component perpendicular to the main excitation direction, the cross-polarization radiation in the H plane is increased. The cross-polarization level in the E plane is seen to be about the same.

D. MEANDERED GROUND PLANE

The meandering technique for lengthening the excited patch surface current path, thus lowering the antenna's fundamental resonant frequency can also be applied to the antenna's ground plane.

Example: Figure 19 shows an example geometry of a compact microstrip antenna with a meandered ground plane. In the study performed in [45], inexpensive FR4 substrates ($\epsilon_r = 4.4$, $h = 1.6$ mm) is used. The dimensions of the rectangular radiating patch were chosen to be 30 mm \times 20 mm ($L \times W$). The slot length l_0 for the prototypes was fixed to be 10 mm and the slot length l_i was varied from 8 to 14 mm.

For the reference antenna, the fundamental resonant mode is excited at 2387 MHz with a 10-dB return-loss bandwidth of 2.0%. For increasing slot length l_i , it is seen that the fundamental resonant frequency is quickly lowered. For antenna with $l_i = 14$ mm, the resonant frequency f is 1587 MHz, which is about 0.66 times that of the reference antenna. This suggests that an antenna size reduction as large as about 56% can be achieved for the proposed antenna operated at a fixed frequency. Moreover, it is clearly seen that the impedance bandwidths of the prototypes (antennas 1–4) are all greater than that of the reference antenna. This behavior is largely owing to the meandering slots embedded in the antenna's ground plane, which also radiate to the back side of the antenna and effectively lower the quality factor of the proposed antenna. Figure 19(c) plots the measured E- and H-plane radiation patterns for antenna with $l_i = 10$ mm. Good broadside radiation patterns are observed. The front-to-back ratio (F/B) was also measured. From the measured results, the backward radiation of antenna 3 is increased by about 7 dBi compared to the reference antenna. This increase in the backward radiation is contributed to by the embedded slots in the ground plane and the decreased ground-plane size in wavelength.

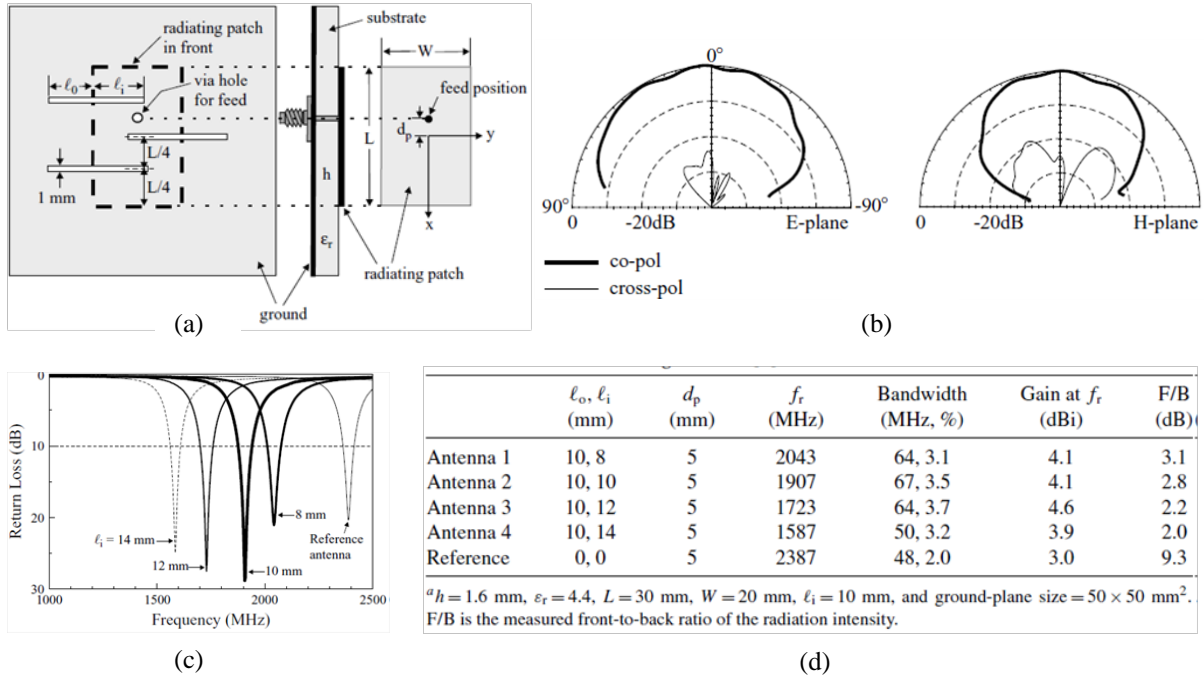


Figure 19 (a) Geometry of a compact microstrip antenna with a meandered ground plane. (b) Measured return loss against frequency; antenna parameters are given in table (d), (c) Measured E-plane (x - z plane) and H-plane (y - z plane) radiation patterns for the compact microstrip antenna, (d) Table: Performance of the compact microstrip antenna with a meandered ground. Results taken from [45].

E. CHIP RESISTORS AND CAPACITORS

Similar to the shorting technique, instead of a shorting wire, a chip capacitor or a chip-resistor can be used to load the microstrip antenna. With a chip capacitor, a decrease in the antenna's fundamental resonant frequency can be obtained, which corresponds to an even larger antenna size reduction at a given operating frequency. Chip resistor will also reduce fundamental resonant frequency if its resistance is very small, but it will also introduce additional losses. Losses enlarge the bandwidth, but are usually not a desirable technique for bandwidth enhancement.

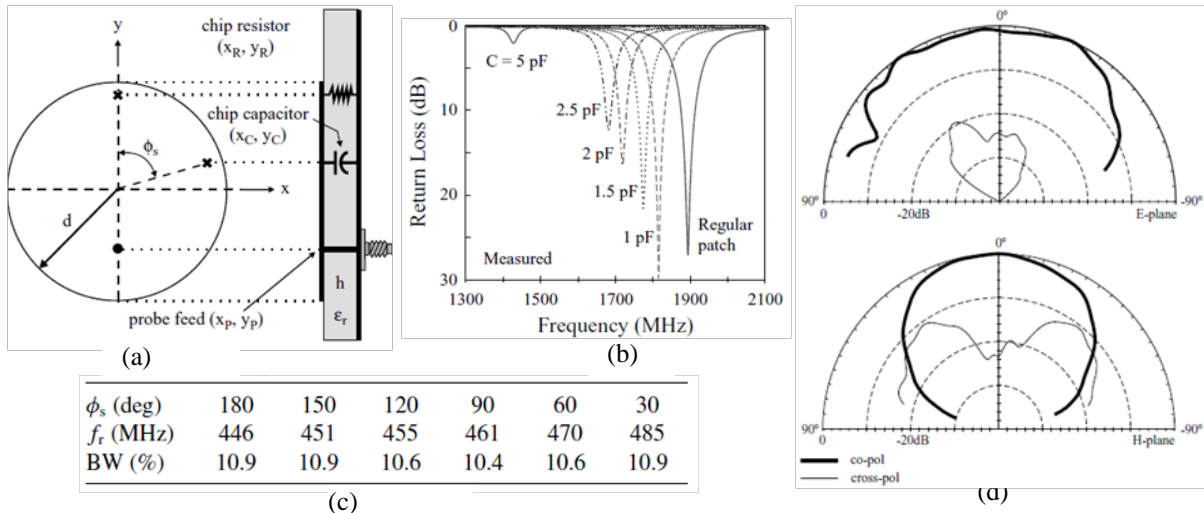


Figure 20 (a) Geometry of a probe-fed circular microstrip antenna with a chip resistor and a chip capacitor. (b) Measured return loss against frequency for the antenna shown in (a) with chip-capacitor loading only; $\epsilon_r = 4.4$, $h = 1.6\text{ mm}$, $d = 21.97\text{ mm}$, $(x_C, y_C) = (0, 21\text{ mm})$, and $(x_p, y_p) = (0, 8.5\text{ mm})$. (c) Table: measured resonant frequency and impedance bandwidth as a function of angle between the loading chip resistor and chip capacitor. (d) Typical measured radiation patterns at resonance. Results taken from [46].

Example: The geometry is shown in Figure 20(a). The chip resistor has a cross section of $2.07 \times 1.27\text{ mm}^2$ and is soldered to the ground plane at (x_R, y_R) , where there is a circular hole drilled through the substrate large enough for the insertion of the chip resistor. The chip capacitor has a cross section of $2.0 \times 1.28\text{ mm}^2$ and is loaded at (x_C, y_C) . The probe feed is at (x_p, y_p) and has a circular cross section of radius 0.63 mm . The spacing angle between the chip resistor and the chip capacitor is denoted ϕ_s . Since the excited electric field under the

circular patch at the fundamental TM_{110} mode has a maximum value around the patch edge, both the chip resistor and chip capacitor are placed at the patch edge for maximum effects on the resonant-frequency lowering of the circular microstrip antenna.

The case with chip-capacitor loading only is discussed first. Figure 20(b) shows the measured return loss of the antenna loaded with various chip capacitors. Note that the feed position in Figure 20 was fixed for various loading capacitances and selected such that good impedance matching was achieved for the case with a 1-pF chip-capacitor loading, in which an impedance bandwidth of about 1.7% is observed. The bandwidth is lower than that (about 1.9%) of a corresponding regular circular microstrip antenna with a center frequency at about 1.9 GHz. This suggests that, although chip-capacitor loading can result in a reduction in the antenna's fundamental resonant frequency, the impedance bandwidth is reduced, which is similar to the case of using the shorting-pin loading technique and also agrees with observations for the case with a parallel plate-capacitor load. By varying the spacing angle of φ_s , good impedance matching is slightly affected and the impedance bandwidth is about the same.

In [46] additional loading of a 1-ohm chip resistor is also studied and it was shown the antenna had an impedance bandwidth of 11.5% with the loading of a 1 Ohm chip resistor and is much larger than that (about 1.5%) of a short-circuited microstrip antenna. Also, by combining chip-resistor and chip-capacitor loadings, a significant effect in lowering the resonant frequency of the microstrip antenna with broadband characteristic can be obtained with only a very slight effect on the optimal feed position, which makes the present compact broadband microstrip antenna design very easy to implement.

1.2.3. Bandwidth enhancement techniques

Here we discuss the bandwidth enlargement techniques for pin fed classical patch antennas and show specific examples. The material loading, height increase and stacked patches examples contain simulation results created by the author while other examples are taken from the literature.

A. ADDING LOSSES

This is generally not the preferred way of increasing bandwidth (lowering the Q factor) and is avoided as it decreases the radiation efficiency. Nevertheless, as all materials have losses, realistic bandwidth is always increased compared to an ideal, lossless case. In the case of the Rogers materials used in our investigations the losses are given in terms of $\tan \delta$ in Table 7. These losses are considered unavoidable and are taken into account in simulations throughout the thesis.

Material	Permittivity	$\tan \delta$
Air	1	0
Rogers 4350	3.66	0.0037
Rogers 3006	6.15	0.002
Rogers 3010	10.2	0.0023

Table 7 List of supstrate materials investigated and the corresponding losses.

B. MATERIAL LOADING

As mentioned in the list of miniaturization techniques, high substrate permittivity reduces the antenna size, however, it also reduces bandwidth. An opposite approach, lowering the substrate permittivity is thus a simple and direct method to enlarge bandwidth.

Example: Demonstration of the effect of the substrate permittivity is shown in Figure 21 for a rectangular patch antenna on an infinite ground plane and substrate. Sizes of the two antennas optimized to resonate at 2.3 GHz are given in Table 6.

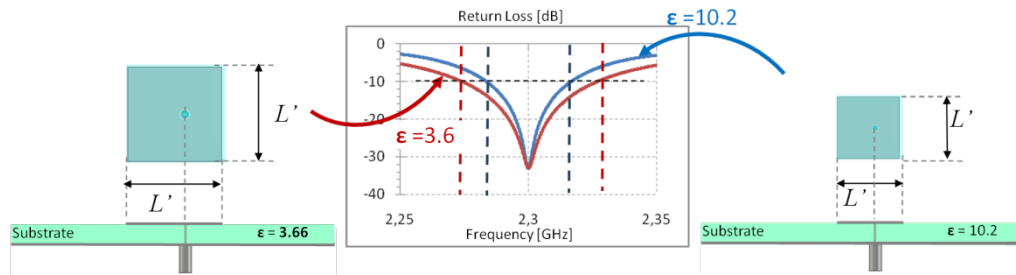


Figure 21 Comparing bandwidth performance for a rectangular patch antenna over substrate of relative permittivity 3.66 and 6.15, demonstrating larger bandwidth for lower permittivity. Figure shows simulation results.

C. HEIGHT INCREASE

Second simple and direct method to enhance the bandwidth is to increase the thickness of the substrate. However, there are thus two major limitations to this technique. First, a thicker substrate supports more surface waves, which will reduce the radiation efficiency. Usually, surface waves travel within the substrate and they are scattered at bends and surface discontinuities, such as truncation of the dielectric and ground plane, and degrade the antenna pattern and polarization characteristics. Surface waves are effectively a loss mechanism and limit the maximum height of the substrate. Second, if the antenna is fed by a probe feed (pin-feed), large thickness will also cause extraneous radiation due to inductive reactance of the probe feed. This will degrade the radiation pattern, and also creates matching problems.

Example: The increase in bandwidth vs. height is demonstrated in Figure 22 for a rectangular and circular patch shape, depicted in Figure 13. Investigation of height dependence was done for several substrate permittivity values. In all cases it is observed that the height can be increased up to about 9 mm ($0.07\lambda_0$) when the effect of the excitation form (pin feed) becomes significant. At the maximum height, where the curves end, the broadside radiation pattern is degraded by radiation from the pin feed. Additionally, due to the inductance of the feed, it is impossible to find a position on the patch surface to match the antenna.

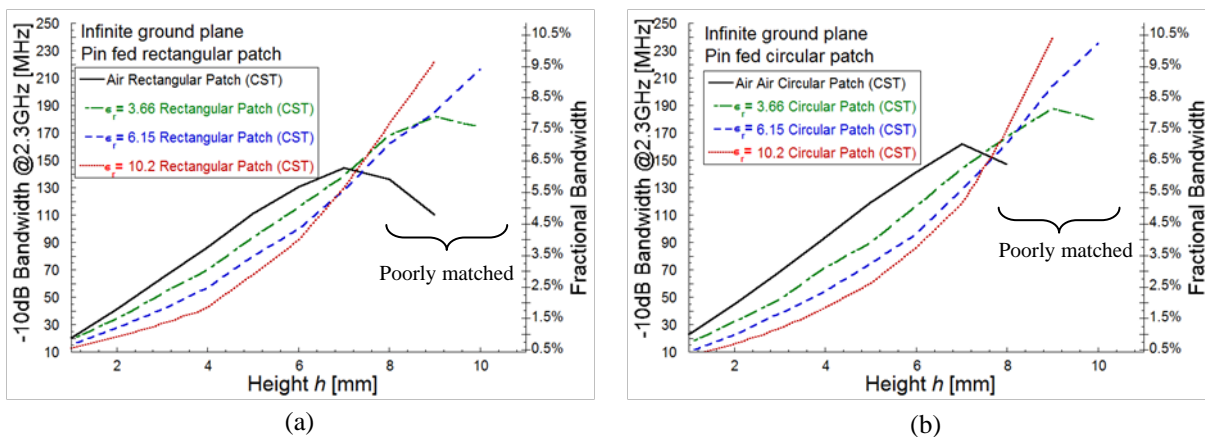


Figure 22 Bandwidth dependence on height for (a) rectangular and (b) circular shaped patch over an infinite ground plane and substrate. Four different values substrate relative permittivity were investigated, namely 1 (air), 3.66, 6.15 and 10.2 to show a more complex behavior as height increases. For heights below about 8 mm the antennas were perfectly matched, however above 8 mm they could not be perfectly matched. Curves end at points where matching the antenna with the pin feed position becomes impossible.

Note that the inductance from the feed can be neutralized by a series capacitor. This is a form of impedance matching the antenna. This capacitor can be fabricated in several different ways as shown in Figure 23. In this way it may be possible to increase the height a little further.

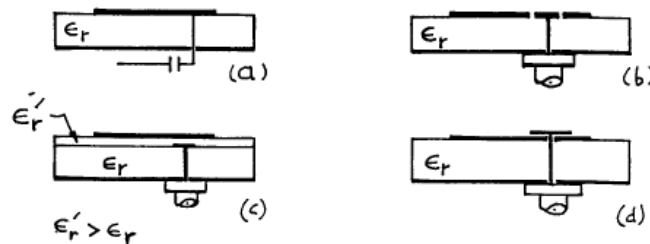


Figure 23 Impedance matching techniques to neutralize the inductance of the probe feed. (a) the capacitor is below the patch ;(b) capacitor takes the form of an annular ring around the feed; (c) the substrate consists of two layers and the high permittivity upper layer is used to create the capacitor; (d) small disk above the patch.

We also note that surface waves can be eliminated, while maintaining large bandwidths, by using cavities, which are introduced in the next Section of this chapter and studied in detail Chapter 2.

D. ADDING ADDITIONAL MICROSTRIP RESONATORS

By using additional microstrip patches, i.e. additional resonators that are coupled to the radiating patch, the antenna can have multiple closely spaced resonances and a bandwidth broadening effect can be achieved. A

condition to have close resonances, i.e. resonances that do not differ in resonance frequency too much, the coupling between the resonators has to be loose. In the case of patch antennas the resonators can be added vertically (stacked patches), or in the same plane as the radiating patch.

Example 1: A typical configuration of stacked patches is shown in Figure 24(a). Simulation result for S_{11} (negative of return loss) for stacked circular patches having two resonances around a central frequency of 2.3 GHz is shown in Figure 24(b). The resonances are close in frequency, and the antenna remains matched in the frequencies between them, this corresponds to the bandwidth broadening effect. Figure 24(c) shows simulated radiation patterns at the two resonant frequencies, showing broadside radiation, typical for a stacked patch configuration. While there is ample information on the optimization and measured results for this antenna, there is very little or no analytical functions to design this antenna and is practically designed by a trial and error method. However, the following is useful in optimizing a design: The top patch should be ‘loosely’ coupled to the bottom patch. To do so a higher dielectric substrate for the lower patch is needed. If the relative permittivity of the top layer is equal or greater than that of the lower substrate, the modes on the two patches will couple too strongly causing tight resonant loops and separation of the resonant frequencies and finally resulting in lower impedance bandwidths.

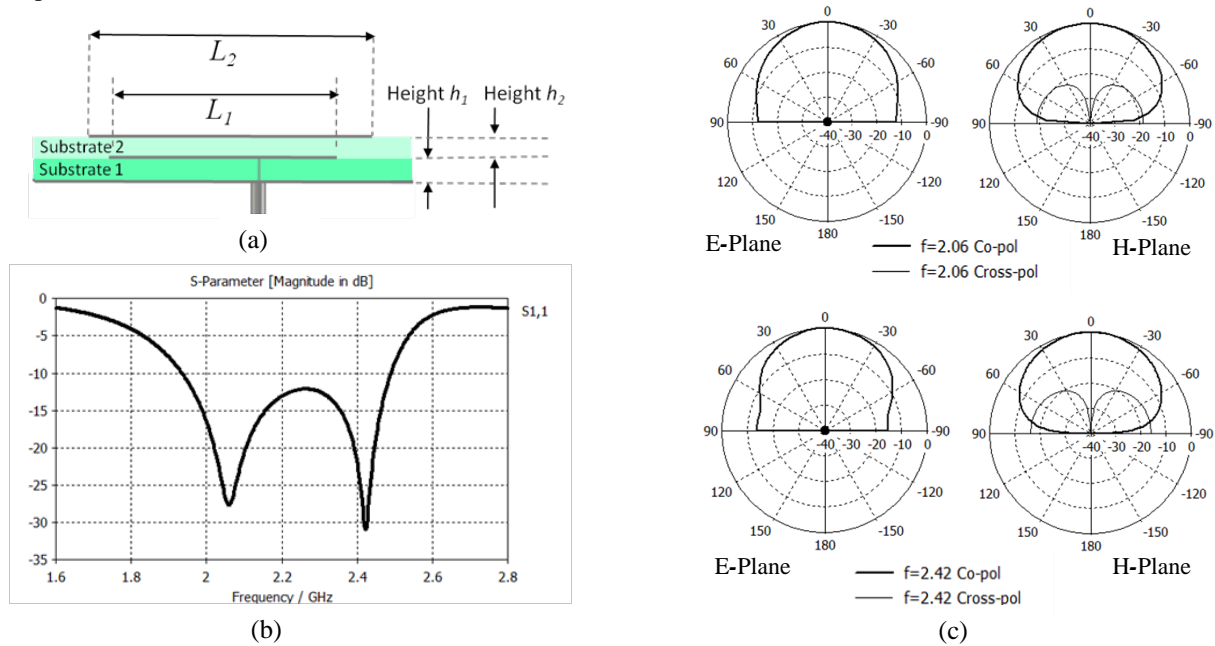


Figure 24 (a) Geometry of a typical stacked patch configuration. (b) Simulated S_{11} parameter for stacked circular patches; $L_1 = 54.16$ mm, $L_2 = 57.41$ mm, $h_1 = 8.87$ mm, $h_2 = 5.37$ mm, Substrate 1 has relative permittivity 2.1 and substrate 2 permittivity of 1.1. (c) Simulated radiation patterns for the two resonant frequencies.

Example 2: Typical geometry of additional resonators in the plane with the radiating patch is shown in Figure 25(a), in this case, a rectangular microstrip antenna with two additional patches directly coupled to its radiating edges. The impedance bandwidth can be five times that of a single rectangular microstrip antenna, as seen from the return loss in Figure 25(b). However, the resulting broadband microstrip antenna also has a much increased antenna size (area) compared to a single rectangular microstrip antenna. Radiation pattern remains broadband and is shown, for several frequencies in Figure 25(c).

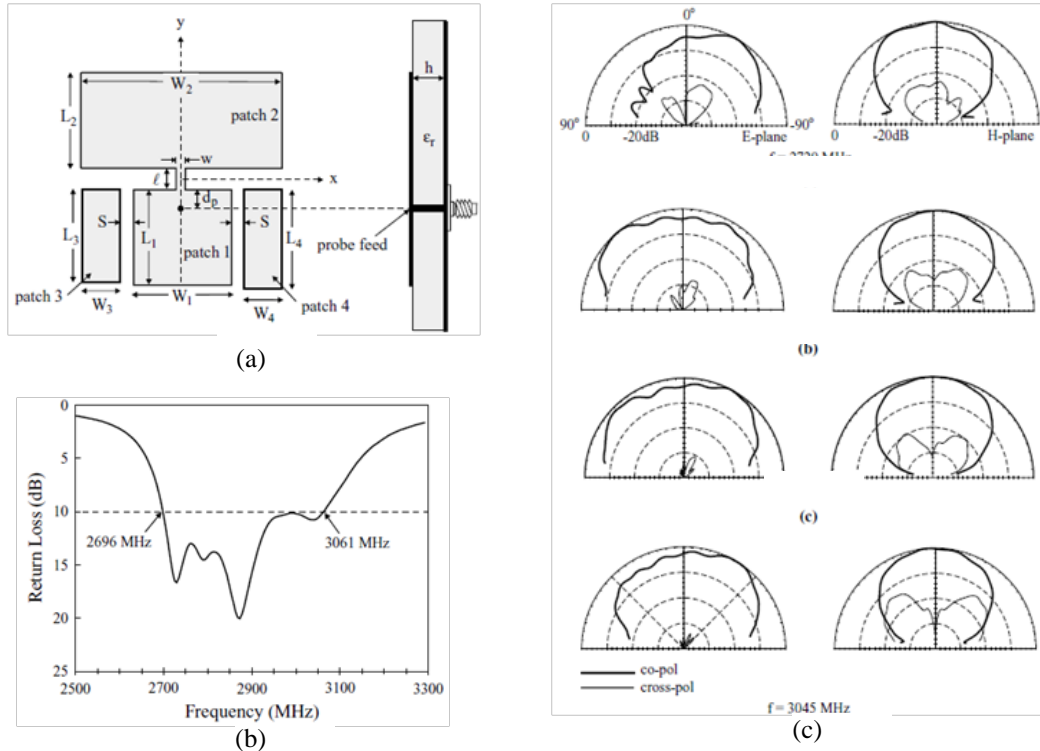


Figure 25 (a) Geometry of a proposed broadband microstrip antenna with directly coupled and parasitic patches; $\epsilon_r = 4.4$, $h = 1.6$ mm, $L_1 = 26.6$ mm, $L_2 = 24.4$ mm, $L_3 = 26.47$ mm, $L_4 = 27$ mm, $W_1 = 16$ mm, $W_2 = 40$ mm, $W_3 = W_4 = 10$ mm, $S = 2$ mm, $l = 2$ mm, $w = 0.2$ mm, and $d_p = 1.2$ mm. (b) Measured return loss against frequency; (c) radiation patterns for several frequencies. Pictures taken from [47].

E. MODIFYING THE PROBE FEED

The antenna geometry is shown in Figure 26 is using a three-dimensional microstrip transition feed. In this case, although the antenna has a thick air substrate, a short probe pin can be used, which is connected to a rectangular patch as a feed transition to the antenna's radiating patch.

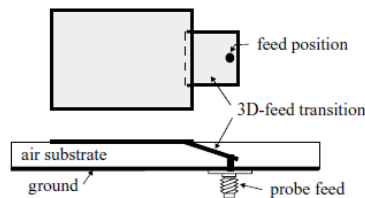


Figure 26 Geometry of a broadband microstrip antenna with a three-dimensional microstrip transition feed. This behavior makes good impedance matching over a wide bandwidth easy to achieve, and it has been shown that the typical operating bandwidth of this antenna is about 40%. Picture taken from [48].

F. INSERTING A U-SLOT

Embedding a suitable U-shaped slot in the antenna's radiating patch introduces a second resonance that is used for a bandwidth broadening effect. In this case the patch area is "re-used" without the need of additional resonators that would increase the antenna overall size like in the previous Section. It is a very effective method for achieving a wide bandwidth for a probe-fed microstrip antenna with a thick air substrate.

Example: Geometry of a rectangular patch antenna with a U-slot is presented in Figure 27(a). Good broadside radiation patterns are observed; see Figure 27(b). However, relatively large cross-polarization radiation in the H -plane pattern is also seen; which is a common characteristic for this kind of probe-fed microstrip antenna with a thick air substrate. Two resonances in are visible in the measured S_{11} parameter seen on Figure 27(c). An impedance bandwidth (10-dB return loss) of 500 MHz, or about 27.5% referenced to the center frequency at 1815 MHz is observed. To reduce the cross-polarization radiation, two out-of-phase feeds

can be used. The antenna gain was also measured, and the results are presented in Figure 27(e). The peak antenna gain is about 9.0 dBi, and the gain variations within the bandwidth are less than about 1.0 dBi.

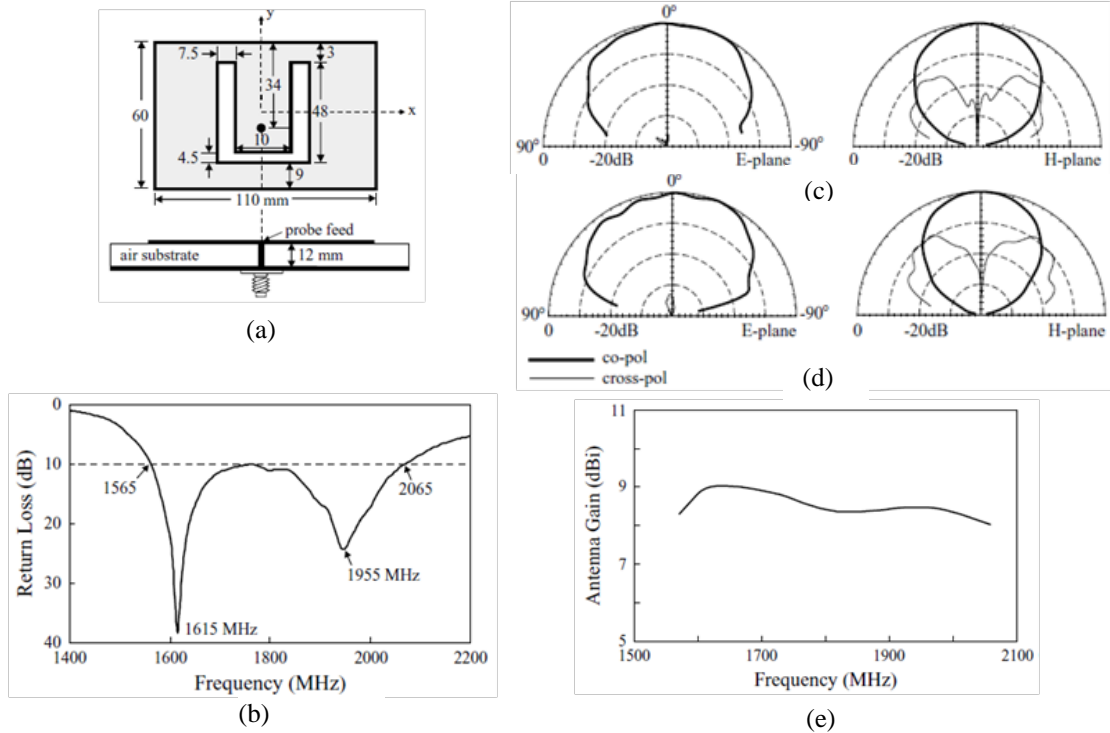


Figure 27 (a) Geometry of a broadband probe-fed rectangular microstrip antenna with a U-shaped slot. (b) Measured return loss for the antenna shown in (a). (c) Measured radiation patterns for the antenna for $f=1615$ MHz; (d) $f= 1955$ MHz. (e) Antenna gain. Results taken from [49].

G. CREATING AN E-SHAPED PATCH

By using an E-shaped patch instead of a U-slotted patch, similar broadband operation can be obtained. The E-shaped patch is formed by inserting a pair of wide slits at the boundary of a microstrip patch.

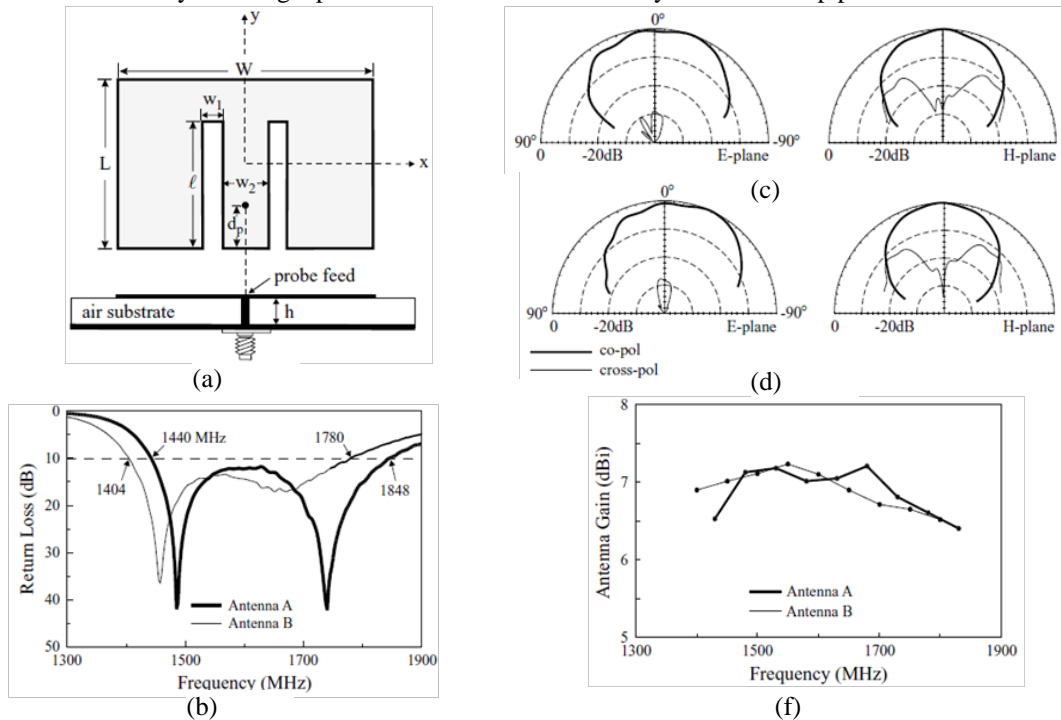


Figure 28 (a) Geometry of a broadband E-shaped microstrip antenna; $L = 65$ mm, $W = 105$ mm and ground-plane size = $150 \times 150 \text{mm}^2$; (b) Measured return loss; Antenna A: $h = 14.3$ mm, $l = 47$ mm, $w_1 = 6.3$ mm, $w_2 = 15.3$ mm, and $d_p = 10$ mm; Antenna B: $h = 15.7$ mm, $l = 53$ mm, $w_1 = 10$ mm, $w_2 = 8$ mm, and $d_p = 13$ mm (c) Measured E-plane ($y-z$ plane) and H-plane ($x-z$ plane) radiation patterns for $f = 1485$ MHz, (d) $f = 1644$ MHz, (d) Measured antenna gain in the broadside direction for antennas A and B. Pictures taken from [50].

Example: Geometry for a rectangular patch is shown in Figure 28(a). Figure 28(b) shows the measured return loss for two constructed prototypes (antennas A and B). For antenna A, the impedance bandwidth is 408 MHz, or about 24.8% with respect to the center frequency at 1644 MHz. For antenna B, the obtained bandwidth is 376 MHz, or about 23.6% referenced to the center frequency at 1592 MHz. The cross-polarization radiation in the E-plane patterns is less than -20 dB, see Figure 28(c) and (d). The H-plane patterns, however, show relatively larger cross-polarization radiation. This behavior is similar to that reported for the U-slotted patch, and is largely due to the thick substrate thickness (about 0.08 times the wavelength of the center frequency in this study) and long probe pin in the substrate layer. For both antennas A and B, the antenna gain, see Figure 28(e), variation is less than 0.8 dBi, with the peak antenna gain at about 7.2 dBi.

H. SLOT-LOADING

The proposed antenna is shown in Figure 29(a). The slots are placed symmetrically with respect to the y axis, on which an optimal probe feed for good impedance matching is located. The distance between the probe feed and disk center is denoted d_p . The inner open-ring slot has a small opening and is fixed. The outer open-ring slot has a relatively large opening and has an angle of φ . In the present design, by choosing a suitable angle φ , two resonant modes can be closely excited at frequencies in the vicinity of the fundamental resonant frequency $(f_r)_{110}$ of the corresponding simple circular microstrip antenna without slots, leading to the enhancement of the impedance bandwidth of the proposed antenna.

Example: Figure 29(b) presents the measured return loss for a constructed prototype. The angle φ is selected to be 32° and the feed position is at $d_p = 13$ mm. Note that, when there are no open-ring slots, the fundamental resonant frequency $(f_r)_{110}$ of the circular microstrip antenna with a radius of 23.36 mm is about 2 GHz. It is also clearly seen that the prototype antenna has two adjacent resonant modes excited at frequencies near 2 GHz: one at 2148 MHz and the other at 2200 MHz. The impedance bandwidth is 90 MHz, or about 4.1% with respect to the center frequency at 2175 MHz. This impedance bandwidth is about 2.1 times that (about 2%) of the corresponding simple circular microstrip antenna without slots. Figure 29(c) and (d) show the measured radiation patterns at the two resonant frequencies of 2148 and 2200 MHz. Similar broadside radiation patterns have been observed for the two resonant modes, and good cross-polarized radiation (less than -20 dB) is seen. Figure 29(f) shows the measured antenna gain in the broadside direction. The results show that the gain variation within the impedance bandwidth of the antenna is within a variation of less than 2.6 dB. It should also be noted that, mainly owing to the FR4 substrate used in this study, which has a large loss tangent (about 0.04), the antenna gain level is lower than about 3.5 dBi.

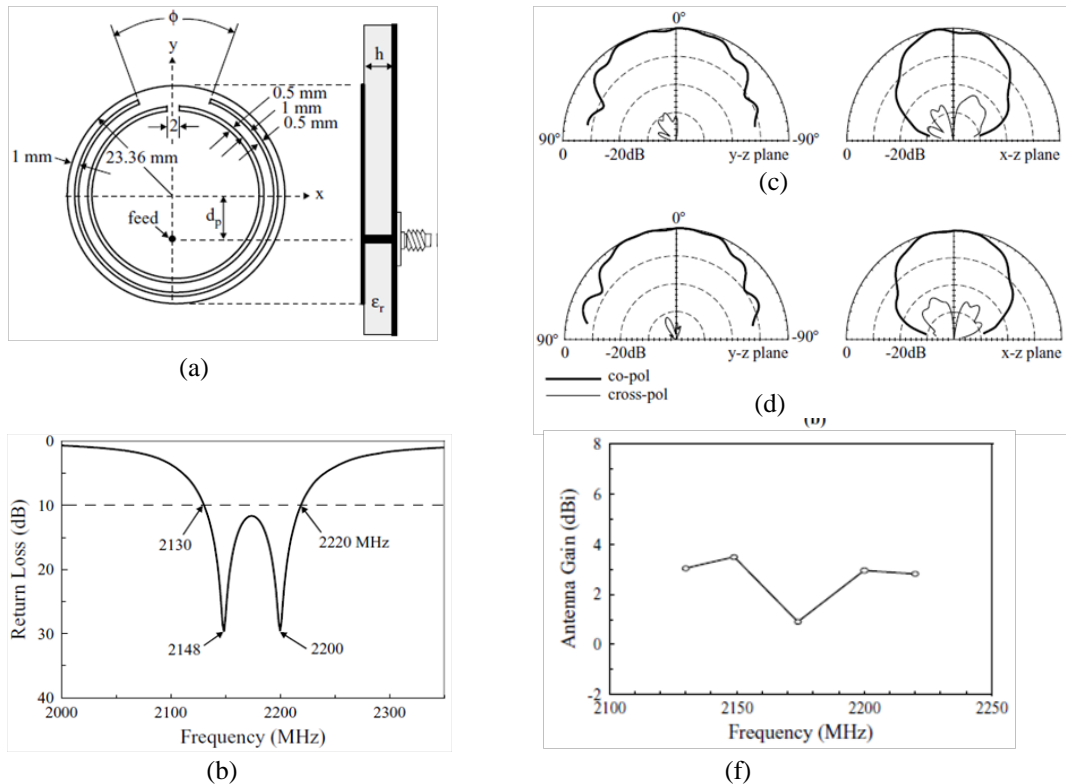


Figure 29 (a) Geometry of a broadband circular microstrip antenna with two open-ring slots. The dimensions shown in the figure are not to scale. (b) Measured return loss for the antenna; $\epsilon_r = 4.4$, $h = 1.6$ mm, $d_p = 13$ mm, $\varphi = 32^\circ$, and ground-plane size = 75×75 mm². Measured y-z plane (E-plane) and x-z plane (H-plane) radiation patterns for the antenna (c) $f = 2148$ MHz, (d) $f = 2200$ MHz. (e) Measured antenna gain in the broadside direction. Pictures taken from [51].

I. INTEGRATING REACTIVE LOADING

The integrated reactive loading technique is applicable to rectangular and circular circular microstrip antennas. However, experimental studies have shown that broadband operation is very sensitive to small variations in the dimensions of the inserted microstrip structure providing the reactive loading, especially when applying the inserted-loading technique to a circular microstrip antenna. To provide the reactive loading, a microstrip structure consisting of a straight microstrip-line section and a tab microstrip-line section is embedded inside a near-rectangular slot cut in the circular patch, shown on Figure 30(a). The occurrence of the two resonant modes is mainly due to the embedded reactive loading, which provides a capacitive load at the lower resonant frequency and an inductive load at the higher resonant frequency.

Example: Both the microstrip structure and the near rectangular slot are symmetric to the y axis; their dimensions are given in Figure 30(a). The straight microstrip-line section of the embedded microstrip structure is connected to the circular patch at the bottom edge of the slot, which is at a position about 0.2 times the disk radius away from the disk center. For the present design with $h = 1.6$ mm, $\epsilon_r = 4.4$, and a ground-plane size of 75×75 mm², a single probe feed located at a position about 0.55 times the disk radius away from the disk center can excite two resonant modes close to each other, in the vicinity of the fundamental resonant mode (TM₁₁₀) of the unloaded patch, to achieve a wide operating bandwidth. Figure 30(b) shows the measured return loss for the proposed design. It is observed that two resonant modes are excited at frequencies close to 1.9 GHz, which is the fundamental resonant frequency of the unloaded circular patch antenna. The measured return loss at the two resonant frequencies is greater than 25 dB. The obtained bandwidth is 116 MHz, or about 6.05%, which is about 3.2 times that (about 1.9%) of the corresponding unloaded circular microstrip antenna. Typical patterns in two orthogonal planes at the two resonant frequencies are presented in Figure 30(c) and (d). It is seen that good broadside radiation characteristics with the same polarization planes are obtained, and the cross-polarization radiation is well below -20 dB. The measured antenna gain in the broadside direction is shown in Figure 30(e). In general, the operating frequencies in the lower resonant mode have a relatively larger antenna gain than those within the higher resonant mode, and the variations of the antenna gain in the entire impedance bandwidth are within a range of less than 2.5 dBi.

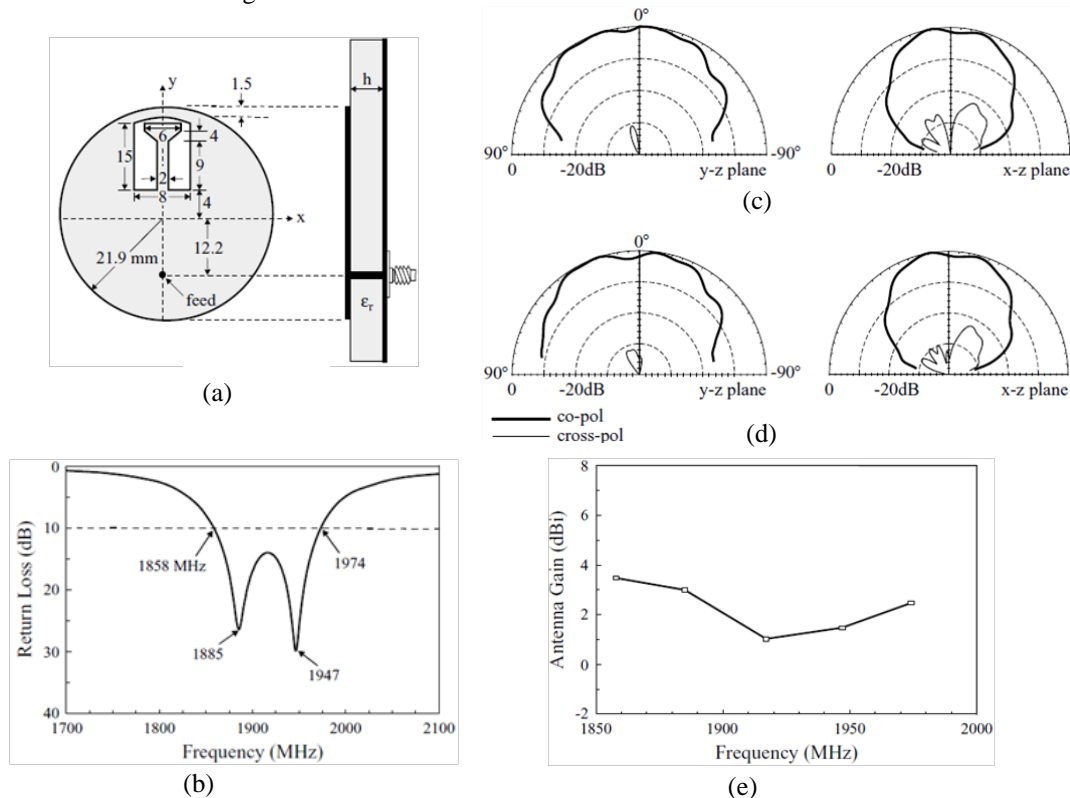


Figure 30 (a) Geometry of a broadband circular microstrip antenna with an embedded reactive loading. The dimensions shown in the figure are not to scale. (b) Measured return loss for the antenna shown in Figure 7.49; $\epsilon_r = 4.4$, $h = 1.6$ mm, and ground-plane size = 75×75 mm². Patch dimensions are given in Figure 7.49. (c) Measured y - z plane (E-plane) and x - z plane (H-plane) radiation patterns for $f = 1885$ MHz; (d) $f = 1947$ MHz. (e) Measured antenna gain in the broadside direction for the antenna studied in (a). Taken from [52]

1.3. Introduction to cavity antennas

Cavities as an antenna design element have been analyzed and used in practice since the middle of the 20th century. One of the first investigations of small cavities acting as antennas themselves was done by Counter and Cohen [53],[54],[55] and this thesis relies heavily the work presented in [53]. The use of cavity backing for antennas of various types in the period from 1950 to 1988 was summarized by Kummar in [56] where it was noted that a cavity reduces back radiation and side lobes, enhances forward gain and the resonant fields in the cavity help in reducing the size of the antenna. Kummar classifies cavity antennas into two basic groups:

- Dual reflector antennas
- Other cavity backed antennas

Dual reflector antennas consist of two reflectors, most frequently plane, with one dimensional field resonance between them, One of the reflectors is much smaller than the other (example: backfire antennas on Figure 31(a)), or else it is a semitransparent sheet (beam waveguide antennas) and acts like an end mirror in a laser cavity, see Figure 31(b). Backfire antennas are named long and short depending on the distance between the two reflectors. The *long backfire antenna* comprises of a surface wave structure which is several wavelengths ($n\lambda_0, n > 1$) long. The surface wave structure connects the reflectors and is usually excited by a crossed dipole or a waveguide aperture. The dominant mode is simply a standing wave surrounding the surface wave structure. The *short backfire antenna* has the spacing between the reflectors only half a wavelength ($\lambda_0/2$), and the surface wave structure becomes unnecessary. The *beam waveguide antennas* represent quasi-optical open resonators, i.e. their dimensions are many times larger than the wavelength ($\gg \lambda_0$). The end reflector is semitransparent; for example, it can be perforated metal. The beam waveguide antenna can be in a plane, plane spherical, or confocal spherical configuration, depending on the profile of the reflector.

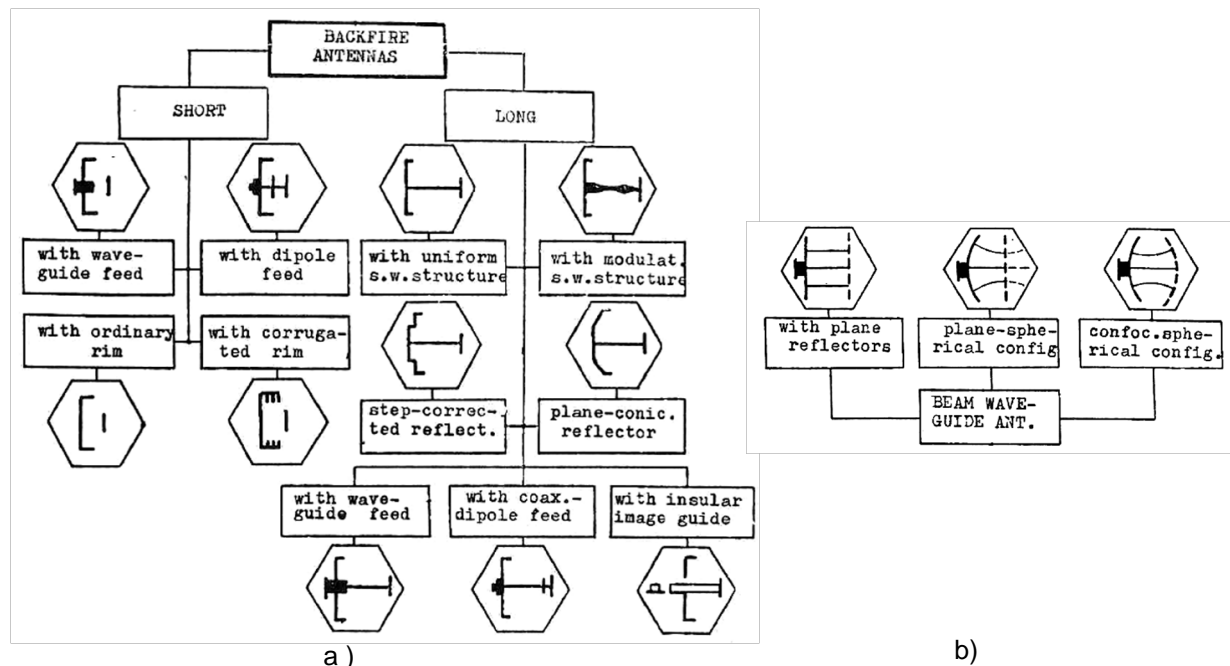


Figure 31 (a) Basic varieties of long and short backfire antennas with a cavity , (b) beam waveguide quasi-optical antenna configurations where dimensions are $\gg \lambda_0$. Taken from [56].

Cavity antennas, on the other hand are more like three dimensional cavity resonators (as dual-reflector antennas are based on open resonators). Figure 32 shows some cavity antenna designs with perforated semitransparent apertures. On the aperture, a multitude of small openings (slots or round holes) are made. Thus the cavity antenna can also be considered either as an antenna array or, generally speaking as a semitransparent aperture backed by a closed resonator cavity. For circular polarization, the basic concept of cavity backed radiator antenna involves the use of a crossed dipole feed, which is located in the aperture of the backing cavity. There are few examples of open cavity-backed antennas to produce circular polarization, shown in Figure 32(f) and (g).

The usual size of the above presented cavities was larger than half the free space wavelength ($> \lambda_0/2$), in all dimensions or at least in the aperture dimension. In recent decades, research interest has also turned to the investigation of microstrip antennas enclosed in a cavity with aperture dimensions comparable to half the free space wavelength ($\sim \lambda_0/2$) or smaller. Patch antennas have two limitations i.e. low bandwidth and low gain, thus

cavity-enclosed patch antennas have been investigated in the past to alleviate in some degree the drawbacks of classical patch antennas

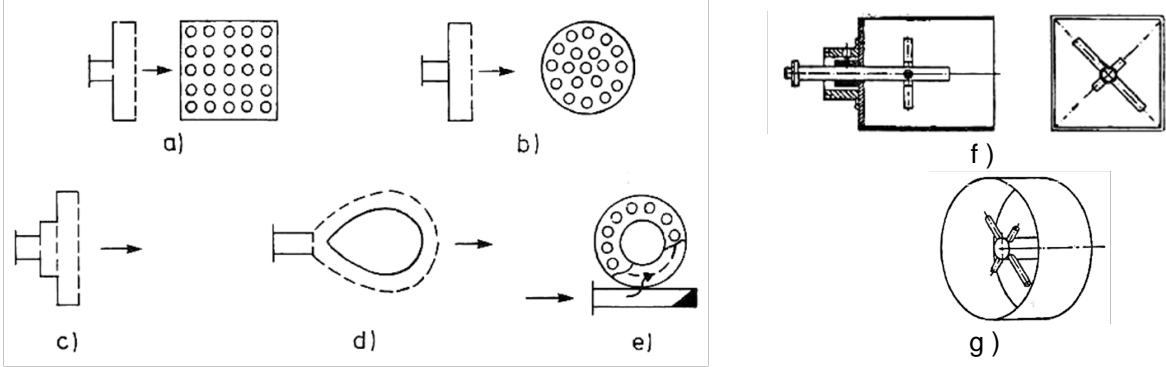


Figure 32 Cavity antenna designs with semitransparent radiating apertures. (a) rectangular single cavity antenna, (b) circular single cavity antenna, (c) two cavity antenna, (d) double-bounded cavity antenna, (e) ring shaped cavity antenna. (f) Cavity backed open resonator antennas in a rectangular and (g) circular cavity. Taken from [56].

In this thesis we are specifically interested and rigorously analyze cavity antennas smaller than half the free space wavelength ($< \lambda_0/2$) which will inevitably have narrow bandwidth. To this end, in this Section we first give a thorough analytical analysis of open ended cavity antennas, and second give an overview of the investigations done with cavity enclosed patch antennas in the literature.

1.3.1. Transmission line model of small open ended cavity antennas

This section is of special importance for the thesis as it lays important groundwork for the analysis in later chapters. It relies on work done by M. Cohen [53] in 1950's on square cavities in infinite ground planes, but due to the importance for later chapters, the author has expanded his results. This section thus includes the analysis of circular cavities in an infinite ground plane and the analysis in case of finite ground planes, not shown in literature so far.

A. RECTANGULAR CAVITY

In his PhD thesis, Cohen [53] gave a thorough analysis of small rectangular cavity antennas. We will reproduce the main results here as they will be of great importance in the rest of the thesis. For simplicity, the investigation was done for a rectangular geometry in an infinite ground plane; however, his results will be extended in this thesis.

Consider a rectangular cavity buried into an infinite ground plane and filled with some homogeneous material of permittivity ϵ_r and permeability $\mu_r = 1$, as shown in Figure 33. The cavity can be regarded as a short-circuited waveguide, open ended toward a half space. It can be modeled by a transmission line having a short circuit on one side and a load at the opposite side (corresponding to the aperture).

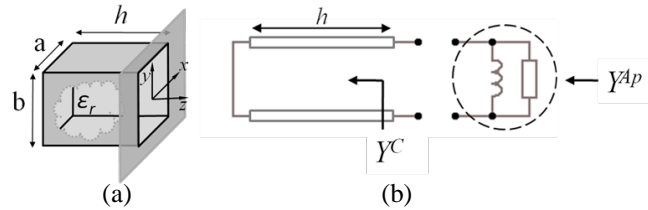


Figure 33(a) A square cavity in an infinite ground plane and (b) the corresponding transmission line model.

Again, for simplicity we assume only the dominant TE_{10} mode in the rectangular waveguide. The propagation constant in a rectangular waveguide is $k_{TE}^2 = \epsilon_r k^2 - k_c^2$ where $k^2 = \omega^2 \mu_0 \epsilon_0$ is the wave-number, and $k_c = \pi/a$ is the cutoff wave-number for the TE_{10} mode. The characteristic admittance for the TE modes is $Y_{TE} = k_{TE} / \omega \mu = k_{TE} / k \eta_0$ and thus the input admittance Y^C into a short circuited waveguide (cavity) is

$$Y^C(k) = Y_{TE} \frac{Y_{TE} + jY_T \tan(k_{TE} h)}{Y_T + jY_{TE} \tan(k_{TE} h)} = -j \frac{k_{TE}}{k \eta_0} \cot(k_{TE} h), \quad (1.55)$$

Where $Y_T = \infty$ is the short circuit admittance. For several values of relative permittivity, the input admittance is plotted against height h in Figure 34. For short cavities, the input admittance is inductive (negative). If the

waveguide is above cutoff, then the admittance crosses zero at a quarter of the guided wavelength inside the waveguide ($\lambda_g/4$). Note that if the waveguide is below cutoff, then the input admittance remains inductive for every height (see the curve for permittivity 3.66 in Figure 34).

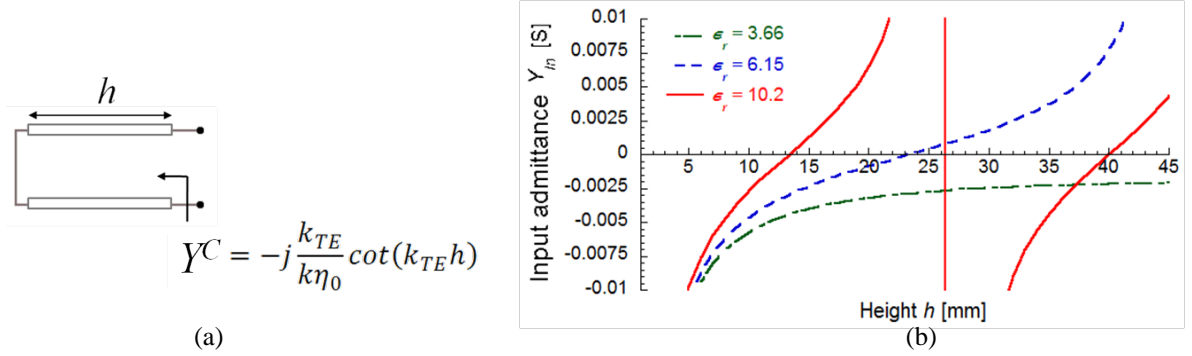


Figure 34 (a) transmission line model of a shorted waveguide representing the cavity. (b) Examples of input admittance into a shorted square waveguide of size $0.245 \lambda_0$ at frequency $f = 2.3$ GHz ($k = 48$) when the volume is homogenously filled with relative permittivity of 3.66, 6.15 and 10.2.

On the other hand, the open end of the structure is modeled by the aperture admittance Y^{Ap} . This admittance can be calculated analytically, using the spectral domain approach. The complete calculation is shown in **Appendix C** for the general TE_{mn} mode. We write here only the final expression for the TE_{10} mode.

$$Y^{Ap}(k) = G^{Ap} + jB^{Ap} = \frac{ab}{8k\eta_0} \iint_{\mathbb{R}^2} \frac{k^2 - k_x^2}{\sqrt{k^2 - k_x^2 - k_z^2}} \left(\frac{\cos\left(\frac{k_x a}{2}\right) \text{sinc}\left(\frac{k_y b}{2}\right)}{\left(\frac{\pi}{2}\right)^2 - \left(\frac{k_x a}{2}\right)^2} \right)^2 dk_x dk_y, \quad (1.56)$$

The integral in (1.56) has to be computed numerically for each value of k . However, the result for Y^{Ap} in the square aperture ($a = b$) case was reported by Cohen in [53] where it was given in the form of a Taylor series,

$$\begin{aligned} G^{Ap}(x) &= g^0 x^2 + g^1 x^4 + g^2 x^6 \dots, \\ B^{Ap}(x) &= b^0 x^{-1} + b^1 x + b^1 x^3 + \dots, \end{aligned} \quad (1.57)$$

with $x = a/\lambda_0 = ka/(2\pi)$. The aperture admittance is shown in Figure 35, where the admittance for the example sizes investigated in this thesis is also noted. In fact, in all cases the admittance is negative (inductive).

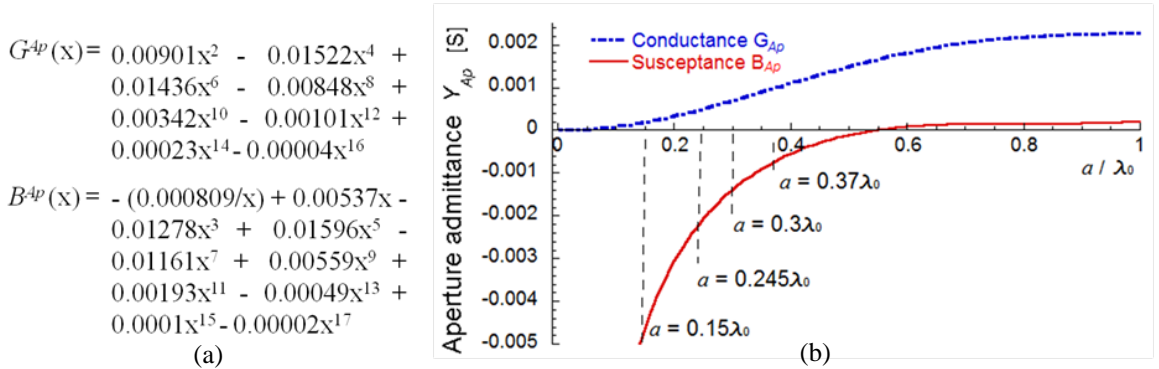


Figure 35 Aperture admittance Y^{Ap} for the TE_{10} mode given by (1.56) or (1.57). See Appendix C for the derivation. (a) Polynomial approximation given in terms of $x = a/\lambda_0 = ka/(2\pi)$. (b) Plotted real and imaginary part of Y^{Ap} as a function of the cavity diameter. Note that for the example aperture sizes the susceptance is inductive.

Without sources, the system Figure 33(b) oscillates when the reactances in the circuit cancel, i.e.,

$$jB^{Ap}(k) - j \frac{k_{TE}}{k\eta_0} \cot(k_{TE} h) = 0, \quad (1.58)$$

where B^{Ap} is the aperture susceptance, $k_{TE}^2 = \epsilon_r k^2 - k_c^2$ where $k^2 = \omega^2 \mu_0 \epsilon_0$, $k_c = \pi/a$ re, a is side of a square aperture and h the cavity height. Notice that we have transformed the geometry into a 1D model that is easy to analyze. Looking at (1.58) physically, a resonant condition means the transmission line must present capacitive admittance to counter the inductive admittance at the aperture. This can happen only when the waveguide, i.e. the transmission line is longer than $\lambda_g/4$ and shorter than $\lambda_g/2$ of guided wavelength, as was

also demonstrated above, in Figure 34. This also means that if the waveguide is below cutoff, (1.58) can never be satisfied.

There are two variables in (1.58) i.e. the height h and the permittivity ε_r . Thus to achieve resonance, one or the other can be adjusted. We can treat height as a function of permittivity or vice versa. This will be explicitly shown in examples on Figure 36(a) and (b). However, in this thesis, it will be more useful to treat ε_r as a function of height h , thus (1.58) is used to obtain the necessary ε_r for a given cavity height.

Once the resonant height is known one can calculate the Q factor of such an antenna using the formulas defined in (A 22) of **Appendix A**

$$Q_{Ant.} = \frac{\omega_0}{2G^{Ap}(\omega_0)} \left| \frac{\partial Y(\omega)}{\partial \omega} \right|_{\omega=\omega_0} = \frac{k_{0r}}{2G^{Ap}(k_{0r})} \left| \frac{\partial Y(k)}{\partial k} \right|_{k=k_{0r}}, \quad (1.59)$$

where ω_0 is the resonant frequency, and equivalently, k_{0r} the resonant wave-number, $Y = Y^C + Y^{Ap}$ is the total admittance of the circuit, sum of the aperture and waveguide admittances, given by

$$Y(k) = G^{Ap}(k) + jB^{Ap}(k) - j \frac{k_{TE}}{k \eta_0} \cot(k_{TE} h). \quad (1.60)$$

Additionally, we are interested in the matched VSWR fractional bandwidth defined in **Appendix A** which is calculated directly from the Q factor as

$$FBW = \frac{2\sqrt{\beta}}{Q}, \quad \beta = \frac{\alpha}{1-\alpha}, \quad \alpha = |\Gamma_0(\omega)|^2 \quad (1.61)$$

where $\Gamma_0(\omega)$ is the reflection coefficient. As in antennas application, the 10dB return loss bandwidth is often the desired goal, by inserting the value $\alpha = 0.1$, one obtains the expression for the bandwidth: .

$$\boxed{FBW_{-10dB} = \frac{2}{3Q_{Ant.}}} \quad (1.62)$$

Using (1.58), (1.59), and (1.61) we can analytically predict the bandwidth of cavity antennas. Predictions for the example aperture sizes of rectangular apertures are shown in Figure 36.

As mentioned, resonance and bandwidth of cavity antennas can be described depending on height (Figure 36(a)) or permittivity (Figure 36(b)), but from now on we will concentrate on the description using height. The calculated fractional bandwidth FBW_{-10dB} , shown on the right vertical axes is used to predict the bandwidth at 2.3GHz that will be useful in the next chapter of the thesis, where a comparison with patch antennas is given.

Most important observation on the bandwidth behavior is the occurrence of bandwidth maximums. This means there are optimum combinations of height-permittivity values for a specific aperture size that will give maximum bandwidth. It is of interest to investigate these ‘‘ideal cavity antennas,’’ i.e to describe how the maximum possible bandwidth depends on the aperture size. To this end, in [53] Cohen has used the mathematical optimization technique of Lagrange multipliers and reported an approximate formula for the minimum Q of cavity antennas when $(a/\lambda_0) < 0.35$, to be

$$Q_{min(Cohen)}^{square} \cong 0.424 \left(\frac{a}{\lambda_0} \right)^{-3}, \quad (1.63)$$

where a is the size of the square aperture, λ_0 the free space wavelength. The cubic dependence bares resemblance to the well known Chu limit formula. For the purpose of comparing (1.63) to the Chu limit we can introduce r as the radius of the smallest sphere that encloses the cavity aperture. The value of r for a square aperture is half the diagonal of the square given by $r = a/\sqrt{2}$. We can write the validity of Q expression $(a/\lambda_0) < 0.35$ in the form $ka < 2.2 \Leftrightarrow kr < 1.55$ and re-express (1.63) as

$$Q_{min(Cohen)}^{square} \cong \frac{105.17}{(ka)^3} = \frac{37.18}{(kr)^3} \quad (1.64)$$

In this form, from (1.64) it is obvious that the prediction for very small cavities is much larger by a factor of about 37 compared to the Chu limit. Note that permittivity nor height do not enter the formula explicitly as it is assumed that for each aperture size the optimum values of h and ε_r are used.

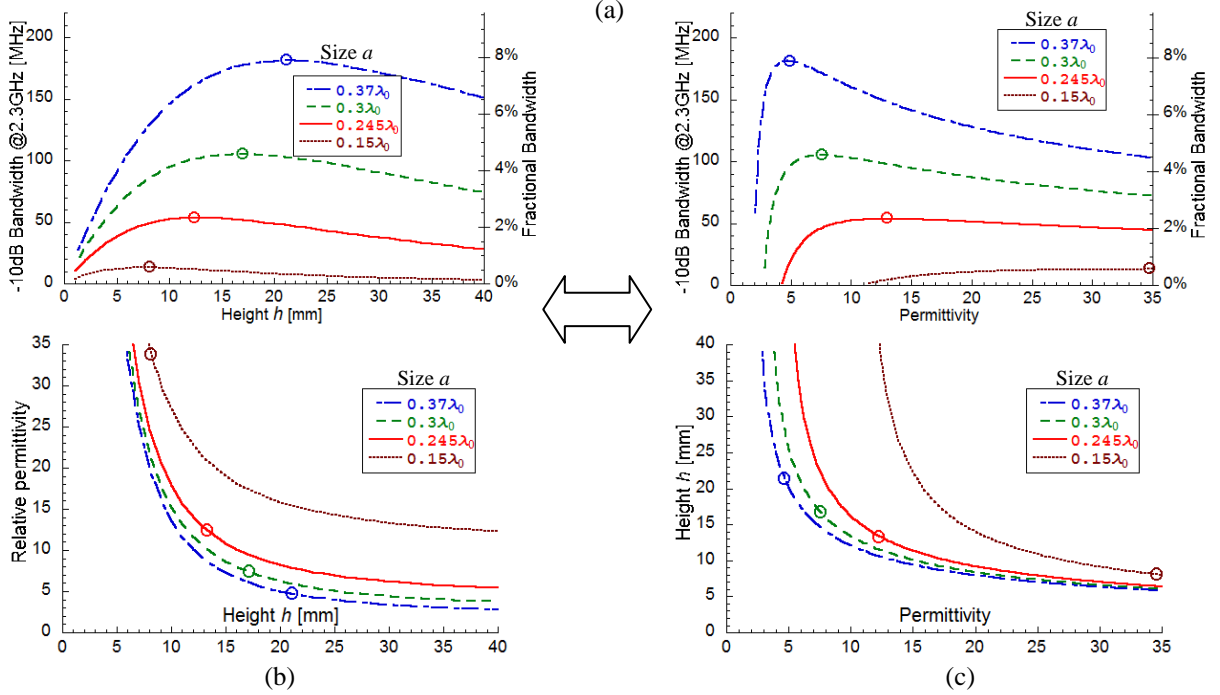
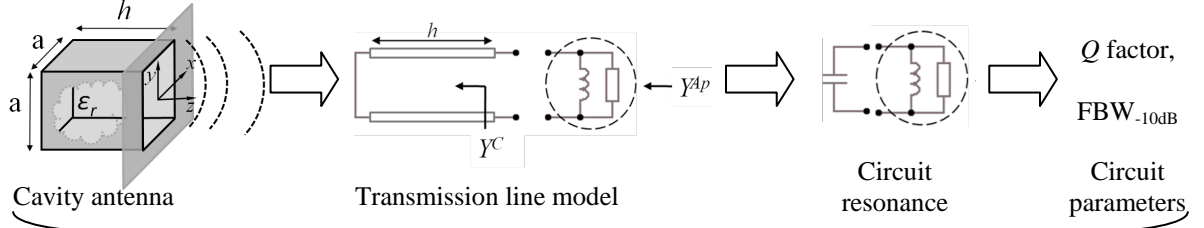


Figure 36 Bandwidth behavior of cavity antennas for the example rectangular aperture sizes. (a) Summary of how the antenna is analyzed. There are two equivalent descriptions: (a) Bandwidth vs. height of the cavity, with a corresponding permittivity for each height values. (b) Bandwidth vs. permittivity inside the cavity volume, with the necessary height for each permittivity value. Circles on the curves indicate the maximum achievable bandwidth for a given size and are related to equation (1.64). This presentation is new compared to the work of Cohen [53] where only Q vs. permittivity was considered.

It must be noted that in 1950., when Cohen derived (1.63) he used an approximate formula to compute the Q factor, compared to the modern formulation (1.59) that we use in this thesis, and expect to be more exact. Because of this we will briefly reproduce the procedure to obtain the result for the minimum Q here. We wish to minimize the Q factor given in (1.59) with respect to the resonance condition for the antenna (1.58) introduced as a constraint. In the Lagrange multiplier technique, for this we introduce the Lagrange multiplier χ and construct a new, Lagrange function Λ as

$$\Lambda = Q_{Ant} - \chi \left(B^{Ap}(k) - \frac{k_{TE}}{k \eta_0} \cot(k_{TE} h) \right). \quad (1.65)$$

We search for stationary points, where partial derivatives of the Lagrange function with respect to permittivity ϵ_r , cavity height h , and the Lagrange multiplier χ are all zero, i.e. $\vec{\nabla}_{\epsilon_r, h, \chi} \Lambda = 0$ or written more explicitly

$$\begin{aligned} \frac{\partial \Lambda}{\partial h} &= \frac{k_{0r}}{2G^{Ap}(k_{0r})} \frac{\partial}{\partial h} \left| \frac{\partial Y(k_{0r})}{\partial \omega} \right| - \chi \frac{k_{TE}^2}{k \eta_0} \csc^2(k_{TE} h) = 0 \\ \frac{\partial \Lambda}{\partial \epsilon_r} &= \frac{k_{0r}}{2G^{Ap}(k_{0r})} \frac{\partial}{\partial \epsilon_r} \left| \frac{\partial Y(k_{0r})}{\partial \omega} \right| + \chi \frac{k}{2\eta_0} \left(\frac{\cot(k_{TE} h)}{k_{TE}} - \frac{h \csc^2(k_{TE} h)}{2} \right) = 0 \\ \frac{\partial \Lambda}{\partial \chi} &= B^{Ap}(k_{0r}) - \frac{k_{TE}}{k \eta_0} \cot(k_{TE} h) = 0. \end{aligned} \quad (1.66)$$

The resulting system of three equations with three variables are, in fact, very cumbersome, but can be solved numerically. One has to solve the system numerically solved to obtain the minimum Q factor (or maximum fractional bandwidth) for each aperture size one is interested in, and then curve fitting to a cubic function can be

done to obtain of coefficient seen in (1.76). The numerical result obtained by the author differs slightly from of the result of Cohen and reads

$$Q_{min}^{square} = 0.422 \left(\frac{a}{\lambda_0} \right)^{-3} = \frac{104.7}{(ka)^3} = \frac{37}{(kr)^3}, \quad (1.67)$$

where the small difference ($< 0.5\%$) compared to (1.76) can be attributed to the use of different formulas for Q , as mentioned. The numerical result along with the fitted curve is plotted in Figure 37. The values on this curve correspond to the maximums presented in Figure 36 with small circles.

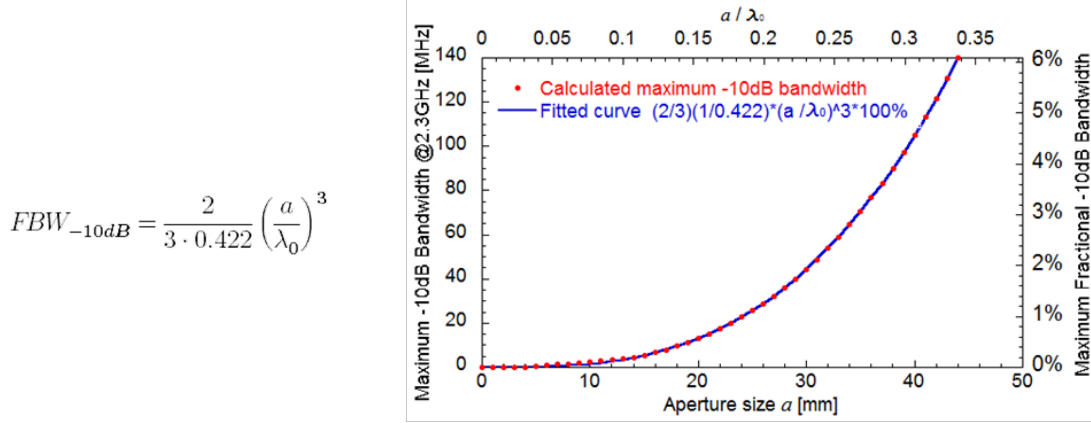


Figure 37 Numerically computed maximum -10dB fractional bandwidth for each cavity aperture size in the range $0 < (a/\lambda_0) < 0.35$ shown by red dots. The blue line shows the fitted curve which is a simple cubic function.

B. CIRCULAR CAVITY

Here we will extend the presented analysis for rectangular cavities to a circular cavity with circular aperture or radius a , shown in Figure 39(a). Again, for simplicity we assume only the dominant mode. For a circular waveguide this is the TE_{11} mode. The propagation constant in a circular waveguide is $k_{TE}^2 = \varepsilon_r k^2 - k_c^2$ where $k^2 = \omega^2 \mu_0 \varepsilon_0$ is the wave-number, and $k_c = p'_{11}/a$ is the cutoff wave-number for the TE_{11} mode, with $p'_{11} = 1.8418\dots$. The characteristic admittance for TE modes is $Y_{TE} = k_{TE}/\omega\mu = k_{TE}/k\eta_0$. Therefore, analogously to (1.55) for the rectangular case, the input admittance into a short circuited waveguide is

$$Y^C(k) = -j \frac{k_{TE}}{k\eta_0} \cot(k_{TE} h), \quad (1.68)$$

or written explicitly for the TE_{11} circular

$$Y^C(k) = -j \frac{\sqrt{\varepsilon_r k^2 - (p'_{11}/a)^2}}{k\eta_0} \cot\left(\sqrt{\varepsilon_r k^2 - (p'_{11}/a)^2} h\right), \quad (1.69)$$

The open end of the structure is modeled by the aperture admittance $Y^{Ap} = G^{Ap} + jB^{Ap}$ for the TE_{11} mode. The complete calculation is shown in **Appendix D**. We write here only the final expression for the TE_{11} mode

$$Y^{Ap}(k) = \frac{2}{((p'_{nm})^2 - 1)\eta_0} \int_0^\infty \left[\frac{k}{k_\rho^2 \sqrt{k^2 - k_\rho^2}} J_1^2(k_\rho a) + \frac{a^2 k_c^4 \sqrt{k^2 - k_\rho^2}}{k(k_c^2 - k_\rho^2)^2} J_1'^2(k_\rho a) \right] k_\rho dk_\rho \quad (1.70)$$

The integral in (1.70) has to be computed numerically for each value of k . Upon the calculation, aperture admittance is approximated by a polynomial to ease further calculations. For presentation purposes it is more convenient to give the result in terms of the diameter to free-space wavelength ratio, or d/λ_0 , where $d = 2a$. The polynomial and the plotted admittance are shown in Figure 38.

The resonance condition is analogous to the rectangular case, given by $jB^{Ap}(k) - jk_{TE}/k\eta_0 \cot(k_{TE} h) = 0$. Using (1.69) for the input admittance into the waveguide, (1.70) for the aperture, and (1.59) - (1.61) from the previous section to compute the Q factor and fractional bandwidth, we can analytically predict the bandwidth of circular cavity antennas. Predictions for the example aperture sizes are shown in Figure 39.

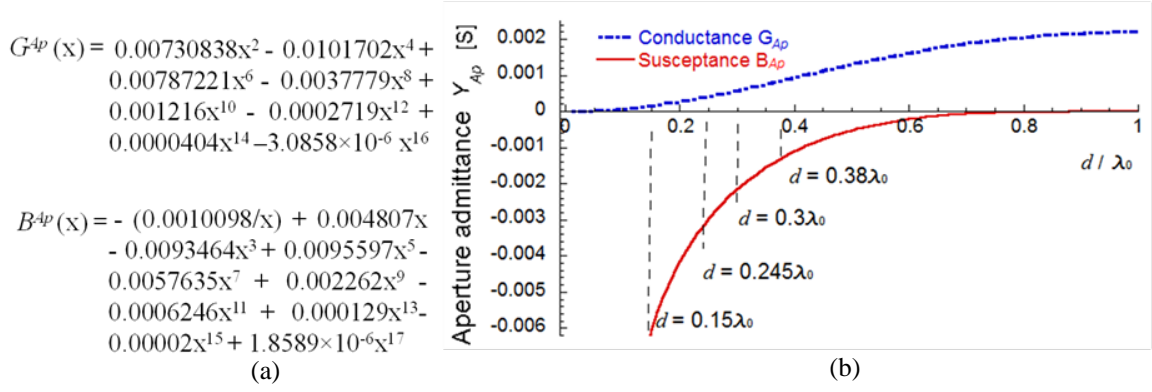


Figure 38 Aperture admittance Y^{Ap} for the TE_{11} circular waveguide mode given by (1.76). See Appendix D for the derivation. (a) Polynomial approximation of given in terms of $x = d/\lambda_0 = kd/(2\pi)$, where $d = 2a$. (b) Plotted real and imaginary part of Y^{Ap} as a function of the cavity diameter. Note that for the example aperture sizes the susceptance is inductive.

Repeating the Lagrange multiplier technique, we solve the system (1.66) for the circular cavity numerically to obtain the minimum Q factor (maximum fractional bandwidth). The result was found to be

$$Q_{min}^{circular} = 0.637 \left(\frac{d}{\lambda_0} \right)^{-3} = \frac{158}{(kd)^3} = \frac{19.75}{(ka)^3} \quad (1.71)$$

Where we also used the radius a along with the diameter d to make the expression directly comparable to the Chu limit. Maximum fractional bandwidth is plotted in Figure 40.

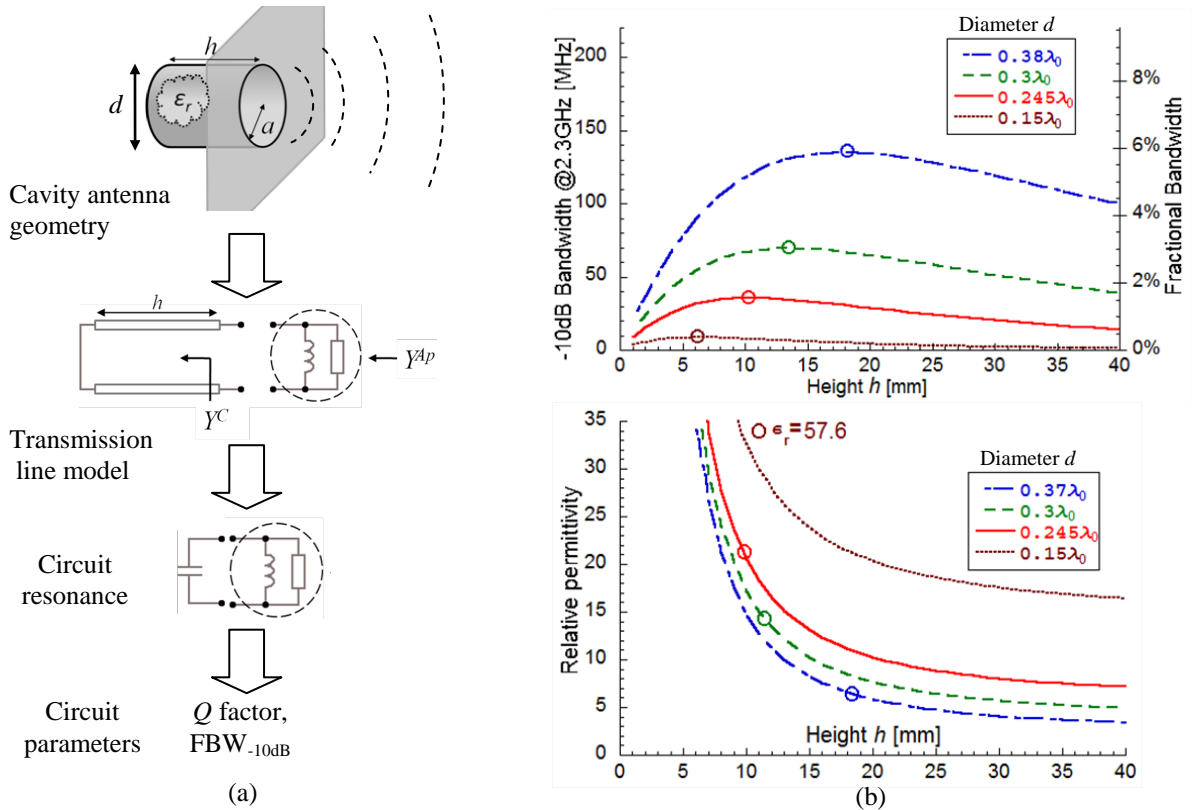


Figure 39 (a) Summary of how the antenna is analyzed (b) Bandwidth behavior of circular cavity antennas for the example rectangular aperture sizes. Circles on the curves indicate the maximum achievable bandwidth for a given size and are related to equation (1.71). This result is an expansion compared to the work of Cohen [53] where only square cavities were considered.

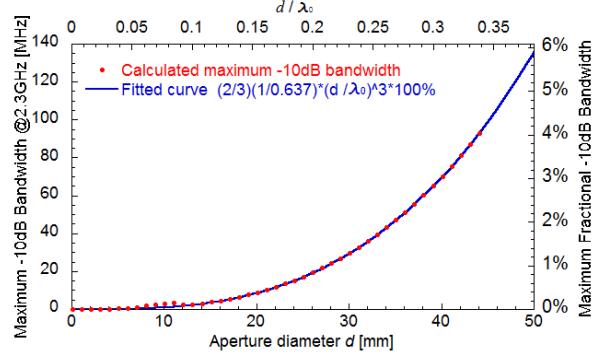


Figure 40 Numerically computed maximum -10dB fractional bandwidth for each cavity aperture size in the range $0 < (a/\lambda_0) < 0.35$ shown by red dots. The blue line shows the fitted curve which is a simple cubic function given in (1.71).

C. EXTENSION TO CAVITIES IN A FINITE GROUND PLANE

In the case of a cavity in a very small ground plane, or better said, capsule, aperture admittance changes due to different geometry of the space surrounding the aperture, while the cavity part remains the same. Analytical techniques for obtaining the aperture admittance are too difficult. It is easier to use commercially available electromagnetic software to obtain the admittance through simulation. Here we show an example using CST Microwave studio [130].

Following simulation procedure was used:

- Create a metallic object in free space that will play the role of the ground plane. Rectangular box of height $h = 15$ mm for the case of a rectangular aperture and a cylinder of height $h = 15$ mm for the case of a circular aperture.
- Create the aperture by inserting smaller object made of vacuum into the metallic object. Rectangular box of height $h = 1$ mm, $a = 20$ mm for the case of a rectangular aperture and a cylinder of height $h = 1$ mm, $d = 20$ mm for the case of a circular aperture. The result is seen in Figure 41(a) and (c).
- Place a waveguide port at the bottom of the object made of vacuum, See Figure 41(a) and (c).
- Set frequency range, run simulation to obtain S_{11} parameter and post processing to get admittance Y .

The waveguide port is slightly recessed inside the metallic object playing the role of ground plane because CST needs several mesh cells in front of the port to establish the mode. The S_{11} parameter can be de-embedded for this 1 mm distance in post processing but the result is almost identical. To ensure strictly the wanted TE mode, the number of waveguide modes has to be set to 1 and the polarization angle option checked in port properties. Additionally, symmetry planes can be used to reduce the simulation domain. Both time domain and frequency domain solvers can be used to get the S_{11} parameter, but the frequency solver is much faster for this kind of problem and offers good accuracy.

Simulation results are shown in Figure 41(b) and (d) for the two cavity cases. The biggest difference compared to apertures in an infinite ground plane is in the real part of the admittance (conductance G^{Ap}). Finite ground plane cavity antennas radiate into the entire free space, opposed to just the half space for the infinite ground plane case. This translates to larger conductance values (radiation loss) and ultimately to larger bandwidth for the finite ground plane antennas. Interestingly, there is also a small lump in the G^{Ap} curves, only slightly visible Figure 41(b) and (d). This lump depends on the overall size of the ground plane compared to the free space wavelength. It is a consequence of the ground plane acting as an antenna itself, excited by aperture.

Based on the simulation data, polynomial approximations of the curves were done in a similar fashion to the previous, infinite ground plane cases. It is important to know that these results are very approximate because for each aperture size the relative size of the ground plane walls, and the whole ground plane are different compared to the wavelength. In fact, a separate simulation should be done for each aperture size to get more accurate results. However we show only one simulation result which is taken to “accurate enough”. The polynomials were found to be; for the square aperture

$$\begin{aligned}
 G_{square}^{Ap}(x) &= 0.0091746x - 0.346865x^2 + 5.40888x^3 - 43.1677x^4 + 207.013x^5 - 635.399x^6 \\
 &\quad + 1277.45x^7 - 1669.5x^8 + 1344.53x^9 - 552.55x^{10} + 92.186x^{12} - 25.6282x^{13} \\
 B_{square}^{Ap}(x) &= -\left(\frac{0.00074516}{x}\right) + 0.00512814x - 0.0691961x^2 + 2.11758x^3 - 24.2464x^4 \\
 &\quad + 147.447x^5 - 546.146x^6 + 1301.39x^7 - 2025.2x^8 + 2021.33x^9 \\
 &\quad - 1208.08x^{10} + 348.878x^{11} - 17.4309x^{13},
 \end{aligned} \tag{1.72}$$

where $x = a/\lambda_0 = ka/(2\pi)$, a being the aperture size.

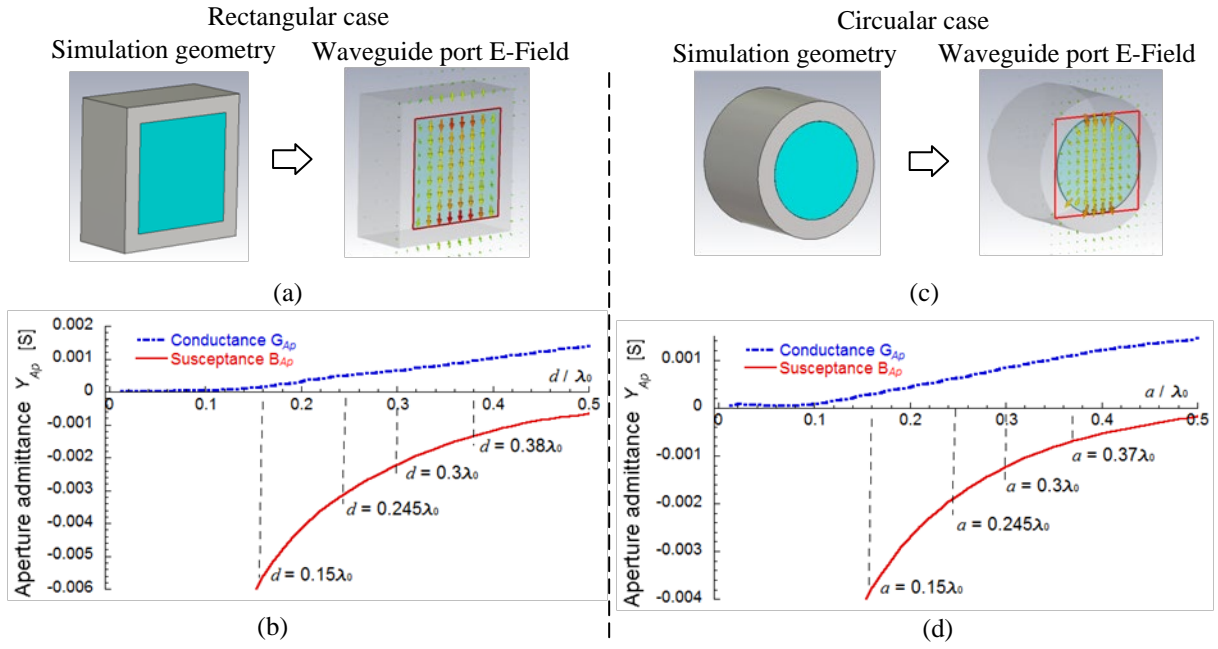


Figure 41 Finite ground plane aperture admittance simulations. (a) Rectangular cavity ($a = 0.15 \lambda_0, h = 15 \text{ mm}$) with 5mm metallic walls in all directions, and the electric field excited by the waveguide port at the aperture. (b) Aperture admittance result obtained by simulation (calculated from the S_{11} parameter in CST). (c) Circular cavity ($d = 0.15 \lambda_0, h = 15 \text{ mm}$) with 5mm metallic walls in all directions, and the electric field excited by the waveguide port at the aperture. (d) Aperture admittance result obtained by simulation (calculated from the S_{11} parameter in CST).

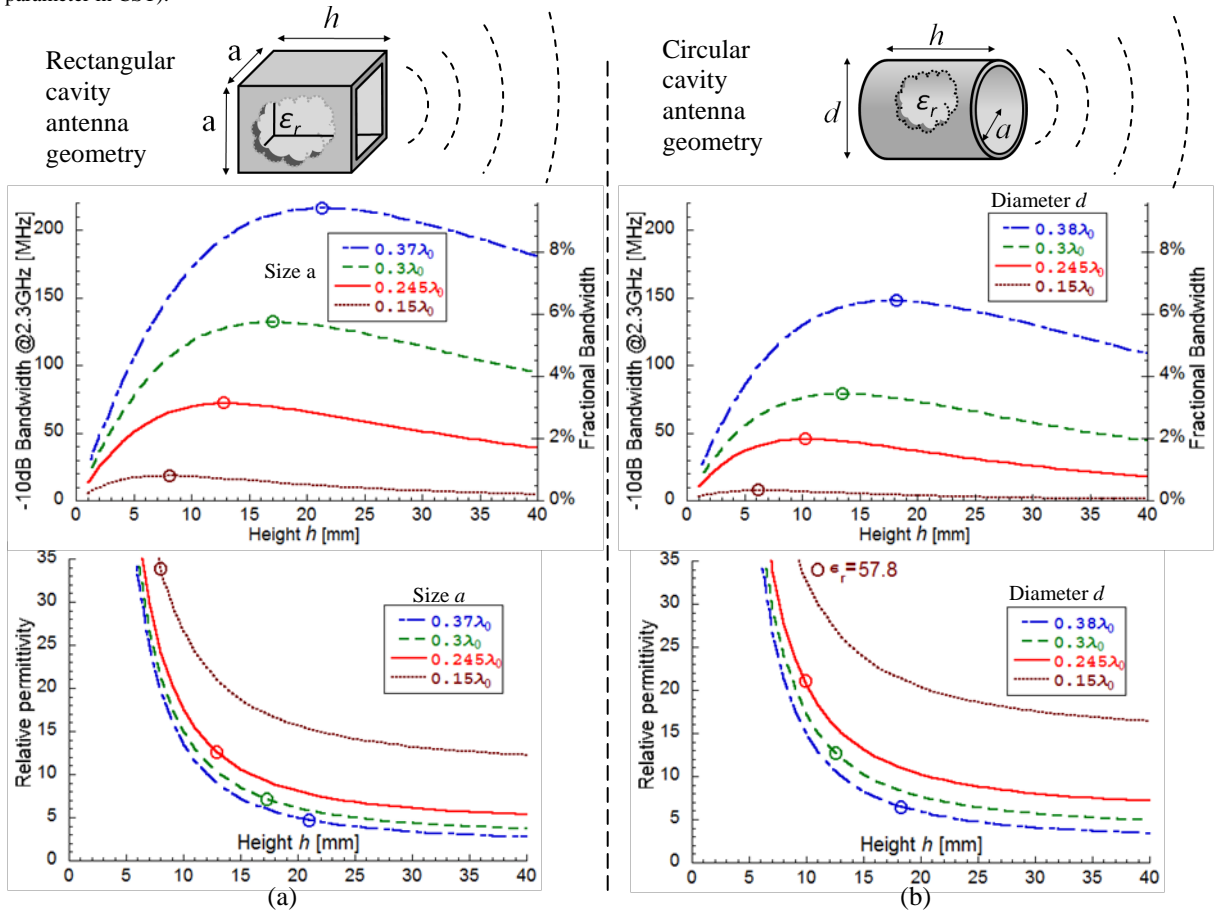


Figure 42 Bandwidth behavior of cavity antennas in a finite ground plane for the example rectangular aperture sizes. Circles on the curves indicate the maximum achievable bandwidth for a given size and are related to equation (1.74). (a) Rectangular cavity case. (b) Circular cavity case. This result is an expansion compared to the work of Cohen [53] where only infinite ground plane was considered.

For the circular aperture we have

$$\begin{aligned}
 G_{circular}^{Ap}(x) &= 0.00655844x - 0.419178x^2 + 12.3159x^3 - 194.759x^4 + 1829x^5 - 10745.4x^6 \\
 &\quad + 40611.4x^7 - 98607.5x^8 + 146502x^9 - 110625x^{10} + 61969.6x^{12} - 31530.7x^{13} \\
 B_{circular}^{Ap}(x) &= -\left(\frac{0.00102734}{x}\right) + 0.00554205x - 0.117314x^2 + 4.84682x^3 - 100.97x^4 \\
 &\quad + 1210.99x^5 - 8880.88x^6 + 41334.4x^7 - 123924x^8 + 235838x^9 \\
 &\quad - 266867x^{10} + 145247x^{11} - 25583.8x^{13},
 \end{aligned} \tag{1.73}$$

where $x = d/\lambda_0 = kd/(2\pi)$, $d = 2a$ being the aperture diameter. Using these polynomials and following the same equations as for the infinite ground plane cases, bandwidth behavior was computed and is shown in Figure 42. Compared to the results shown in Figure 36 and Figure 39 for the rectangular and circular antennas respectively, we observe higher overall bandwidth performance with the finite ground plane

Repeating the Lagrange multiplier technique, we solve the system (1.66) for the two cases numerically, taking into account the new aperture admittances (1.72) and (1.73). We obtain the minimum Q factor (maximum fractional bandwidth) for the rectangular and circular case as

$$Q_{min}^{square} \approx 0.334 \left(\frac{a}{\lambda_0}\right)^{-3} = \frac{82.85}{(ka)^3} = \frac{29.3}{(kr)^3}, \quad Q_{min}^{circular} \approx 0.564 \left(\frac{d}{\lambda_0}\right)^{-3} = \frac{139.9}{(kd)^3} = \frac{17.5}{(ka)^3}. \tag{1.74}$$

Comparing (1.74) with (1.67) and (1.71) we see the minimum Q factor is indeed slightly smaller. Maximum fractional bandwidth is shown in Figure 43 where the approximate nature of our calculation is clearly visible. The fit between the numerically computed points and the simple cubic dependence is far from perfect. As mentioned, this is a consequence of the shape of the ground plane and its size relating to the free space wavelength.

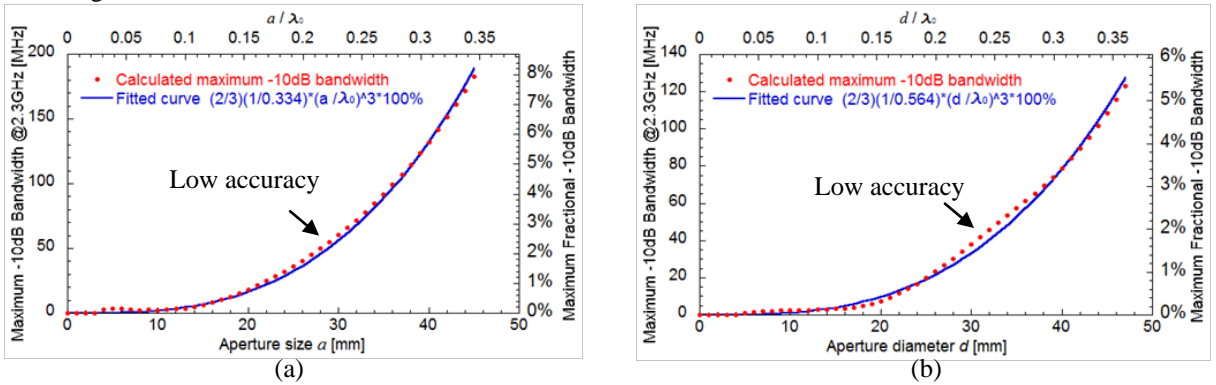


Figure 43 Numerically computed maximum -10dB fractional bandwidth for each cavity aperture size in the range $0 < (a/\lambda_0) < 0.35$, shown by red dots. The blue line shows the fitted curve which is a simple cubic function related to (1.74). Black arrow points to an area of biggest disagreement between the computed points and the fitted curve. (a) Rectangular aperture in a finite ground plane. (b) Circular aperture in a finite ground plane.

D. EXCITATION OF CAVITY ANTENNAS

In his Ph.D. thesis, Cohen made experiments with a short dipole at the aperture of a cavity to confirm his results from the transmission line model. He has found relatively good agreement between theory and experiment. A thin, short dipole (much shorter than half wavelength in a small cavity) at the aperture is capable of exciting the fundamental mode. The antenna Q is due to the cavity and not to the dipole exciting it. However, the presence of the dipole also slightly changes the fields at the aperture as there is a capacitive effect between the dipole and the cavity wall. This introduces small discrepancies between the model, which is ideal, and the realistic antenna which has some form of excitation posing as an additional object inside the cavity.

Several other forms of exciting cavity antennas have already been presented on Figure 32. An excitation of special interest however, is the patch antenna inside a cavity. A review of research on patch antennas in cavities is given below, but a detailed, systematic study of this form of excitation is explored in Chapter 2.

1.3.2. Microstrip antennas in cavities with examples

Cavity-enclosed patch antennas have been investigated in the past to alleviate in some degree the drawbacks of classical patch antennas. For example, bandwidth of a patch antenna can be substantially increased through the use of a thick substrate, seen in Chapter 1.2.3.C. However, the grounded dielectric substrate supports surface wave modes, which lower the antenna efficiency. Thus the maximum substrate thickness (and hence bandwidth)

is limited by the radiation efficiency required. One way to circumvent this limitation is to surround the patch elements with metal walls. This effectively prevents surface wave modes from being excited in the substrate, thus allowing the substrate thickness to be increased without deleterious effects. Cavity enclosure, in addition, gives the antenna a compact, miniature configuration and rigid shape, isolates the antenna from surroundings, and reduces backward radiation. It is also worth noting that in microstrip-patch arrays guided-wave effects result in a scan-bandwidth performance tradeoff. Cavity backing eliminates the scan-bandwidth tradeoff. Furthermore, as the substrate thickness is increased, the scan performance actually improves. These characteristics of the cavity backed patch antennas, as reported in literature, were summarized by Karmakar in [58] and read as follows:

- Shielding is used to suppress back lobes in finite ground plane patch antenna and aperture coupled microstrip patch antenna [59]-[60].
- Cavities can suppress surface waves and mutual coupling in thick substrates and act as heat sinks in a highpowered large transmit array [61].
- Including stacked patch antenna configuration in a cavity further increases the bandwidth of patch antennas [62], [69].
- Inclusion of high-permittivity superstrates on the cavity backed patch antenna improves the antenna gain significantly. Zavosh and Aberle [64]-[65] have reported single element gain of 22dB with superstrates of dielectric constant in the range of 100.
- In a phased array antenna, cavities can prevent scan blindness, yield less coupling and improve good matching over wider scan angles [63],[66]-[68].
- Standard microstrip patch antennas exhibit zero field strength near the horizon. A patch antenna in a cavity enclosure can improve the radiation near and beyond the horizon; thus, a truly unidirectional radiation pattern can be achieved [70]. This pattern is very useful for satellite communications.
- Gain and radiation patterns can be changed significantly by placing the patch antenna into a cavity enclosure and changing the shape of the enclosure. Noghianian and Shafai [71] have reported 3-dB gain improvement and significantly reduced back lobe by introducing a chock on the circular cavity.
- Volakis *et al.* [72] showed that patch with metallic cavity beneath it, filled with dielectric material reduces the antenna dimensions. Up to 30% reduction in antenna diameter is achieved.
- Waterhouse [73] has reported an electrically small resistive loaded cavity backed circular patch antenna for integration with hand phones. More compact design is achieved due to the cavity housing.
- Spectral noise of an active patch antenna can be suppressed by as much as 25 dB using a rectangular cavity [74].
- Nurnberger *et al.* [75] have reported an extremely broad-band planar slot spiral antenna in a cavity.

Despite the mentioned benefits, fabrication of cavity backed patch antennas is not common due to increased fabrication cost for the metallic cavity and complicated structural assemblage. To address this problem, recently, substrate integrated (SIW) technology was utilized as an alternative low cost approach in fabricating cavity backed antennas and arrays [76]-[77]. The investigated cavities sizes presented in SIW technology are close to $0.5 \lambda_0$.

Cavity enclosed antennas present complex boundary conditions, which make the analytical approach a difficult task. Different numerical techniques are available in the literature to analyze the cavity enclosed patch antenna structures. Although these techniques can predict considerably well the characteristics of the structures in both single layer and multilayer substrates, they are conceptually involved and computationally intensive. Analytical and experimental investigations of a circular patch in a cylindrical cavity have been presented in [58] and [78]-[79] giving only some empirical formulas.

Example 1: Patch antennas backed by a cavities of various sizes were investigated in [57] and [58] by Karmakar, where experimental results on bandwidth behavior with height were reported. Figure 44 shows the design investigated, and the corresponding bandwidth dependence on height for example cavity.

Karmakar reports that due to the proximity of the cavity enclosure, the patch diameter affects not only the resonant frequency, but also the operational bandwidth of the antenna. This is due to the edge diffraction of the cavity wall. Investigation reveals that the gap between the patch and cavity determines the coupling between the radiated field and the enclosure. If the spacing is too small, an over coupling occurs. The fringe fields around the patch edge for radiation are distorted by the proximity of the cavity wall and the bandwidth decreases. Also, the resonant frequency and the bandwidth of the antenna decrease with the cup wall height. This may be due to the prominence of the mode excited by the cavity enclosure over that of the patch resonance and fringe field distortion, respectively.

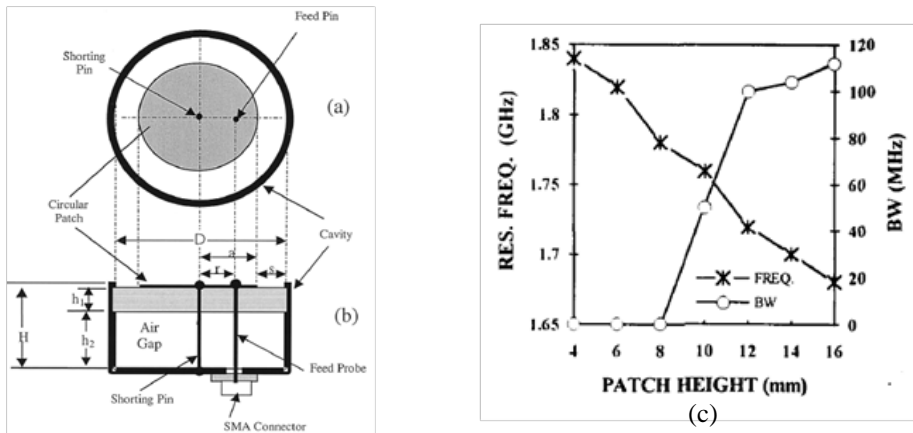


Figure 44 A circular cavity enclosed circular microstrip patch antenna (a) Top view. (b) Side view. (c) Bandwidth and resonance frequency vs. height for aperture diameter $D = 115$ mm and patch diameter of 90mm. The cavity volume is filled mostly with air.

Example 2: Volakis *et al.* [72] placed perturbances below the rectangular patch and observed as much as 30% decrease from the resonant frequency compared with the unperturbed patch. The specific configurations considered include a cavity-backed and an aperture-backed patch as shown in Figure 45. The shift in the resonant frequency can be understood by resorting to a transmission line model of the patch antenna. In this case, the inserted aperture below the patch can be represented by an equivalent reactance placed between the admittances representing the patch terminations. The bandwidth of these cavity-backed and aperture-backed configurations was not altered although some minor differences were observed in the actual values of the input impedance.

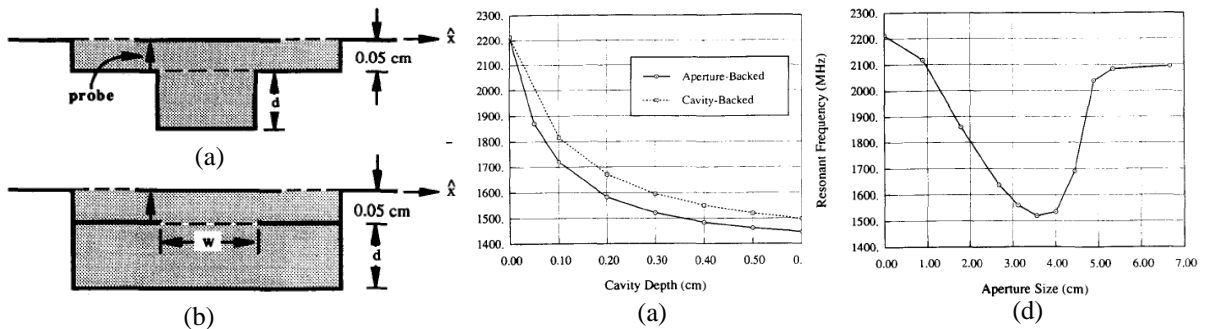


Figure 45 Modified cavity configurations: (a) cavity-backed, (b) aperture backed. (c) Resonant frequency of the aperture- and cavity-backed patch configurations as a function of the bottom cavity depth d . Original cavity depth is retained at 0.05 cm and the entire cavity region is filled with a dielectric having $(\epsilon_r = 2.17)$. Aperture of the second cavity is 3.56 cm x 3.56 cm. (d) Resonant frequency of the aperture-backed patch as a function of the square aperture dimension W . Depth of the bottom cavity was kept at $d = 0.3$ cm and all other parameters are the same with those used for (c)

Example 3: Recessing of the patch into the antenna cavity and the placing of a dielectric layer above the patch (superstrate), reduces the resonant frequency [69]. This shift is primarily a function of the superstrate material and height. Illustration of the effect of superstrate height on the resonant frequency is shown in Figure 46. Although substantial reduction in the operating frequency is achieved, there is a corresponding decrease in impedance bandwidth. Therefore, a compromise between resonance shift and impedance bandwidth must be made for the recessed structure.

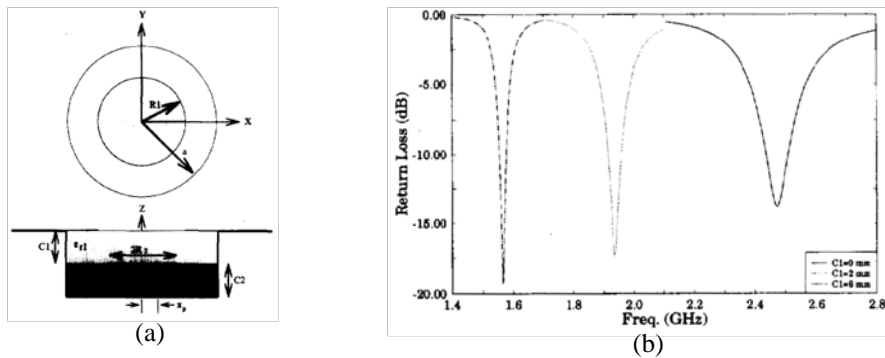


Figure 46 (a) Recessed (single configuration) cavity-backed patch antenna and (b) the return loss versus frequency for varying superstrate height. Picture taken from [69].

Example 4: A common approach for improving the bandwidth performance of a patch antenna, as mentioned before, is to add parasitic elements to the antenna structure. This reduces the impedance variation of the antenna with frequency which enhances bandwidth performance. In [62] and [69] a stacked configuration of circular patches is investigated, see Figure 47. The cavity-backed patch antenna in a stacked configuration has two important features for enhancing bandwidth performance. First, the addition of a parasitic patch reduces the frequency variation of the input impedance resulting in an improved bandwidth. Second, the cavity backing allows the substrate thickness to be increased without loss of radiation efficiency resulting in further bandwidth improvement.

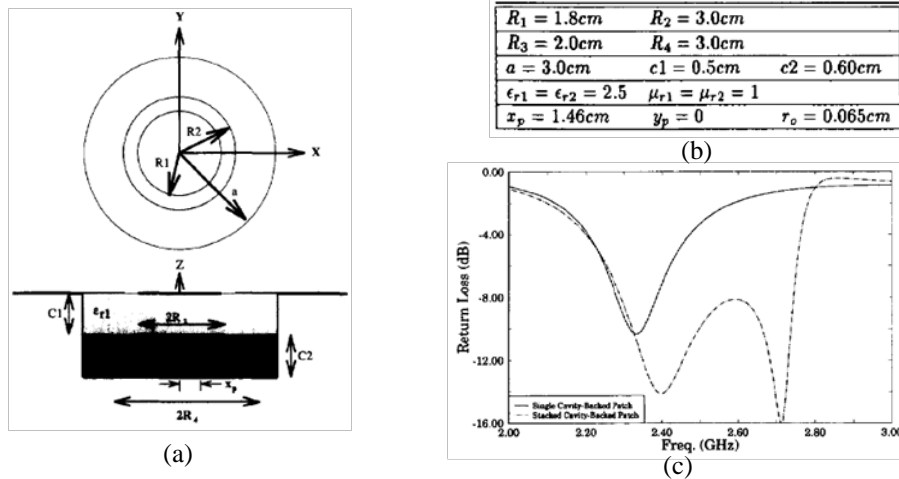


Figure 47 (a) Stacked cavity-backed patch antenna. (b) parameters for the probe-fed cavity-backed circular patch antenna in a stacked configurations. (c) Return loss of a probe-fed cavity-backed circular patch in single and stacked configurations versus frequency

In conclusion, cavities were shown to have numerous benefits for microstrip patch antennas in the literature. However in all cases the investigated cavity aperture sizes were about $0.5 \lambda_0$ or larger. Many of the studies were done experimentally in the time when the computing power of computers was low and commercial software for electromagnetic simulations was not yet available. Therefore, systematic studies of antenna parameters were limited. A thorough study of the antenna parameter dependencies is given in Chapter 3.

1.4. Introduction to metamaterials and applications to antennas

The word “meta” implies “beyond” and artificial, man-made, materials engineered to have properties that may not be found in nature. Because we do not encounter them in nature, their properties are often described as counterintuitive. For an attempt at an easier explanation of the source and cause of metamaterial properties, the author included his own short explanation in Appendix E. Here we proceed to specifically describe electromagnetic metamaterials and classify their types and applications to antennas.

1.4.1. General Concepts of metamaterials (MTMs)

The terminology “electromagnetic meta-materials” today implies artificial, man-made, effectively homogeneous electromagnetic structures in which the electromagnetic properties, as represented by the permittivity and permeability, can be controlled and they exhibit superior properties not found in nature. An effectively homogeneous structure is a structure whose structural average cell size p is much smaller than the guided wavelength λ_g . Therefore, this average cell size should be at least smaller than a quarter of wavelength, ($p < \lambda_g/4$) to ensure that refractive phenomena will dominate over scattering/diffraction phenomena when a wave propagates inside the MTM medium. A common “rule of thumb” or metamaterial criteria, is that the cell size should be smaller than one tenth of the wavelength, ($p < \lambda_g/10$). If this condition of effective-homogeneity is satisfied, the structure behaves as a real material in the sense that electromagnetic waves are essentially myopic to the lattice and only probe the average, or effective, macroscopic and well-defined constitutive parameters, which depend on the nature of the unit cell; the structure is thus electromagnetically uniform along the direction of propagation. [80]

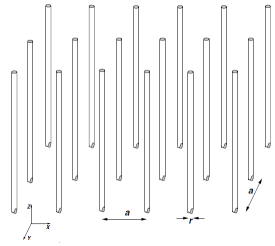
Although many of the ideas of metamaterials have their origin in the theories of homogenization of composites, metamaterials also differ from those in that they are crucially dependent on resonances for their properties. Typically, the resonances in metamaterials can induce large amounts of dispersion (large changes with frequency) in the effective medium parameters at frequencies close to resonance. By properly driving and enhancing these resonances, one can cause the materials parameters ϵ or μ to become negative in a frequency band slightly above the resonance frequency [81].

It is important to stress that all known passive metamaterials (transmission-line based [80], wire based [82], split ring resonator based [83][84], complementary-split ring resonator based [85], “fishnet”-based etc. [86]) behave very similarly. Thus, all known passive metamaterials (within some frequency range) show resonant behavior, inevitably, also exhibit dispersion.

It should be noted that, although the term MTM has been used most often in reference to LH structures in the literature, MTMs may encompass a much broader range of structures. Examples are MTMs with only one of the two constitutive parameters negative, anisotropic MTMs, or any type of functional effective engineered structure. In addition, many existing materials obtained by novel nanotechnology and chemistry processes may be regarded as MTMs.

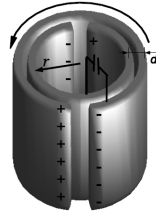
Negative permittivity: Plasmas are described by a permittivity function that becomes negative below a plasma frequency ω_p . Essentially, metals are plasmas, since they consist of an ionized “gas” of free electrons. Below their plasma frequency, the real component of the permittivity of bulk metals can be said to be negative. A structure consisting of a mesh of very thin conducting wires arranged in a periodic lattice, as in Figure 48 is also a “gas” of free electrons. Due to the spatial confinement of the electrons to thin wires, the effective electron concentration in the volume of the structure is decreased, which also decreases the plasma frequency. More significant, however, is that the self-inductance of the wire array manifests itself as a greatly enhanced effective mass of the electrons confined to the wires. This enhancement reduces the effective plasma frequency of the structure by many orders of magnitude, placing it well into the gigahertz range. Thus, an array of thin metallic wires, by virtue of its macroscopic plasma-like behavior, produces an effectively negative permittivity at microwave frequencies.

Negative permeability: In 1999, Pendry *et al.* [87] claimed to have developed micro-structured artificial materials exhibiting strange magnetic properties. The resulting split-ring resonator (SRR), depicted in Figure 49, exhibits strong electric fields, supported by a very large capacitance, between the rings. Furthermore, although currents cannot traverse the gaps, the application of magnetic fields oriented normal to the plane of the rings induces simultaneous currents in both rings. This synthesized capacitance, along with the natural inductance of the cylindrical structure, results in a resonant response characterized by an effective relative permeability that can be negative in a finite bandwidth above resonance.



$$\epsilon = 1 - \frac{\omega_p^2}{\omega \left(\omega + i \frac{\epsilon_0 a^2 \omega_p^2}{\pi r^2 \sigma} \right)}$$

Figure 48 An array of infinitely long, thin metal wires of radius r on a lattice of period of a behaves as a low frequency plasma for an electric field oriented along the wires. Taken from [81].



$$\mu_{\text{eff}} = 1 + \frac{f\omega^2}{\frac{2c^2 d}{\epsilon\pi^2 r^3} - \omega^2 - i\frac{2\rho\omega}{r\mu_0}}$$

Figure 49 Pictorial view of the cylindrical unit for the SRR proposed in Pendry *et al.* (1999). The inner conducting ring acts as a capacitive load on the outer ring. The charge buildup across the ends of the split rings, the direction of the currents, and the mutual capacitance are schematically depicted. Taken from [87].

The first left handed metamaterial (LHM) The long-anticipated demonstration of a double negative medium (DNG), predicted by Veselago in [88] was finally reported in *Science* in 2001 by R. A. Shelby, D. R. Smith, and S. Schultz [89] who had experimentally verified negative refraction using a composite wire/SRR negative-refractive-index medium.



Figure 50 Depiction of the wire-SRR metamaterial of Shelby *et al.* used to verify negative refraction. The sample was irradiated by a microwave beam at 10.5 GHz incident at 18.43° , and a microwave detector was scanned azimuthally around the exit point in the plane of incidence. A control sample made of Teflon reported a positive angle of refraction of 27° , corresponding to the well-known refractive index of Teflon of + 1.4, and calibrating the apparatus. Using the wire/SRR metamaterial, the same beam was observed to exit at an angle of -61° , which, applied to Snell's Law, yields an effectively negative index of refraction of -2.7.

1.4.2. Use of metamaterials in antenna size reduction and bandwidth

What kind of benefits can the metamaterial concepts bring to small antennas? Metamaterials are proposed to provide antennas with a means to manipulate the dispersion relation or the near-field boundary conditions, which could result in antenna size miniaturization while maintaining a good radiation performance. Metamaterial antennas open a way to overcome the restrictive efficiency-bandwidth limitation for small antennas. Yet this approach is still far from being mature.

Surveying the literature, one observes that various engineered materials have been investigated and numerous antenna applications have been proposed. For example, Figure 51 illustrates some representative engineered electromagnetic materials with unique electromagnetic properties [91]. **Frequency selective surfaces (FSS)** are widely used in random and reflector antenna designs as wave filters. **Double negative (DNG)** material refers to those materials with effective negative permittivity and permeability, which results in properties such as left-handed (LH) wave propagation and negative index of refraction (NIR). Periodic structures that prohibit the propagation of electromagnetic waves in a certain frequency band for certain arrival angles and polarization senses are classified as **electromagnetic band gap (EBG)** structures. Another important category consists of ground planes that exhibit unique reflection characteristics other than conventional PEC, known as complex artificial ground planes. This chapter summarizes several typical engineered electromagnetic materials and illustrates their applications in patch antenna engineering. It is demonstrated that they not only improve the performance of conventional antennas such as gain, bandwidth, and efficiency, but also lead to novel radiator concepts and structures like surface wave antennas and reconfigurable antennas. [31]

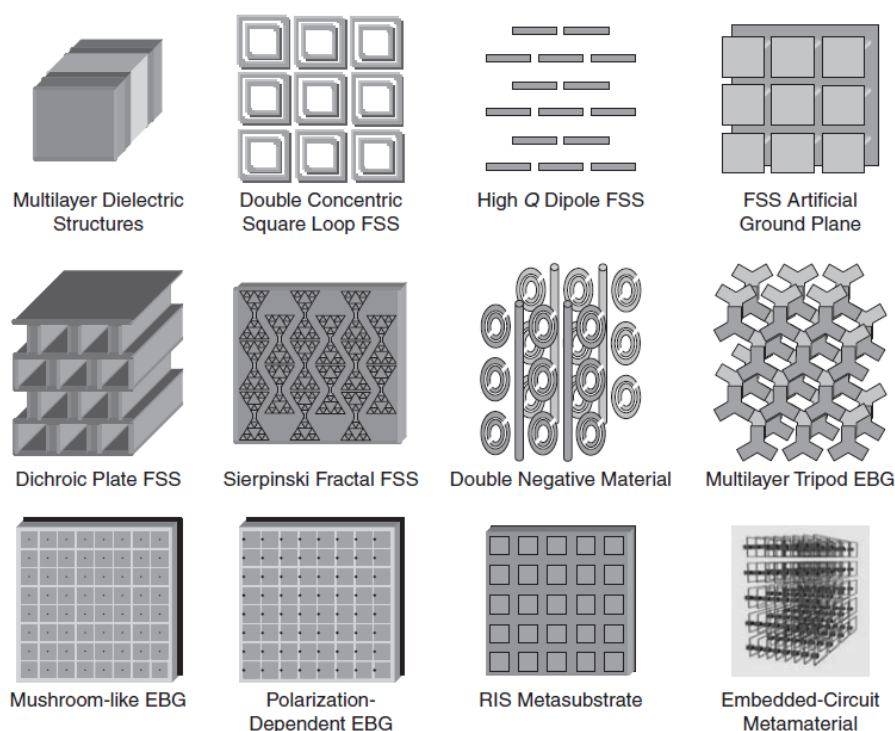


Figure 51 Different classes of engineered electromagnetic materials. Taken from [31].

Metamaterial based and inspired design: According to Ziolkowski [90] metamaterial based antennas are those made of ideal homogenized metamaterials. On the other hand, metamaterial inspired antennas are all those radiators obtained by applying the metamaterial concepts but that in reality consist of regular antennas loaded with few (or even just one) metallic inclusions. Therefore, almost all the miniature antenna experimental designs proposed so far in the literature can be considered, indeed, as metamaterial-inspired antennas.

In the case of metamaterial inspired antennas it is understood that there is no need for theoretically correct definition of the effective parameters of a sample made of few inclusions, which anyway loses most of its “bulk” physical meaning in such small samples. The procedure to design and optimize the inclusions may therefore become straight forward. The retrieved parameters of the sample cannot be considered as constitutive parameters of the medium, but they represent an operational definition of the effective parameters for the specific problem at hand.

Classification: Basically, metamaterial concepts for antenna applications can be classified in the following four categories [91]:

- 1) **CRLH-based** or dispersion engineered resonant antennas. This includes the antennas with negative-order modes and zeroth-order resonators. There are a variety of antennas in this type that have been developed based on the engineered dispersion curves ($k - \omega$ diagram) [80],[92]-[96].
- 2) **Metamaterial loading**, such as the epsilon/mu-negative materials ([16], [18], [101]-[103]), high permeability shells [104], and the magnetic photonic crystals (MPC) [106]-[107]. The metamaterial-inspired near-field resonant antennas proposed by Ziolkowski [105] are also included here.
- 3) **Antennas loaded with metasurfaces** [108]-[113], such as the electromagnetic band gap (EBG) mushroom structures or patch-type reactive impedance surface (RIS). They are able to miniaturize the antenna size, reduce the surface wave as well as to improve the radiation characteristics.
- 4) **Metaresonator** antennas [114]-[118], particularly for the antennas based on the split-ring resonators (SRRs) and complementary split-ring resonators (CSRRs).

These different types of metamaterial-based small antennas are explored in terms of antenna miniaturization and bandwidth enhancement.

1.4.3. Use of metamaterials in antenna miniaturization

A. CRLH metamaterial resonant antennas

In parallel to the development of resonant metamaterials, Eleftheriades and Grbic [92] and Caloz and Itoh [93] independently developed a transmission line theory of negative index media (also called Composite Right/Left Handed Transmission Lines) with lumped circuit elements for planar metamaterials which could support backward waves, or, in other words, an effectively planar negative refractive index medium. Example of the CRLH TL is given in Figure 52. The captivating elegance of the distributed L–C circuit network representation lies in the fact that the capacitive and inductive elements directly determine the constitutive parameters—the desired permittivity and permeability, respectively—of the effective medium.

The thin wire – split ring resonator structures are inherently narrow band or severely lossy due to their resonant nature. In contrast, non-resonant transmission line (TL) MTMs, can exhibit simultaneously broad bandwidth and low losses.

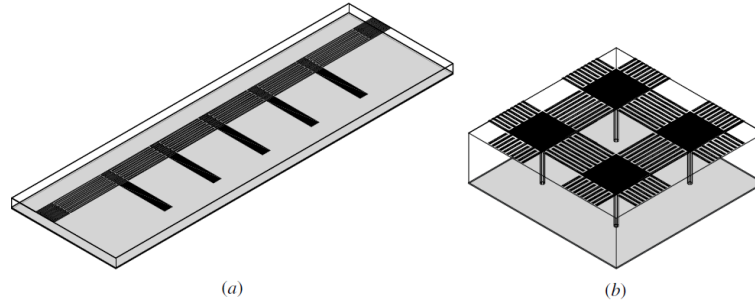


Figure 52 Planar CRLH TL structures in microstrip technology, constituted of series interdigital capacitors and shunt stub inductors (including via connections to ground). The gray areas represent the ground planes and the black areas represent the metal traces. The unit cell size p is much smaller than the guided wavelength (at least, $p < \lambda_g/4$) to ensure effective homogeneity of the structure and subsequent effective-uniformity behavior of the TL. (a) One-dimensional structure. (b) Two-dimensional structure. Taken from [80].

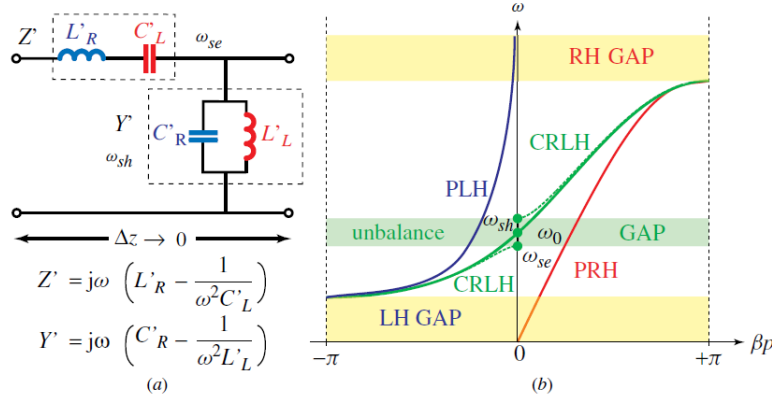


Figure 53 Incremental circuit model of CRLH TL. The subscripts R and L stand for RH and LH, respectively. (a) Unit-cell prototype. (b) Corresponding microwave network dispersion diagram, corresponding to idealized uniform TL relations (bandwidth extending from $\omega = 0$ to $\omega = \infty$), except for existence of LH and RH gaps ($\omega_{se} < \omega_{sh}$ or $\omega_{se} > \omega_{sh}$, depending on the LC parameters). The curves for a purely LH (PLH) structure ($L_R = C_R = 0$) and for a purely RH (PRH) structure ($L_L = C_L = \infty$) are also shown for comparison.

The equivalent circuit model of a typical symmetrical CRLH TL unit cell is depicted in Figure 53 where the loss is neglected for simplicity. By including the right-handed (RH) effect into a purely left-handed (LH) circuit, it represents the most general form of a practical metamaterial TL structure. The series capacitor (C_L) and the shunt inductor (L_L) contribute to the left-handedness while the series inductor (L_R) and the shunt capacitor (C_R) form its RH dual counterpart.

By applying the periodic boundary conditions, dispersion relation is determined to be [80]

$$\beta(\omega) = \frac{1}{p} \cos^{-1} \left(1 - \frac{1}{2} \left(\frac{\omega_L^2}{\omega^2} + \frac{\omega^2}{\omega_R^2} - \frac{\omega_L^2}{\omega_{se}^2} - \frac{\omega_L^2}{\omega_{sh}^2} \right) \right), \quad (1.75)$$

where $\beta(\omega) = 2\pi/\lambda$ is the wave number, p is the length of the unit cell and

$$\omega_L = \frac{1}{\sqrt{C_L L_L}}, \quad \omega_R = \frac{1}{\sqrt{C_R L_R}} \quad (1.76)$$

$$\omega_{se} = \frac{1}{\sqrt{C_L L_R}}, \quad \omega_{sh} = \frac{1}{\sqrt{C_R L_L}}$$

Apparently, there are two frequency points referred to as the infinite wavelength points $\beta(\omega) = 0$, with a band-gap in between. In the balanced case ($\omega_{se} = \omega_{sh}$) the band-gap vanishes. Usually only one particular **zeroth-order resonance** will be excited which depends on the circuit values and the boundary conditions. For the open-ended resonator, it is determined by series resonance ω_{sh} , while for the short-ended case, it is represented by shunt resonance ω_{se} [80]. Multiple resonances including the negative-order, zeroth-order, and positive-order resonances can be generated by cascading more than one unit cell.

Example 1: Due to the size consideration, most of the CRLH resonator-type antennas are designed on the negative-order or the zeroth-order modes. Zeroth-order resonance, of which the frequency is independent of the physical length, actually gains more popularity for antenna applications. Figure 54 shows the most original zeroth-order resonance antenna with four unit cells [94].

A virtual ground capacitor is employed achieving a via-free design. This antenna was implemented on a 31-mil substrate with a dielectric constant of 2.68. The measured reflection coefficient is -11 dB at the resonance frequency of 4.88 GHz. Compared to a patch antenna on the same substrate, this antenna leads to a 75% size reduction. The radiation of this antenna broadside due to the configuration.

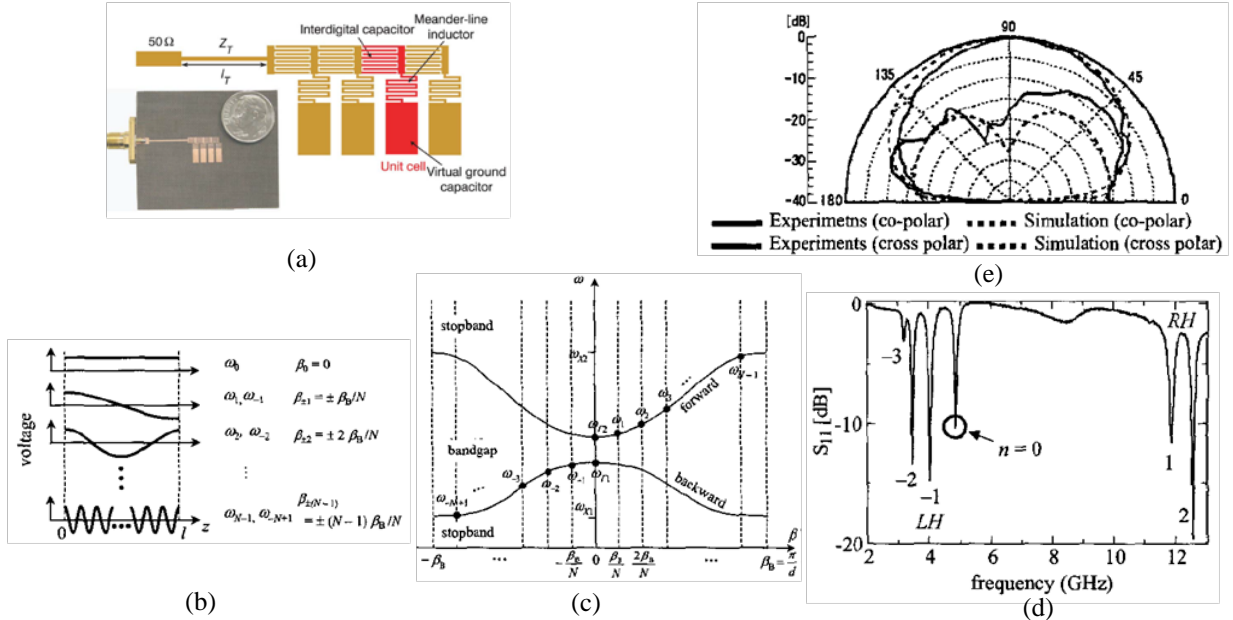


Figure 54 (a) Four-cell zeroth-order resonance (ZOR) antenna based on microstrip technology operated at 4.88 GHz. (b) Resonant modes of the open-ended CRLH TL resonator. The zeroth-order resonance corresponds to $\beta = 0$. The CRLH TL resonator also resonates with $n = \pm k$ modes ($k = 1, 2, \dots, (N-1)$). (c) Typical dispersion relation of the CRLH TL. (d) Measured S_{11} of the prototype ZOR antenna. (e) Measured radiation patterns. Taken from [94].

Example 2: CRLH loops provide particularly interesting monopole antennas, both of electric and magnetic nature [95]. The CRLH magnetic and electric monopoles are based on the series and shunt CRLH zeroth order resonances, respectively, as shown in Figure 55(a). The CRLH loop structures are infinitely periodic and do not have any termination. What determines the resonances that are excited (ω_{se} or ω_{sh}) is then the excitations, as illustrated in Figure 55, where two different excitation slots excite separately the series and shunt resonances. Consequently, the series and shunt may exist simultaneously in a given design, yielding a dual-monopole antenna, and even at the same frequency when the CRLH structure is balanced. Moreover, when the series/shunt frequencies are tuned so as to radiate quadrature fields, the dual-monopole antenna may provide circular polarization in the far-field.

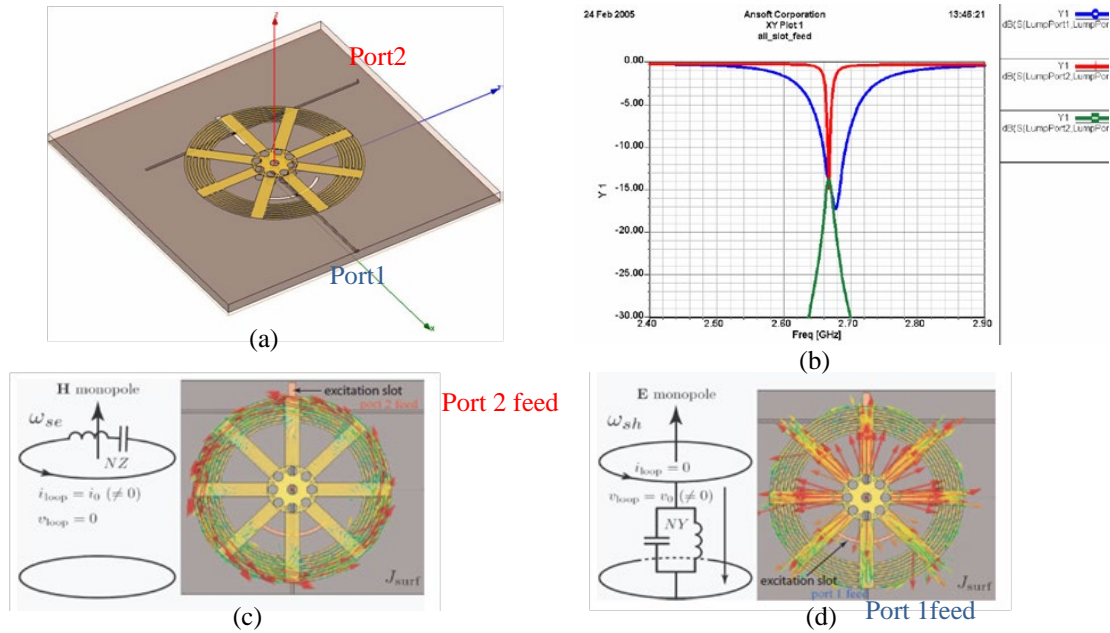


Figure 55 (a) Simulation model of an 8-cell CRLH ring resonator. The diameter of the outer ring dimension is 27.5 mm. The modes are excited by two slots in the ground that couple with the resonator. (b) Simulated s-parameters for the ring. The zeroth order voltage mode (S_{11}) and current mode (S_{22}) operated at the same frequency and are reasonably decoupled. (c) Magnetic and (d) electric monopole ring antennas using the series and shunt CRLH zeroth order resonances, respectively. Principle and current distributions. Taken from [96].

B. METAMATERIAL LOADING BASED SMALL ANTENNAS

Double positive (DPS) materials are characterized by standard values of the permittivity and permeability (regular dielectrics). Epsilon negative (ENG) and mu-negative (MNG) metamaterials do not support wave propagation, instead the fields are evanescent in such media. However, electrically small antennas have been achieved by ENG and MNG metamaterial loadings. They have provided an alternative approach to address those conflicting issues between the antenna size and radiation performance. Specifically, the metamaterial loadings discussed here include the MNG [101], ENG [102]-[104], the so-called near-field resonant parasitic (NFRP) elements [105], and the magnetic photonic crystals [106][107].

Most of these antennas eventually fall into the same RLC resonator type as shown in Figure 56, although they may have different forms or design approaches. For instance, the loadings can be either uniform shells or resonant elements, and the coupling can be either electric or magnetic type. The ENG shells for antenna applications were actually first proposed by Ziolkowski and Erentok [103] and a depiction of the idea is shown on Figure 56.

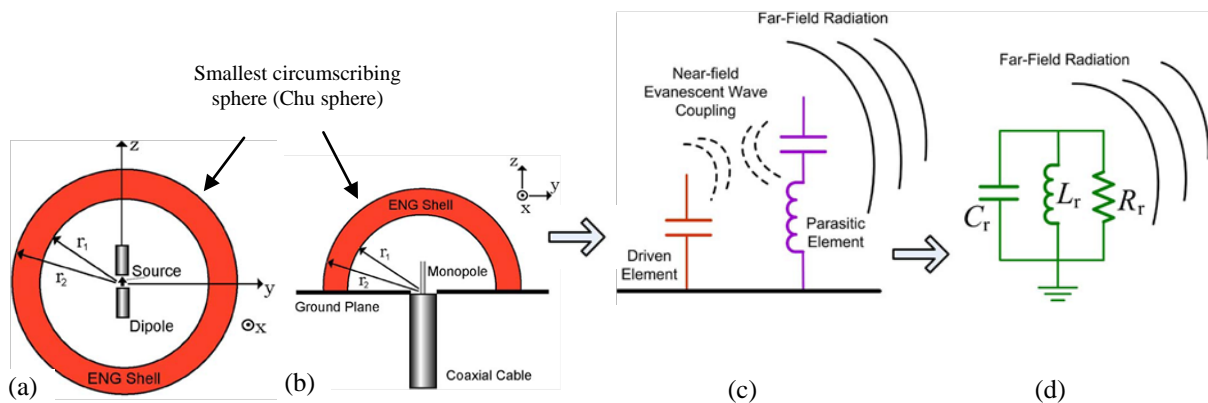


Figure 56 Example of metamaterial-based, efficient ESAs consisting of (a) a center-fed dipole antenna and (b) a coax-fed monopole antenna surrounded by an ENG shell. (c) The coupling and radiation behavior of the near-field metamaterial-loaded small antenna. (d) Final RLC resonator approximation for the whole antenna. Taken from [103]

The driven element can be either a small dipole or a monopole. It is demonstrated that the outside shell is essentially an electrically small resonator with a capacitive core inside and an inductive surrounding outside, yielding a lossy RLC resonator as shown in Figure 56(c). The small driven dipole or monopole is also a capacitive element. The total antenna resonance frequency is determined as

$$f_0 = \frac{1}{2\pi\sqrt{L_r C_r}}, \quad (1.77)$$

where L_r and C_r are the effective inductance and capacitance as shown in Figure 56(d). The properties of the negative permittivity sphere differ dramatically from that of a positive permittivity sphere in many aspects, many of which are desirable for an ESA [103][16]. Stuart *et. al.* [16] report the negative permittivity shell or sphere provides bandwidth performance close to the Chu-limit (same as spherical helix examples in Chapter 1.1.2) and good impedance matching which can be easily obtained. The practical challenge of implementing these designs is in the development of low-loss uniform materials with negative permittivity. Actually, these materials are attainable in nature. For instance, the plasmas may achieve similar functions as the ENG materials.

Example 1: One way to physically approximate the concept of a ENG shell is using the NFRP element proposed by the group led by Ziolkowski [103]. One of those examples is the antenna shown in Fig. 13 with a meander line element driven by a monopole. The monopole is printed on the Rogers 5880 substrate and coaxially fed through a ground plane. The coupling between the two elements is electrical. The small meander line, which is connected to the ground, has been demonstrated to be a unit cell of ENG metamaterial [103]. Therefore, it can be roughly approximated as a near-field shell with a negative permittivity. It is reported that an ESA operated at 1.37 GHz with a ka close to 0.49 has been achieved with an overall efficiency of 88% and a fractional bandwidth (half power instead of the 10dB bandwidth) around 4.1%.

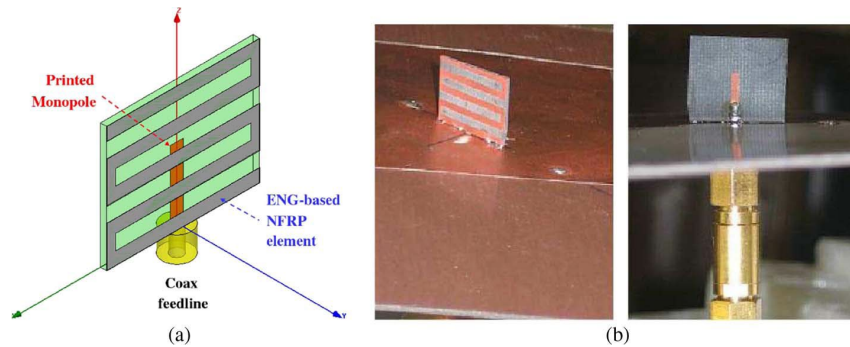


Figure 57 The fabricated 1373-MHz 2-D electric-based small antenna consisting of a meander line and a monopole element. (a) HFSS model. (b) Fabricated prototype [103]

Example 2: Alu *et al.* [101] explored pairs of metamaterial slabs with oppositely signed constitutive parameters and used them to obtain sub-wavelength patch antennas. If two materials have opposite signs in their parameters across the interface, the slopes of variation of the tangential electric and magnetic fields result in a peak at this interface. If the parameters of the two materials are chosen judiciously it is possible to excite a resonant mode confined to the interface which does not depend on the thickness of the two material slabs, meaning that the bi-layer composed of such materials can be made arbitrarily small compared with the wavelength. The resonance condition for a sub-wavelength operation of the antenna is determined by a change in the sign of only one constitutive parameter (permittivity or permeability, depending on the application). This means that there is no need for complicated DNG slabs. ENG or MNG materials, which may be arguably simpler to realize are enough to obtain the desired behavior. However, it has been shown that such patches do **not** radiate energy efficiently in free space. The electric field underneath the patch is almost constant and the ratio between the radiated and the stored energy is very low implying that the radiators of [101] are more resonators than efficient radiators.

With a circular patch it is possible to achieve the aforementioned miniaturization using a MNG metamaterial depicted in Figure 58(a)-(b). The metamaterial is composed of split ring resonators that provide negative permeability slightly above their resonance frequency. First resonance seen in Figure 58(c) is due to the MNG metamaterial, while the second resonance is the standard patch antenna resonance, which is due to its geometrical dimensions (i.e. when the patch diameter's of the order of half wavelength) because at that frequency the permeability becomes positive again.

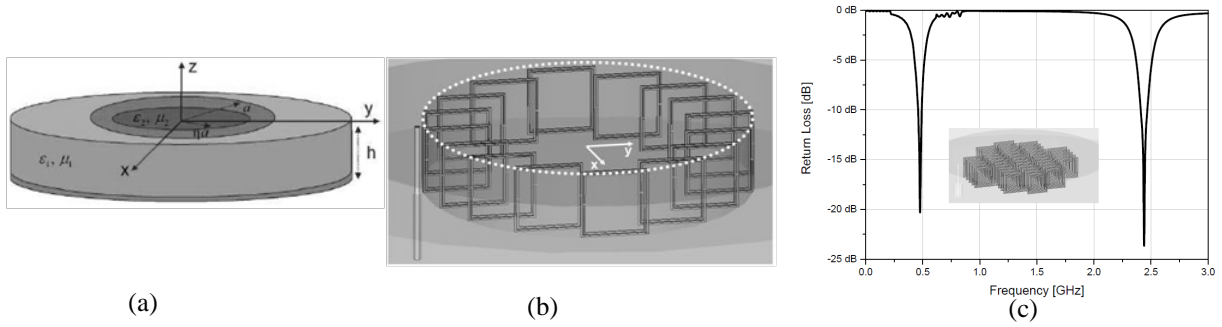


Figure 58 (a) A circular patch antenna loaded with a radially inhomogeneous substrate. (b) Conceptual implementation of a single ring of magnetic resonant inclusions underneath the patch to obtain the required MNG behavior at the desired frequency. (c) Matching features of the antenna. Picture taken from [101]

Real life issues with implementation of miniaturized metamaterial components: The first issue with realistic inclusions is the *inherent anisotropy* of the inclusions. This may be solved by properly aligning the inclusions as a function of the expected field polarization in proximity of the metamaterial sample (parameters are not important in the direction where the field is zero). The second issue is the *size of the inclusions* that have to fit the electrically small volume of the radiators. The theoretical results show that in principle there is no limit to the size of the metamaterial samples loading the two radiators. Of course, in reality there is a final limit, dictated by losses and the material granularity. Miniature inclusions are essential for achieving miniaturization of the radiators. A big problem with artificial magnetic inclusions is that the more electrically smaller they are, the narrower the bandwidth is! The third difficulty is to design the inclusions in order to get the same needed values of permeability or permittivity derived from theoretical analysis of the components.

C. METASURFACE GROUND PLANE BASED MINIATURIZATION

As a subfield of metamaterials, meta-surfaces have also drawn increasing attention in recent years, finding widespread applications in microwave circuits and antennas [109]-[113]. They are usually designed by making only a 2D array of metallic inclusions which then a partially reflecting and partially transmitting surface (PRS). However, in connection with patch antennas, here we are interested in metasurface ground planes, which are basically a PRS placed close to a ground plane and allow only reflection of incoming waves. They are often called high impedance structures (HIS) for their ability to reflect waves with zero reflection phase, just like magnetic conductors, which also earned them the name of artificial magnetic conductors (AMC).

We can divide metasurface ground planes into two main categories: electromagnetic band gap structures (EBG) and reactive impedance surfaces (RIS). EBG structures were introduced by Sivenpiper in [109] and are composed of a mushroom-like array of periodic metallic patches with vias while a RIS was introduced by Mosallaei and Sarabandi in [108] and is composed only of periodic metallic patches and no via.; both are shown on Figure 59. The main difference in operation between EBG and RIS structures is that the presence of via in a mushroom-type structure can impose an electromagnetic band-gap at the same frequency range as the AMC property and suppress the surface waves. In other words, the mushroom structure exhibits high surface impedance for both normally incident and surface waves at the same frequency band. In the absence of via, the band-gap does not normally coincide with the AMC frequency band. This can deteriorate the benefits of AMC surfaces in certain applications, where surface wave suppression is advantageous.

Similar to metamaterials, we can observe in Figure 59(a) and (b) that metasurfaces depend on resonant phenomena for their operation and their properties are thus frequency dependant. Because of this, perfect AMC operation is possible only at a single frequency. However, bandwidth of metasurfaces is often considered by looking at the frequency range where the reflection phase is between $-45^\circ < \varphi < 45^\circ$. Unfortunately, this bandwidth is also dependent on the angle of the incoming waves. Figure 60 shows typical dependence of metasurface bandwidth performance depending on the incidence angle for a TE and a TM wave polarization. We can observe that with increasing angle bandwidth reduces for TE polarized waves and increases for TM polarized waves.

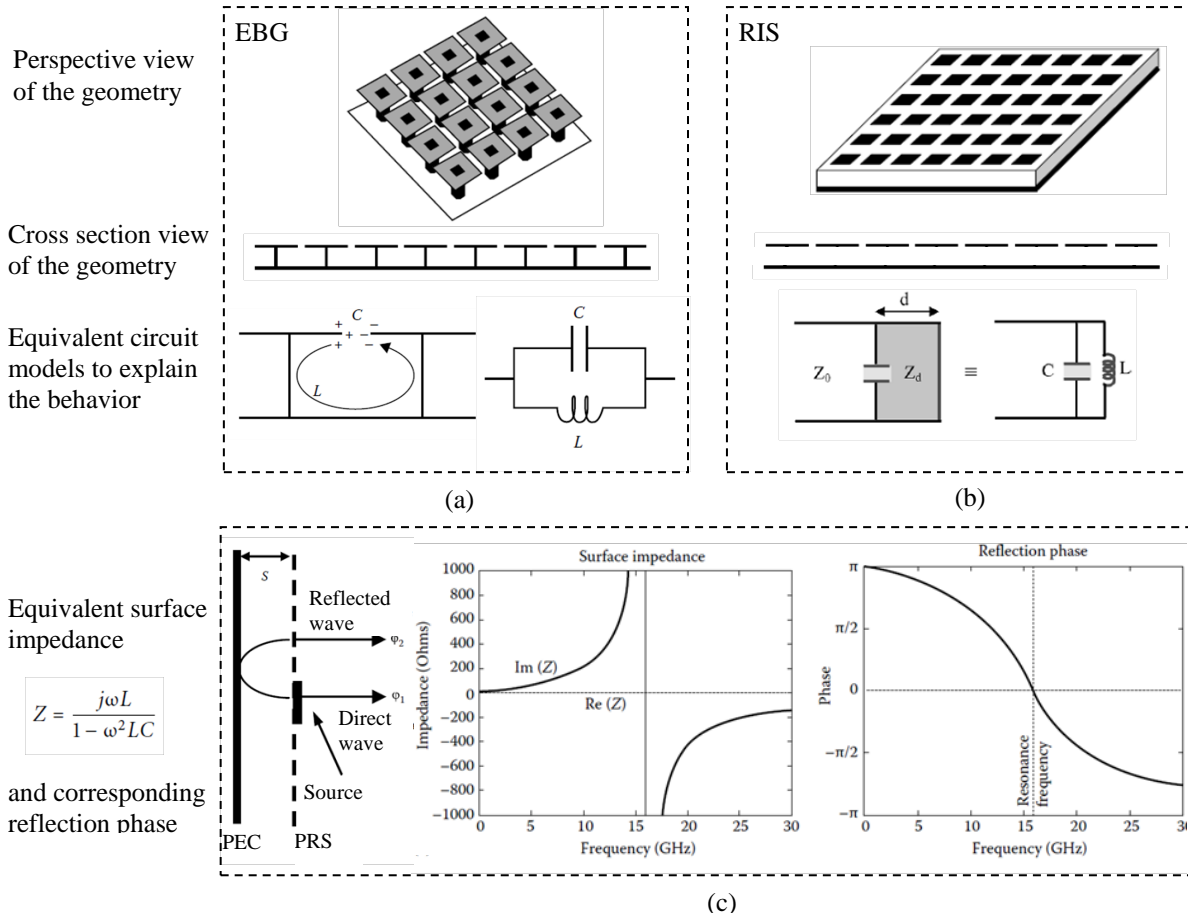


Figure 59 (a) EBG mushroom type ground plane and its equivalent circuit. (b) RIS type ground plane and its equivalent circuit. (c) Schematic of waves reflecting from a metasurface ground plane, the equivalent surface impedance and the corresponding phase of the reflected wave. Pictures taken from [86].

Generally speaking, the novel characteristics of the metasurfaces, including the RIS, AMC, EBG can be harnessed in several ways for antenna applications. First, their band-gap features can be utilized as a high impedance ground plane to enhance radiation performance (gain, patterns, side lobes, etc.) by suppressing undesired surface waves and mutual coupling. Second, they can provide a zero-phase reflection at the PMC frequency which could lead to a low-profile antenna realization. Third, the reactive impedance provided by metasurface underneath the radiating element, either inductive or capacitive, offers a way to store the magnetic or electric energy which could reduce Q of the antenna and therefore achieve a better bandwidth and size miniaturization. Last, they can work as a reflecting surface or a frequency-selective surface which could change the field distribution or wave direction thus increasing the antenna gain or change the radiation patterns.

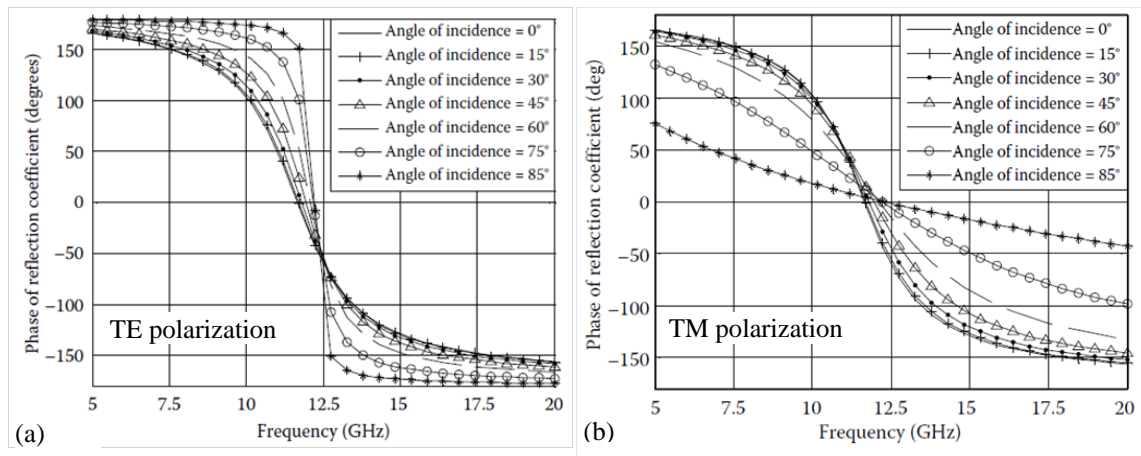


Figure 60 Typical reflection phase of printed patch metasurface structure for (a) TE-polarized oblique plane wave excitation and (b) for the TM-polarized oblique plane wave excitation. Taken from [86].

Example 1: Mosallaei and Sarabandi originally introduced reactive impedance surfaces in [108] and immediately considered performance of a patch antenna over the RIS and compared its performance with a traditional patch over a PEC surface. To make the comparison, they used the same size patch and ground plane, as shown in Figure 61; however, they allowed the permittivity of the substrate of the conventional patch to be a variable to achieve the same resonant frequency.

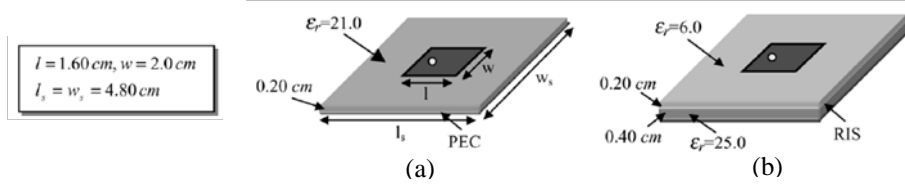


Figure 61 Patch antenna on the (a) conventional substrate and (b) RIS substrate (a 4×4 array of square patches printed on the PEC-backed dielectric material). Taken from [108].

In their experiment, the patch antenna was printed on a relatively low dielectric material $\epsilon_r = 6$ of thickness 2 mm and located above an RIS. The RIS substrate was made of trans-tech MCT-25 magnesium calcium Titanate composition with a dielectric constant of 25, a thickness of 4 mm, and $\tan \sigma = 0.001$. Their measured results show that the antenna resonance frequency is at 1.92 GHz and it exhibits a 10-dB fractional bandwidth of $BW=6.7\%$. The measured gain is 4.5 dBi and the radiation efficiency is about 90%. The antenna exhibits a patch size of $0.102 \lambda_0 \times 0.128 \lambda_0 \times 0.038 \lambda_0$ at the resonance frequency.

To achieve the same resonant frequency (1.86 GHz), a conventional patch over a substrate thickness of 2 mm, a high dielectric substrate $\epsilon_r = 21$ was needed, as shown in Figure 61(a). The conventional patch antenna, over the ground plane, shows a very narrow bandwidth of and an efficiency of about $BW=0.6\%$ and efficiency of about 70%. This effectively demonstrates that over a reactive impedance ground plane the patch size would be miniaturized if it were placed over the same substrate as a regular patch working above a PEC ground plane.

D. METARESONATOR BASED SMALL ANTENNAS

Metaresonator antennas are true examples of metamaterial inspired design, as they usually consist of a few or only one metamaterial inclusion. The antennas directly using the metaresonators, specifically the SRR and the CSRR, are shown in this section. SRR can be considered as a resonant magnetic dipole which has been widely used to synthesize metamaterials. The applications of SRR and CSRR to miniaturize microwave devices and various antennas were widely investigated and presented [85],[117]-[118]

Example 1: One original example using the SRR for ESA application was proposed in [117]. In that design, the SRR is electrically excited with a coaxial cable or a monopole antenna. The SRR is printed on the standard FR-4 material with a relatively permittivity of 3.5. That antenna achieves a size of $0.095 \lambda_0 \times 0.100 \lambda_0 \times 0.019 \lambda_0$ and a radiation efficiency of 43.6%. Here we demonstrate a planar ESA using the vertical SRR to show its capability and performance. The proposed antenna structure is shown in Fig. 18(a) and the photograph of the fabricated antenna is shown in Fig. 18(b).

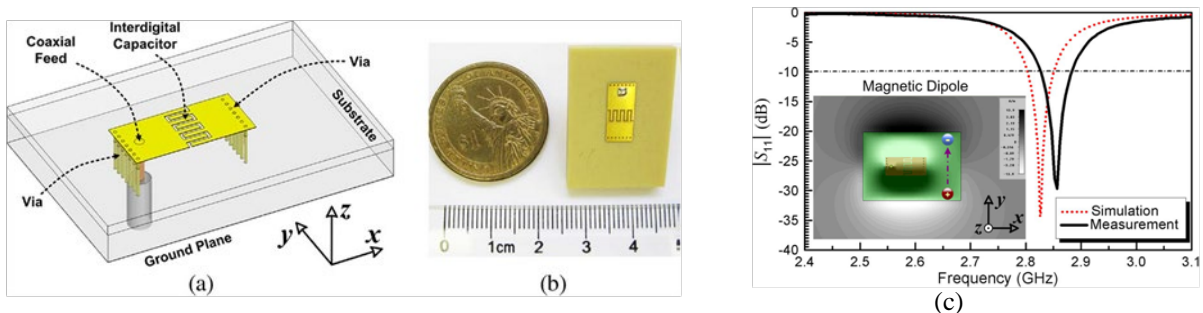


Figure 62 Configuration of the proposed inductively-fed vertical SRR antenna. (a) Perspective view and (b) fabricated prototype of the antenna. (c) The measured and simulated reflection coefficients for the inductively fed VSRR antenna. The magnetic field distribution at the resonance frequency is also plotted in the inset. Taken from [117].

A coaxial feeding probe is directly connected to the top surface of the SRR which can be represented by a series inductor. The interdigital capacitor, which is the split of the VSRR, is able to store the electric energy for the resonator and miniaturize the antenna size. The VSRR is modeled as a high- Q LC resonator with a parallel radiation resistance associated with the capacitor. This circuit is excited by simply applying a voltage difference across the capacitor, which generates current along the loop and induces axial magnetic field inside the loop. In this manner, it can be equivalent to a magnetic dipole placed along the y -direction above a PEC surface. Figure

62(c) shows the simulated and measured reflection coefficients for this VSRR antenna. It exhibits an overall size of $0.112 \lambda_0 \times 0.051 \lambda_0 \times 0.028 \lambda_0$ at the operating frequency, which corresponds to a ka of 0.427. The measured -10 dB fractional bandwidth is found to be 2.1%. The measured gain and efficiency are 2.05 dBi and 68.1%. It is noted that the reduced efficiency is mainly due to the lossy substrate with a loss tangent of 0.009. The simulated magnetic field at the resonance frequency is also provided in. It is clearly seen that this antenna behaves similarly to a magnetic dipole antenna over a PEC surface.

Example 2: Miniaturized planar antennas based on another metaresonator, CSRRs, are investigated in [118]. The CSRR has been proved to behave as an electric dipole which needs an axial electric field excitation. It is a high-Q resonator but not a good radiator [118]. However, it can couple the energy to the antenna patch and make the patch radiate. An illustrative example is shown Figure 63 where two CSRRs are embedded on the top surface.

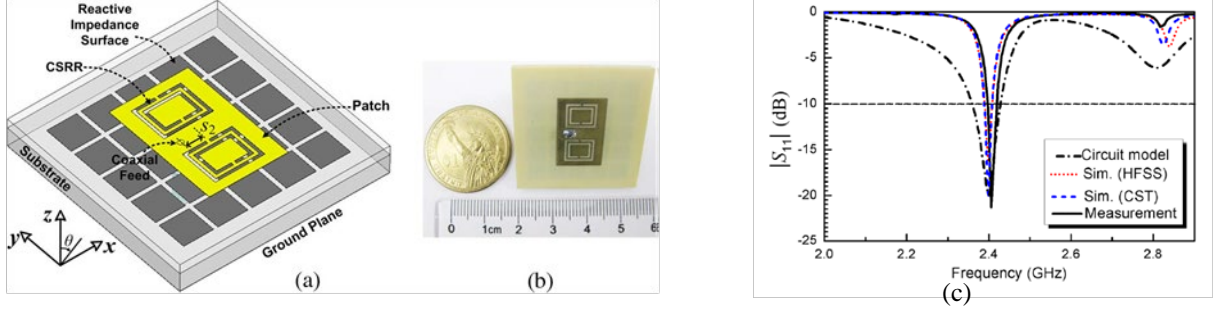


Figure 63 (a) Perspective view and (b) a photograph of the proposed dual-band dual-polarized antenna with face-to-back CSRRs. An RIS is used to improve the antenna radiation performance. (c) The measured reflection coefficient compared with the results from circuit simulation and full-wave simulation using HFSS and CST. Taken from [118]

They are face-to-back oriented in terms of the direction of the ring split. An RIS, which is composed of a periodic array of metallic square patches printed on a metal-backed dielectric substrate, is introduced below the top surface to improve the radiation efficiency. A coaxial probe feeding is utilized and placed a little off the center along the x-direction of the patch. It is a three-layer structure where the top and bottom dielectric substrate with a relative permittivity of 4.02 and a measured loss tangent of 0.009 at 2.4 GHz. This antenna is operated as a dual-band antenna where the first resonance is excited by the CSRRs while the second resonance is provided by the patch [110]. The two resonances have orthogonal polarizations. The two bands are measured at 2.41 and 3.82 GHz, respectively. The patch size is around $0.099 \lambda_0 \times 0.153 \lambda_0 \times 0.024 \lambda_0$, where λ_0 is the free-space wavelength at the first resonance. The corresponding measured radiation efficiencies are 22.8% and 74.5%. The low efficiency at the first band is mainly due to high dielectric loss and the conductor loss caused by the strong current.

1.4.4. Use of metamaterials in antenna bandwidth enhancement

A. METAMATERIAL LOADING BASED BANDWIDTH ENHANCEMENT

Hansen and Burke [119] have shown bandwidth for a patch antenna over a magneto-dielectric substrate with thickness t can be approximated by:

$$BW \approx \frac{96 \sqrt{\frac{\mu_r}{\epsilon_r}} \frac{t}{\lambda_0}}{\sqrt{2}(4 + 17 \sqrt{\mu_r \epsilon_r})} \quad (1.78)$$

Thus for a given miniaturization factor (constant $\mu_r \epsilon_r$), the antenna bandwidth can be enhanced by increasing the ratio μ_r/ϵ_r . One could therefore use natural magneto-dielectric material with moderate values of μ_r and ϵ_r that provide the same miniaturization factor, while a wider bandwidth can be achieved. The alternative is to try and create a metamaterial that artificially increases the permeability. However, as is demonstrated in the examples below, because of the inherent dispersion (frequency dependence) of metamaterials, there is no real benefit from using them.

Example 1: Performance of a patch antenna printed on an ideal magneto-dielectric substrate was investigated experimentally in [120] using a structure composed of layers with $\epsilon_r = 16 - j0.032$, $\mu_r = 1$ and $\epsilon_r = 2.2 - j0.022$, $\mu_r = 16 - j0.32$, as is shown in Figure 64. A patch antenna with size 10 cm 8 cm is printed on the four layer dielectric and magneto-dielectric materials with thickness 2 cm. The size of the ground plane is 20 cm 20 cm. The antenna resonance is at $f_0 = 277$ MHz and it provides a wide bandwidth of about FBW = 3.2%. The size of the antenna is around $0.09 \lambda_0$ with a miniaturization factor of 5.4. The antenna efficiency is

about 67%. If a magneto-dielectric material with lower magnetic loss tangent around 0.01 is used the efficiency is increased to 82% where the bandwidth is decreased to $BW=2.8\%$.

To achieve the same miniaturization factor utilizing only a dielectric material ($\mu_r = 1$) one must use $\epsilon_r = 23.7$. This reduces the bandwidth to about $BW = 0.5\%$, with the efficiency in this case for a dielectric loss tangent of 0.001 is about 64%. Therefore, utilizing the magneto-dielectric meta-substrate one can offer a miniaturized wideband planar antenna with high efficiency.

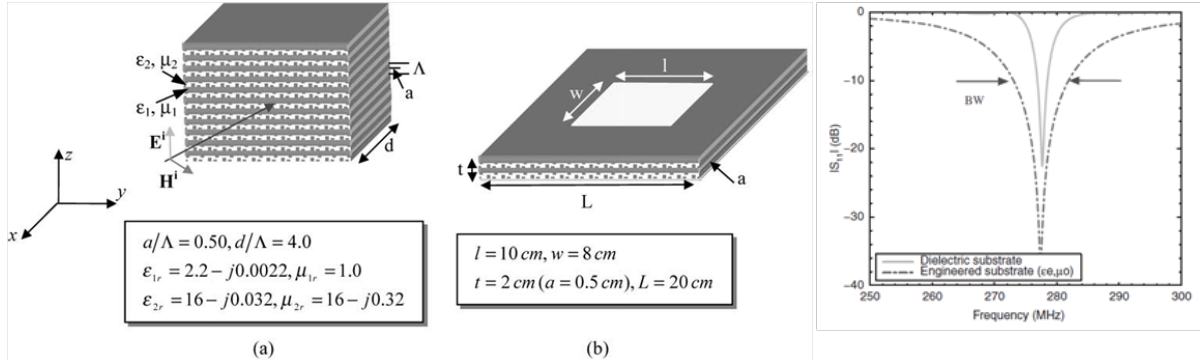


Figure 64 (a) Composite periodic dielectric and magneto-dielectric structure (periodicity in z directions). (b) A patch antenna over the engineered magneto-dielectric meta-substrate. (four-layer dielectric and hexaferrite substrate). (c) comparison of return loss for a regular patch antenna over a dielectric material and a patch antenna over the engineered substrate.[120]

Example 2: A metasubstrate from the embedded-circuit inclusions (split ring resonators) was investigated in [121], as shown in Figure 65(a). The FDTD method is applied to characterize the antenna printed on the embedded-circuit metasubstrate, and the result for return loss is shown in Figure 65(b). A resonant frequency of $f_0=1.74$ GHz (miniaturization factor of about 4) and bandwidth of about $BW=1\%$ are determined. The patch antenna printed on a dielectric substrate with $\epsilon_r=13.92$ (keeping the same resonant frequency) has bandwidth of about $BW=0.6\%$. It must be highlighted that the dispersion behavior of the permeability function plays an important role in degrading the impedance bandwidth performance. Both the dielectric and embedded-circuit substrates provide similar radiation patterns. In [121] it was reported that a metasubstrate offers a relatively wider bandwidth, but this claim was also criticized by [122]. We can conclude that no practical benefit in bandwidth is gained from using split ring resonators.

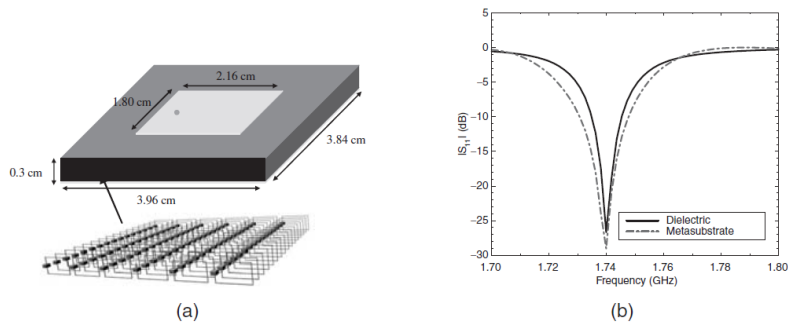


Figure 65 Patch antenna printed on an embedded-circuit metasubstrate: (a) the geometry and (b) return loss [121]

A. METASURFACE BASED BANDWIDTH ENHANCEMENT

A patch antenna is capacitive below its natural resonance, while a RIS is inductive below its respective resonance. Basically, RIS has the ability to store magnetic energy that can compensate for the near-field electric energy of the radiating patch; this fact allows for antenna miniaturization. In addition, RIS spatially distributes the image representation of the patch on the ground plane; this minimizes mutual coupling between the antenna and its image, allowing for ease of impedance matching over a wider bandwidth.

Example 1: Connected to the already given example in part C of the previous Section on the miniaturization benefit of a RIS, here we show the bandwidth broadening effect. In the experiment with patch antennas, shown in Figure 66(a) and (b), Mosallaei and Sarabandi [108] measured the RIS-patch antenna resonance frequency is at 1.92 GHz and it a 10-dB fractional bandwidth of 6.7%, shown in Figure 66(d). The measured gain is 4.5 dBi and the radiation efficiency is about 90%. The corresponding conventional patch at the same resonant frequency (1.86 GHz) was designed on a high dielectric substrate to have the same patch size as the patch over a RIS. The return loss of this antenna is also shown in Figure 66(d) for comparison. The conventional patch antenna, over

the ground plane, shows a very narrow bandwidth $BW = 0.6\%$ and efficiency of about 70%. With the RIS ground plane the bandwidth was thus increased 8 times.

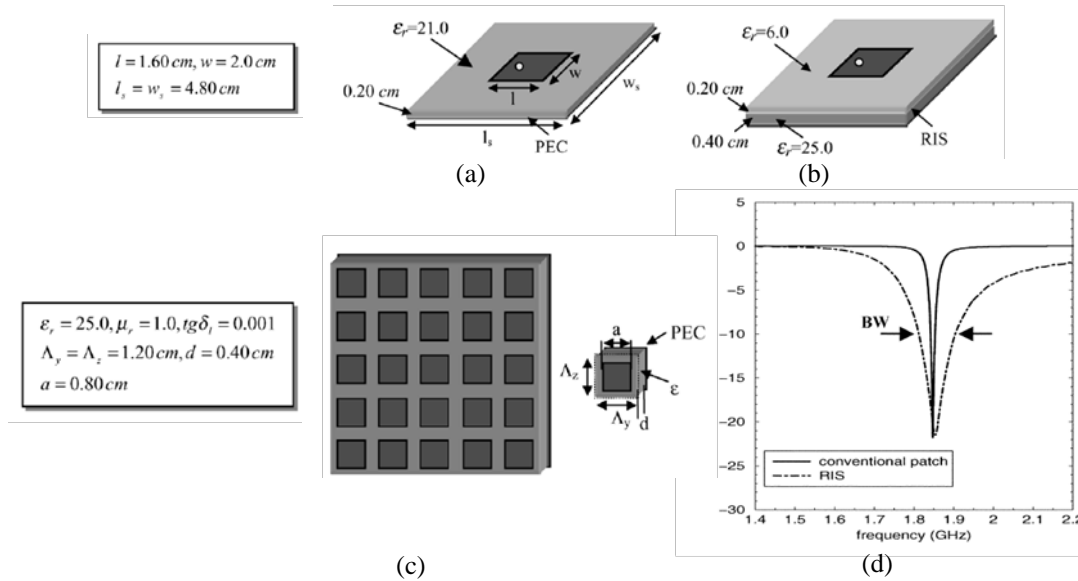


Figure 66 Patch antenna on the (a) conventional substrate and (b) RIS substrate (a 4×4 array of square patches printed on the PEC-backed dielectric material). (c) RIS substrate composed of periodic squared patches printed on the PEC-backed dielectric material and its building block unit cell. (d) Return loss of patch antenna over the conventional and RIS substrates. Notice to the wideband performance of the miniaturized patch on the RIS substrate. Taken from [108].

Example 2: A demonstration of circular polarization bandwidth enhancement using a RIS ground plane was demonstrated in [111]. The paper gives a step by step demonstration of bandwidth enhancement by comparing numerically and experimentally the performance of various antenna configurations: conventional slot-loaded patch antenna over a single substrate; over a dual-layer substrate; over a RIS made of square patches; and over a RIS optimized for giving broader CP polarization. The final optimized structure exhibits an axial-ratio bandwidth of about 15% and an impedance bandwidth better than 11%, which is much wider than the conventional printed antenna on the same materials. The comparison is given in Figure 67.

SUMMARY OF METASURFACE BENEFITS:

- Metasurfaces can be tuned anywhere between the PEC surface and the PMC surface offering a property to achieve the optimal bandwidth and miniaturization factor.
- Metasurfaces provide a total reflection of power that can also enhance the antenna front-to-back ratio.
- The image of a point source located above the metasurface is a spatially distributed current element that has the minimum interaction with the point source. This has the significant advantage of reducing the mutual coupling between the antenna and its substrate, resulting in the impedance bandwidth enhancement.
- RIS has the ability to store magnetic (or electric) energy that can be properly used to compensate for the near-field electric (or magnetic) energy of the radiating structure resulting in the antenna size reduction

The fact that a metasurface can offer miniaturization, and is **the only metamaterial type proven to bring substantial benefits for bandwidth** makes it the most important this metamaterial concept in this thesis. In Chapter 4 it is demonstrated that indeed, metasurfaces can bring benefits for cavity antennas.

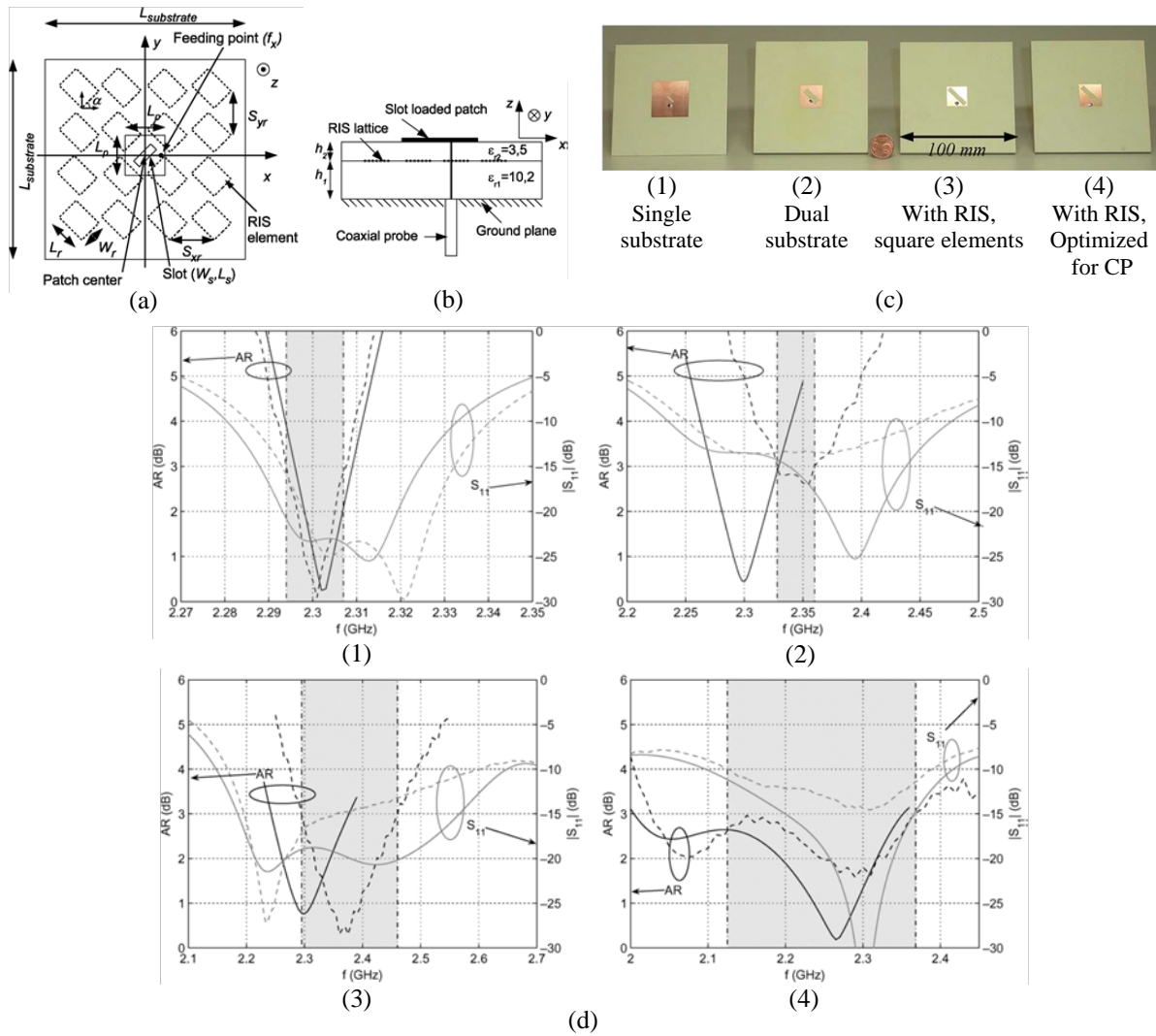


Figure 67 Geometry of the proposed structures (basic dimensions are $L_{substrate}=100$ mm, $h_1 = 6$ mm, $h_2 = 1.5$ mm). (a) Top view. (b) Side view. (c) Fabricated prototypes. In all cases, the radiating element is a probe-fed slot-loaded patch. (1) Single-substrate configuration (“1 sub.,” i.e., no RIS ($h_1 = 0$, $h_2 = 1.5$ mm)). (2) Dual-substrate configuration, no RIS. (3) RIS with square elements and angle $\alpha = 0^\circ$. (4) RIS with CP-optimized rectangular elements. Taken from [111].

1.4.5. Challenges and future trends of metamaterials

So far we have introduced various different metamaterial based antennas. Readers may have this question: *What are the challenges and limitation of these antennas?*

- The first challenge is how to obtain better homogeneous metamaterials. Many discussions and solutions are actually based on the assumption of low-loss homogeneous metamaterials, such as the ENG, MNG, DNG, and high-Mu materials. How to physically realize these materials would still be a long standing problem. The best approach should still rest on the discovery of new materials that are novel and low loss, which could be used by antennas.
- The second challenge, just like the conventional antennas, still lies in the contradiction between the bandwidth, efficiency, and the antenna size. The size miniaturization apparently is not a problem with metamaterial concepts. The challenges therefore become the **bandwidth broadening and efficiency improvement**. How to approach the lower bounds of Q (determined by Chu-limit), or even go beyond, for metamaterial-inspired antennas would still be a kernel of the problem that is a challenge for the future.

One “outside the box” solution to the bandwidth problem are active non-Foster elements used in a matching network to broaden the bandwidth. They are usually built via a combination of active devices (transistors) as well as lumped capacitors and inductors. Ideally they are able to realize negative inductance and capacitance values which are designed to excite the antenna resonance as well as to optimize the power delivered to its

terminals. Realistically, they suffer from many stability issues and limitations on the highest frequency of operation that have yet to be resolved by researchers around the world. In this thesis we do not explore non-Foster elements and restrict ourselves to passive antennas only.

1.5. Conclusion of Chapter 1

In this chapter we introduced important topics which are essential to the rest of the thesis. These are: antenna bounds, microstrip antennas, cavity antennas, and metamaterials. In fact, these topics will be merged together to form new results.

The Chu bound has been investigated since the middle of the 20th century and is regarded as an important benchmark by many antenna researchers although it is applicable to spherical antennas only. The newer, Gustafsson bound, is applicable to arbitrary geometries and is therefore a perfect candidate in analyzing cavity antennas.

Pin fed microstrip patch antennas have been shown to offer many possibilities for miniaturization and bandwidth enhancement. The usefulness of these techniques when a patch is inserted into a small cavity will be discussed in the next chapter. Patch antennas in cavities have been investigated in the literature before, but their bandwidth behavior has never been directly compared to the bandwidth behavior of simple cavity antennas, nor has any relationship between the two been established. The analysis of simple square cavities was first presented in 1950s but has been expanded in this chapter by the author to include circular apertures and finite ground planes, because these results will be of importance in the next chapters.

Finally, metamaterials have been shown to be very useful for miniaturization, but there are very few examples where they enhance bandwidth. The best candidates for bandwidth enhancement of patch antennas seem to be metasurfaces. They were shown to offer both miniaturization and better bandwidth.

Chapter 2.

Bandwidth of patch antennas in small cavities

In this chapter, simulation results for single patch antennas in cavities will be presented and discussed. Studies have been made on rectangular and circular shaped cavities in an infinite and a finite ground plane. Section 2.1 explains the reasons for investigating strictly single patch configurations. Section 2.2 and Section 2.3 combine the knowledge of cavity antennas data from simulations of patch antennas to draw new conclusions and explain the operation of such antennas. Section 2.4 presents several transmission line models to describe the phenomena seen in simulation results.

2.1. On the restriction to single patch configuration

In Chapter 1.2. several miniaturization and bandwidth enhancement techniques were discussed. The motivation for considering these techniques is the requirement to place the antenna in a small cavity, requiring miniaturization, and enhancing bandwidth performance for data transmission. All techniques were considered and investigated using the FD solver in simulation software CST [130].

An elimination process was applied based on the simulations and is briefly summarized here. Emphasis in the elimination process is on the behavior of the antenna performance with increasing height, since in the end application, height is less restricted than aperture size. Summary of miniaturization techniques for microstrip antennas applied in a small cavity environment:

- Figure 68(a) shows material loading technique where the volume of the cavity is filled with a high permittivity material up to the aperture. At low height, patch size is miniaturized just as the case without a cavity. Increasing height miniaturizes the patch size further. Due to the cavity environment, height can be increased further compared to the case without a cavity. There is no radiation from the feeding pin and no surface waves in the substrate. Furthermore, cavity enclosure can be considered as a miniaturization technique itself. Namely, when the cavity size is smaller than the calculated patch on the given substrate permittivity, the antenna will still resonant with a patch smaller than the cavity size, due to the strong capacitive effect between the patch and the wall. All these positive characteristics, along with the antenna simplicity, make this design the best choice for a detailed investigation
- Figure 68(b) shows the concept of loading the patch with a shorting pin and making it a $\lambda_g/4$ resonator. Shorting pin was found to work well if the height of the cavity was small. Increasing height diminished the effect of the shorting pin. As will be explained in this chapter, for thick cavities, waveguide TE modes are of most importance, and the shorting pin is affecting only the patch TM_{010} mode.
- Figure 68(c) shows the meandering technique. In the case of cavity environment, only the patch structure can be meandered. For thin cavities, the effect is analogous to the no cavity case. With increased height the patch remains miniaturized compared to a classical patch and it is possible to match the antenna with a pin feed. However, for the same aperture size and substrate, the antenna with a meandered patch has narrower bandwidth compared a classical patch. The reason for this effect on bandwidth will be explained in Section 2.4 (with transmission line models). Due to the objective of achieving good bandwidth performance, the meandering technique is eliminated form a detailed study in favor of classical patch and the material loading technique.
- Finally, lumped elements were eliminated due to the end application of the antenna which required reliability under high acceleration.

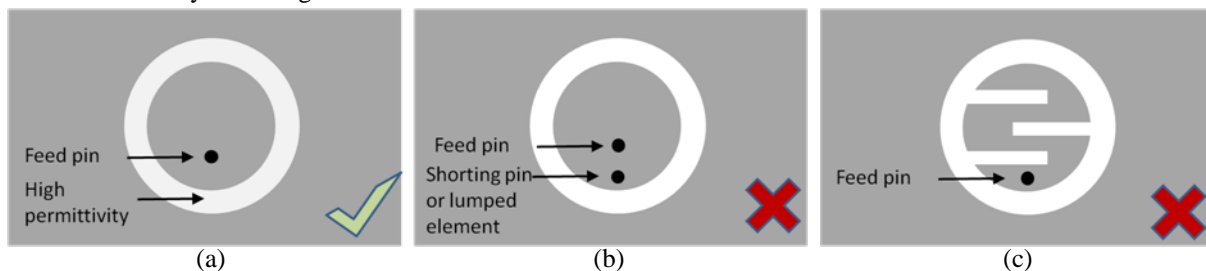


Figure 68 Investigated miniaturization techniques. (a) material loading, (b) shorting pin, (c) mantering.

One final note is that cavity enclosure can be considered as a miniaturization technique itself. Namely, when the cavity size is smaller than the calculated patch on the given substrate permittivities, the antenna will still resonate with a patch smaller than the cavity size. The strong capacitive effect between the patch and the wall allows.

Summary of bandwidth enhancement techniques for microstrip antennas applied in a small cavity environment

- Figure 69(a)-(d) shows several examples of achieving multiple resonances all suffering from the same drawbacks. With these design concepts, simulations at different heights showed that matching was possible only for very thin cavities. In this case the bandwidth broadening effect was not significant compared to what can be achieved with a simple patch in a thicker cavity.
- Figure 69(e) shows a stacked patches configuration with two patches. As in the previous examples, bandwidth broadening is achieved with two closely spaced resonances. The configuration is very simple and works even if cavity height is large. However, there are many restrictions. The two resonators must be loosely coupled. In general, this means the substrate between the patches has to be low, and larger distance between the patches is actually preferable (leading to higher cavities). Unfortunately, simulations have shown that in small cavities, having the aperture dimension smaller than $0.3\lambda_0$ the resonators are always tightly coupled. As a consequence, two resonances separate and there is no bandwidth broadening effect.
- Figure 69(f) shows material loading, and is the simplest technique broadening a single resonance of the antenna. However, in small cavities, when the aperture size is smaller than the corresponding patch size calculated in the case without a cavity, severe bandwidth reduction occurs. Detailed investigation of this design is shown in the remainder of the chapter.

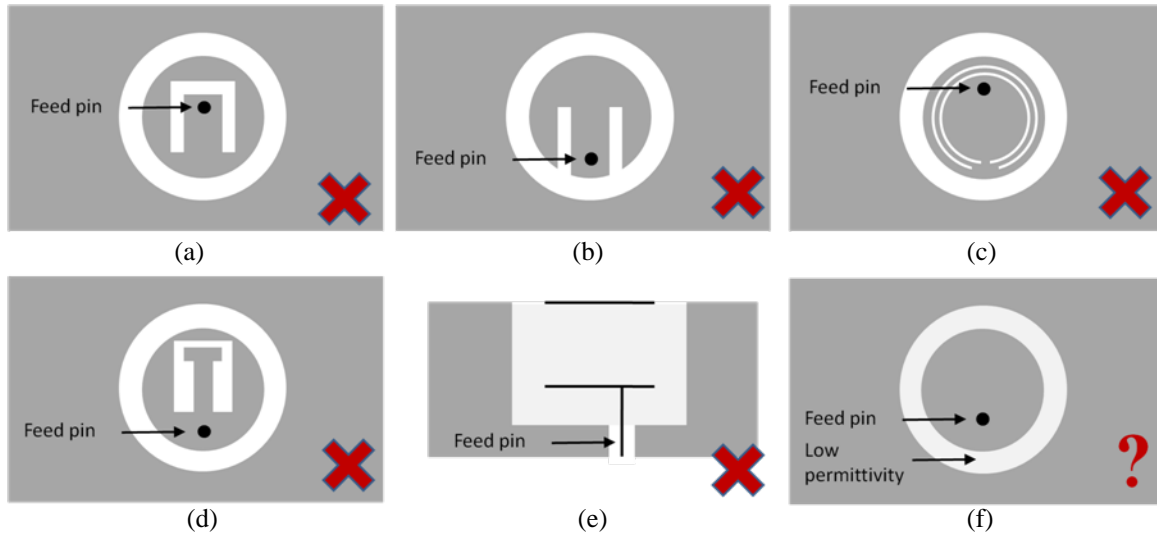


Figure 69 Schematics of bandwidth enhancement concepts. (a) U-slot, (b) E-shape patch, (c) stacked patches, (d) slot loading, (e) reactive loading, (f) material loading.

To conclude, upon considering the miniaturization and bandwidth techniques presented, we are left with a single option, i.e. the single patch in cavity filled with some substrate material. Based on the knowledge about classical patch antennas presented in introductory Chapter 1.2, it seems we are faced with opposite requirements on substrate permittivity (miniaturization vs. bandwidth increase). However, it is unclear how the cavity environment affects the antenna when height is increased. Can we draw the same conclusions we drew for the classical patch antennas without a cavity? What is the maximum bandwidth of patch antennas inside a cavity, how does it depend on the substrate inside, and how does it depend on the aperture size? These questions led to a detailed numerical study of the single patch configuration inside the cavity.

Particular interest was given to rectangular cavities and patches of square shape, for simplicity, and to circular shaped cavities for comparison.

2.1.1. Simulation procedure for single patch antennas in cavities

Before showing the simulation results the optimization procedure and goal is discussed. A schematic of the studied geometries (both for square and circular shaped cavities) is given in Figure 70. As the main interest is -10dB antenna bandwidth (or 10dB return loss) at 2.3 GHz, it was decided:

- To study the bandwidth behavior depending on the cavity height in discrete increments of $\Delta h = 1$ mm.

- To study the bandwidth dependence on permittivity, we chose $\epsilon_r = 3.66, 6.15$ and 10.2 which coincide with materials available for purchasing from Rogers inc. [3].
- To study the dependence on aperture size, example cavity sizes 20 mm ($0.15 \lambda_0$), 32 mm ($0.245 \lambda_0$), 40 mm ($0.3 \lambda_0$), and 48 mm ($0.37 \lambda_0$). In case of a circular aperture 50 mm ($0.38 \lambda_0$) was chosen for the last case.
- To study the ground plane effect, we chose to investigate an antenna embedded in an infinite ground plane, see Figure 70(a), and a finite ground plane, i.e. a cavity with walls of 5 mm thickness, as depicted in a schematic on Figure 70(b).

Thus for each cavity height h , for each example cavity size, and for each permittivity value, a separate optimization had to be made to match the antenna to 2.3 GHz . The variables for optimizing the resonance at 2.3 GHz were patch size p and feed position f_p .

Excitation in the simulations was done through a waveguide port attached to the bottom of the coaxial cable. The coaxial cable had a central wire 0.5 mm in diameter and was filled with Teflon ($\epsilon_r = 2.1$) having a 1.7 mm diameter, giving a 50 Ohm characteristic impedance.

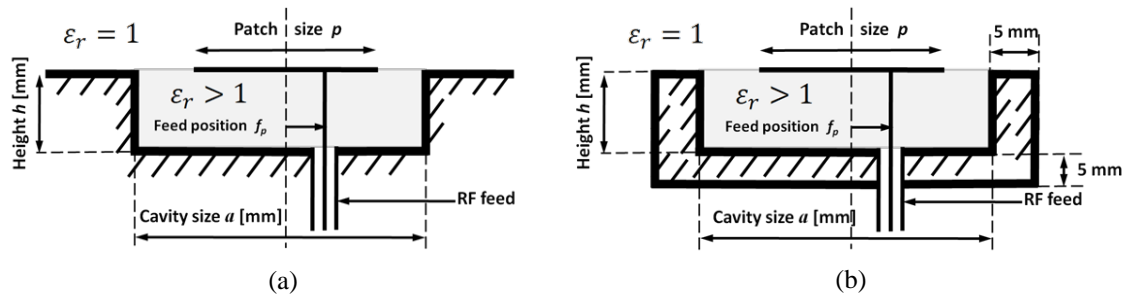


Figure 70 Schematic depiction of the single patch configuration chosen for a detailed study. (a) Configuration in an infinite ground plane. (b) Configuration in a finite ground plane with wall thicknesses of 5 mm on all sides. The schematics are valid for both square and circular shaped geometries

It is well known that a patch antenna can be perfectly matched for a specific patch size and feed position giving extremely low S_{11} values. Nevertheless, a reasonably good match at the same frequency is also possible for slightly different combinations of these two variables. Here, we specifically discuss this detail, i.e. tolerance in feed position and patch size. It is the belief of the author that the subtle effect of this tolerance needs to be understood. It is important in considering the optimization goals and errors in bandwidth determination.

Imagine that a patch antenna is resonant at 2.3 GHz and perfectly matched ($S_{11} = -\infty$) for a specific patch size p and feed position f_p . What is observed in simulations is that when a patch antenna is not perfectly matched at the resonant frequency, but only well matched, there are in fact two different ways in which this could happen. First option is with a smaller patch size ($p_1 < p$) and feed position closer to the center ($f_{p1} < f_p$). The second option is with a slightly larger patch size ($p_2 > p$) and a feed position slightly closer to the patch edge ($f_{p2} > f_p$). These two options, however, do not have the same bandwidth, and may lead to errors in bandwidth determination.

Example: This curiosity in patch antenna matching is depicted in Figure 71 for one antenna example (probed single patch antenna in a cavity of 32 mm size, 8 mm height, printed on a substrate of 10.2 permittivity and designed to resonate at 2.3 GHz). Figure 71 reveals that perfect match occurs near patch size $p = 16.5\text{ mm}$ and feed position $f_p = 3.8\text{ mm}$ from the center. Two circles on Figure 71(b) indicate the two options when the S_{11} parameter is only -25 dB , and Figure 71(c) shows the actual S_{11} parameter from simulation where it is obvious the two options do not have the same bandwidth. The second option is preferable in terms of bandwidth.

Additionally, it is observed in the bandwidth curve on Figure 71(b) that there exists an optimum bandwidth. In the example antenna, optimum bandwidth is observed for $p = 16.7$ and $f_p = 4.3\text{ mm}$ respectively. It can then be concluded that this can lead to an ambiguity in bandwidth determination. Specifically, for a non-perfect match there can be two optimization solutions, we may call them the local and the global optimum, giving a lower and a higher value of bandwidth. The difference in bandwidth at perfect matching and at maximum bandwidth exists for all patch antennas but is negligible when the substrate is thin. However, it becomes important for very thick antennas. For this reason the optimization goals have to be set carefully, and regardless of the interest in bandwidth, the perfect matching condition is more robust.

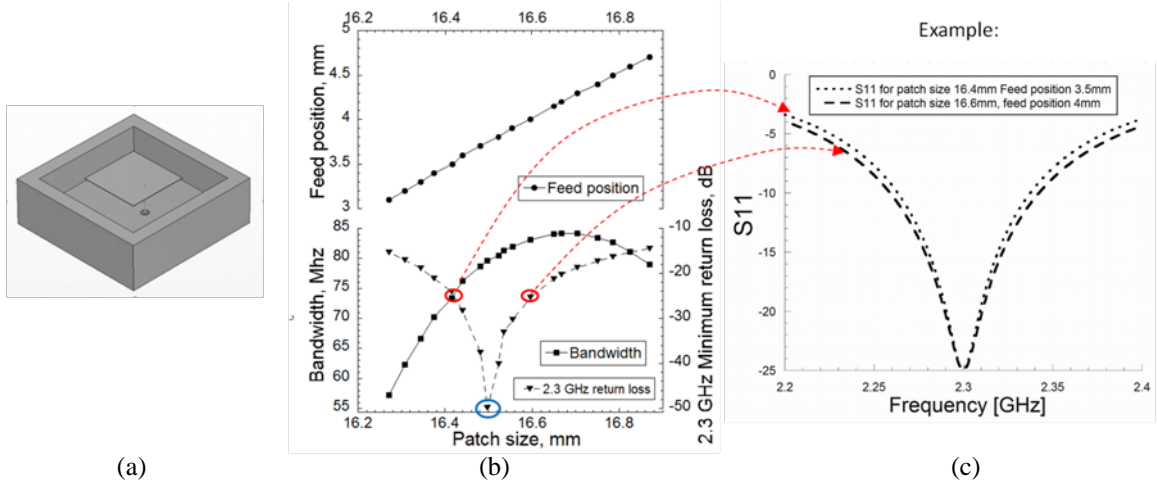


Figure 71: Example study of the matching tolerance. (a) The effect of patch size/feed position tolerance is depicted for one example antenna geometry i.e. a 32mm square cavity with 8mm substrate height and substrate permittivity 10.2 inside. (b) Plot showing the bandwidth and minimum S_{11} at the resonance, depending on patch size/feed position. There are two optimums – “perfect matching” noted by a blue circle, and maximum bandwidth (c) Example simulation result of S_{11} parameter when the antenna has 25dB return loss at resonance. Note that the bandwidth is not the same for the two curves.

Here we will briefly explain the behavior presented in Figure 71. We can start by looking at the patch as two transmission lines connected in parallel at the feed point (see Figure 15; transmission line model for patch antenna in Section 1.2.1 of Chapter 1). Termination of the lines is a high impedance (resistive and capacitive open end) in which case the input admittance of the lines is mostly imaginary and varies almost as a tangent function. The Q factor of antennas is proportional to the derivative of impedance (A 22), or equivalently, admittance as given by

$$Q_{Ant} = \frac{\omega_0}{2 G(\omega_0)} \left| \frac{\partial Y(\omega)}{\partial \omega} \right|_{\omega=\omega_0}, \quad (2.1)$$

where $G(\omega_0)$ is the conductance and $Y(\omega_0)$ is the total admittance at a specific frequency. The imaginary part of the total admittance is varying almost as a tangent function; it will have a lower derivative the closer the argument of the tangent function is to zero (short line) or to π ($\lambda_g/2$ line). Therefore, the admittance derivative decreases as the feed point moves closer to the edge and hence bandwidth in that case is higher. In the meanwhile, the real part of the admittance also varies as we move the feeding point; best matching condition can occur only at one point where the real part matches the characteristic impedance of the feed, not at the edge position.

2.1.2. Optimization goal

To standardize the simulations, all antennas were optimized to have a return loss larger than 35dB at 2.3GHz. According to Figure 71, this is close to the perfect matching condition, and thus robust enough to reduce the error in bandwidth determination. For simulations we used the frequency domain solver in CST Microwave Studio [130].

2.2. Bandwidth behavior of patch antennas in square cavities

Here we describe and compare simulation results for a rectangular (square) geometry. An example of the actual geometry simulated is shown in Figure 72 for two different ground plane cases. Additionally we compare the simulation results with results from Chapter 1.3.1 on cavity antennas. This is crucial, as we will see that the cavity antenna operation is a limiting case of patch antennas inside a cavity.

To better understand the results for various cases, and all the details on the graphs, one example was chosen and presented in full detail on Figure 73. The geometry with aperture size $a = 0.245 \lambda_0$ in a finite ground plane was chosen for it possesses all the important traits that appear in other results.

First, on Figure 73(a) the theoretical result for a cavity antenna of this size is presented. This curve is the same curve as on Figure 42 in Chapter 1.3.1 given for cavities in a finite ground plane. However, here we concentrate on a single size of the cavity and the potential bandwidth when the volume is filled with specific permittivity ($\epsilon_r = 3.66, 6.15$ and 10.2). Note that only a single point on the curve denotes a cavity antenna. A

cavity antenna requires specific combination of height and permittivity values. Additionally, there is no possibility of making a cavity antenna if the volume is filled with $\epsilon_r = 3.66$ as the waveguide is under cut-off.

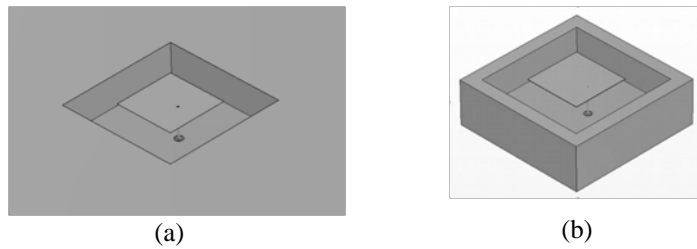


Figure 72: Simulation geometry for square cavity and patch in (a) an infinite ground plane and (b) in a finite ground plane, i.e. a cavity with wall thickness of 5 mm. Pictures taken from simulations in CST ($a = 32$ mm, $h = 8$ mm, $\epsilon_r = 10.2$). Dimensions are given in the schematic on Figure 71. .

Second, on Figure 73(b) we see the simulation results for a patch antenna inside the cavity. Main differences compared to the cavity antenna are that instead of a single point for a specific permittivity, we now have a curve for each permittivity value. However, points from the graph on Figure 73(a) are translated to Figure 73(b). Importantly, these points appear at the end of the bandwidth curves for patch antennas, i.e. above the maximum height where matching the patch antenna was still possible. As there is no point for a cavity antenna filled with $\epsilon_r = 3.66$, the curve for the corresponding patch antenna can actually extend indefinitely, but it was decided to present results up to a height of 40 mm.

Third, on Figure 73(c) actual pictures from simulations of the antennas for various heights are presented. This shows that the size of the patch is reduced as cavity height h is increased. In fact, for the cases of $\epsilon_r = 6.15$ and 10.2 the size reduces to zero (and is unmatchable), and thus the antenna turns into a cavity antenna. For the case $\epsilon_r = 3.66$ the size reduces but above some height remains at a fairly constant value.

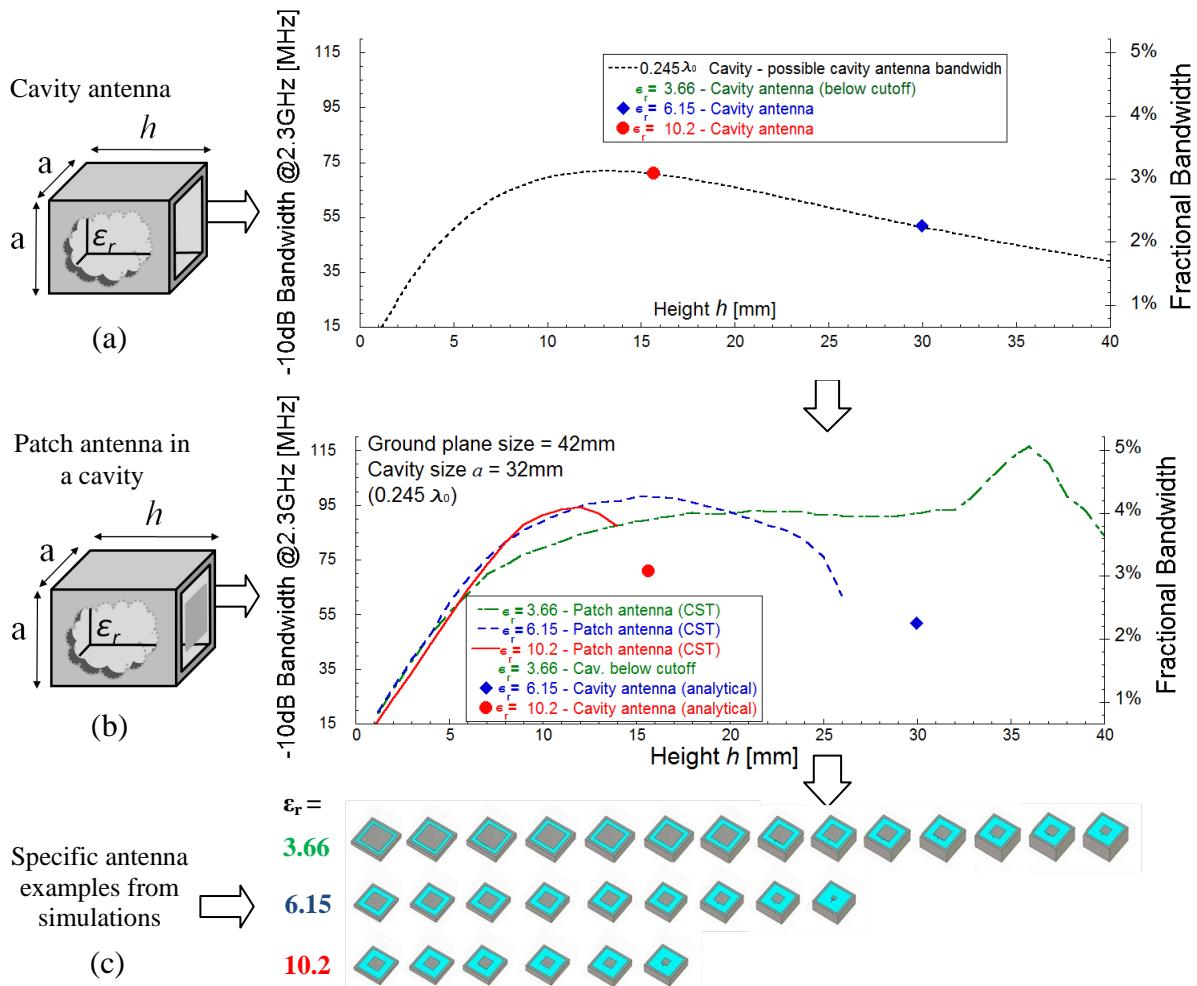


Figure 73 Detailed Example for a $0.245 \times 0.245 \lambda_0$ cavity aperture in a finite ground plane. (a) Analytical prediction for bandwidth of a cavity antenna. Line indicated a general bandwidth behavior that depends on ϵ_r , see Chapter 1.3.1. Points indicate specific cases when the volume is filled with $\epsilon_r = 3.66, 6.15$ and 10.2 . (b) Simulation results for -10 dB bandwidth of patch antennas in a cavity, along with the

points for the cavity antenna case. (c) Actual antenna geometries taken from CST. Due to lack of space, the CST pictures are presented for increments in height $\Delta h = 2$ mm.

In the further text, results will be presented in the form seen on Figure 73(b) above.

2.2.1. Simulation results

In Figure 74 all the simulation results for example cavity sizes are presented in two columns. In this way a direct visual comparison can be made between the infinite ground plane case (left) and a finite ground plane (right).

Note that (Rogers) materials used in the simulations included losses, with specifications given in Table 2.

It is also recommended to compare these results with the “no cavity” case presented in Chapter 1.2.3 on Figure 22(a) for bandwidth increase by increasing height. As mentioned, increasing substrate height enhances bandwidth, but the height is limited by surface wave generation, unwanted inductance and radiation from of the probe feed. For example, Figure 22(a) shows that a rectangular patch antenna is difficult to match (impossible with just a probe feed) for substrate thickness greater than about $0.11\lambda_0$. There is no such restriction when the patch is enclosed in a cavity.

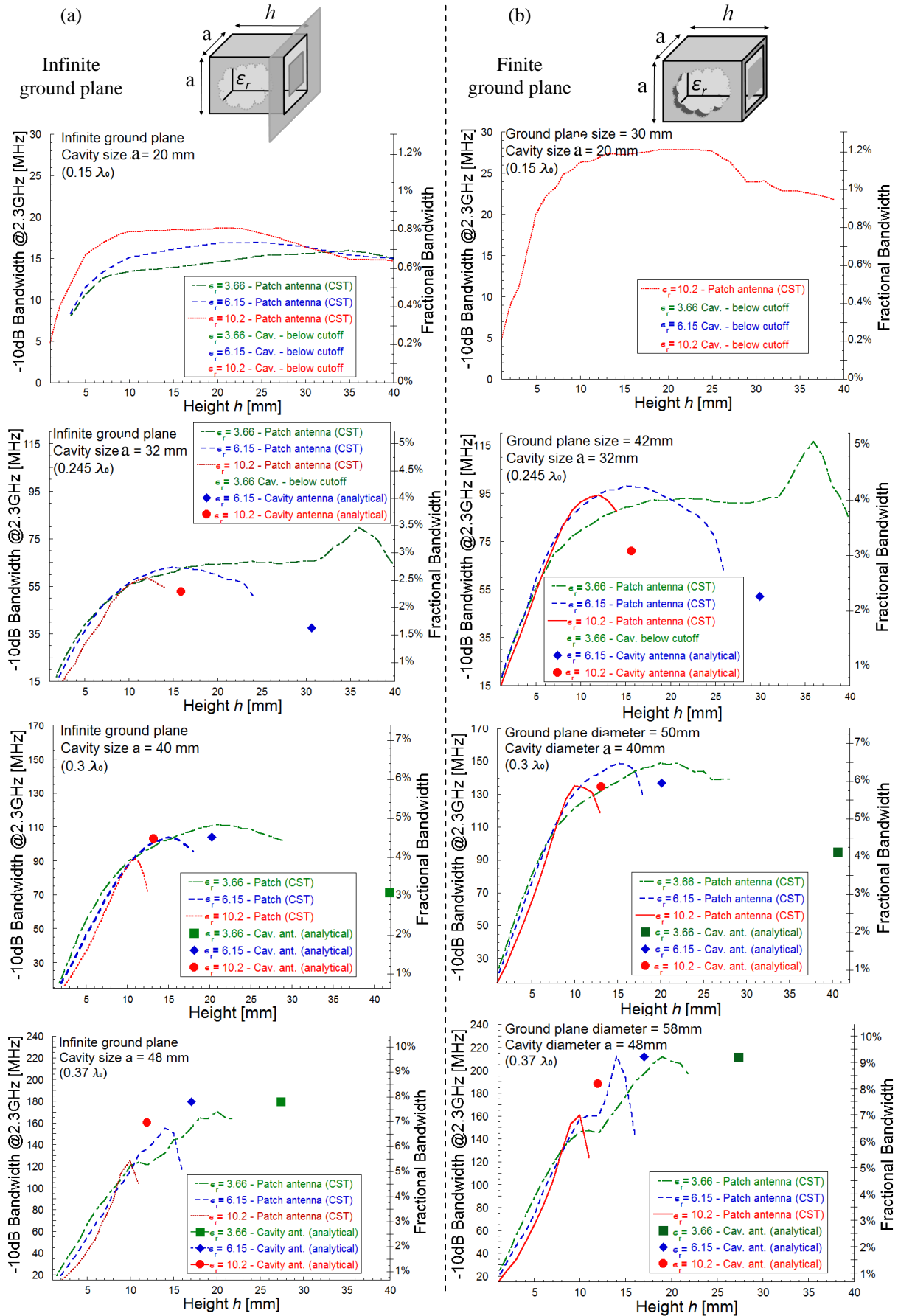
Contrary to a classical probe fed patch antenna without the cavity, when the probe is inside a small cavity, the walls act as a shield of a coaxial cable and help to establish a TEM mode. The cavity and the probe act as an off center coaxial cable, with a characteristic impedance different than 50 Ohms. The exact characteristic impedance is obtained numerically through a simulation. The establishment of the TEM mode inside the cavity is a major reason for the possibility to increase height beyond what is possible for classical patch antennas.

Furthermore, a classical probe fed patch antenna excites only its fundamental patch mode (TM_{010}), as discussed in Chapter 1.2.1. However, for thick substrates, the cavity represents a short part of a waveguide so the patch is also exciting the fundamental waveguide TE_{10} mode of the rectangular (square) waveguide. As will be seen in the following theoretical sections, this fact is crucial in the explanation of presented results. The “waveguide mode” allow us to increase the height further than is possible for classical patch antennas. It is also responsible for the gradual transformation of the patch antenna into a cavity antenna as was seen in the detailed example on Figure 73(c).

Our simulation results show that a cavity environment can quite dramatically change the aforementioned simple behavior rules of classical patch antennas (increasing substrate permittivity leads to patch size miniaturization and a decrease in bandwidth and increasing substrate height enhances bandwidth).

There are several observations on bandwidth behavior we make on Figure 74 that will be discussed in the further text, these are

- For very small cavities $a \lesssim 0,15 \lambda_0$ best results are obtained with the highest permittivity
- For larger cavities, with $a \gtrsim 0,15 \lambda_0$ we can recognize two regions in bandwidth behavior
 - Thin cavity ($h \lesssim 8$ mm) region where classical patch antenna behavior is observed
 - Thick cavity region ($h \gtrsim 8$ mm) where unusual phenomena occurs
- Inversed dependence of bandwidth on permittivity can be seen in part of the thick cavity region
- Unusual “bumps” in bandwidth curves are observed for some cases, for example the 32 mm cavity.
- For cavity sizes, bandwidth is higher in the finite ground plane case.



2.2.2. Effect of the cavity aperture size:

We notice that in a small cavity the maximum patch size is restricted by the size of the aperture, but the antenna can still be made resonant. For example, consider the 32 mm or 20 mm sized cavities in Figure 74. As mentioned, patch size depends on the substrate permittivity; low values leading to larger patch sizes. A classical rectangular patch without a cavity on a thin substrate of 3.66 would have a patch size p larger than 32 mm, however, inside the cavity, due to a large capacitive effect with the wall, patch size can be smaller than 32 mm, and the antenna resonant. Nevertheless, in such cases the patch covers the aperture almost completely, making the radiating gap between the patch and the wall very small, and bandwidth very narrow. Hence larger bandwidth is achieved with higher permittivity values, where the patch size is significantly smaller than the aperture.

Bigger aperture size allows for larger maximum bandwidth; however the exact relationship is not clear for patch antennas as it was for cavity antennas. What is observed in, for example Figure 74(a), for the example cavity sizes is that for sizes of 32 mm and 20mm patch antennas can achieve larger bandwidth than a cavity antenna, but for 40 mm and 48 mm patch antennas can be worse than cavity antennas.

In addition to larger maximum bandwidth, bigger aperture sizes reduce the maximum height where matching the antenna is possible, see the curve endings on Figure 74(a)-(b). Essentially, the geometry is approaching the no cavity case, for which the results can be found in Chapter 1.3.1.

We note that in the case of a large cavity ($a = 48 \text{ mm}$ ($0.37 \lambda_0$)) it was necessary to add a second wire in the center of the cavity and connect it to the patch to short out the TM_{11} waveguide mode that can be excited in thick substrates.

To summarize, we list the general conclusions as:

- Miniaturization effect: Cavity enclosure can be used to reduce the patch size, as the antenna is resonant even with very small apertures.
- Bandwidth effect: Size of the aperture dramatically affects bandwidth, but the relationship with bandwidth is not clear
- Height effect: Maximum cavity height reduces as the aperture size increases.
- Modes: In large cavities, unwanted, higher modes might be excited

2.2.3. Effect of cavity height:

The most important effect of increasing height is the transformation of the cavity into a short portion of a waveguide. Analogously the probe feed transforms into a portion of a coaxial line supporting a TEM mode, as it is shielded by the cavity. Energy inside the cavity is thus “guided” to the patch. Unlike classical patch antennas, there is no generation of surface waves by the patch, as the substrate is finite, and surrounded by walls forming the waveguide. For small and thick cavities, we can thus assume the energy from the TEM mode is coupled by the patch to excite the fundamental TE_{10} waveguide mode. Because of this efficient coupling to the TE mode, the cavity allows us to increase the antenna height further compared to classical patch antennas.

Electrical length of the waveguide supporting the fundamental TE_{10} mode is of crucial importance. In Figure 74, if the waveguide is above cut-off (indicated by the existence of a cavity antenna) we observe bandwidth curves have a maximum. These maximums appear as the waveguide length is approaching a quarter of the guided wavelength ($h \approx \lambda_g/4$). As λ_g is shorter for a larger permittivity value, the maximum occur at a lower height. If the a waveguide is below cut-off at 2.3GHz.

On the other hand, if the TE_{10} mode is under cutoff at 2.3 GHz another very interesting phenomenon is observed. In that case, height can be extended indefinitely. The TE mode energy inside the waveguide is evanescent, and not affecting the antenna if the height is large. Another interesting phenomenon is seen in the 32 mm sized cavity. We observe sharp bandwidth peaks or “bumps” in the curves, both in Figure 74(a) and (b). This phenomena is considered and explained the section on the modeling patch antennas in cavities.

For all cavity sizes we mention that the patch size decreases with height and the feed position moves closer to the edge. In fact, for a larger cavity size, the feed position moves to the edge at a certain height and then needs to be outside the patch, in which case a small microstrip extension was created to connect the feed and the patch. This crossing of patch boundary is seen in Figure 73(c). Increasing the height even further leads to diminishing patch sizes and we can say that the antenna is effectively becoming a cavity antenna described in Chapter 1.3.1.

To summarize, we list the general conclusions as:

- Waveguide effect: Increasing height transforms the cavity part of the antenna into a waveguide.
- Bandwidth effect: Maximum bandwidth occurs when $h \approx \lambda_g/4$, unless the waveguide is below cut-off
- Cavity antenna effect: Increasing height reduces patch size up to the maximum height, at which the antenna is operating like a cavity antenna, unless the waveguide is below cut-off.

- Bandwidth “bumps”: This unusual phenomena is explained by analytical models in the following Sections.

2.2.4. Effect of substrate permittivity:

The most important effect of substrate permittivity is on the operation of the waveguide part of the antenna, making the waveguide either above or below cut-off for the TE_{10} mode at 2.3 GHz. Information on the cut-off frequencies are given in Table 1. If the waveguide is above cut-off, the antenna is limited to a maximum height corresponding to cavity antenna operation. If the waveguide is below cut-off, height is not limited.

For cavities with $a \gtrsim 0,15 \lambda_0$ in Figure 74, we can recognize classical patch behavior for thin substrates ($h \lesssim 8$ mm), i.e. larger ϵ_r leads to a decrease in bandwidth and increasing substrate height enhances bandwidth. For thick substrates we can, most interestingly, observe a region where better bandwidth performance is achieved with a higher permittivity. This is contrary to regular operation of patch antennas, and will be referred to as “inversed bandwidth-permittivity relationship” region. Height of about 8 mm is usually the intersection point between the classical and inverse relationship region. of substrate height and this behavior is present until the curve for the highest permittivity reaches its maximum.

For very small cavities, $a \lesssim 0,15 \lambda_0$ the miniaturization effect is most important. As the cavity aperture is smaller than the regular patch size in the no cavity case, the patch covers the aperture area almost completely and bandwidth is severally reduced. Using high permittivity to make the necessary patch size smaller than the aperture size helps bandwidth performance in this case. In Figure 74(a) all three permittivity results are shown for cavity aperture size $a = 0,15 \lambda_0$. However, in Figure 74(b) for $a = 0.15 \lambda_0$ only the highest permittivity, $\epsilon_r = 10.2$, is shown as it gives the best bandwidth performance for all height values.

To summarize, we list the general conclusions as:

- Waveguide effect: Permittivity determines if the waveguide is below cut-off, and thus if there exists a maximum height of the antenna.
- Bandwidth effect: A region of inversed bandwidth-permittivity relationship is observed in all examples. For $a \lesssim 0,15 \lambda_0$ in the whole region, and for $a \gtrsim 0,15 \lambda_0$ in a region with $h \gtrsim 8$ mm

2.2.5. Effect of the ground plane

A direct comparison between Figure 74(a) and (b) clearly shows that a finite ground plane offers superior bandwidth in all examples compared to an infinite ground plane. This can be explained by considering just the radiation patterns of these two cases. The antenna in an infinite ground plane can only radiate into a half-space while the finite ground plane antenna radiates into the whole space. This additional radiation effectively increases the radiation loss and thus increases bandwidth. The exact amount of increase depends on the ground plane shape.

2.3. Bandwidth behavior patch antennas in circular cavities

Here we describe and compare simulation results for a circular geometry. An example of the actual geometry simulated is shown in Figure 75 for two different ground plane cases. Additionally we compare the simulation results with results from Chapter 1.3.1 on cavity antennas. As seen in the rectangular case, cavity antenna operation is a limiting case of patch antennas inside a cavity.

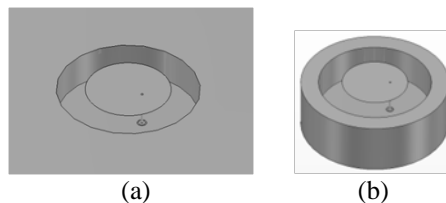


Figure 75 Simulation geometry for circular cavity and patch in (a) an infinite ground plane and (b) in a finite ground plane, i.e. a cavity with wall thickness of 5 mm. Pictures taken from simulations in CST ($d = 32$ mm, $h = 8$ mm, $\epsilon_r = 10.2$). Dimensions are given in the schematic on Figure 71.

To better understand the results for various cases, and all the details on the graphs, one example was chosen and presented in full detail on Figure 76. The geometry with aperture diameter $d = 0.245 \lambda_0$ in a finite ground plane was chosen for it possesses all the important traits that appear in other results.

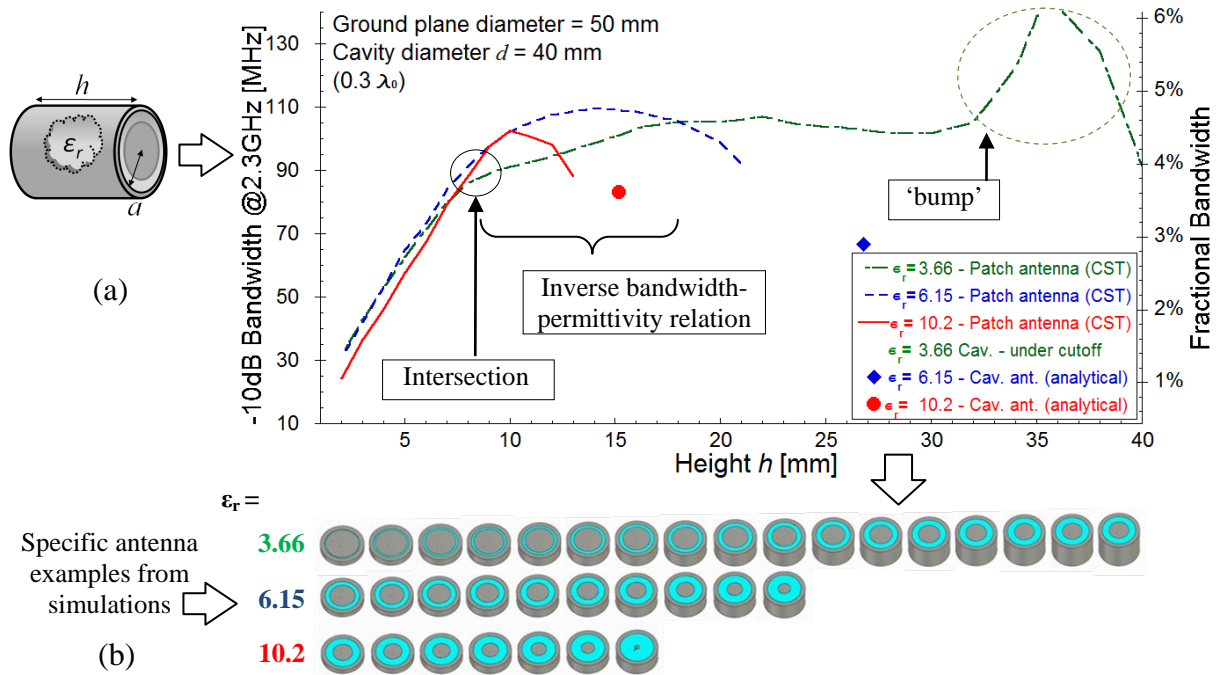


Figure 76 Detailed Example for a $0.3 \lambda_0$ diameter cavity aperture in a finite ground plane. (a) Simulation results for -10 dB bandwidth of patch antennas in a cavity, along with the points for the cavity antenna case. (b) Actual antenna geometries taken from CST. Due to lack of space, the CST pictures are presented for increments in height $\Delta h = 2$ mm.

First, on Figure 76(a) the theoretical result for a cavity antenna are placed in the same manner as for the rectangular geometry. Note that only the cavity filled with $\epsilon_r = 10.2$ is above cutoff and hence only one point is shown in this particular example.

Second, we see the simulation results for a patch antenna inside the cavity. Several, effects noticed in the rectangular case are noted in this example. The intersection point denotes the antenna height where the bandwidth-permittivity relation becomes reversed compared to classical patch antennas. In this particular example only the $\epsilon_r = 6.15$ and 10.2 curves intersect while the $\epsilon_r = 3.66$ curve is below them for all height values.

Third, on Figure 76(b) actual pictures from simulations of the antennas for various heights are presented. This shows that the size of the patch is reduced as cavity height h is increased. For the case $\epsilon_r = 3.66$ and 6.15 the size reduces but above some height remains at a fairly constant value. For the case of $\epsilon_r = 10.2$ the size reduces to zero (and is unmatchable), and thus the antenna turns into a cavity antenna.

2.3.1. Simulation results

In Figure 77 all the simulation results for example cavity sizes are presented in two columns. In this way a direct visual comparison can be made between the infinite ground plane case (left) and a finite ground plane (right).

Note that (Rogers) materials used in the simulations included losses, with specifications given in Table 2. It is also recommended to compare these results with the “no cavity” case presented in Chapter 1.2.3 on Figure 22(b) for bandwidth increase by increasing height. Analogously to the square case, our simulation results show that a cavity environment can quite dramatically change the simple behavior rules of classical patch antennas.

Conclusions about the behavior patches in circular cavities and the effects of various parameters are analogous to the rectangular case. For thick substrates, we can consider that the cavity represents a short part of a waveguide so the patch is no longer exciting only its fundamental mode but also the fundamental TE_{11} mode of the circular waveguide. If the TE_{11} mode is propagating (above cutoff) in the cavity, we can connect the appearance of maximums in the bandwidth curves when the electrical length of the waveguide is approaching a quarter of the guided wavelength. On the other hand, if the TE_{11} mode is under cutoff at 2.3 GHz another very interesting phenomenon is observed. In that case, height can be very large and we can see sharp bandwidth peaks or “bumps” on the curves (see in Figure 77 for $d = 0.15 \lambda_0$ and $0.245 \lambda_0$). All these phenomena are considered and modeled in the following section.

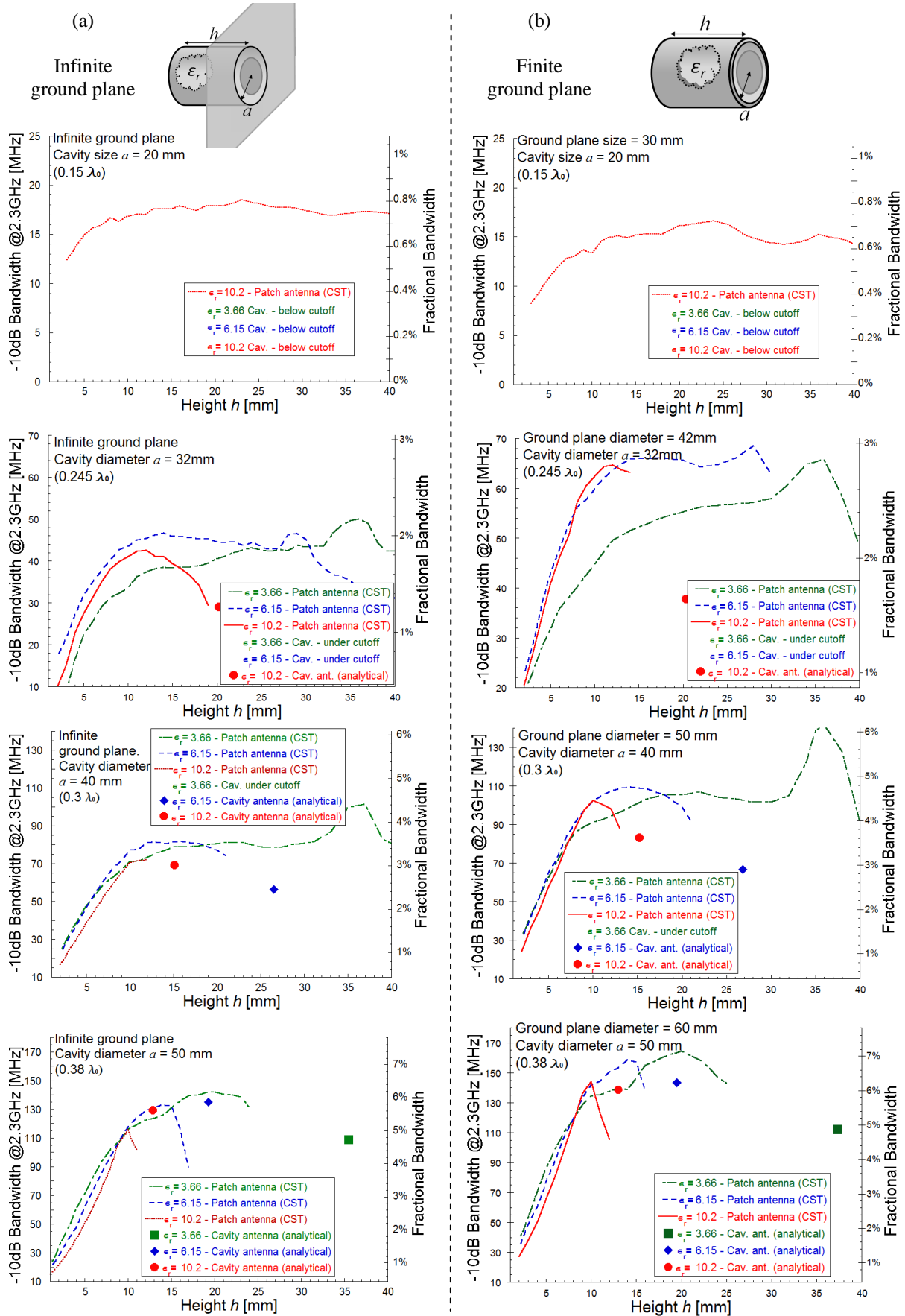


Figure 77 Simulation results for patch antennas in example cavity aperture sizes, $d = 20$ mm ($0.15 \lambda_0$), 32 mm ($0.245 \lambda_0$), 40 mm ($0.3 \lambda_0$), 48 mm ($0.37 \lambda_0$), and permittivity $\epsilon_r = 3.66, 6.15$ and 10.2 . (a) Infinite ground plane case. (b) finite ground plane case, i.e. cavity wall thickness is 5 mm.

Analogous to the rectangular case, there are several observations on bandwidth behavior we make on Figure 74:

- For very small cavities $d \lesssim 0,245 \lambda_0$ better results are usually obtained with the higher values permittivity
- For larger cavities, with $d \gtrsim 0,245 \lambda_0$ we can recognize two regions in bandwidth behavior
 - Thin cavity ($h \lesssim 8$ mm) region where classical patch antenna behavior is observed
 - Thick cavity region ($h \gtrsim 8$ mm) where unusual phenomena occurs
- Inversed dependence of bandwidth on permittivity can be seen in part of the thick cavity region
- Unusual “bumps” in bandwidth curves are observed for some cases, for example the 20 and 32 mm cavity.
- Interestingly, the 20 mm cavity in an infinite ground plane displayed higher bandwidth than a finite ground plane. The reason was later determined to be due to losses. In a lossless case the finite ground plane case has larger bandwidth. Losses are affecting performance more significantly if the gap between the patch and the cavity wall is small, and this gap is smaller in the infinite ground plane case. For other cavity sizes, bandwidth is higher in the finite ground plane case.

2.4. Proposed model for patch antennas in cavities

Is it possible to describe the bandwidth behavior presented in this chapter in a similar manner as simple cavity antennas from Chapter 1.3.1? In this section we will make several assumptions and approximations that lead to a simplified model which can offer a qualitative understanding of two effects i.e. inversion of bandwidth dependence on permittivity and the “bumps” that occur at large heights in cavities operating under cutoff.

A. MODEL EXPLAINING INVERSED BANDWIDTH-PERMITTIVITY RELATION

For a thin substrate, a patch antenna excites the TM_{010} mode and the correct transmission line model for a patch antenna was given in Chapter 1.2.1 on Figure 15. However, when the substrate is high, a patch can excite the fundamental TE mode of the cavity, the same mode assumed to exist in cavity antennas. Compared to an open-ended aperture from a cavity antenna, a patch at the aperture will change the aperture admittance. Nevertheless, we will make the assumption that the patch can be modeled as a circuit connected in parallel to the aperture admittance, and keep the aperture admittance unchanged. The idea for a circuit comes from considering the fields around the patch, i.e. strong electric fields exist between the patch and the cavity wall, which can be modeled with capacitors, and a current flowing on the patch surface creates a magnetic field which is modeled by an inductor. The complete model is a simple modification of the cavity antenna model and is shown in Figure 78.

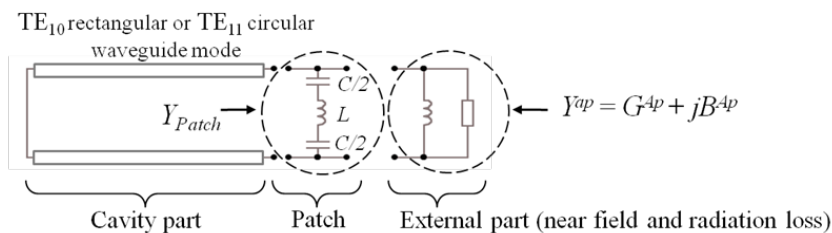


Figure 78: Transmission line model of a cavity with a patch at the aperture. The patch is modeled by a series resonant circuit in parallel to the aperture admittance. We should note that the model is reasonable for thick cavities with aperture sizes smaller than half the free space wavelength.

Considering Figure 78 model from a circuit perspective, we are lead to the following conclusions; assuming the waveguide (cavity part) is shorter than $\lambda_g/4$, it presents inductive admittance; aperture admittance (external part) is also inductive; thus the series LC resonant circuit representing the patch needs to be capacitive to counteract the inductance from the cavity and the external part, and bring the whole structure into resonance. To be capacitive, the series resonant LC circuit must operate below its series resonance frequency. In practice, this means the inductance value L is low, making the series resonance frequency high.

In small aperture sized cavities, the gap between the cavity wall and the patch antenna is very small, making the capacitive effect strong. Therefore, small changes in patch size are strongly affecting the capacitor values in Figure 78, while we can assume the inductance value L is only slightly affected. Resonance is thus achieved by adjusting the patch size. Furthermore, resonance can be adjusted for different heights as the patch size can always be made large enough (i.e. gap to the cavity wall small enough) for the capacitive effect to counteract the inductance added by the waveguide (cavity) and the external part. However, if the waveguide is above cutoff, its input admittance varies as a cotangent function; it is changing from inductive to capacitive reactance with

increasing height. If the input admittance into the waveguide is capacitive, then the necessary capacitance added by the patch decreases. This leads to a reduction of patch size with height, discussed in our simulations results. The antenna is, effectively, approaching the behaviour of an open ended cavity antenna, i.e. with no patch at the aperture. If the waveguide is below cutoff, its input admittance is always inductive and tends to a constant value as height increases (for example see the input admittance plotted on Figure 34(b) for a cavity with $a = 32$ mm and $\epsilon_r = 3.66$). This leads to a fairly constant patch size with large height and the possibility to increase height indefinitely.

The resonance condition for the model in Figure 78 can be written as

$$jB^{Ap} - j\frac{k_{TE}}{k\eta_0} \cot(k_{TE} h) + \frac{1}{\frac{1}{j\omega C} + j\omega L} = 0, \quad (2.2)$$

Where k_{TE} and B_{Ap} depend on the particular cavity type under investigation. The problem with (2.2) from the analysis point of view is that it presents one equation with too many variables, namely height h , relative permittivity ϵ_r , capacitance C , and inductance L . Compared to cavity antennas, we can regard height h as a function $h(\epsilon_r, C, L)$. Capacitance C can now be treated as the main variable responsible for resonance, while relative permittivity can be regarded as a given parameter, but that still leaves L as an unknown. The value of L could in principle be obtained from the patch geometry through some analytical technique or simulation. However, this would be a difficult task and would not lead to any further insight. Here we wish just to use the proposed model to explain the phenomena seen in our simulation results.

Example: let us take L as just a parameter, just like ϵ_r and treat the height as a function of capacitance $h(C)$ only. To demonstrate the predictions of bandwidth behavior from the model in Figure 78 we use (2.2) along with (1.59) and (1.62). We show an example bandwidth vs. height result in Figure 79 for a rectangular cavity of size 32 mm and the example permittivity values. We will assume the value for $L = 7$ nH in the three permittivity cases. The value of capacitance C varies as height is increased, and is mostly in the range of a few pF. The model predicts bandwidth curves extending to the maximum height, depicted with points, corresponding to cavity antenna operation, where the necessary C is zero. Two regions are noted in Figure 79(b); thin cavity region where the model is obviously not predicting the correct behavior due to ignoring the TM_{010} patch mode, and the thick cavity region where the behavior can be said to have similarities with simulation results in Figure 74.

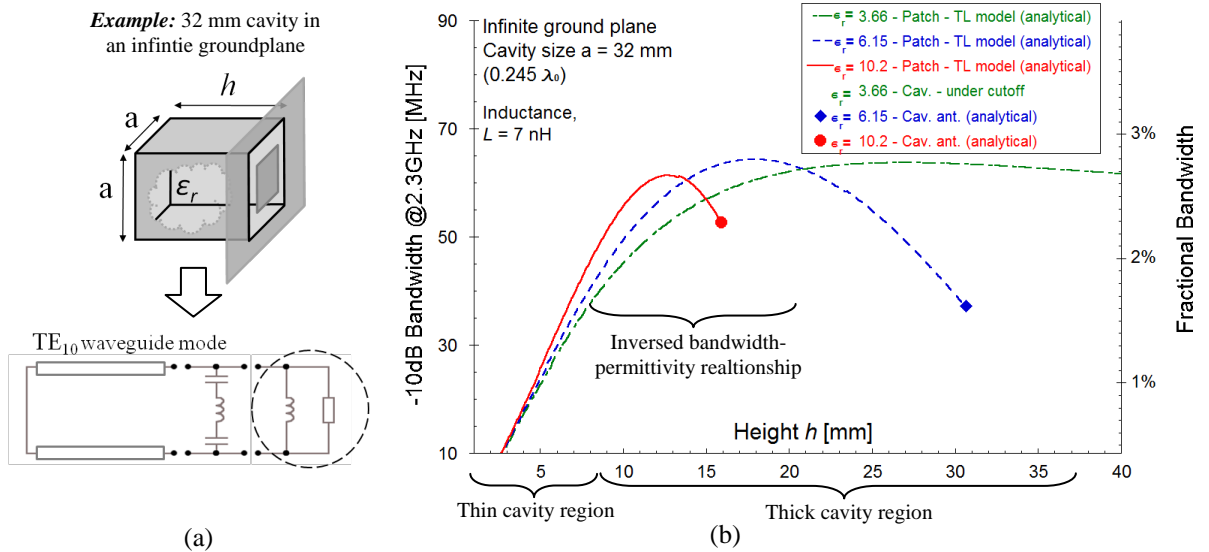


Figure 79 Qualitative analytical predictions. (a) The model used to calculate bandwidth behavior. (b) Analytical results shown for the example permittivity values. The value of inductance L was assumed to be 7 nH in all three cases of permittivity values.

To demonstrate the dependence of bandwidth on inductance L specifically, we can investigate the bandwidth behavior for several values of L . This is shown in Figure 80.

What is observed is that the model is able to predict the inversion of bandwidth dependence on permittivity. The extent of this phenomenon as well as the maximum bandwidth depends on the value of the inductance L . For lower inductance values, the phenomenon disappears and the maximum bandwidth is much higher. This is the most important conclusion gained from the model.

The reason for this behaviour is understood by considering again formula (2.1) for bandwidth calculation. Since the bandwidth of the whole structure is proportional to the derivative of the total admittance, we must consider the frequency dependence of the series resonant circuit. If there was no inductance L in the series circuit

then the admittance would be just a linear function $j\omega C$, and the derivative a constant. However, with the introduction inductance the admittance of the series circuit varies faster than a constant. This automatically increases the Q factor and reduces bandwidth. Additionally, the waveguide part also plays a role as its admittance variation depends on the permittivity inside it. In fact, the inductance value added by the waveguide is largest for low permittivity, when it is evanescent. Thus evanescent and low permittivity filled waveguides call for a larger capacitance added by the series resonant circuit. As mentioned, the variation of the series circuit admittance is faster than a constant, but also increases with larger values of capacitance. Again, this leads to increased Q factor for such cases, and in turn to the bandwidth inversion phenomenon. Another note to be made is that for waveguide above cut-off, the admittance derivative will be smallest when the shorted transmission line has electrical length of $\pi/2$ ($\lambda_g/4$ guided wavelength). This corresponds to the maximum seen in the bandwidth cure predictions.

The assumption of a fixed inductance value for all permittivity cases is of course very crude, but the purpose here was to show that the simple model allowed explaining the physical reason for inversion the bandwidth.

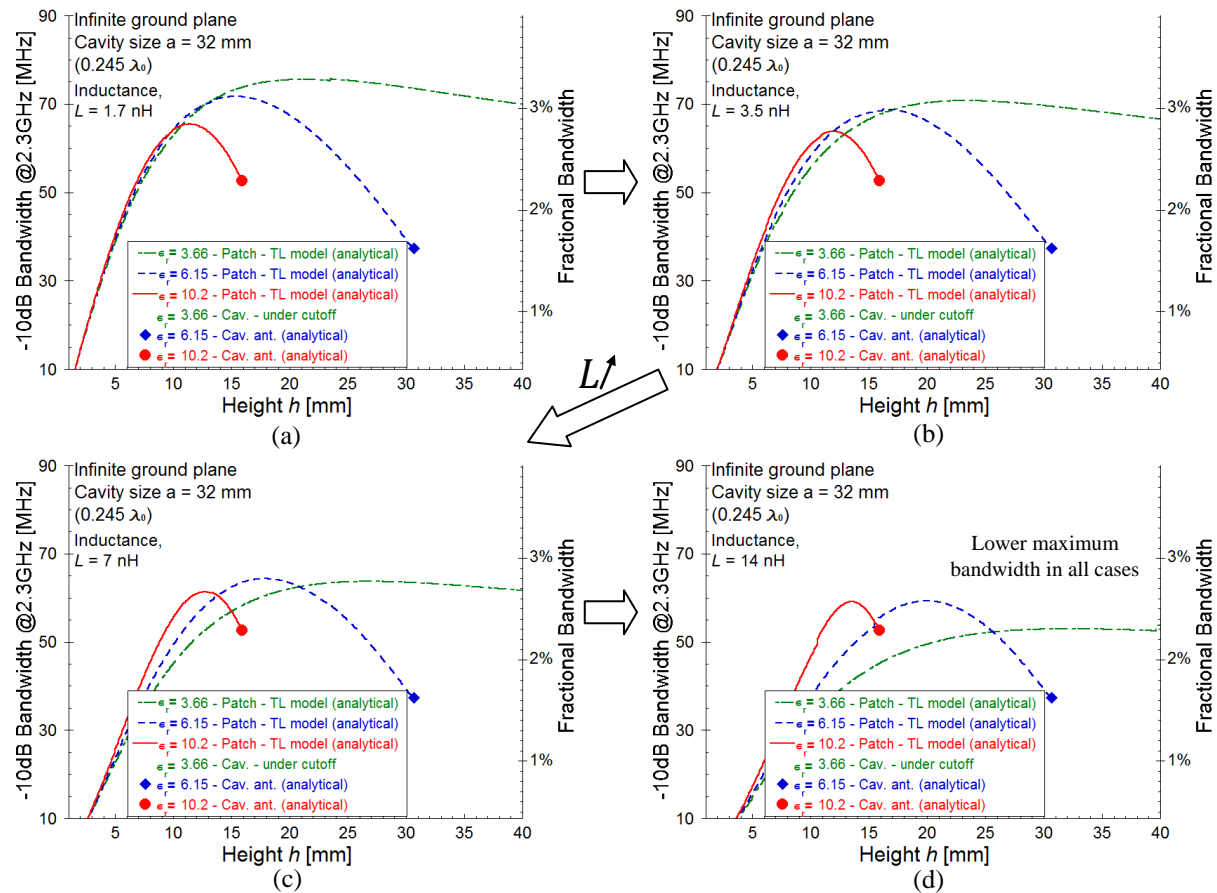


Figure 80 Predicted bandwidth behavior as the series resonant circuit inductance is increased. (a) $L = 1.7$ nH (b) $L = 3.5$ nH (c) $L = 7$ nH (d) $L = 14$ nH

Upon discussing the role of inductance L , and seeing its effect on bandwidth in Figure 80, we can better explain why the meandered patch antenna was eliminated from a detailed study. Understanding that the meandering technique effectively prolongs the current path in the patch, and thus increases energy stored in the magnetic field we can immediately conclude that this design would lead to an increased value of L compared to a classical patch. The comparison between the two designs and models is shown in Figure 81. The meandered patch is expected to produce stronger bandwidth inversion phenomena, but also reduced overall bandwidth performance. Due to this second reason it was not considered for further study.



Figure 81 Problematic of meandered patch antennas. (a) regular patch antenna at the aperture of the cavity. (b) meandered patch antenna at the aperture and the model havin increased inductance compared to the regular case.

B. MODEL EXPLAINING BANDWIDTH BUMP PHENOMENON

The proposed model in Figure 78 cannot account for the “bumps” in bandwidth curves in the cases of cavities operating below cutoff. To remedy this drawback, we need to also model the feeding part of the antenna. The wire probe and the circular cavity form an off-centered coaxial cable supporting a coaxial TEM mode. The characteristic impedance and propagation constant of such an off-center “coax” can be obtained through simulation or approximate analytical methods. As presented in Figure 82, an additional transmission line with the same length as the cavity height is attached to one of the capacitors in the model. This position for the connection is justified by the fact that the feeding probe is in fact very near the edge of the patch when the cavity is thick. The values of the two capacitors in the model are now different, denoted by C_1 and C_2 (the value of capacitor with the attached line C_2 being much larger).

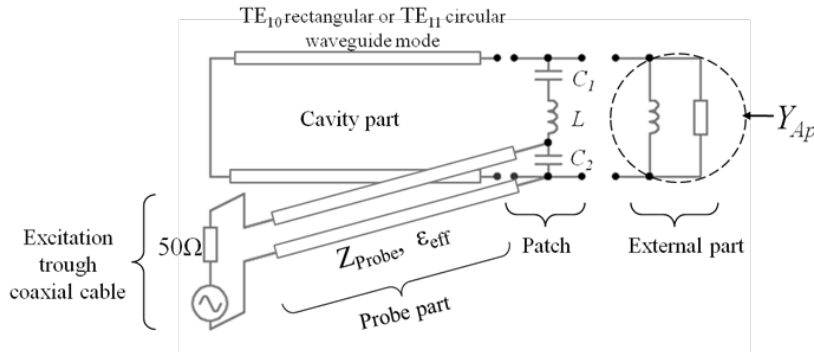


Figure 82 Model including the feeding part of the antenna; the 50 Ohm coaxial cable coming to the ground plane of the cavity and the central wire enclosed by the cavity forming a second part of the coaxial line. Both the waveguide and probe transmission lines have length h .

The added “probe” transmission line brings in fact an additional load (resistive and reactive) because the feeding line can be replaced with its input impedance seen from the capacitor towards the generator. At $\lambda_{g(\text{probe})}/4$ length the “probe” line transforms the 50 Ohm termination into a much higher real value that does not affect the structure significantly. At $\lambda_{g(\text{probe})}/2$ the termination is transformed again to a real value of 50 Ohms which constitutes an additional loss mechanism, giving rise to higher bandwidth. As mentioned earlier, if the waveguide part of the antenna structure is below cutoff then the height can be increased indefinitely. In such a case, the height where the “probe” line is $\lambda_{g(\text{probe})}/2$ is achievable and its effect noticeable.

Figure 83 presents the calculated bandwidth using the model in Figure 82. By comparing to Figure 79, the difference is seen as the “bump” in the case of the cavity filled with a permittivity of 3.66 (and is thus below cutoff).

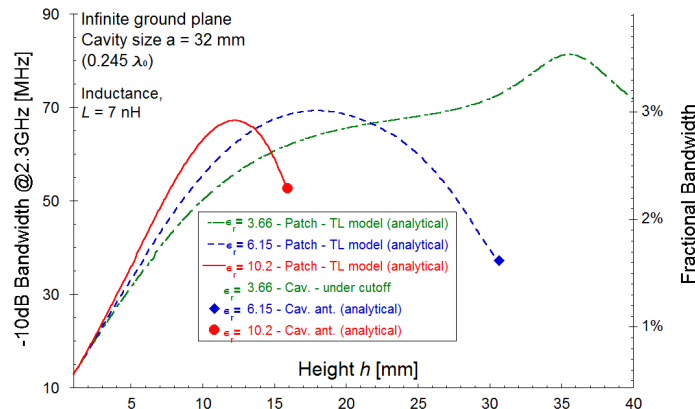


Figure 83 Qualitative analytical predictions using the model in Figure 82. The value of inductance L was estimated to be 7nH in all three cases of permittivity values. The “bump” is visible at height about 35 mm which is similar to the simulation data.

2.5. Measurement results

Unusual results about patch antennas in cavities include the case of obtaining the same bandwidth with different permittivity values in the cavity volume or even more surprising, obtaining higher bandwidth with a higher permittivity. In order to confirm the unusual result that cavities filled with different substrates can have the same bandwidth, two prototypes were manufactured at the French-German Research Institute of Saint-Louis.

It was decided that the simulations of the 32 mm cavity diameter in a finite ground plane, seen on Figure 77, are of particular interest. Especially the point on the plot where simulations showed the same bandwidth for a

cavity filled with $\epsilon_r = 6.15$ and $\epsilon_r = 10.2$, occurring at about $h=12$ mm. Therefore, prototypes were constructed using Rogers 3006 and Rogers 3010 materials.

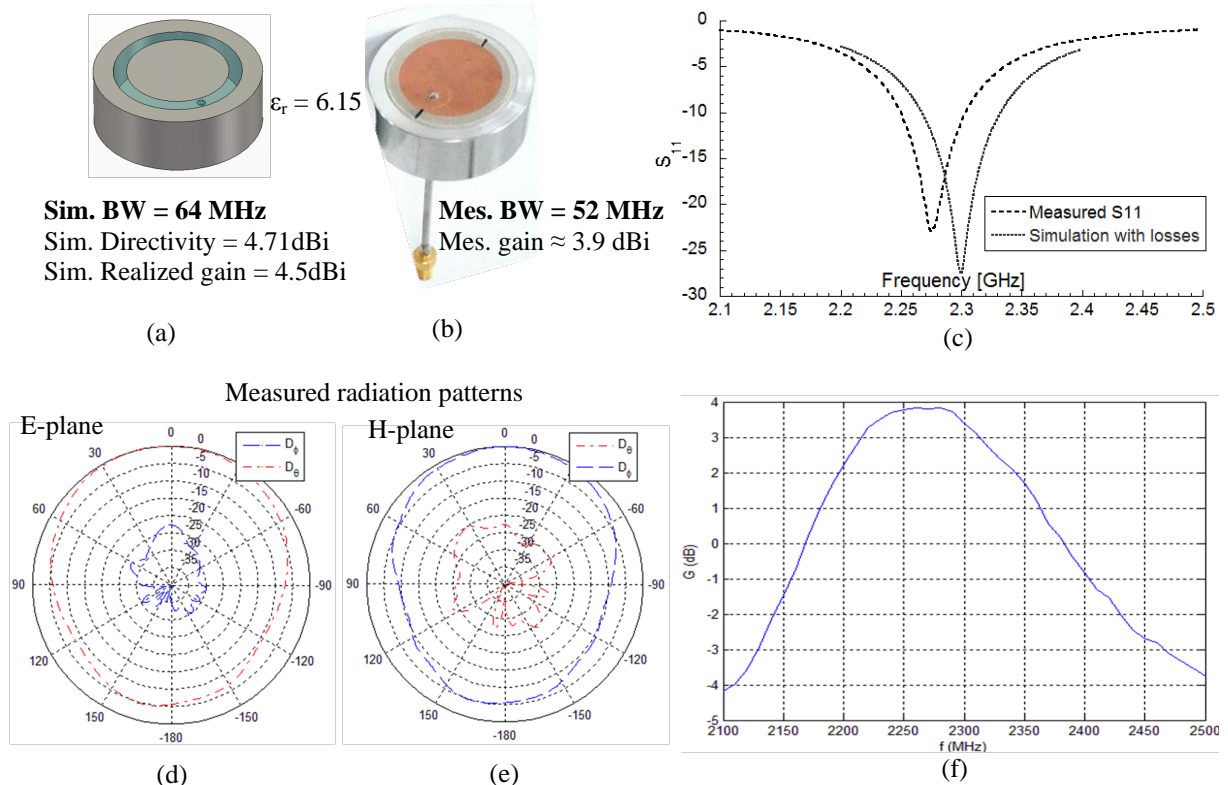


Figure 84 Prototype 32 mm ($0.25\lambda_0$) diameter, classical patch antenna in a cavity filled with $\epsilon_r = 6.15$. (a) Simulation results and geometry upon which the prototype was built. (b) The manufactured prototype. (c) Comparison of simulated and measured S_{11} parameter. (d) Measured radiation pattern in the E plane and (e) in the H plane. (f) Measured gain vs. frequency.

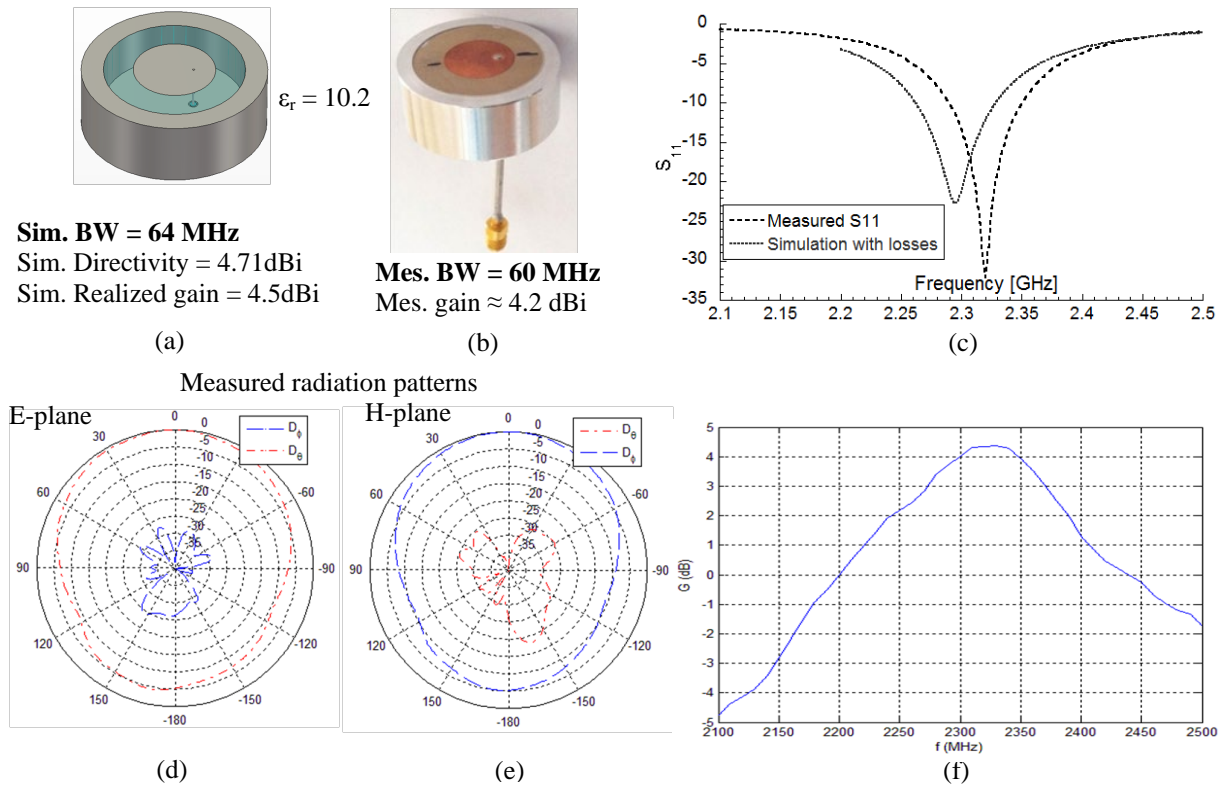


Figure 85 Prototype 32 mm ($0.25\lambda_0$) diameter, classical patch antenna in a cavity filled with $\epsilon_r = 10.2$. (a) Simulation results and geometry upon which the prototype was built. (b) The manufactured prototype. (c) Comparison of simulated and measured S_{11} parameter. (d) Measured radiation pattern in the E plane and (e) in the H plane. (f) Measured gain vs. frequency.

Construction of the prototypes proceeded in the following way: in both cases, 9 layers with 1.28 mm thickness each were glued together to form a substrate of 11.52 mm height. Metallization of the patch was etched on the top layer. A hole for the probe was drilled in the substrate and it was then glued with the cavity and the probe soldered to the patch. The cavity was an aluminum cylinder with a 32 mm diameter hole of 11.5 mm height.

Simulation results predicted 65 MHz bandwidth in both cases. Measured results are not in perfect agreement with simulations. Issues with the manufactured antennas are a slight difference in height and uncertainty in the exact value of the permittivity. Both issues can slightly shift the resonance frequency. In the end, what is observed from the measurements is that higher bandwidth was achieved in the $\epsilon_r = 10.2$ case.

2.6. Conclusion of chapter 2

Bandwidth of classical patch antennas is reduced by increasing substrate permittivity, however, by surrounding the patch with metallic walls, thus creating a short waveguide, this dependence can be reversed at a larger height and best performance can be achieved with highest permittivity. We have named this phenomenon the inversed bandwidth-permittivity relation and explained it with a simple transmission line model. Still, height of a patch antenna in a cavity cannot be increased indefinitely, bandwidth reaches a maximum for a certain height, then drops off and matching the antenna soon becomes impossible with our design. The maximum depends on the cavity size and the permittivity inside.

To explain the reasons for observed phenomenon, simple transmission line models were introduced to describe and analyze the bandwidth behavior. These transmission line models provide insight for understanding why the bandwidth curve has a maximum at a certain height. Furthermore, the model can account for the inversion of bandwidth dependence on permittivity and show that, in cavities representing waveguides below cutoff, the observed “bumps” in bandwidth curves are a consequence of the feeding part of the antenna. The proposed models give, at present, just qualitative insight, and are not sufficiently precise for giving quantitative results and accurate predictions.

Chapter 3.

Bound on Q and bandwidth for cavity antennas

In this chapter we aim to present the bound on minimum Q in the case of cavity antennas of rectangular and circular shapes. Section 3.1 discusses the inadequacy of the Chu bound and motivates the need for the Gustafsson bound. Section 3.2 describes how the more general, scattering approach can be applied to cavities in infinite ground planes and gives an exact formulation of the problem. Sections 3.3 and 3.4 use the presented formulation to derive the precise bounds for rectangular and circular cavities respectively. Section 3.5 discusses the validity of the newfound bound in the presence of antennas or objects inside the cavity. Finally, Section 3.6 gives an alternative way of arriving at the same bound giving, perhaps, more insight into the whole matter.

3.1. Motivation for a precise bound

The concept of physical bounds on Q for electrically small antennas was discussed in Chapter 1, and two approaches for deriving the bounds have been presented. For the first, spherical mode expansion approach, it was demonstrated that an inherent assumption in the bound is an imaginary sphere circumscribing the antenna. If all fields are zero inside the sphere the Chu bound is derived; if the fields are non zero, a higher, Thal bound is derived. These bounds are very general, and in fact, due to the assumptions, only spherical antennas can come close to these bounds.

In the case of a cavity it is not clear how this approach should be applied. Some puzzling questions are:

- Should the sphere size depend on the aperture of the antenna or on the whole cavity?
- What spherical mode has to be considered, TE or TM?
- Should the whole structure be circumscribed if the cavity is in a finite ground plane?

Regarding the first question; Figure 86(a) shows a demonstration of how the Chu sphere could be imagined to take into account only the aperture size of a cavity antenna, disregarding what might be present inside the volume of the cavity and its length. A circular cavity was chosen for it best fits the shape of a sphere.

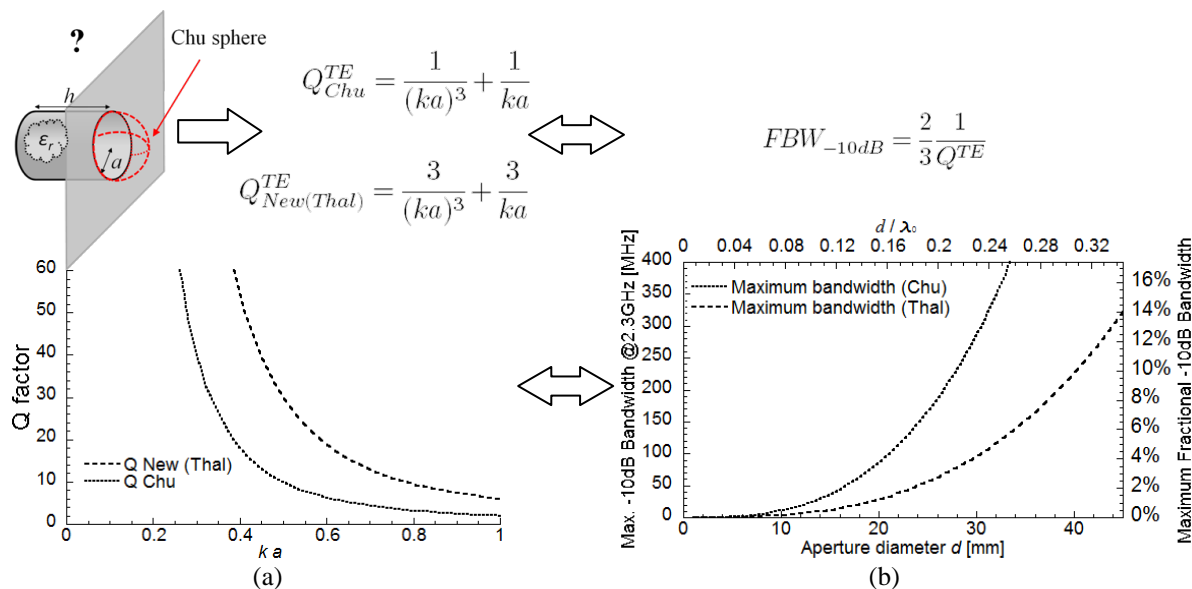


Figure 86 (a) Placement of the smallest circumscribing sphere in the case of a circular cavity aperture and the corresponding Chu and Thal limit. (b) calculated fractional bandwidth from the Chu and Thal limits, presented vs. aperture diameter d .

Regarding the second question; for a cavity radiating broadside, like cavity antennas and patch antennas in a cavity, we saw that the cavity is excited with the fundamental TE mode. From this fact, it follows that in the case of the Chu or Thal limit, we should also consider the limit for the TE spherical mode. Figure 86(b) shows also the predictions for bandwidth of the Chu and Thal bound. It is observed is that the Chu limit predicts ridiculously

large values compared to what was observed in simulations with patch antennas. The Thal bound is also giving large values, 2 to 3 times bigger compared to simulations with patch antennas. The comparison is given in Table 8.

For the third question, it is hard to give an exact answer, because enlarging the sphere would drastically reduce the Q factor while, as we saw in Chapter 2.2-3, bandwidth results for finite ground planes are not dramatically different compared to infinite ground plane.

We can conclude that the spherical mode expansion technique is too crude to be applied to the problematic of cavity antennas, and gives unrealistically large predications. It cannot account properly for the shape of the cavity aperture and the volume inside. For this reason we turn to the second, scattering approach leading to a new set of isoperimetric bounds introduced by Gustafsson *et al.* The main advantage of the new bound is that it holds for arbitrary geometries, and is thus applicable to the problem of a cavity, which is a finite scatterer, linear, time invariant, causal and reciprocal. The goal is to find a precise, realistic bound for cavity antennas and determine the utility of patch antennas.

Circular cavity size	FBW_{Patch} (from simulations)	FBW_{Thal} (predicted)	FBW_{Chu} (predicted)	$\frac{FBW_{Patch}}{FBW_{Thal}}$	$\frac{FBW_{Patch}}{FBW_{Chu}}$
20 mm	0.6 %	1.25 %	3.7 %	2.08	6.17
32 mm	2.1 %	4.9 %	15 %	2.33	7.14
40 mm	3.5 %	9.8 %	29.5 %	2.8	8.43
50 mm	6 %	19.2 %	57.5 %	3.2	9.58

Table 8 Comparison of simulation data for circular cavities in an infinite ground plane to theoretical predictions given by the Chu and Thal bound.

3.2. Scattering approach applied to cavity antennas

In chapter 1.1.3, we introduced the Gustafsson limit through the forward scattering analysis of antennas. The method was originally applied to wire and metallic structures in open space [26]-[27], we extend it here to aperture and cavity antennas. The new bound on the minimum achievable Q factor of a linearly polarized antenna is given as follows

$$Q_{min} = \frac{2 \pi D}{\eta k^3 \gamma}, \quad (3.1)$$

where k is the free space wave number and D the antenna directivity. η represents the ratio of absorbed power to the sum of absorbed and scattered powers, called absorption efficiency. For well matched minimal-scattering antennas one can take $\eta = 0.5$, and we will assume this value throughout the thesis. Finally, γ is the total polarizability of the receiving antenna considered as a scattering object.

According to (3.1), Q_{min} is proportional to the antenna directivity D which is a familiar antenna parameter and its calculation in the case of rectangular and circular cavities is given in **Appendix C** and **D**, respectively. Q_{min} is also inversely proportional to the antenna polarizability γ . Here we are interested to derive this, less familiar parameter than D , in the case of a rectangular and circular cavity. To this end, we aim to find the scattered electric field \mathbf{E}^S from a cavity in an infinite ground plane. In general, the scattered field in the direction $\hat{\mathbf{k}}$ from any object, can be expressed by

$$\mathbf{E}^S(k, \mathbf{r}) = E_0^+ \frac{e^{-jkr}}{r} \underline{\mathbf{S}}(k, \hat{\mathbf{k}}) \cdot \hat{\mathbf{p}}_e + \mathcal{O}(r^{-2}) \quad \text{as } r \rightarrow \infty, \quad (3.2)$$

where $\underline{\mathbf{S}}(k, \hat{\mathbf{k}})$ is the scattering dyadic, $\hat{\mathbf{p}}_e$ the electric polarization and E_0^+ the amplitude of the incident electric field. From (3.2) the extinction volume ϱ is introduced as

$$\varrho(k) = \frac{\hat{\mathbf{p}}_e^* \cdot \underline{\mathbf{S}}(k, \hat{\mathbf{k}}) \cdot \hat{\mathbf{p}}_e}{k^2}, \quad (3.3)$$

As described in chapter 1.1.3, $\varrho(k)$ is well-defined quantity in the long wavelength limit $k \rightarrow 0$, by the polarizabilities of the scattering object, thus from (3.3) we define

$$\gamma = 4 \pi \varrho(0) = (\hat{\mathbf{p}}_e^* \cdot \underline{\gamma}_e \cdot \hat{\mathbf{p}}_e + \hat{\mathbf{p}}_m^* \cdot \underline{\gamma}_m \cdot \hat{\mathbf{p}}_m). \quad (3.4)$$

where $\hat{\mathbf{p}}_m = \hat{\mathbf{k}} \times \hat{\mathbf{p}}_e$ represents the magnetic polarization of the incident wave. $\underline{\gamma}_e$ and $\underline{\gamma}_m$ are the electric and magnetic polarizability dyadics of the target. They allow determining the induced electric and magnetic dipole

moments $\mathbf{p} = \varepsilon_0 \underline{\gamma}_e \cdot \hat{\mathbf{p}}_e E_0$ and $\mathbf{m} = \mu \underline{\gamma}_m \cdot \hat{\mathbf{p}}_m H_0$ when the target is immersed in a uniform electrostatic or magnetostatic field of amplitude E_0 and H_0 respectively.

3.2.1. Restriction to broadside radiation pattern

In the case of electrically small apertures in a conducting screen the field on the aperture can be decomposed into TE and TM modes. In the case of a TE mode there are tangential electric fields \mathbf{E}_t at the aperture that can be replaced by an equivalent magnetic current \mathbf{M} and the aperture shorted. Far from the aperture the resultant fields of magnetic currents are equivalent to the field of a magnetic dipole \mathbf{m} tangential to the screen. Therefore, TE modes are connected to components of the $\underline{\gamma}_m$ dyadic. Analogously, in the case of TM modes, the magnetic field is replaced by electric current \mathbf{J} that lead to the fields of an electric dipole \mathbf{p} perpendicular to the screen, and are thus connected to components of the $\underline{\gamma}_e$ dyadic.

Importantly, in the case of axial symmetry (symmetry about two perpendicular planes), as for example in the square or circular apertures, the problem of polarizability in all three axes is greatly simplified. First, if the axes of symmetry is the $\hat{\mathbf{z}}$ axes, then $\underline{\gamma}_e$ and $\underline{\gamma}_m$ are diagonal ($(\gamma_e)_{ij} = (\gamma_m)_{ij} = 0, i \neq j$) and from the the invariance to a $\pi/2$ rotation about the z axis we have $(\gamma_m)_{xx} = (\gamma_m)_{yy}$. As mentioned, in the case of small apertures, the electric polarizability differs than zero only in the z axes; $(\gamma_e)_{zz} \neq 0$ while $(\gamma_m)_{zz} = 0$. However, there is an identity linking the electric and magnetic polarizabilities in the case of such symmetry. This identity was shown by Kleinman and Senior in [34] and applied to a cavity case it reads $(\gamma_e)_{zz} = 1/2(\gamma_m)_{xx}$. In practical terms this means that for square and circular apertures and cavities, determining $\underline{\gamma}_m$ in one direction is sufficient to completely describe the polarizability of the antenna.

Because the magnetic dipole \mathbf{m} is oriented tangential to the screen, its radiation pattern is broadside from the ground plane. On the other hand, from the orientation of the electric dipole \mathbf{p} it follows it will have a monopole radiation pattern. Here, we are interested only in broadside radiation from cavity antennas. This restriction means we have to consider TE modes that lead to the magnetic dipole \mathbf{m} . We thus assume the electric dipole \mathbf{p} is not excited and does not enter the Q formula (3.1). In the further text only $\underline{\gamma}_m$ will be of interest.

3.2.2. Formulation of the scattering problem

This formulation assumes an infinite ground plane around the aperture. The ground plane presents a slight problem in defining the “forward” scattering direction, as there is nothing behind the cavity. However this problem is circumvented by image theory, which effectively removes the ground plane. To obtain $\underline{\mathbf{S}}(k, \hat{\mathbf{k}})$, and thus $\varrho(0)$ in the case of an aperture backed by a cavity, we assume a plane wave normally impinging on the aperture. Again, because of the infinite ground plane, one may think there is infinite scattering from it. However, this would only be the reflected wave, not the wave scattered by the object of interest – the cavity. As we will see, the reflected wave is taken into account in the boundary condition derived in this section.

A. AMPLITUDE CALCULATION

The tangential field at the aperture can be written as a sum of modes

$$\mathbf{E}_t = \sum_{n=1,3,\dots}^{\infty} A_n \mathbf{E}_n, \quad (3.5)$$

At the surface area S of the aperture and zero outside. Where A_n represent unknown amplitudes of modes excited in the cavity. Next, we will follow the generalized network formulation, originally introduced by Harrington [125]. From the equivalence theorem, the total field is separated into three distinct contributions. First, the field scattered by the aperture in the half-space ($\mathbf{E}^S, \mathbf{H}^S$), i.e. the *radiation problem*. Second, the waveguide field ($\mathbf{E}^C, \mathbf{H}^C$), excited by the aperture field distribution, i.e. the *cavity problem*. Third, in the half space, there is the sum of incident and reflected field ($\mathbf{E}^{sc}, \mathbf{H}^{sc}$) obtained by substituting the aperture with a short circuit. Therefore $\mathbf{H}^{sc} = 2\mathbf{H}^{inc}$, that must be added to obtain the total field. Subsequently, the original problem is separated into three different problems, as in Figure 87.

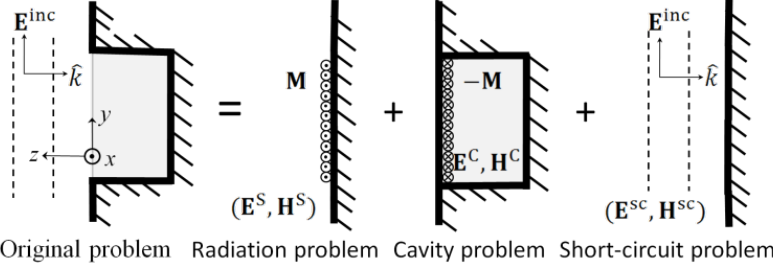


Figure 87 Separation of the problem.

In the radiation and cavity problems an equivalent magnetic surface current

$$\mathbf{M} = -\hat{\mathbf{z}} \times \mathbf{E}_t \quad (3.6)$$

and its negative are placed over the exterior and interior side of the closed aperture region, respectively. The magnetic current can be expanded using (3.5) as

$$\mathbf{M} = \sum_{n=1,3,\dots}^{\infty} A_n \mathbf{M}_n. \quad (3.7)$$

To express the boundary condition at the aperture, we denote the tangential magnetic field on the exterior side as $\mathbf{H}_t^+ = \mathbf{H}_t^S(\mathbf{M}) + \mathbf{H}_t^{\text{sc}}$ where $\mathbf{H}_t^S(\mathbf{M})$ is the field due to \mathbf{M} considered as the scattered field and \mathbf{H}_t^{sc} is the sum of the incident and reflected wave when the aperture is short circuited. The field on the interior side is denoted by $\mathbf{H}_t^- = \mathbf{H}_t^C(-\mathbf{M}) = -\mathbf{H}_t^C(\mathbf{M})$ by linearity. Equating \mathbf{H}_t^+ to \mathbf{H}_t^- leads to the boundary condition

$$\boxed{\mathbf{H}_t^S(\mathbf{M}) + \mathbf{H}_t^C(\mathbf{M}) = -\mathbf{H}_t^{\text{sc}}}. \quad (3.8)$$

We substitute (3.7) into (3.8), and use linearity of the field operators to obtain

$$\sum_n A_n \mathbf{H}_t^S(\mathbf{M}_n) + \sum_n A_n \mathbf{H}_t^C(\mathbf{M}_n) = -\mathbf{H}_t^{\text{sc}}. \quad (3.9)$$

In order to compute the unknown coefficients A_n we take the symmetric product of the conjugate of (3.9) with functions \mathbf{M}_m , where $m = 1, 3, 5, \dots$ and integrate over the whole aperture, by indicating the Hermitian product as

$$\langle F, G \rangle = -\frac{1}{2} \int_S \mathbf{F} \cdot \mathbf{G}^* dS \quad (3.10)$$

we have

$$\sum_n A_n \langle \mathbf{M}_m, \mathbf{H}_t^S(\mathbf{M}_n) \rangle + \sum_n A_n \langle \mathbf{M}_m, \mathbf{H}_t^C(\mathbf{M}_n) \rangle = -\langle \mathbf{M}_m, \mathbf{H}_t^{\text{sc}} \rangle. \quad (3.11)$$

The Hermitian products can be interpreted as cross-power integrals in the following way; since $\mathbf{M}_m = -\hat{\mathbf{z}} \times \mathbf{E}_m$ and the general vector identity $\mathbf{A} \cdot (\mathbf{B} \times \mathbf{C}) = \mathbf{B} \cdot (\mathbf{C} \times \mathbf{A})$ holds, we can write

$$\mathbf{M}_m \cdot \mathbf{H}_t^* = -(\hat{\mathbf{z}} \times \mathbf{E}_m) \cdot \mathbf{H}_t^* = -\hat{\mathbf{z}} \cdot (\mathbf{E}_m \times \mathbf{H}_t^*) \quad (3.12)$$

where $\mathbf{H}_t^* = \mathbf{H}_t^S(\mathbf{M}_n)$, $\mathbf{H}_t^C(\mathbf{M}_n)$, \mathbf{H}_t^{sc} depending on the integral considered. This is a more familiar form of power, written in terms of the Poynting vector.

$$\begin{aligned} \langle \mathbf{M}_m, \mathbf{H}_t^S(\mathbf{M}_n) \rangle &= P_{nm}^S = \frac{1}{2} \int_S \hat{\mathbf{z}} \cdot (\mathbf{E}_m \times \mathbf{H}_t^{S*}) dS \\ \langle \mathbf{M}_m, \mathbf{H}_t^C(\mathbf{M}_n) \rangle &= P_{nm}^C = \frac{1}{2} \int_S \hat{\mathbf{z}} \cdot (\mathbf{E}_m \times \mathbf{H}_t^{C*}) dS, \\ \langle \mathbf{M}_m, \mathbf{H}_t^{\text{sc}} \rangle &= \frac{1}{2} \int_S \hat{\mathbf{z}} \cdot (\mathbf{E}_m \times \mathbf{H}_t^{\text{sc}*}) dS \end{aligned} \quad (3.13)$$

Where P_{nm}^S is the power transmitted into the half space and P_{nm}^C is the power transmitted into the cavity. The right hand term of (3.13) is interpreted as a source term. Writing (3.13) in a more concise matrix form we have

$$\boxed{(\mathbf{P}_S + \mathbf{P}_C) \cdot \mathbf{A} = \mathbf{V}}, \quad (3.14)$$

where $\underline{\mathbf{P}}_S$ and $\underline{\mathbf{P}}_C$ are admittance matrices whose general entry is P_{nm}^S and P_{nm}^C , respectively. The vector \mathbf{A} collects unknown amplitudes A_n , and the right-hand vector \mathbf{V} contains the source terms.

B. FAR FIELD CALCULATION

In the previous section we used the assumption of the electric field at the aperture and the equivalence principle to define the magnetic current \mathbf{M} and derive its amplitude. Next, we need to determine the radiation produced by magnetic currents which constitutes the scattered field. We consider the solution of Maxwell equations driven by magnetic charge and current densities ρ_m, \mathbf{M} to obtain the radiation fields.

The generalized form of Maxwell's equations

$$\begin{aligned} \nabla \times \mathbf{H} &= \mathbf{J} + j\omega\varepsilon\mathbf{E}, & \nabla \times \mathbf{H} &= j\omega\varepsilon\mathbf{E}, \\ \nabla \cdot \mathbf{E} &= \frac{\rho}{\varepsilon} & \nabla \cdot \mathbf{E} &= 0 \\ \nabla \times \mathbf{E} &= -\mathbf{M} - j\omega\varepsilon\mathbf{H} & \nabla \times \mathbf{E} &= -\mathbf{M} - j\omega\varepsilon\mathbf{H} \\ \nabla \cdot \mathbf{H} &= \frac{\rho_m}{\varepsilon} & \nabla \cdot \mathbf{H} &= \frac{\rho_m}{\varepsilon} \end{aligned} \quad \xrightarrow{\text{reduces to}} \quad (3.15)$$

The solution of (3.15) is obtained in terms of the two magnetic type potentials φ_m, \mathbf{A}_m

$$\begin{aligned} \mathbf{E} &= -\frac{1}{\varepsilon} \nabla \times \mathbf{A}_m, \\ \mathbf{H} &= -\nabla \varphi_m - j\omega\varepsilon\mathbf{A}_m \end{aligned} \quad (3.16)$$

The scalar and vector potentials satisfy the Lorentz conditions and Helmholtz wave equations:

$$\begin{aligned} \nabla \cdot \mathbf{A}_m + j\omega\varepsilon\varphi_m &= 0 \\ \nabla^2 \varphi_m + k^2 \varphi_m &= -\rho_m / \varepsilon \\ \nabla^2 \mathbf{A}_m + k^2 \mathbf{A}_m &= -\mu \mathbf{J} \end{aligned} \quad (3.17)$$

Using the Lorentz conditions in (3.17), the scalar potentials φ, φ_m may be eliminated in favor of the vector potentials, resulting in the alternative expression for (3.16) as

$$\begin{aligned} \mathbf{E} &= -\frac{1}{\varepsilon} \nabla \times \mathbf{A}_m, \\ \mathbf{H} &= \frac{1}{j\omega\mu\varepsilon} [\nabla \times \nabla \times \mathbf{A}_m - \mu \mathbf{M}] - \frac{1}{\mu} \nabla \times \mathbf{A} \end{aligned} \quad (3.18)$$

The solutions of Helmholtz equations in (3.17) are given in terms of $G(\mathbf{r} - \mathbf{r}') = \frac{e^{-jk|\mathbf{r}-\mathbf{r}'|}}{4\pi|\mathbf{r}-\mathbf{r}'|}$

$$\mathbf{A}_m = \int_V \mu \mathbf{M}(\mathbf{r}') \frac{e^{-jk|\mathbf{r}-\mathbf{r}'|}}{4\pi|\mathbf{r}-\mathbf{r}'|} dV', \quad (3.19)$$

where V is the volume over which the current densities are non-zero. The observation point \mathbf{r} is taken outside this volume.

The radiation fields in the far field can be obtained by making the far field approximation, which consists of the approximations

$$\frac{e^{-jk|\mathbf{r}-\mathbf{r}'|}}{4\pi|\mathbf{r}-\mathbf{r}'|} \simeq \frac{e^{-jkr}}{4\pi r} e^{jk \cdot \mathbf{r}'} \quad \text{and} \quad \nabla \simeq -j\mathbf{k} \quad (3.20)$$

where $\mathbf{k} = k\hat{\mathbf{r}}$. Then, the vector potentials in (3.25) take the simplified form

$$\mathbf{A}_m = \varepsilon \frac{e^{-jkr}}{4\pi r} \mathbf{F}_m, \quad (3.21)$$

where the radiation vectors are the Fourier transforms of the current density

$$\boxed{\mathbf{F}_m = \int_V \mathbf{M}(\mathbf{r}') e^{jk \cdot \mathbf{r}'} dV'} \quad (3.22)$$

When we are evaluating the fields far from the current sources, the currents in (3.24) are set to zero ($\mathbf{J}, \mathbf{M} = 0$). Using the far field approximation $\nabla = -j\mathbf{k} = -jk\hat{\mathbf{r}}$. And the relationship $k/\varepsilon = \omega\eta_0$, we find the radiated \mathbf{E} and \mathbf{H} fields

$$\begin{aligned}\mathbf{E} &= j\omega\eta_0\hat{\mathbf{r}} \times \mathbf{A}_m = jk\frac{e^{-jkr}}{4\pi r}\hat{\mathbf{r}} \times \mathbf{F}_m, \\ \mathbf{H} &= \frac{j\omega}{\eta_0}[\eta_0\hat{\mathbf{r}} \times \mathbf{A}_m \times \hat{\mathbf{r}}] = -\frac{jk}{\eta_0}\frac{e^{-jkr}}{4\pi r}\hat{\mathbf{r}} \times \mathbf{F}_m \times \hat{\mathbf{r}}\end{aligned}\quad (3.23)$$

Now we turn to the far field (scattering \mathbf{E}^S) for the specific case of apertures in an infinite ground plane. Note that previously we have separated the problem into different parts, see Figure 87, to find the amplitude of the magnetic current. Now, using image theory the perfect electric conducting plane is eliminated and replaced by an image magnetic surface current, doubling its value over the aperture. As the scattering approach relies on the forward scattering theorem we are interested in only the $\hat{\mathbf{z}}$ direction, the electric field in (3.23) is reduced to

$$\boxed{\mathbf{E}^S = 2jk\frac{e^{-jkr}}{4\pi r}\hat{\mathbf{z}} \times \mathbf{F}_m}\quad (3.24)$$

Where the factor 2 results from image theory, i.e. the fact that the magnetic current is radiating only into a half-space.

In the low frequency limit we can simplify the computation by using the fact that $e^{jkr} \rightarrow 1$ when $k \rightarrow 0$. We insert and obtain the value of the integral

$$\mathbf{F}_m = \int_V \mathbf{M}(\mathbf{r}')e^{j\mathbf{k}\cdot\mathbf{r}'}dV' \xrightarrow{k \rightarrow 0} \int_V \mathbf{M}(\mathbf{r}')dV' = A_n \sum_{n=1,3,\dots}^{\infty} \int_V \mathbf{M}_n dS' \quad (3.25)$$

which, together with (3.24) and (3.11) for determines the scattered field from the cavity in the static limit.

Since the equivalent aperture currents producing \mathbf{E}^S are bounded, time-invariant, and causal, the field \mathbf{E}^S respect the hypotheses stated in [26].

3.3. Applying the scattering approach to specific geometries

Here we apply the described scattering formulation to two specific geometries, i.e. rectangular and circular cavities in an infinite ground plane. Precise bounds are derived in both cases and shown to have a similar form to the familiar Chu bound, but having different coefficients. Finally, predictions for maximum bandwidth are made and compared with simulation results of patch antennas from the last chapter.

3.3.1. Bound on bandwidth for rectangular cavities

In the case of a rectangular cavity, the field at the aperture is assumed as

$$\mathbf{E}_t = \sum_{n=1,3,\dots}^{\infty} A_n \mathbf{E}_n, \quad \mathbf{E}_n(x, y) = \hat{\mathbf{y}}E_0^+ \cos\left(\frac{n\pi}{a}x\right), \quad (3.26)$$

for $|x| < a/2$, $|y| < b/2$. Where a and b are the lateral and vertical dimensions, E_0^+ is the amplitude of the incident wave and A_n represent unknown amplitudes of TE_{n0} modes excited at the aperture. The magnetic current, in accordance with (3.7) is then

$$\mathbf{M}_n = \hat{\mathbf{x}}E_0^+ \cos\left(\frac{n\pi}{a}x\right) \quad (3.27)$$

We now proceed to calculate here the three cross-power terms in (3.13).

A. CAVITY PROBLEM CALCULATION

The cavity geometry can be considered as a rectangular waveguide whose cross sections is parallel to the aperture plane and whose longitudinal direction is the z axis, orthogonal to the aperture plane. The magnetic field $\mathbf{H}_t^C(\mathbf{M}_n)$, excited by a magnetic current \mathbf{M}_n on the aperture, is then the magnetic field of the TE_{n0} mode of this rectangular waveguide. Due to mode orthogonality, the cross-power integral for the cavity part P_{nm}^C in (3.13) is different from zero only if $n = m$. In that case, it is the power crossing the aperture associated with the TE_{n0} mode. For this reason we write it as

$$\begin{aligned}
 P_n^C &= \frac{\delta_{nm}}{2} \int_S \hat{\mathbf{z}} \cdot (\mathbf{E}_m \times \mathbf{H}_t^{C*}(\mathbf{M}_n)) dS = \\
 &= \frac{\delta_{nm}}{2} \int_{-a/2}^{a/2} \int_{-b/2}^{b/2} \hat{\mathbf{z}} \cdot (\mathbf{E}_n \times \mathbf{H}_t^{C*}(\mathbf{M}_n)) dx dy = \frac{\delta_{nm}}{2} \int_{-a/2}^{a/2} \int_{-b/2}^{b/2} Y_n^{C*} |\mathbf{E}_n|^2 dx dy \\
 &= \frac{\delta_{nm}}{2} Y_n^{C*} |E_0^+|^2 \int_{-a/2}^{a/2} \int_{-b/2}^{b/2} \cos^2\left(\frac{n\pi}{a}x\right) dx dy = \\
 &= \delta_{nm} \frac{ab}{4} Y_n^{C*} |E_0^+|^2
 \end{aligned} \tag{3.28}$$

where δ_{nm} is the Kronecker delta, and Y_n^C is the input admittance seen at the aperture toward the interior of the cavity. Where we have assumed $\mathbf{H}_t^{C*}(\mathbf{M}_n) = Y_n^C (\hat{\mathbf{z}} \times \mathbf{E}_n)$. Since the latter is equivalent to a short circuited transmission line, the input admittance is

$$Y_n^C = -j \frac{k_{zn}}{k\eta_0} \cot(k_{zn} h) \tag{3.29}$$

with $k_{zn}^2 = \epsilon_r k^2 - (n\pi/a)^2$, where k is the vacuum wave-number, η_0 is the vacuum impedance, ϵ_r is the relative permittivity inside the cavity, a is the larger aperture size and h the cavity depth.

Low frequency limit: A Taylor expansion of (3.29) around $k = 0$ gives

$$Y_n^C = -j \frac{1}{k} \frac{n\pi \coth\left(\frac{nh\pi}{a}\right)}{a\eta_0} + \mathcal{O}(k) \text{ as } k \rightarrow 0 \tag{3.30}$$

And we see all the higher terms except the first $1/k$ term go to 0 as $k \rightarrow 0$. Therefore, the first term is the only significant one.

B. HALF-SPACE PROBLEM CALCULATION

Here the cross-power integrals are more difficult to evaluate, since no orthogonality rule or transmission-line formalism can be invoked to simplify the expressions. The magnetic field $\mathbf{H}_t^S(\mathbf{M}_n)$, excited by a magnetic current \mathbf{M}_n on the aperture, does not have a simple dependence on the electric field at the aperture. Still, the integral can be computed numerical in the spectral domain as shown in detail in *Appendix C*. We assume admittance is defined also in this case, in coherence with (3.28). The final expression is

$$P_{nm}^S = \frac{1}{2} \int_S \hat{\mathbf{z}} \cdot (\mathbf{E}_m \times \mathbf{H}_t^{S*}(\mathbf{M}_n)) dS = \frac{ab}{4} Y_{nm}^{Ap} |E_0^+|^2, \tag{3.31}$$

where

$$Y_{nm}^{Ap} = \frac{abnm}{8k\eta} \iint_{\mathbb{R}^2} \frac{(k^2 - k_x^2) \left(\cos\left(\frac{k_x a}{2}\right) \text{sinc}\left(\frac{k_y b}{2}\right) \right)^2 dk_x dk_y}{\sqrt{k^2 - k_x^2 - k_y^2} \left[\left(\frac{n\pi}{2}\right)^2 - \left(\frac{k_x a}{2}\right)^2 \right] \left[\left(\frac{m\pi}{2}\right)^2 - \left(\frac{k_y a}{2}\right)^2 \right]}. \tag{3.32}$$

Low frequency limit:

We can use the series (Taylor) approximation for the aperture admittance introduced for simple, open ended, cavity antennas (described in Chapter 1.3.1). The aperture admittance $Y_{nm}^{Ap} = G_{nm}^{Ap} + jB_{nm}^{Ap}$ in as expanded as

$$\begin{aligned}
 G_{nm}^{Ap} &= g_{nm}^0 x^2 + g_{nm}^1 x^4 + g_{nm}^2 x^6 \dots, \\
 B_{nm}^{Ap} &= b_{nm}^0 x^{-1} + b_{nm}^1 x + b_{nm}^2 x^3 + \dots,
 \end{aligned} \tag{3.33}$$

where $x = ka/(2\pi)$. We can see only b_{nm}^0 is significant when $k \rightarrow 0$. Thus the low frequency limit of the admittance is

$$Y_{nm}^{Ap} = j \frac{2\pi}{ka} b_{nm}^0 + \mathcal{O}(k) \text{ as } k \rightarrow 0, \tag{3.34}$$

To obtain the necessary coefficients b_{nm}^0 we thus take the first term in a Taylor expansion around $k = 0$ of (3.32), and substitute the variables $k_x a/2$ and $k_y b/2$ by α and β respectively. We finally obtain the expression

$$b_{mn}^0 = -\frac{mn}{2\pi\eta_0} \iint_{\mathbb{R}^2} \frac{\alpha^2 \cos(\alpha)^2 \text{sinc}(\beta)^2 d\alpha d\beta}{\sqrt{\alpha^2 + \left(\frac{a}{b}\right)^2 \beta^2} \left(\left(\frac{n\pi}{2}\right)^2 - \alpha^2\right) \left(\left(\frac{m\pi}{2}\right)^2 - \alpha^2\right)} \quad (3.35)$$

which is integrated numerically. Example results for the first 7 odd modes are given in Table 9.

b_{mn}^0	\mathbf{m}			
\mathbf{n}	1	3	5	7
1	-0.000809	0.000219	0.000179	0.000152
3	0.000219	-0.003442	0.000259	0.000242
5	0.000179	0.000259	-0.006094	0.000268
7	0.000152	0.000242	0.000268	-0.008745

Table 9 Numerically computed values of b_{mn}^0 for modes 1 to 7

C. SHORT-CIRCUIT PROBLEM CALCULATION

Finally, the cross-power integral in the right-hand side of (3.11) can be computed in closed form

$$\begin{aligned} \langle \mathbf{M}_m, \mathbf{H}_t^{\text{sc}} \rangle &= \frac{1}{2} \int_S \hat{\mathbf{z}} \cdot (\mathbf{E}_m \times \mathbf{H}_t^{\text{sc}*}) dS = \\ &= \frac{1}{2} \int_{-a/2}^{a/2} \int_{-b/2}^{b/2} \hat{\mathbf{z}} \cdot (\mathbf{E}_m \times (2\mathbf{H}_t^{\text{inc}*})) dx dy = \\ &= - \int_{-a/2}^{a/2} \int_{-b/2}^{b/2} E_0^+ \cos\left(\frac{m\pi}{a}x\right) \left(\frac{E_0^+}{\eta_0}\right)^* dx dy = \\ &= -\sin\left(\frac{m\pi}{2}\right) \frac{2ab}{m\pi} \frac{|E_0^+|^2}{\eta_0}. \end{aligned} \quad (3.36)$$

The low frequency limit leaves the expression unchanged.

D. AMPLITUDE CALCULATION

We shall first demonstrate the analytical solution involving only the fundamental TE₁₀ mode. This is the simplest and in fact the most significant case. Expression (3.11) for only the TE₁₀ mode in the cavity yields

$$A_1 [P_{11}^S + P_1^C] = -\langle \mathbf{M}_1, \mathbf{H}_t^{\text{sc}} \rangle, \quad (3.37)$$

which is expanded as

$$A_1 \left[\frac{ab}{4} Y_{11}^{Ap*} |E_0^+|^2 + \frac{ab}{4} Y_1^{C*} |E_0^+|^2 \right] = \frac{2ab}{\pi} \frac{1}{\eta_0} |E_0^+|^2, \quad (3.38)$$

and leads to

$$A_1 = \frac{8}{\pi\eta_0} \frac{1}{Y_{11}^{Ap*} + Y_1^{C*}}. \quad (3.39)$$

In the low frequency limit, inserting expansions (3.30) and (3.34) we have

$$A_1 = \frac{8}{\pi\eta_0} \frac{1}{j \frac{\pi \coth\left(\frac{h\pi}{a}\right)}{ka\eta_0} - j \frac{2\pi}{ka} b_{11}^0 + \mathcal{O}(k)}, \quad (3.40)$$

which is reduced to

$$A_1 = \frac{8}{\pi - 2\pi b_{11}^0 \eta_0 + \pi \coth\left(\frac{h\pi}{a}\right)} \frac{-jka}{\pi} + \mathcal{O}(k^3) \text{ as } k \rightarrow 0, \quad (3.41)$$

The complete solution, involving higher modes gets increasingly more complicated as a larger number of modes is taken into account. An example of a more accurate solution including up to 7 would lead to the matrix system

$$\begin{bmatrix} Y_{11}^{Ap*} + Y_1^{C*} & Y_{13}^{Ap*} & Y_{15}^{Ap*} & Y_{17}^{Ap*} \\ Y_{31}^{Ap*} & Y_{33}^{Ap*} + Y_3^{C*} & Y_{35}^{Ap*} & Y_{37}^{Ap*} \\ Y_{51}^{Ap*} & Y_{53}^{Ap*} & Y_{55}^{Ap*} + Y_5^{C*} & Y_{57}^{Ap*} \\ Y_{71}^{Ap*} & Y_{73}^{Ap*} & Y_{75}^{Ap*} & Y_{77}^{Ap*} + Y_7^{C*} \end{bmatrix} \begin{bmatrix} A_1 \\ A_3 \\ A_5 \\ A_7 \end{bmatrix} = \begin{bmatrix} 8/\pi\eta_0 \\ 8/3\pi\eta_0 \\ 8/5\pi\eta_0 \\ 8/7\pi\eta_0 \end{bmatrix}, \quad (3.42)$$

that can be solved for the unknown amplitudes using a computer, but is too cumbersome to express here. It was found however that the difference in γ with included higher modes in the calculation is very small. In Figure 89 there is a visual demonstration between bandwidth results that involved 1 mode approximation and 7 mode approximation. Numerically, final bandwidth calculation between the two approximations differs by less than 3%.

E. FAR FIELD CALCULATION FOR THE TE_{10} MODE

For brevity we concentrate only on the solution involving the TE_{10} mode while the full solution for higher modes would involve an infinite series. By inserting the magnetic current (3.27) into (3.25) to immediately obtain the low frequency limit of the radiation vector, we have

$$\mathbf{F}_m = \int_S \mathbf{M} dS = \int_{-a/2}^{a/2} \int_{-b/2}^{b/2} A_1 \mathbf{M}_1 dx dy = \hat{\mathbf{x}} E_0^+ A_1 \frac{2ab}{\pi}, \quad (3.43)$$

which together with (3.24) determines the scattered field from the cavity in the static limit given by

$$\mathbf{E}^S = \hat{\mathbf{y}} j 2k E_0^+ \frac{e^{-jkr}}{4\pi r} A_1 \frac{2ab}{\pi}. \quad (3.44)$$

Putting (3.41) for the amplitude, gives the far field expression

$$\mathbf{E}^S = E_0^+ \frac{e^{-jkr}}{r} \left\{ \hat{\mathbf{y}} \frac{1}{4\pi} \frac{32}{\pi^3} \frac{a^2 b k^2}{-2b_{11}^0 \eta_0 + \coth(\frac{\pi}{a} h)} + \mathcal{O}(k^3) \right\}, \quad (3.45)$$

where the expression in the brackets indicates $\underline{\mathbf{S}}(k, \hat{\mathbf{k}}) \cdot \hat{\mathbf{p}}_e$ introduced in (3.2) for the specific case of a rectangular cavity. Inserting the bracket into (3.3) we get

$$\varrho(k) = \frac{1}{4\pi} \frac{32}{\pi^3} \frac{a^2 b}{-2b_{11}^0 \eta_0 + \coth(\frac{\pi}{a} h)} + \mathcal{O}(k^3). \quad (3.46)$$

We can now easily obtain $\varrho(0)$ by putting $k = 0$ in (3.46). Using the definition for γ in (3.4) we finally get

$$\boxed{\gamma \cong \frac{32}{\pi^3} \frac{a^2 b}{-2b_{11}^0 \eta_0 + \coth(\frac{\pi}{a} h)}}. \quad (3.47)$$

Where the sign \cong is used to indicate that this is only a close approximation of the real γ that would need to take into account all higher modes. With our assumptions, this total polarizability γ is in fact equal to an $\hat{\mathbf{y}}\hat{\mathbf{y}}$ element of $\underline{\gamma}_m$ dyadic.

F. CONFIRMING POLARIZABILITY VALUE THROUGH SIMULATIONS

It is of interest to verify the correct value of polarizability by some other method. Fortunately, using (1.37), there is an alternative definition for polarizability, (derived in Chapter 1.1.3), given by

$$\int_0^\infty \sigma_{ext}(\lambda) d\lambda = \pi^2 (\hat{\mathbf{p}}_e^* \cdot \underline{\gamma}_e \cdot \hat{\mathbf{p}}_e + \hat{\mathbf{p}}_m^* \cdot \underline{\gamma}_m \cdot \hat{\mathbf{p}}_m) = \pi^2 \gamma, \quad (3.48)$$

which can be used to confirm (3.47). To do this, broadband simulations (0 – 80 GHz) were performed using the time domain solver available in commercial software CST [130] to obtain and integrate $\sigma_{ext}(\lambda)$.

CST, in fact, produces Radar Cross Section (RCS) data that is equal to σ_{ext} if the investigated object is passive and lossless. If the object is lossy, then absorption and radar cross sections have to be added together. For our simulations, we modeled a cavity recessed in a large ground plane and included a plane wave incident normally on a large ground plane. Open boundary conditions were set directly at the side edges of the ground plane. With such boundary conditions CST is effectively simulating an infinite ground plane. The RCS_{tot} was obtained using the far-field/RCS monitor in more than 2000 frequency points.

Cavities considered in our simulations had a square aperture ($a = b$). We used example aperture sizes of 20, 32, 40 mm. For each aperture size, simulations for several heights ($\Delta h = 5$ mm) and permittivity were performed. One remarkable result is that while RCS_{tot} depends on the relative permittivity ϵ_r , the final integral (3.48) does not. As is also visible from (3.47), magnetic polarizability does not depend on relative permittivity ϵ_r inside the cavity. Polarizability obtained through these broadband simulations was used to determine the Q_{min} from (3.1) and the corresponding maximum bandwidth using (3.55) (shown below). The resulting predictions are combined with analytical results in Figure 89.

Example: To make the numerical method of obtaining the polarizability more clear, an example is given in Figure 88. A 32×32 mm aperture size was chosen with cavity height of 13 mm and filled with air, as shown in Figure 88(a). For better accuracy, the frequency range was split into 4 simulations, each spanning 20 GHz, and finally combined into a result spanning the range of 0 to 80 GHz, as shown in Figure 88(c). It is important to realize that scattering at higher frequencies are contributing less to the total polarizability. This is immediately visible in Figure 88(d), where the RCS data is plotted versus wavelength instead of frequency. All the high frequency data is squeezed together in Figure 88(d) and thus the area underneath is very small. The first peak, corresponding to the fundamental resonance of the object, turns out to be most important. Numerically obtained value of polarizability is $\gamma = 0.00001992$, while with one mode approximation given by (3.47) one obtains $\gamma = 0.00001901$.

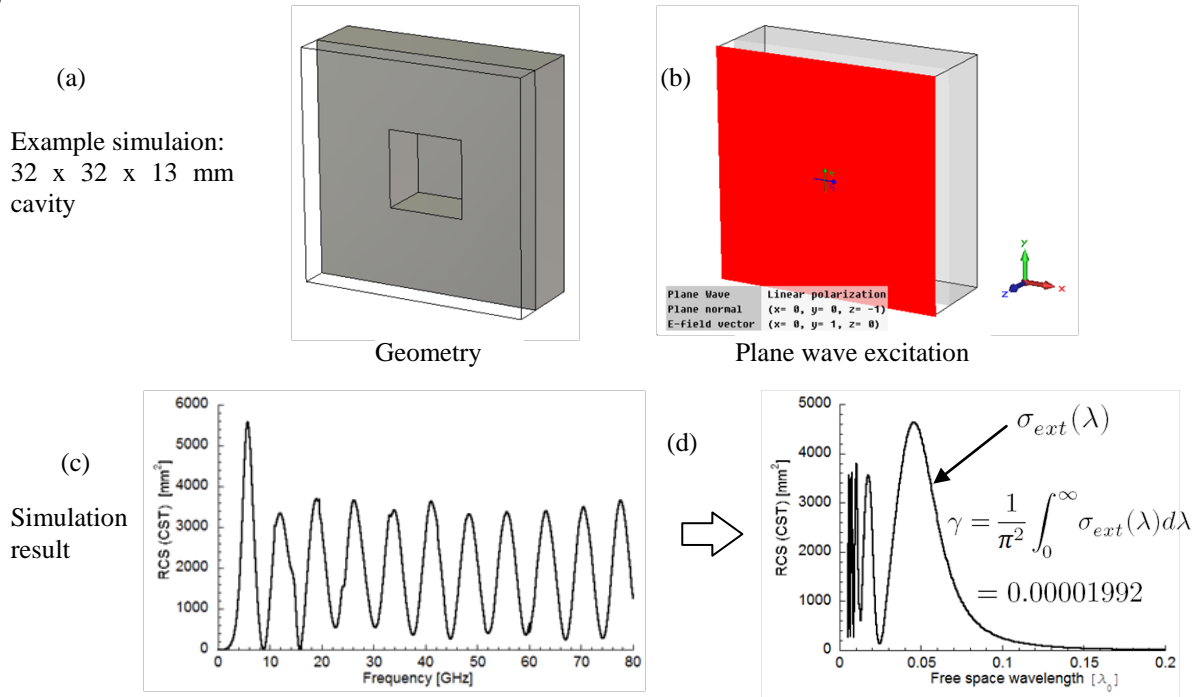


Figure 88 Example of the alternative method for obtaining the polarizability. (a) Image from CST showing the chosen geometry and (b) the position of the plane wave excitation. (c) Obtained broadband RCS result using the time domain solver. CST gives the result depending on frequency. (d) Using post-processing options in CST, the result is transformed to depend on the wavelength and then integrated and divided by π^2 to get the total polarizability.

G. BOUND ON Q_{min} AND MAXIMUM BANDWIDTH

Putting (3.47) into (3.1) gives the complete formula for the minimum Q factor a general rectangular cavity ($a \neq b$) antenna can achieve.

$$Q_{min}^{rect} \cong \frac{\pi^4 D}{16\eta k^3 a^2 b} \left(\coth\left(\frac{\pi h}{a}\right) - 2b_{11}^0 \eta_0 \right) \quad (3.49)$$

Where the sign \cong is again used due to the fact we are neglecting higher order modes. The form of (3.49) is a bit cryptic when compared to the well known Chu limit. We are still left with the directivity D which depends on the size of the aperture and to see a more direct resemblance with the Chu limit we shall have to expand it in terms of ka . For this purpose, and easier understanding, we shall restrict ourselves to square cavities ($a = b$). The complete derivation of directivity for a square aperture is given in Appendix C, here we write the final result in the form of a Taylor series

$$D = \frac{32}{\eta_0 g_{11}^0 \pi} - \frac{8g_{11}^1 (ka)^2}{\eta_0 g_{11}^0{}^2 \pi^3} + \mathcal{O}(ka)^4, \quad (3.50)$$

Inserting the numerical values of the coefficients the directivity is $D \approx 3 + 0.1283(ka)^2 + \mathcal{O}(ka)^4$. Combining (3.50) with (3.49) gives a form closer to the form of the Chu limit

$$Q_{min}^{rect.} \cong \underbrace{\frac{2\pi^3}{\eta g_{11}^0 \eta_0} \left(\coth\left(\frac{\pi}{a}h\right) - 2b_{11}^0 \eta_0 \right)}_{\text{geometric factors due to the cavity}} \left[\underbrace{\frac{1}{(ka)^3} - \frac{g_{11}^1}{4\pi^2 g_{11}^0} \frac{1}{(ka)}}_{\text{similar to Chu limit}} + \mathcal{O}(ka) \right], \quad (3.51)$$

Putting in the numerical coefficients ($\eta = 0.5, \eta_0 = 376.7, b_{11}^0 = -0.00809, g_{11}^0 = 0.00901, g_{11}^1 = -0.01522$) and making the limit $h \gg a$ makes the term $\coth(\frac{\pi}{a}h) \rightarrow 1$ giving

$$Q_{min}^{rect.} \cong \frac{58.785}{(ka)^3} + \frac{2.52}{(ka)}, \quad (3.52)$$

or in terms of radius $r = a\sqrt{2}$ from the center of the cavity. The form directly comparable with the Chu bound is

$$Q_{min}^{rect.} \cong \frac{20.78}{(kr)^3} + \frac{1.78}{(kr)}. \quad (3.53)$$

In all cases, the maximum fractional bandwidth (FBW) of the antennas calculated directly from Q_{min} by

$$\text{FBW} = \frac{2\sqrt{\beta}}{Q_{min}}, \quad \beta = \frac{\alpha}{1-\alpha}, \quad \alpha = |\Gamma_0(\omega)|^2 \quad (3.54)$$

where $\Gamma_0(\omega)$ is the reflection coefficient. Inserting the value $\alpha = 0.1$ for assuring a return loss of 10dB, one obtains the expression for the bandwidth

$$\text{FBW}_{-10\text{dB}} = \frac{2}{3Q_{min}}, \quad (3.55)$$

which is used from making bandwidth predictions. Note that (3.54) is only approximate, as explained in **Appendix A**.

Figure 89 shows bandwidth predictions of various degrees of approximation; the single mode approximation calculated using the polarizability (3.47), shown with full lines; a seven mode approximation where polarizability is calculated using (3.42) and shown with dashed lines. Additionally, predictions made using the polarizability obtained through simulations (see part F of this section) are shown with points. The 7 mode approximation is of-course, closer to the values obtained by simulations in CST.

The conclusion that can be made from Figure 89 is that the single mode approximation is truly a good enough approximation for small cavities. Therefore, in the further text (concerning circular cavities) we shall concentrate only on the analysis with the fundamental mode.

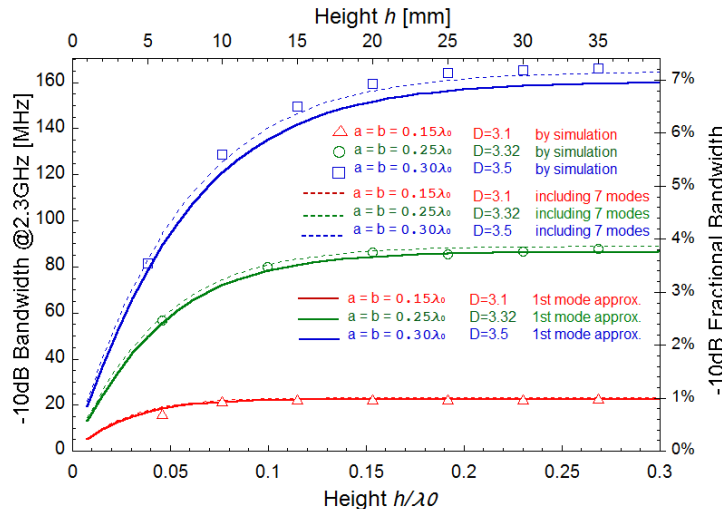


Figure 89 Maximum theoretical bandwidth derived from scattering (simulation and analytical) for several square cavity sizes. Directivity values are noted in the legend. Results are independent of the medium filling the cavity.

3.3.2. Bound on bandwidth for circular cavities

Here we apply the scattering formulation specifically to circular cavity geometry and derive a precise bound on Q_{min} . Analogously to the rectangular case, the field at the circular aperture is also a sum of modes. Due to excitation by a plane wave we could assume TE_{n1} modes expressed as

$$\mathbf{E}_t = \sum_{n=1,3,\dots}^{\infty} A_n \mathbf{E}_n, \quad \mathbf{E}_n(\rho, \phi) = \hat{\rho} E_0^+ \frac{J_n(k_c \rho)}{\rho} \sin(\phi) + \hat{\phi} E_0^+ k_c J_n'(k_c \rho) \cos(\phi) \quad (3.56)$$

for $0 \leq \rho \leq a$, $0 \leq \phi \leq 2\pi$. Where a is the circular aperture radius, E_0^+ is the amplitude of the incident wave, A_n represent unknown amplitudes of TE_{n0} modes excited at the aperture, and $k_c = p'_{n1}/a$ is the cut-off wave-number, where p'_{n1} are first zeroes of the Bessel function derivative $J_n'(x)$. However, as seen in the rectangular case, the fundamental mode is the most significant one. Therefore we will immediately make the restriction of our analysis to just the TE₁₁ mode. The field at the aperture is assumed as

$$\mathbf{E}_t \cong \mathbf{E}_1(\rho, \phi) = A_1 \left\{ \hat{\rho} E_0^+ \frac{J_1(k_c \rho)}{\rho} \sin(\phi) + \hat{\phi} E_0^+ k_c J_1'(k_c \rho) \cos(\phi) \right\}, \quad (3.57)$$

The magnetic current, in accordance with (3.57) is then $\mathbf{M}_1 = \hat{\phi} E_0^+ \frac{J_1(k_c \rho)}{\rho} \sin(\phi) - \hat{\rho} E_0^+ k_c J_1'(k_c \rho) \cos(\phi)$.

We now proceed to calculate here the three cross-power terms in (3.13).

A. CAVITY PROBLEM CALCULATION

The cavity geometry can be considered as a circular waveguide whose longitudinal direction is the z axis, orthogonal to the aperture plane. The magnetic field $\mathbf{H}_t^C(\mathbf{M}_1)$, excited by a magnetic current \mathbf{M}_1 on the aperture, is then the magnetic field of the TE₁₁ mode of this rectangular waveguide. For this reason

$$\begin{aligned} P_1^C &= \frac{1}{2} \int_S \hat{\mathbf{z}} \cdot (\mathbf{E}_1 \times \mathbf{H}_t^{C*}(\mathbf{M}_1)) dS = \frac{1}{2} \int_0^a \int_0^{2\pi} E_\rho H_\phi^* - E_\phi H_\rho^* \rho d\rho d\phi \\ &= \frac{1}{2} Y_1^C \int_0^a \int_0^{2\pi} |E_\rho|^2 + |E_\phi|^2 \rho d\rho d\phi = \\ &= \frac{\pi}{4} Y_1^C |E_0^+|^2 ((p'_{11})^2 - 1) J_1^2(p'_{11}) \end{aligned} \quad (3.58)$$

where Y_1^C is the input admittance seen at the aperture toward the interior of the cavity. Since the latter is equivalent to a short circuited transmission line, the input admittance is

$$Y_1^C = -j \frac{k_{zn}}{k \eta_0} \cot(k_{zn} h) \quad (3.59)$$

with $k_{zn}^2 = \epsilon_r k^2 - (p'_{11}/a)^2$, where k is the vacuum wave-number, η_0 is the vacuum impedance, ϵ_r is the relative permittivity inside the cavity, a is the aperture radius and h the cavity depth.

Low frequency limit: The input admittance, fully expressed, is

$$Y_1^C = -j \frac{\sqrt{\epsilon_r k^2 - \left(\frac{p'_{11}}{a}\right)^2}}{k \eta_0} \cot \left(\sqrt{\epsilon_r k^2 - \left(\frac{p'_{11}}{a}\right)^2} h \right). \quad (3.60)$$

Taylor expansion around $k = 0$ gives

$$\boxed{Y_1^C = -j \frac{1}{k} \frac{p'_{11} \coth\left(\frac{h p'_{11}}{a}\right)}{a \eta_0} + \mathcal{O}(k^3) \text{ as } k \rightarrow 0,} \quad (3.61)$$

where analogously to a rectangular waveguide, all terms except the first one go to 0 as $k \rightarrow 0$.

B. HALF-SPACE PROBLEM CALCULATION

The magnetic field $\mathbf{H}_t^S(\mathbf{M}_1)$, excited by a magnetic current \mathbf{M}_1 on the aperture, does not have a simple dependence on the electric field at the aperture. Still, the integral can be computed numerical in the spectral domain as shown in detail in **Appendix D**. We assume admittance is defined also in this case, in coherence with

(3.58). The final expression is

$$P_{11}^S = \frac{1}{2} \int_S \hat{\mathbf{z}} \cdot (\mathbf{E}_1 \times \mathbf{H}_t^{S*}(\mathbf{M}_1)) dS = \frac{\pi}{4} Y_{11}^{Ap*} |E_0^+|^2 ((p'_{11})^2 - 1) J_n^2(p'_{11}), \quad (3.62)$$

where

$$Y_{11}^{Ap} = \frac{2}{((p'_{11})^2 - 1)\eta_0} \int_0^\infty \left[\frac{k}{k_\rho^2 \sqrt{k^2 - k_\rho^2}} J_1^2(k_\rho a) + \frac{a^2 k_c^4 \sqrt{k^2 - k_\rho^2}}{k(k_c^2 - k_\rho^2)^2} J_1'^2(k_\rho a) \right] k_\rho dk_\rho. \quad (3.63)$$

The low frequency limit of the admittance is

$$Y_{11}^{Ap} = j \frac{2\pi}{ka} b_{11}^0 + \mathcal{O}(k^2) \text{ as } k \rightarrow 0, \quad (3.64)$$

where, again, the first coefficient of the susceptance is the most important. this particular coefficient b_{11}^0 for the TE_{11} mode can be expressed directly. In making the low frequency limit $k \rightarrow 0$, we see that the first term in disappears, and only the second term is important. Making the change in variables $k_\rho a = X$, $dk_\rho a = dX$ we transform the integral into a slightly more suitable form for numerical computation

$$b_{11}^0 = \frac{1}{\pi((p'_{nm})^2 - 1)\eta_0} \int_0^\infty \frac{(p'_{nm})^4 X^2 J_1'^2(X)}{((p'_{nm})^2 - X^2)^2} dX \quad (3.65)$$

The result of numerical integration gives value $b_{11}^0 = 0.000504$.

C. SHORT-CIRCUIT PROBLEM CALCULATION

Finally, the cross-power integral in the right-hand side of (3.12) can be computed in closed form. We start by expressing cross power integral as

$$\langle \mathbf{M}_1, \mathbf{H}_t^{sc} \rangle = \frac{1}{2} \int_S \hat{\mathbf{z}} \cdot (\mathbf{E}_1 \times \mathbf{H}_t^{sc*}) dS = \frac{1}{2} \int_0^a \int_0^{2\pi} \hat{\mathbf{z}} \cdot (\mathbf{E}_1 \times 2\mathbf{H}_t^{inc*}) \rho d\rho d\phi \quad (3.66)$$

Where the incident field at the aperture is $\mathbf{H}_t^{inc} = \hat{\mathbf{x}} E_0^+ / \eta_0$. To resolve the mixed product in the integrand we write the unit vector in polar coordinates as $\hat{\mathbf{x}} = \hat{\rho} \cos(\phi) - \hat{\phi} \sin(\phi)$ and multiply the vectors as

$$\begin{aligned} \hat{\mathbf{z}} \cdot \left(\left(\hat{\rho} E_0^+ \frac{J_1(k_c \rho)}{\rho} \sin(\phi) + \hat{\phi} E_0^+ k_c J_1'(k_c \rho) \cos(\phi) \right) \times (\hat{\rho} \cos(\phi) - \hat{\phi} \sin(\phi)) \left(\frac{E_0^+}{\eta_0} \right)^* \right) \\ = \hat{\mathbf{z}} \cdot \left(-\hat{\mathbf{z}} \frac{J_1(k_c \rho)}{\rho} \sin^2(\phi) - \hat{\mathbf{z}} k_c J_1'(k_c \rho) \cos^2(\phi) \right) \frac{|E_0^+|^2}{\eta_0} = \\ = -\frac{|E_0^+|^2}{\eta_0} \left(\frac{J_1(k_c \rho)}{\rho} \sin^2(\phi) + k_c J_1'(k_c \rho) \cos^2(\phi) \right) \end{aligned} \quad (3.67)$$

Inserting the integrand (3.67) back into (3.66) we can easily integrate the angular variable from 0 to 2π to obtain

$$\langle \mathbf{M}_1, \mathbf{H}_t^{sc} \rangle = -\frac{|E_0^+|^2}{\eta_0} \pi \int_0^a \frac{J_1(k_c \rho)}{\rho} + k_c J_1'(k_c \rho) \rho d\rho. \quad (3.68)$$

Finally, integration in the radial variable finally yields

$$\begin{aligned} \langle \mathbf{M}_1, \mathbf{H}_t^{sc} \rangle &= -\frac{|E_0^+|^2}{\eta_0} \pi k_c \int_0^a \frac{J_1(k_c \rho)}{k_c \rho} + J_1'(k_c \rho) \rho d\rho = \\ &= -\frac{|E_0^+|^2}{\eta_0} \pi k_c \int_0^a \frac{1}{2} [J_0(k_c \rho) + J_2(k_c \rho)] + \frac{1}{2} [J_0(k_c \rho) - J_2(k_c \rho)] \rho d\rho = \\ &= -\frac{|E_0^+|^2}{\eta_0} \pi k_c \int_0^a J_0(k_c \rho) \rho d\rho = \\ &= -\frac{|E_0^+|^2}{\eta_0} \pi a J_1(p'_{11}) \end{aligned} \quad (3.69)$$

The low frequency limit leaves the expression unchanged.

D. AMPLITUDE CALCULATION

Combining the solutions of (3.58), (3.62), and (3.69) with expression (3.14) for only the TE₁₁ mode in the cavity yields

$$A_1 \frac{\pi}{4} |E_0^+|^2 ((p'_{11})^2 - 1) J_n^2(p'_{11}) [Y_{11}^{Ap*} + Y_1^{C*}] = \frac{|E_0^+|^2}{\eta_0} \pi a J_1(p'_{11}), \quad (3.70)$$

and leads to

$$A_1 = \frac{4a}{\eta_0 ((p'_{11})^2 - 1) J_1(p'_{11}) (Y_{11}^{Ap*} + Y_1^{C*})}. \quad (3.71)$$

In the low frequency limit when we use expansions (3.61) and (3.64) we get

$$A_1 = \frac{-j4ka^2}{(-2\pi b_{11}^0 \eta_0 + p'_{11} \coth(\frac{p'_{11}}{a} h)) ((p'_{11})^2 - 1) J_1(p'_{11})} + \mathcal{O}(k^3), \text{ as } k \rightarrow 0, \quad (3.72)$$

where we have used the Taylor expansion formulas in (3.61) and (3.64)(3.36) to express the result.

E. FAR FIELD CALCULATION FOR TE₁₁ MODE

We insert the magnetic current \mathbf{M}_1 into the low frequency limit of the radiation vector and have

$$\mathbf{F}_m = \int_0^a \int_0^{2\pi} A_1 \mathbf{M}_1 \rho d\rho d\phi = A_1 E_0^+ \int_0^a \int_0^{2\pi} \hat{\phi} \frac{J_1(k_c \rho)}{\rho} \sin(\phi) - \hat{\rho} k_c J_1'(k_c \rho) \cos(\phi) \rho d\rho d\phi \quad (3.73)$$

Expanding the unit vectors in Cartesian coordinates as $\hat{\rho} = \cos(\phi) \hat{x} + \sin(\phi) \hat{y}$ and $\hat{\phi} = -\sin(\phi) \hat{x} + \cos(\phi) \hat{y}$, and upon doing the integration in the ϕ variable the result is

$$\mathbf{F}_m = \hat{x} A_1 E_0^+ \pi k_c \int_0^a \left(\frac{J_1(k_c \rho)}{k_c \rho} + J_1'(k_c \rho) \right) \rho d\rho = \hat{x} A_1 E_0^+ \pi k_c \int_0^a J_0(k_c \rho) \rho d\rho, \quad (3.74)$$

where we have used (D 15) to transform the integrand. Finally, integration of (3.74) gives

$$\mathbf{F}_m = \hat{x} A_1 E_0^+ \pi a J_1(k_c a), \quad (3.75)$$

where $J_1(k_c a)$ can also be written as $J_1(p'_{11})$. Putting (3.75) together with (3.24) determines the scattered field from the cavity in the static limit

$$\mathbf{E}^S = \hat{y} 2jk E_0^+ \frac{e^{-jkr}}{4\pi r} A_1 \pi a J_1(p'_{11}). \quad (3.76)$$

Putting (3.72) into (3.76) gives the far field expression

$$\mathbf{E}^S = E_0^+ \frac{e^{-jkr}}{r} \left\{ \hat{y} \frac{1}{4\pi} \frac{8\pi k^2 a^3}{(-2\pi b_{11}^0 \eta_0 + p'_{11} \coth(\frac{p'_{11}}{a} h)) ((p'_{11})^2 - 1)} + \mathcal{O}(k^3) \right\}, \quad (3.77)$$

where the expression in the brackets indicates $\underline{\mathbf{S}}(k, \hat{\mathbf{k}}) \cdot \hat{\mathbf{p}}_e$ introduced in (3.2) for the specific case of a rectangular cavity. Inserting the bracket into (3.3) we get

$$\varrho(k) = \frac{8\pi a^3}{-2\pi b_{11}^0 \eta_0 + p'_{11} \coth(\frac{p'_{11}}{a} h) ((p'_{11})^2 - 1)} + \mathcal{O}(k^3). \quad (3.78)$$

We can now easily obtain $\varrho(0)$ by putting $k = 0$ in (3.46). Using the definition for γ in (3.4) we finally get

$$\boxed{\gamma \cong \frac{8\pi}{((p'_{11})^2 - 1) (-2\pi b_{11}^0 \eta_0 + p'_{11} \coth(\frac{p'_{11}}{a} h))} a^3}. \quad (3.79)$$

F. BOUND ON Q_{min} AND MAXIMUM BANDWIDTH

Putting (3.79) into (3.1) gives the complete formula for the minimum Q factor a general circular cavity antenna can achieve

$$Q_{min}^{rect.} \cong \frac{D}{4\eta(ka)^3} \left(p'_{11} \coth\left(\frac{p'_{11}h}{a}\right) - 2\pi b_{11}^0 \eta_0 \right) \left((p'_{11})^2 - 1 \right) \quad (3.80)$$

Where the sign \cong is again used due to the fact we are neglecting higher order modes. The form of (3.49) is a bit cryptic when compared to the well known Chu limit. We are still left with the directivity D which depends on the size of the aperture and to see a more direct resemblance with the Chu limit we shall have to expand it in terms of ka . For this purpose, and easier understanding, we shall restrict ourselves to square cavities ($a = b$). The complete derivation of directivity for a circular aperture is given in **Appendix D**, here we write the final result in the form of a Taylor series

$$D = \frac{8\pi^2}{\eta_0 g_{11}^0 \left((p'_{11})^2 - 1 \right)} - \frac{2g_{11}^1 (ka)^2}{\eta_0 g_{11}^0{}^2 \left((p'_{11})^2 - 1 \right)} + \mathcal{O}(ka)^4, \quad (3.81)$$

Inserting the numerical values of the coefficients the directivity is $D \approx 3 + 0.42265(ka)^2 + \mathcal{O}(ka)^4$. Combinig (3.50) with (3.49) gives a form closer o the form of the Chu limit

$$Q_{min}^{rect.} \cong \underbrace{\frac{2\pi^2}{\eta g_{11}^0 \eta_0} \left(p'_{11} \coth\left(\frac{p'_{11}h}{a}\right) - 2\pi b_{11}^0 \eta_0 \right)}_{\text{geometric factors due to the cavity}} \left[\underbrace{\frac{1}{(ka)^3} - \frac{g_{11}^1}{4\pi^2 g_{11}^0} \frac{1}{(ka)}}_{\text{similar to Chu limit}} + \mathcal{O}(ka)^4 \right], \quad (3.82)$$

Putting in the numerical coefficients ($\eta = 0.5$, $\eta_0 = 376.7$, $b_{11}^0 = -0.0005049$, $g_{11}^0 = 0.02923$, $g_{11}^1 = -0.1627$, $p'_{11} = 1.8418$) and making the limit $h \gg$ makes the term $\coth(\frac{p}{a}h) \rightarrow 1$ giving

$$Q_{min}^{circ.} \cong \frac{10.88}{(ka)^3} + \frac{1.53}{(ka)} \text{ for } h \gg \quad (3.83)$$

Which is directly comparable with the Chu bound. Alternatively, in terms of the diameter $d = 2a$ we have

$$Q_{min}^{circ.} \cong \frac{87.04}{(kd)^3} + \frac{3.06}{(kd)} \text{ for } h \gg, \quad (3.84)$$

Analogous to the square case, the maximum fractional bandwidth (FBW) of the antennas calculated directly from Q_{min} by

$$\text{FBW}_{-10\text{dB}} = \frac{2}{3Q_{min}}, \quad (3.85)$$

Which directly gives a prediction for 10dB return loss bandwidth. However, note that this expression linking bandwidth and Q is only approximate, as explained in **Appendix A**. Nevertheless, (3.86) is used in further text to create predictions on the bound on bandwidth and determine the level to which patch antennas reach it.

3.3.3. Comparison with patch antennas

Simulation results from Chapter 2 have been presented in Figure 90 along with the maximum bandwidth calculated using Gustafsson's bound for square and circular cavities. Note that patch antenna simulations were made using (Rogers) materials with losses while Gustafsson's bound assumes a lossless antenna. This fact presented a problem for the circular cavity of the smallest size where losses play a very significant role. The simulations had to be redone without losses in this case in order to confirm that the bandwidth is not larger than the predicted maximum.

Figure 90 visually demonstrates that patch antennas do not reach the predicted bound on bandwidth. For small cavities, the difference between the bound and the patch bandwidth is small, but for larger cavities, the difference is significant. This indicates that patches are not the best choice when it comes to cavity antennas. The problem of finding the antenna type that does reach the bound is left for Chapter 4.

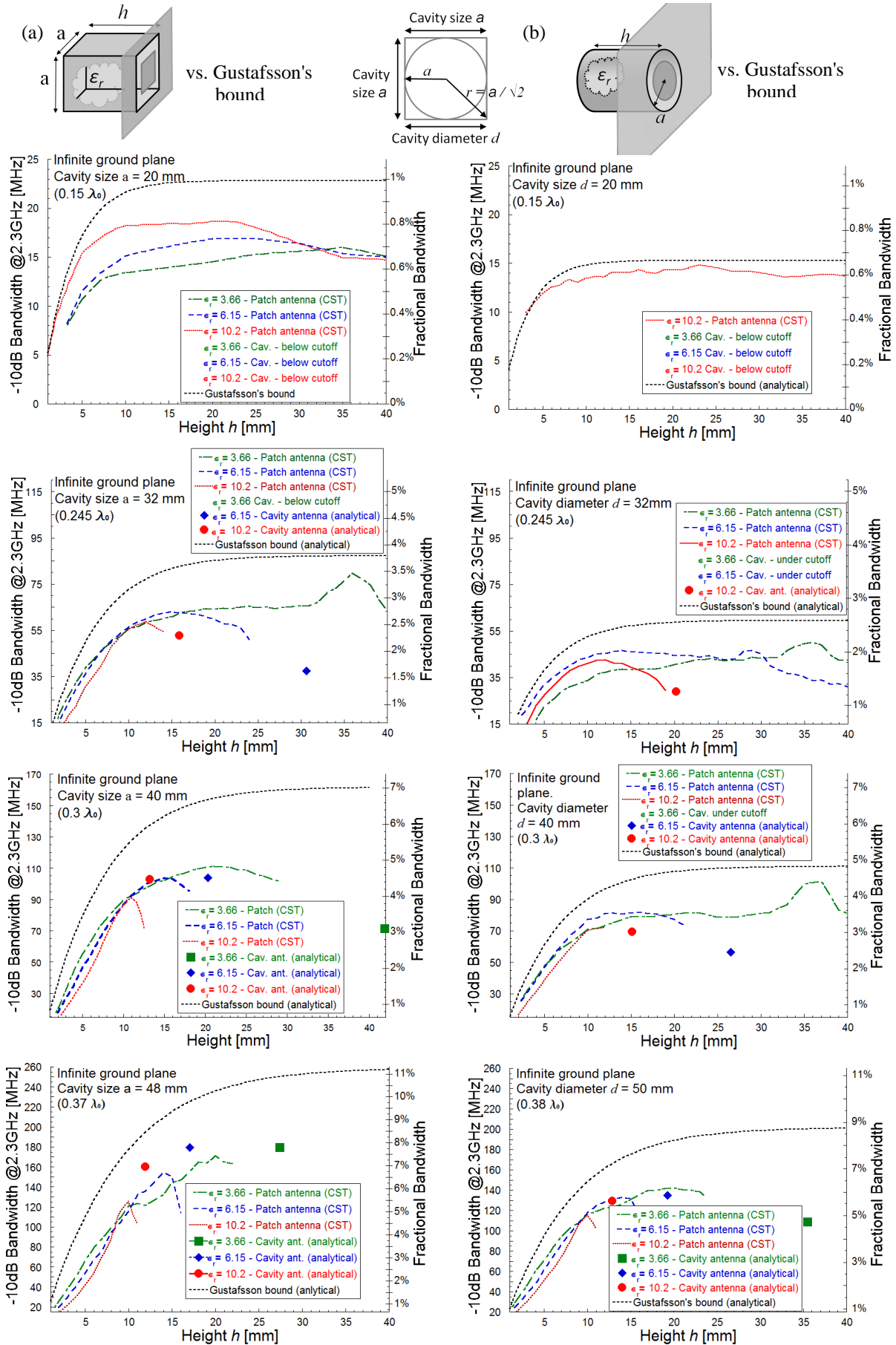


Figure 90 Comparison of simulation results of patch antennas in a cavity to Gustafsson's bound.

3.4. On objects inside the cavity

The antenna (object) inside the cavity will change only the cavity part of our formulation, meaning that the input admittance is modified, and only the input admittance. Here, we discuss the validity of the bound in the presence of objects and we restrict ourselves to a rectangular cavity for brevity, but the same conclusions are valid for a circular case.

Note that the antenna (or objects) inside the cavity might couple energy from the TE modes to any other modes. Existence of these modes might contribute to the radiation by the electric dipole moment \mathbf{p} which is oriented perpendicular from the cavity, in addition to radiation by the magnetic moment which is tangential to the aperture. If both dipole moments are excited, then both electric and magnetic polarizabilities enter the Q formula and the resulting Q could be lower. Of course, such an antenna would not have a strictly broadside radiation pattern because a perpendicular electric moment has a monopole radiation pattern. By working under the assumption of searching for **strictly broadside** radiation pattern, we eliminate antenna types that would also excite the electric moment of the cavity and in this case the field at the aperture can be represented by TE modes.

By assuming the presence of only TE modes inside the waveguide, objects inside can be represented by lumped elements connected in parallel in the transmission line model of the waveguide. The possible equivalent circuits can be found in Pozar [41] and are also depicted in Figure 91.

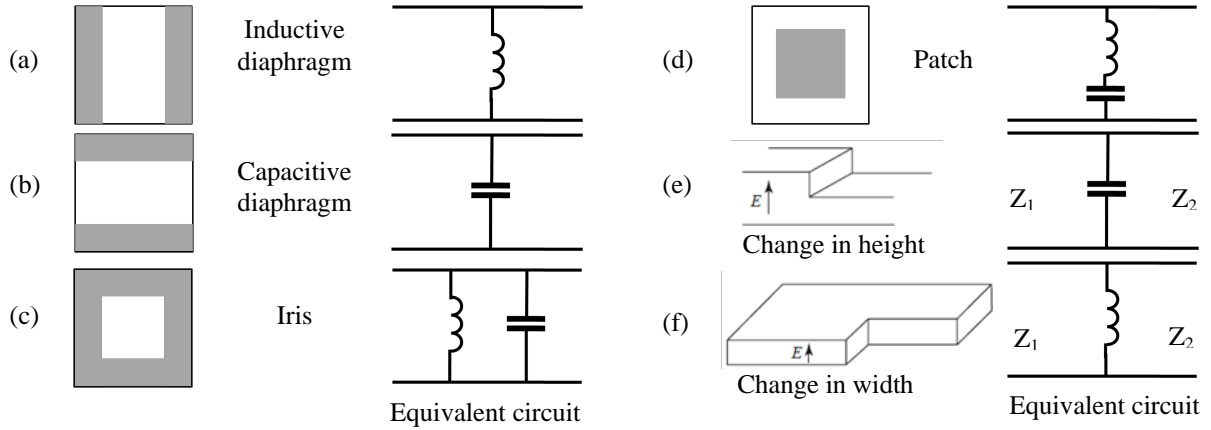


Figure 91 Example discontinuities inside a rectangular excited with a TE mode and their equivalent circuit models.

The input admittance is changed with the addition of objects, but the bound depends on the static limit only. As we have seen throughout the chapter, in the static limit of admittance, only the inductive term with the $1/k$ dependence is significant. The limits for various cases are:

1) *Capacitor at the aperture:*

$$Y_n^C = -j \frac{k_{TE}}{k \eta_0} \cot(k_{TE} h) + j c_0 k C \xrightarrow{as \ k \rightarrow 0} -j \frac{1}{k} \frac{n \pi \coth\left(\frac{n h \pi}{a}\right)}{a \eta_0} + \mathcal{O}(k) \quad (3.86)$$

As $j c_0 k C$ term simply goes to zero with $k \rightarrow 0$, there is no change in the inductive term compared to no capacitor case. The bound for such an antenna would remain the same. Note that $j \omega C = j c_0 k C$, where c_0 is the speed of light.

2) *Series resonant circuit at the aperture:*

$$Y_n^C = -j \frac{k_{TE}}{k \eta_0} \cot(k_{TE} h) + \frac{1}{\frac{1}{j c_0 k C} + j c_0 k L} \xrightarrow{as \ k \rightarrow 0} -j \frac{1}{k} \frac{n \pi \coth\left(\frac{n h \pi}{a}\right)}{a \eta_0} + \mathcal{O}(k) \quad (3.87)$$

Because $1/(1/j c_0 k C + j c_0 k L) = j c_0 k C / (1 - c_0^2 k^2 L C)$ this term also tends to zero as k in the nominator tends to zero. The bound for such an antenna would remain the same. Interestingly, this model was investigated in Chapter 2 to explain bandwidth behaviour of patch antennas. Although the bound is the same, Figure 90 clearly shows patch antennas do not reach the bound.

3) *Inductor at the aperture:*

$$Y_{nn}^C = -j \frac{k_{TE}}{k\eta_0} \cot(k_{TE} h) + \frac{1}{jc_0 kL} \xrightarrow{as \ k \rightarrow 0} -j \frac{1}{k} \left(\frac{n\pi \coth\left(\frac{nh\pi}{a}\right)}{a\eta_0} + \frac{1}{c_0 L} \right) + \mathcal{O}(k) \quad (3.88)$$

In this case there is directly a $1/k$ term added and this leads to a new polarizability given by

$$\gamma \cong \frac{32}{\pi^3} \frac{a^2 b}{-2b_{11}^0 \eta_0 + \coth\left(\frac{\pi}{a} h\right) + \frac{a\eta_0}{\pi c_0 L}}. \quad (3.89)$$

However, as we can see from (3.89) the polarizability can only be smaller because of the added positive term in the denominator, thus the Q can only be larger than the minimum bound. We can conclude that an inductor at the aperture is undesirable.

- 4) *Other cases:* The cases of capacitors or inductors not at the aperture, but along the transmission line essentially reduce to the conclusions shown above; only an additional inductance in parallel changes the end result, and only for the worse.

Having this analysis in mind, the following conclusion seems sound: in the static limit there are only currents on the infinite ground plane and the magnetic field produced by those currents. The tangential electric field in the static limit should be zero (short circuit by the ground plane). This is also why only the magnetic polarizability/dipole moment is important. Currents cannot flow through a capacitor in DC (static) limit, nor a series circuit, so it does not contribute to the polarizability. The bound is hence not affected by objects inside the cavity that do not touch the walls. Objects that are connected with the cavity walls can be represented by inductors and lead to worse results.

3.5. A “quick and dirty” derivation of the bound

The following derivation is not very rigorous and is presented only to show how different approaches can lead to the same result. The author has found this derivation only after deriving the result (3.51), i.e. once he knew what to look for and which assumptions are important. For brevity, here we will concentrate on the rectangular case only. We will derive the bound by considering the behavior for small k of the general Q formula for antennas

$$Q_{Ant} = \frac{k}{2G(k)} \left| \frac{\partial Y(k)}{\partial k} \right|, \quad (3.90)$$

where $Y = G^{Ap}(k) + jB^{Ap}(k) - jk_{TE}/(k\eta_0) \cot(k_{TE} h)$ with $k_{TE} = \sqrt{\varepsilon_r k^2 - (\pi/a)^2}$. For the conductance G , we can use the entire expansion formula $G^{Ap}(k) = g_{11}^0 (ka/2\pi)^2 + g_{11}^1 (ka/2\pi)^4 + \dots$. However, for the susceptance $B^{Ap}(k)$ we will have to be more careful and think about the meaning of the expansion formula. Let us first remember the susceptance of a simple parallel resonant circuit (see **Appendix A**). The inductive susceptance $1/(j\omega L) = 1/(jc_0 kL)$ has a $1/k$ dependence, while the capacitive susceptance $j\omega C = c_0 kC$ is proportional to k . Using the parallel circuit as a guideline, the expansion of $B^{Ap}(k)$ can be divided into the following parts

$$B^{Ap}(k) = \underbrace{b_{11}^0 \frac{2\pi}{ka}}_{\text{inductive part}} + \underbrace{b_{11}^1 \frac{ka}{2\pi}}_{\text{capacitive part}} + \underbrace{b_{11}^2 \left(\frac{ka}{2\pi}\right)^3}_{\text{no interpretation}} + \dots \quad (3.91)$$

The importance of this interpretation comes when $B^{Ap}(k)$ needs to be inserted into (3.90). To calculate the Q factor we can take only the inductive part. At resonance, the energy stored in each reactive part is the same, thus Q factor can be calculated using only the inductive part with a doubled value (see example for a simple circuit in **Appendix B**). The presence of a capacitance that brings the whole circuit into resonance is silently assumed! Hence, we can restrict the susceptance to only $B(k) = b_0 2\pi/ka$, and because the cavity admittance is also inductive for small k we can write

$$Y = G(k) + 2 \left(j b_{11}^0 \frac{2\pi}{ka} - j \frac{k_{TE}}{k\eta_0} \cot(k_{TE} h) \right) \quad (3.92)$$

We can now insert (3.92) into (3.90) and make a Taylor series expansion around $k = 0$ of the whole formula, which should be a good approximation because we are interested in the behavior for electrically small antennas

(small k). After a considerable effort, or by using software for symbolic manipulation (for example: Mathematica), we arrive at the following expansion

$$\begin{aligned}
 Q_{Ant} = & \frac{4\pi^3 \left(-2b_{11}^0 \eta_0 + \coth\left(\frac{h\pi}{a}\right) \right)}{\eta_0 g_{11}^0 (ka)^3} + \\
 & + \frac{\pi g_{11}^1 \left(-2b_{11}^0 \eta_0 + \coth\left(\frac{h\pi}{a}\right) \right)}{(g_{11}^0)^2 (ka)} + \varepsilon_r \frac{2\pi}{g_{11}^0 (ka)} \left(\coth\left(\frac{h\pi}{a}\right) + \frac{h\pi}{a} \operatorname{csch}\left(\frac{h\pi}{a}\right)^2 \right) + \mathcal{O}(ka)
 \end{aligned} \tag{3.93}$$

Where we can immediately see that the third term can be eliminated if $\varepsilon_r = 0$. Rearranging the first two terms then leads to

$$\boxed{Q_{Ant} = \frac{4\pi^3}{g_{11}^0 \eta_0} \left(\coth\left(\frac{h\pi}{a}\right) - 2b_{11}^0 \eta_0 \right) \left(\frac{1}{(ka)^3} - \frac{g_{11}^1}{4\pi^2 g_{11}^0} \frac{1}{(ka)} \right) + \mathcal{O}(ka),} \tag{3.94}$$

which is the same as what was derived in (3.51). Note that in (3.51) we had the absorption efficiency $\eta = 1/2$. The drawback of this derivation is that it is less revealing than Gustafsson's limit, where we could clearly distinguish which antenna parameters are contributing to the Q , namely the directivity, polarizability and absorption efficiency. Gustafsson's limit brings more understanding to Q factors' dependencies and possible tradeoffs antenna engineers can make. On the other hand, this derivation did reveal that low permittivity inside the cavity (ideally $\varepsilon_r = 0$) is beneficial, while this could not be immediately concluded from Gustafsson's bound.

3.6. Conclusion of Chapter 3

In this chapter we have presented an analytical approach to determine the polarizability of cavities and thus a way to determine the bound on Q_{min} . The physical bound was investigated by applying the scattering method, and assuming non-magnetic materials inside the cavity. Additionally, a strictly broadside radiation pattern is assumed, thus restricting the aperture field distribution to a TE modal expansion.

When only the fundamental TE mode is assumed inside the cavity, it is possible to derive a simple approximate formula for the polarizability of the cavity and thus for the maximum theoretical bandwidth of an antenna inside it. The approximate formula gives results within 3% of the accurate values confirmed by simulations.

Maximum bandwidth is derived directly from Q_{min} but one has to have in mind the link between Q and FBW is only approximate (see **Appendix A**). One also has to keep in mind that the assumption of the scattering method is a single resonance with a high Q . If objects are electrically large, more modes are supported by their geometry which can lead to multiple resonances and then the calculated bandwidth bound loses its meaning.

Importantly, the newly derived formulas for Q_{min} of square and circular cavities are written in the same form as the Chu bound, making them directly comparable. It can be seen that Q of cavity antennas is much higher than the one predicted by the Chu, or even Thal bound.

The final, most important conclusion of this chapter is that patch antennas in cavities do not reach the predicted bound on bandwidth and are thus not the optimal antenna type.

Chapter 4.

Bandwidth improvement using metamaterial concepts

The unsettling conclusion of the last chapter, namely that patch antennas do not reach the bandwidth limit of cavity type antennas, is addressed in this chapter. We aim here to remove the drawback of patch antenna design and discover ways to design a new type of cavity antenna capable of reaching the bandwidth bound. Gustafsson's theory is very abstract and the resulting formulas do not provide insight into what antennas would actually reach the bandwidth bound. To get the idea of what antenna design is needed, we combine the knowledge of Gustafsson's bound with transmission line models of simple, open ended, cavity antennas described in Chapter 1.3.1.

In section 4.1, based on a few logical arguments we introduce a new transmission line model of a cavity antenna and show it predicts the same bandwidth behavior as the Gustafsson bound. This remarkable agreement is the key to the novel design methodology of cavity antennas, as the transmission line model is not as abstract as Gustafsson's theory.

In Section 4.2, starting from the assumptions used in our transmission line model a new physical design is discussed. Instead of a patch, a metasurface at the aperture is introduced and the excitation part of the antenna is modified compared to simple patch antennas. The novelty of this antenna type is considered.

In Section 4.3, the new physical design of square and circular cavities of various sizes is discussed in detail, simulation results demonstrating that a metasurface at the cavity aperture is needed to reach the bound instead of a patch are presented and measured prototypes shown.

In section 4.4, achieving circular polarization with metasurface cavity antennas is briefly discussed. Two forms of excitations are described and two examples are given.

4.1. Transmission Line model for cavity antennas achieving the bound

A thorough analysis of simple, open ended, cavity antennas in an infinite ground plane using the transmission line models was given in Chapter 1.3.1. However in Chapter 3 we have analyzed the same geometric structure, but arrived at different results! For example, a direct comparison of plotted bandwidth behavior in Figure 36 (in Chapter 1.3.1) for transmission line theory and Figure 89 (in Chapter 3.3.1) for Gustafsson's bound visually shows the discrepancy between the two theories. In short, Gustafsson's bound predicts larger overall bandwidth values in all examples and bandwidth asymptotically approaches a maximum value as height is increased.

The discrepancy between the two theories asks for an explanation. First insight about the discrepancy comes from the meaning of the magnetic polarizability used in deriving Gustafsson's bound. If minimum Q depends on the low frequency limit (in this case – the magneto-static limit), then it effectively depends on the static (DC) current in the ground plane and the cavity. An addition of a capacitor at the aperture does not influence the result since static current does not flow through a capacitor. This indicates that “hidden” capacitor(s) could be a reason for predicting different bandwidth with the scattering theory.

Second insight comes from considering just the transmission line model of a cavity antenna. We ask the question: how can cavity antennas achieve larger bandwidth? The argument goes as follows. The waveguide part of a cavity antenna has an input admittance $Y_{in} = -j(k_{TE}/k\eta_0)\cot(k_{TE} h)$ which is capacitive when height is $\lambda_{TE}/4 < h < \lambda_{TE}/2$ and can bring the cavity structure into resonance. The problem with this capacitance is its frequency dependence, proportional to a cotangent function. In essence, larger the capacitive value needed, steeper the admittance gets. Consider again that $Q_{Ant} = 0.5 k_0/G_{Ap}(k_0)|\partial Y'(k_0)|$, i.e. quality factor is proportional to the steepness of the admittance function. Hence, we see the cotangent frequency dependence is undesirable. It would be more beneficial if the frequency dependence of capacitive admittance was just linear, like a typical capacitor $Y_C = j\omega C$.

Therefore, a transmission line model with added capacitor(s) should in fact be checked against the Gustafsson's bound.

4.1.1. Introduction of parasitic capacitance at the aperture

To avoid the need for any capacitive admittance added by the cavity part of the antenna, we introduce an additional capacitor at the aperture, as in Figure 92.

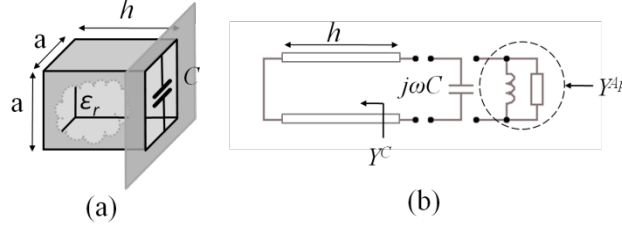


Figure 92 (a) Cavity antenna with parasitic capacitance at the aperture, and (b) its transmission line model.

If we wish to keep the aperture admittance used in the analysis of cavity antennas so far, we need to assume that the field distribution at the aperture remains the same. This means that the capacitor does not disturb the field too much and rules out a lumped element that would concentrate the field in a very small volume. The capacitor should be an ideal reactive impedance sheet.

From this model, the resonance condition is now given by

$$jB_{Ap}(k) - j \frac{k_{TE}}{k \eta_0} \cot(k_{TE} h) + jc_0 kC = 0, \quad (4.1)$$

where everything is written in terms of the wave-number k , with c_0 being the speed of light. The resonance condition is now one equation with three variables, h and C , and ϵ_r . However we will treat permittivity ϵ_r only as an additional parameter which we will fix to the best value. This allows us to consider capacitance C to be a function of height h . Therefore, for each height we calculate the necessary value of C to achieve resonance, then calculate Q and corresponding fractional bandwidth.

Importantly, the structure can now be resonant at low heights (compared to ordinary cavity antennas) because the input inductance of a shorted waveguide for $0 < h < \lambda_{TE}/4$ can be countered by an appropriately large value of the capacitance C at the aperture.

Additionally, with the introduction of C to achieve resonance, we are now free to choose any value of permittivity ϵ_r . We can argue that low permittivity is most beneficial for bandwidth. The waveguide becomes evanescent in this case and its effect is reduced. This argument can be rigorously demonstrated using the optimization method of Lagrange multipliers. Similar to the case of ordinary cavity antennas, we can minimize the Q factor with respect to the resonance condition for the antenna (4.1) introduced as a constraint. We introduce the Lagrange multiplier χ and construct a new, Lagrange function as

$$\Lambda = Q_{Ant}(\epsilon_r, h, C) - \chi \left(B_{Ap}(k) - \frac{k_{TE}}{k \eta_0} \cot(k_{TE} h) + c_0 kC \right). \quad (4.2)$$

Analogously to ordinary cavities, we search for stationary points, where partial derivatives of the Lagrange function with respect to permittivity ϵ_r , cavity height h , aperture capacitance C and the Lagrange multiplier χ are all zero, i.e.

$$\vec{\nabla}_{\epsilon_r, h, C, \chi} \Lambda = 0. \quad (4.3)$$

The resulting system of four equations is very cumbersome, and needs to be solved numerically on a computer. We skip the analytical expressions for brevity. Result of maximum bandwidth depending on permittivity ϵ_r is shown in Figure 93 for the example aperture sizes. The curves demonstrate that $\epsilon_r \leq 1$ gives the largest maximum bandwidth. The difference between $\epsilon_r = 0$ and $\epsilon_r = 1$ is in fact negligible, thus no real improvement is gained by theoretically using ideal metamaterials with $\epsilon_r < 1$ nor materials with $\epsilon_r \gg 1$.

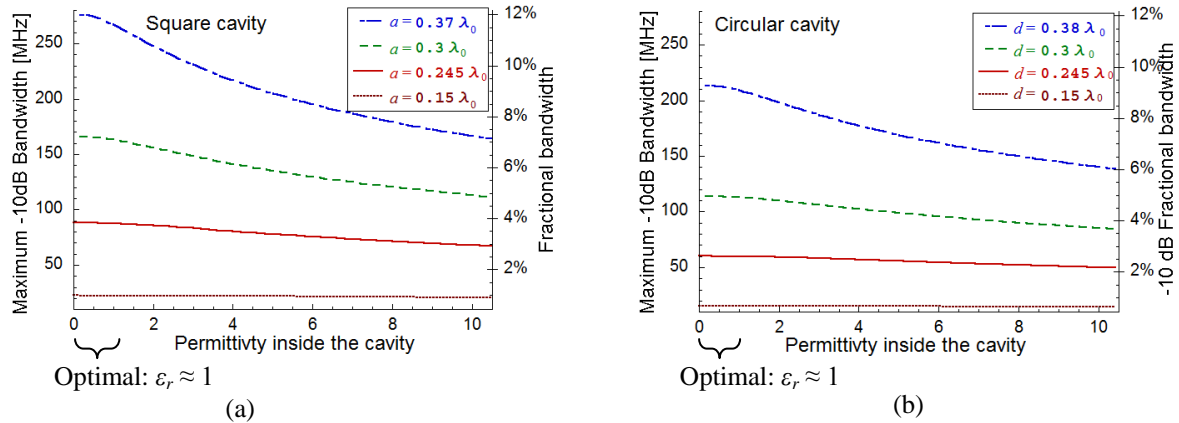


Figure 93 Dependence of maximum bandwidth on the permittivity inside the cavity. Values near $\epsilon_r = 1$ correspond to the asymptotic maximums visible in

We note that the concept of loading an aperture with a capacitor is not new; it has been investigated by Harrington [125] in a resonant scattering and transmission problem. However, Harrington did not discuss an antenna problem and suggested a lumped load. There was also a mention that wire dipoles shorter than half wavelength can be used to produce the capacitive susceptance. This is similar to a microstrip patch that can, in the case of thick cavities, be regarded as a very wide dipole at the aperture. Although a patch does present capacitive susceptance, we have shown through Chapters 2 and 3 that patch antennas do not reach the bound. The reason is that the patch acts as a series LC circuit at the aperture (suggested by the model in Chapter 2). The novelty of this work, compared to Harrington’s suggestions, is also in demonstrating that the ideal capacitor must be considered as a reactive impedance sheet.

Example: Bandwidth predictions from the model in Figure 92 are demonstrated in Figure 94 for a 32mm rectangular cavity infinite ground plane. Figure 94 can be directly compared with Figure 80 from Chapter 2, given for patch antennas at the aperture.

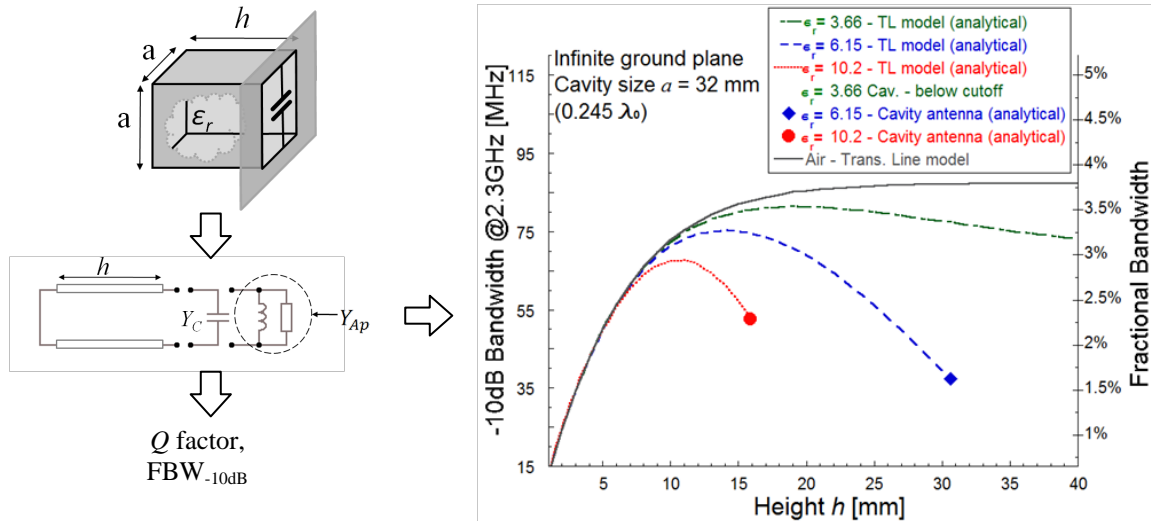


Figure 94 Calculated results for a square cavity ($a = 32$ mm) using the transmission line model. Points indicate ordinary cavity antenna operation. Grey full line for a cavity filled with air indicates the best case scenario.

4.1.2. Comparison with Gustafsson’s bound

Figure 95 visually demonstrates the similarity between predictions given by and ones made with the transmission line model. Excellent agreement is observed except for small discrepancies for larger cavity sizes where the transmission line model gives higher bandwidth predictions. Note that we use the approximate Gustafsson’s bound that involves polarizability obtained by assuming only the fundamental mode; with a more accurate bound the prediction from the transmission line model would be below the bound.

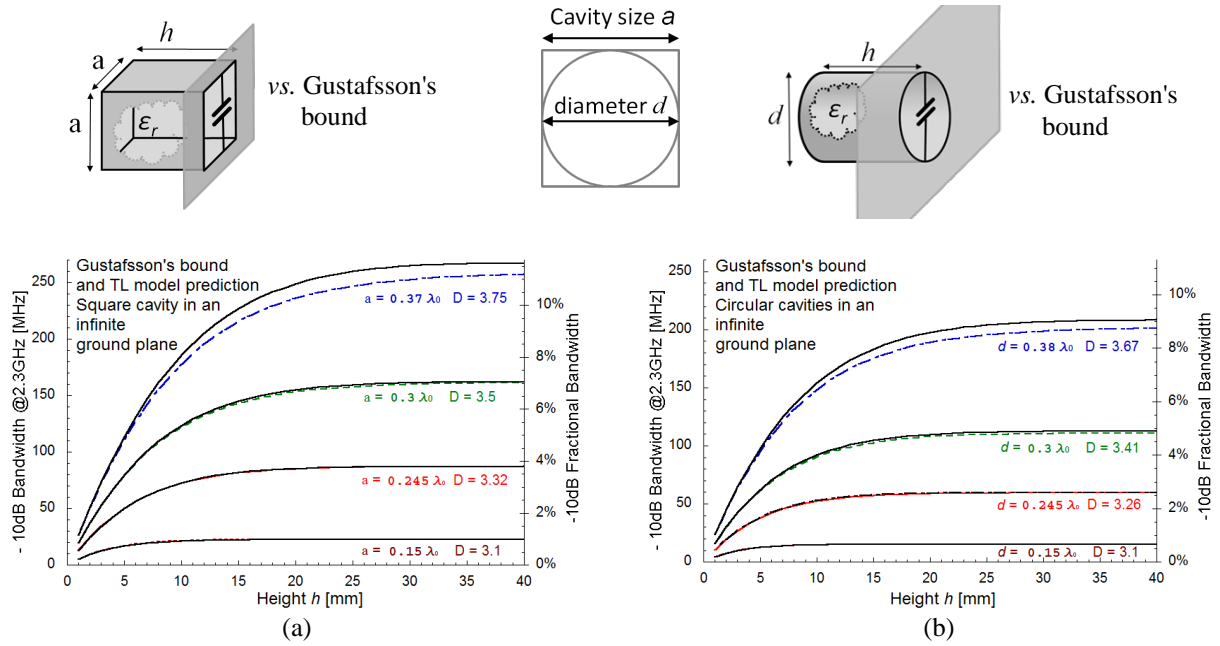


Figure 95 Comparing transmission line model results to Gustafsson's bound.

Using the Lagrange multiplier method again, we can calculate the maximum bandwidth depending on the aperture size or diameter. Result of the calculation is plotted with dots on Figure 96. Based on the calculated data, curve fitting was performed to obtain an analytical expression of the Q_{min} as

$$Q_{min}^{square} \approx \frac{59.24}{(ka)^3} + \frac{2.09}{ka}, \quad Q_{min}^{circular} \approx \frac{87.04}{(kd)^3} + \frac{3.06}{kd} \quad (4.4)$$

Or, to be more comparable with the Chu bound, in terms of the cavity radius

$$Q_{min}^{square} \approx \frac{20.95}{(kr)^3} + \frac{1.48}{kr}, \quad Q_{min}^{circular} \approx \frac{10.88}{(ka)^3} + \frac{1.35}{ka} \quad (4.5)$$

Where $r = a = a/\sqrt{2}$. Keep in mind that Q_{min} is achieved when cavity height h is large. Finally, we can conclude that the calculated Q_{min} 's using the transmission line model are indeed similar to the ones computed in Chapter 3.

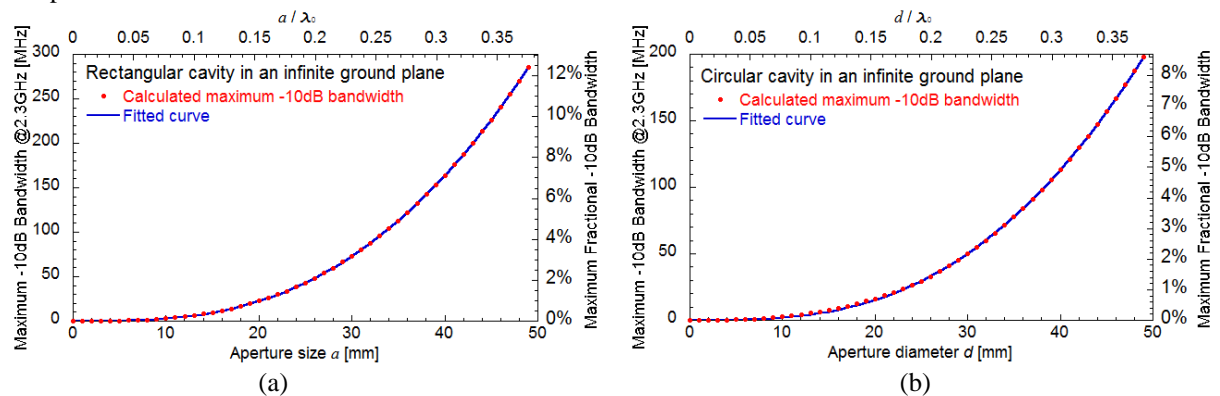


Figure 96 Maximum bandwidth ($FBW_{-10dB} = 2/(3Q_{min})$) for cavities in an infinite ground plane depending on (a) square aperture size a ; (b) circular aperture diameter d . Permittivity ϵ_r is taken to be 1.

4.1.3. Extension to finite ground plane antennas

The drawback of Gustafsson's scattering method is that it is applicable only to cavities in an infinite ground planes. In the finite ground plane case the scattering method would consider the whole object as a potential antenna, which is not realistic.

Transmission line model can easily be extended to the finite ground plane case and give realistic predictions on the Q factor and bandwidth. The only part that changes in the model is the aperture admittance. Obtaining the

aperture admittance for finite ground planes was already described in Chapter 1-261.3.1 for simple, open ended, cavity antennas. Using the the results (1.72) and (1.73) we can also repeat the procedure with the Lagrange multipliers to obtain maximum bandwidth and Q_{min} for the finite ground plane cavities. However, since the shape as ground affects the aperture admittance irregularly (the cavity exterior might have its own resonances) the obtained results are very approximate. Computed maximum bandwidth is shown in Figure 97. Curve fitting the data gives the approximate minimum quality factors as

$$Q_{min}^{square} \approx \frac{40.42}{(ka)^3} + \frac{3.39}{(ka)}, \quad Q_{min}^{circular} \approx \frac{65.98}{(kd)^3} + \frac{5}{(kd)}, \quad (4.6)$$

or, in terms of the cavity radius

$$Q_{min}^{square} \approx \frac{14.29}{(kr)^3} + \frac{2.4}{(kr)}, \quad Q_{min}^{circular} \approx \frac{8.25}{(ka)^3} + \frac{2.5}{(ka)}, \quad (4.7)$$

where $r = a = a/\sqrt{2}$.

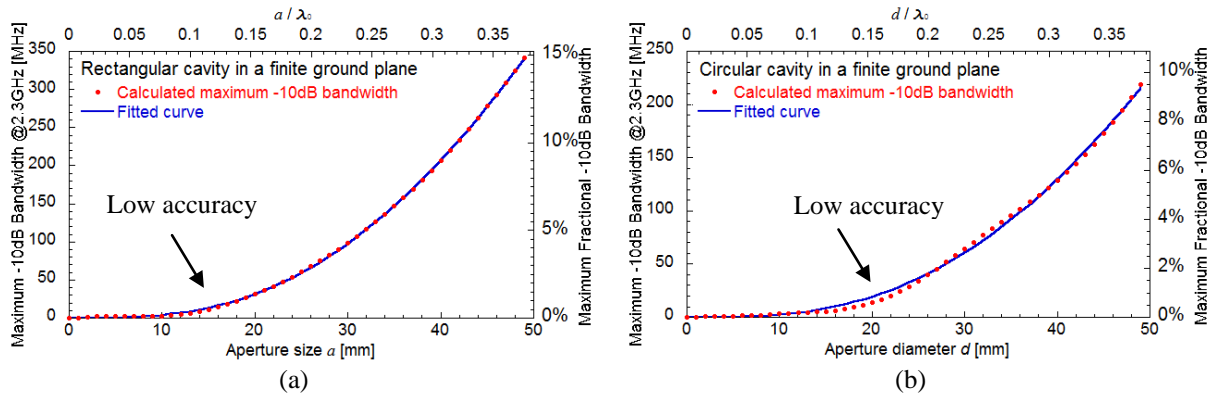


Figure 97 (a) Maximum bandwidth ($FBW_{-10dB} = 2/(3Q_{min})$) for cavities in a finite ground plane depending on (a) square aperture size a ; (b) circular aperture diameter d . Permittivity ϵ_r is taken to be 1.

4.2. From model to reality

Development of a real world working antenna is a completely different matter than analyzing a simple model that describes it. How should this capacitor at the aperture be made, since it is not a lumped element? There is no excitation indicated in the model, how should it be excited? These are real world questions that need to be answered; that will ultimately lead to an advancement in the field of cavity antennas.

4.2.1. Physical design of the capacitor at the aperture

As mentioned, instead of a lumped element, the capacitor introduced in the model on Figure 92 should correspond to a thin reactive sheet positioned at the aperture of the cavity. A single patch design does provide capacitance but was shown not to give desired performance due also to the inductance related with its geometry. Arranging multiple smaller patches instead of a single large patch leads to a decrease in the inductance and the desired result of “pure” capacitance at the aperture. The evolution of this process is depicted in Figure 98 for both circular and rectangular apertures. The geometry effectively creates a series connection of capacitors. Their values have to be larger if the total capacitance is to remain the same, thus the gaps between the elements get smaller when increasing the number of elements. By reducing the size of the metallic patches we are essentially “cutting” the current that usually exists in the center of a single patch into smaller pieces that contribute less to the inductance. Note that designs shown in Figure 98 are suitable only for a linearly polarized antenna.

Practical manufacturing considerations like precision tolerances create restrictions on the design. As discussed above, more elements approximate the parasitic capacitance better, but the exact gap size between the elements might be difficult to manufacture in a precise manner, especially the gap between the cavity and the elements if they are manufactured separately. It was found by simulation that the minimum number of elements to reach the bandwidth bound depends on the cavity size. For example, in the case of a $0.25 \lambda_0$ cavity the design with two elements at the aperture (Figure 98(b)) does not give satisfactory bandwidth results, but a design with three elements (Figure 98(c)) is already a good enough approximation for a pure capacitance. Additionally, four elements are satisfactory for a $0.3 \lambda_0$ cavity and 6 elements in the case of a $0.37 \lambda_0$ cavity.

Conclusion of our experimentation with simulations is a rough estimate that elements smaller than about $1/13 \lambda_0$ are needed to correctly approximate the capacitor at the aperture, depicted in Figure 99. Hence, elements satisfy the metamaterial criteria (element size $< 1/10 \lambda_0$). The structure can be called a metasurface.

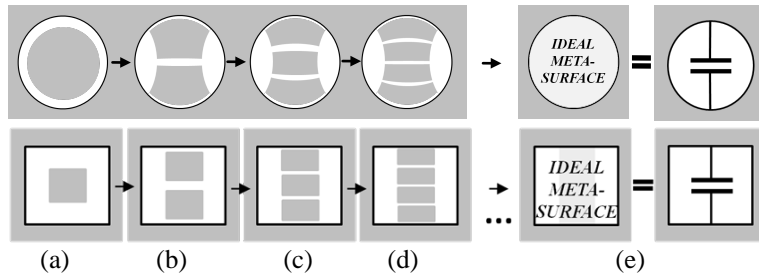


Figure 98 Possible designs of microstrip elements at the aperture of a square cavity. (a) a single patch design – used so far in the literature, (b) two element design, (c) three element design which is the first to give good enough approximation of a pure capacitance at the aperture, (d) four element design, (e) ideal case of a pure capacitance at the aperture.

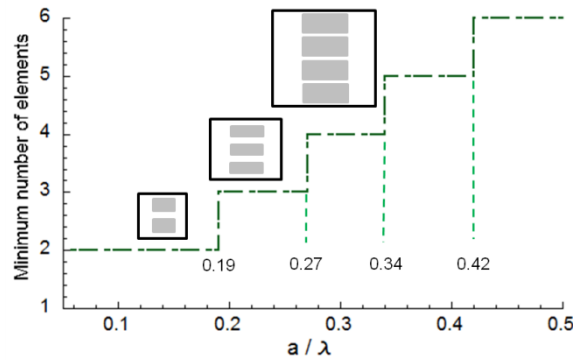


Figure 99 “Rule of thumb” for the minimum number of small patches to be used at the aperture, depending on its size, in order to correctly approximate a capacitor. Gaps between the elements then adjust the value of the needed capacitance C .

4.2.2. Antenna excitation

Proper excitation should not disturb the fundamental TE mode inside the cavity nor at the aperture. In this work we investigated several different types of excitation using a probe or an extended coaxial cable with a short probe, as shown in Figure 100. Just like classical patch antenna, the metasurface at the aperture can be probe fed as in Figure 100(a). The probe has to be close to the cavity wall so the TEM mode energy is confined mostly between the wire and the wall. With low permittivity in the cavity the distance between the wire and the wall becomes too small for practical purposes. The excitation with a loop, shown in Figure 100(b) also has a drawback of working only in cavities filled with a higher permittivity whereas our theory showed that best results are to be expected in a cavity filled with air. Figure 100(c) shows an excitation type that will work even if the cavity is filled with air. The coaxial cable is brought near the aperture where the central wire is then extended to the metasurface while its shield is electrically connected to the wall by a small transmission line. However, the connection with the wall is a practical difficulty in the manufacturing process. Figure 100(d) finally shows a design that is practical for manufacturing and suitable for any permittivity value inside the cavity. The coaxial cable is near the aperture with the central wire extended to the edge of the first element in the metasurface. A short transmission line is extended from the cables’ shield and is capacitive coupled to the edge of the second element in the metasurface.

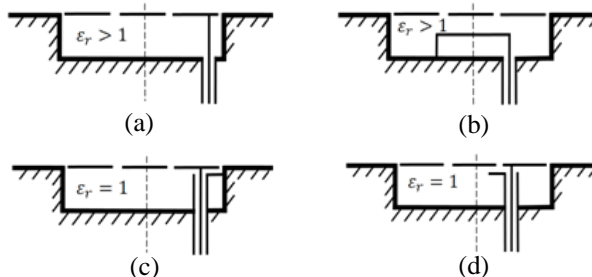


Figure 100 Several possible excitation types: (a) Probe feed attached directly to the metallization on the aperture, (b) loop created inside the cavity, (c) shielded cable raised to the aperture and connected to the cavity wall, (d) shielded cable raised to the aperture with a small transmission line attached to the shield.

Examples in Figure 100(a) and (b) will not be able to reach the bound on bandwidth at large cavity heights since they require materials with $\epsilon_r > 1$ in practice. Examples in Figure 100(c) and (d) are both capable of reaching the bound for any cavity height; however, example in Figure 100(d) is more practical.

4.2.3. What is new?

Dealing with electrically small cavities, we had to add a semitransparent capacitive structure and propose the correct way to design it. The proposed cavity antenna is a metasurface inspired antenna, based on the definition given in Chapter 1.4.1. In a comparison to previous uses of metasurfaces, we conclude the following

- Metasurfaces were previously used to form artificial ground planes for other types of antennas. However in the proposed cavity antenna the novelty is that the metasurface is the main radiating element and not a ground plane for something else.
- Metasurfaces, as semitransparent surfaces, were previously used in cavity type antennas which were large. Additionally, the cavity ground plane and the metasurface could be distanced an appreciable amount of the wavelength and form a Fabry-Perot resonator. However, in the proposed cavity antenna the fields are evanescent inside the cavity; in fact, operation below the cut-off frequency of the cavity is necessary to obtain best bandwidth performance.

From the theoretical perspective, new physical bounds on bandwidth were derived for cavity antennas with strictly broadside radiation pattern and can be directly compared to the old Chu bound. Remarkably, it is found that by a simple modification of the model describing the simple cavity antenna, namely the addition of parasitic capacitive reactance at the aperture, the new model is able to predict the same bound. This allows for a complete understanding of the antenna and a roadmap for its design. Thus, the most important novelty of all is the actual, feasible antenna that reaches the theoretical bound on bandwidth. Additionally, compared to patch antennas, the directivity and gain of such antennas is not compromised.

4.3. Cavity antennas reaching the bound on bandwidth

Here we present examples of feasible metasurface antenna designs for the square and circular cases. In practice, the metasurface has to be manufactured on a substrate of some permittivity and the cavity part is often manufactured separately. In the end the two have to be glued together. We discuss the effects of these real world necessities on the antenna operation.

We show full wave simulation results carried out with the newly designed antenna to confirm the analytical predictions from the transmission line model are presented. Good agreement is found for small cavity antennas with $(a/\lambda_0) < 0.35$. Finally, manufactured prototypes are presented to confirm the simulations and prove the feasibility of such antennas.

4.3.1. Design of a square cavity antenna

Shown on Figure 101(a) is a schematic antenna design fulfilling the practical needs. The gap g between the elements is adjusted for the right value of capacitance. The gap between the cavity wall and the first element of the metasurface is $g/2$. Presence of the glue with thickness g , in this gap can substantially affect the performance. Glue changes the overall capacitive effect of the metasurface because of its different permittivity value and introduces additional (high) losses. For realization purposes it is therefore desirable to make the gaps between the elements of the metasurface and the wall as wide as possible, to relatively reduce the effect of the glue. This can be done by using a high permittivity substrate on which the metasurface is etched and to use multiple layers to increase the capacitance.

A Metasurface with multiple layers of metallization, shown in Figure 101(b), will effectively make the metasurface a “thick” capacitor. This concept is discussed in detail in Chapter 5 and only mentioned in this section. We note here that too many layers will decrease the bandwidth performance because a “thick” capacitor cannot be regarded as being strictly at the aperture. Designing with multiple layers should therefore be avoided if possible. Only in very small cavities, where a large capacitive effect needed, are we forced to consider this option.

Additionally, it was found that tapering the transmission line (see Figure 101(b)) attached to the coaxial cable shield can give slightly better results. The width w of the metallic elements also effects bandwidth performance. Wider elements will force the electric field at the aperture to be more uniform instead of a sinusoidal distribution, which will lead to slightly better performance. However, with wider metasurface elements the gap between the elements had to be reduced. Finally, a width of one half the cavity size was found to be convenient.

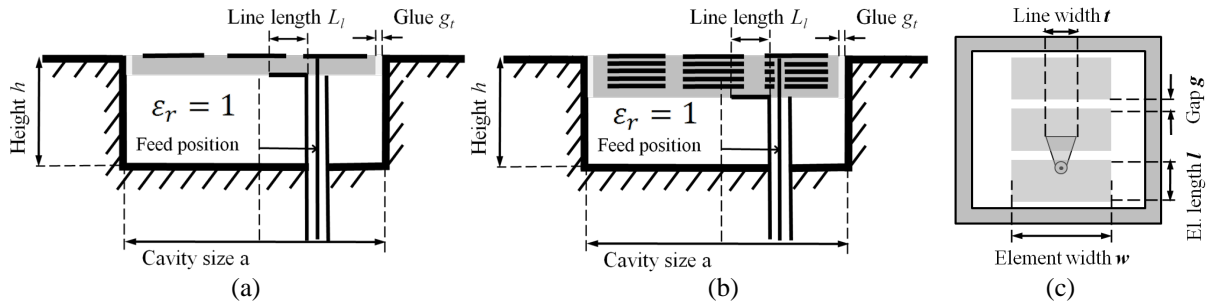


Figure 101 Schematic example of a practical design for manufacturing purposes in the case of a $0.245 \lambda_0$ square cavity. The single layer of substrate material at the aperture has $\epsilon_r \gg 1$, in our work, $\epsilon_r = 10.2$ was chosen. (a) Side view of a single layer design. (b) Side view of a multiple layer design necessary for very small cavity sizes. (c) Top view.

SIMULATION RESULTS

For the example cavity sizes, we investigated bandwidth performance depending on height up to 40 mm ($0.3 \lambda_0$) in discrete increments of height ($\Delta h = 5$ mm). Full wave simulations using the design shown in Figure 101(a) were carried out using commercial software CST [130]. The multilayer design from Figure 101(b) was used only in the case of the smallest cavity size (20 mm). The matching condition was optimized for each height by adjusting the gap size between the elements, the coaxial feed position and the length of the tapered transmission line extended from the shield of the coaxial cable. In the simulations we used lossless substrates. With realistic materials, having losses, an increase in bandwidth compared to shown result is expected, with a corresponding decrease in radiation efficiency. The results are shown in Figure 102.

It is seen that for $a/\lambda_0 < 0.35$ the correct bandwidth behavior is observed. For the case of an infinite ground plane, bandwidth curves are close to within a few percent to the predictions the Gustafsson's bound obtained in Chapter 3. Predictions by the transmission line model, introduced in this chapter are added for comparison with Gustafsson's bound. For each cavity size, a schematic is added to the figure to note the number of metasurface elements used in the simulations.

In the case of a finite ground plane predictions are possible only with the transmission line model. These predictions are only approximate due to effect of the finite ground plane size which was taken to be constant in the model, but is in fact changing with height in the simulations (the ground plane is becoming larger with increasing height). Because of this, there is some disagreement between the predictions and simulation data. However, the general bandwidth behavior and bandwidth values are not far apart. The biggest differences are seen in the smallest and largest example size; these differences are addressed below.

Comments on the 20 mm ($0.15 \lambda_0$) cavity size:

For this example size, the antenna design shown in Figure 101(b) had to be used to achieve a large enough capacitive effect to bring the antenna resonance to 2.3 GHz. Simulation data shows that the bandwidth of such antenna design is slightly below the bound, which is unfortunate. The difference between the physical bound or the transmission line model prediction and the simulation results is attributed to the finite thickness of the multilayer metasurface at the aperture. If the capacitor that the metasurface represents is not at the aperture, but has a small portion of a waveguide to the aperture, the transmission line model can correctly predict a decrease in bandwidth. Therefore, when possible, multiple layers should be avoided by using an even higher substrate permittivity which will lead to antennas performing even closer to the bound.

Comments on the 48 mm ($0.37 \lambda_0$) cavity size:

The case of $a/\lambda_0 = 0.37$ shows significant deviation from theory, both in the infinite and finite ground plane case. In fact, a second higher cavity resonance starts affecting performance of the antenna. In such antennas the S_{11} parameter becomes highly asymmetric around the center frequency of 2.3 GHz. This second cavity resonance is a consequence of the behavior of the aperture admittance at higher frequencies. Additionally, the assumptions in deriving the Gustafsson bound where a single resonance antenna with a high Q factor, while in this case the predicted minimum Q factor is close to 6, which is low value. Furthermore, the link between the Q factor and fractional bandwidth is not clear in the case of multiple resonances. Due to these reasons, we can claim the validity of the theory presented in this thesis up to cavity sizes with $a/\lambda_0 < 0.35$.

On the other hand, this bandwidth broadening effect of the second resonance can be effectively used to design broadband cavity antennas; topic further explored in Chapter 5.

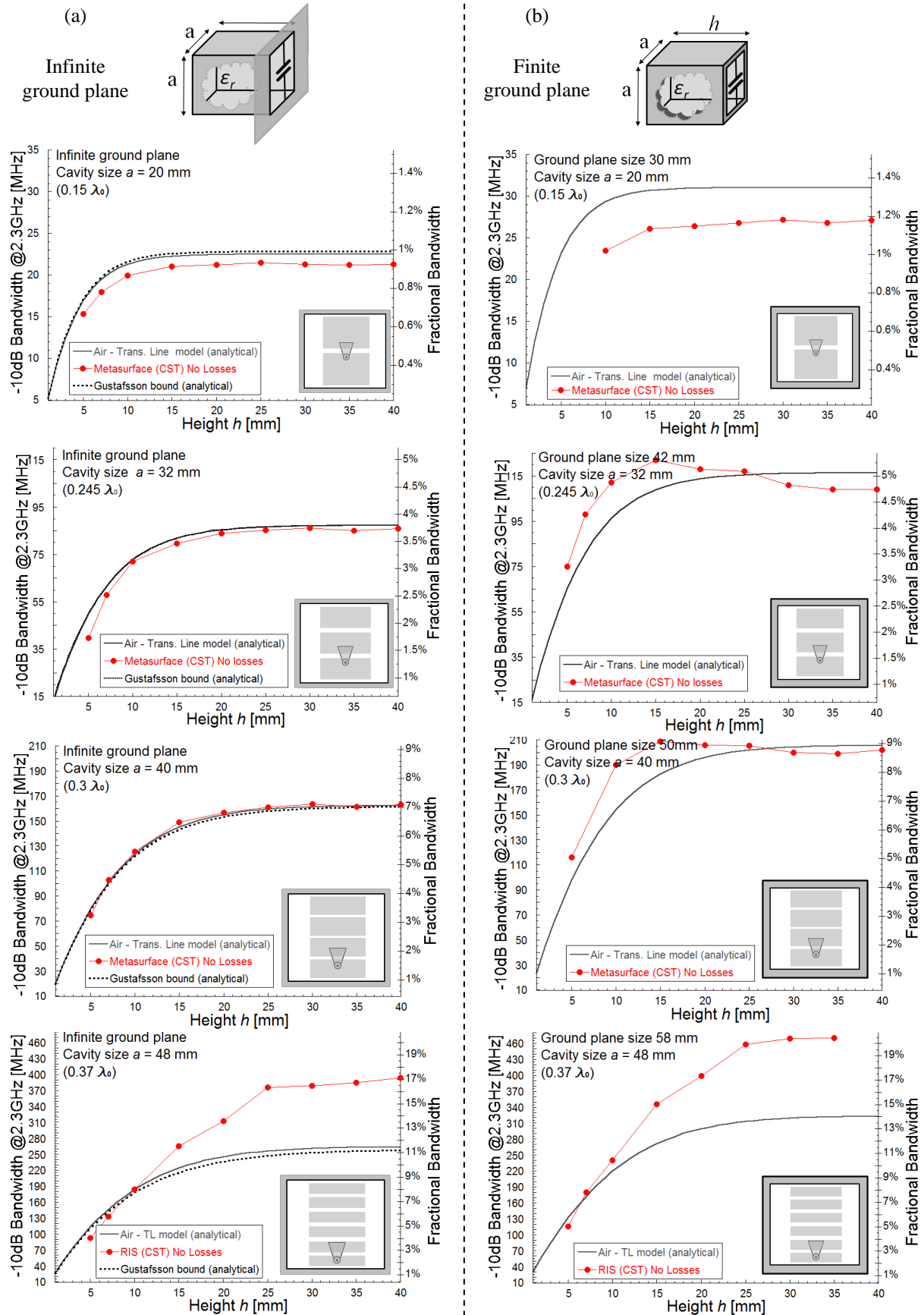


Figure 102 Comparison of simulation results of a metasurface design to analytical predictions from the transmission line model and to the Gustafsson bound on bandwidth (where the polarizability approximation (3.47) is used). (a) infinite ground plane and (b) finite ground plane results.

4.3.2. Design of a Circular cavity antenna

Shown on Figure 103(a) is a schematic antenna design for circular cavity geometry fulfilling the practical needs. Similar to the rectangular case, the gap g between the elements is adjusted for the right value of capacitance. The gap between the cavity wall and the first element of the metasurface is $g/2$ and the presence of glue with thickness g_t in this gap can substantially affect the performance. For realization purposes it is therefore desirable to make the gaps between the elements of the metasurface and the wall as wide as possible, to reduce the relative effect of the glue. This can be done by using a high permittivity substrate on which the metasurface is etched and to use multiple layers to increase the capacitance, shown in Figure 103(b). However, too many layers will decrease the bandwidth performance. A small transmission line extending from the coaxial cable, seen in Figure 103(c) is used to match the antenna. Tapering this transmission line reduces its necessary length and was found to lead to slightly better bandwidth performance.

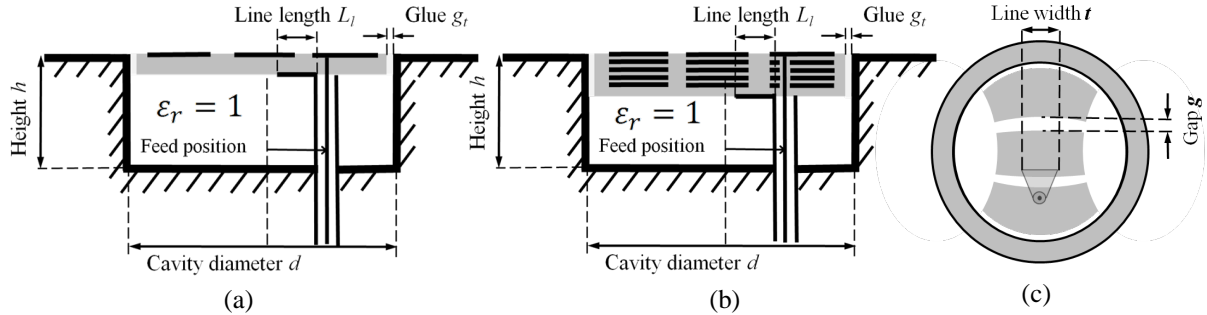


Figure 103 Schematic example of a practical design for manufacturing purposes in the case of a $0.245\lambda_0$ circular cavity. The single layer of substrate material at the aperture has $\epsilon_r \gg 1$, in our work, $\epsilon_r = 10.2$ was chosen. (a) Side view of a single layer design. (b) Side view of a multiple layer design necessary for very small cavity sizes. (c) Top view.

Designing a metasurface that will approximate a capacitor at the aperture for circular geometry is considerably more challenging than for rectangular geometry. The reason is that the shape of the metallization should follow the electric and magnetic field lines of the TE_{11} mode which are curved. An example of how these shapes have to look like was already shown on Figure 98 and also on Figure 103(c). The main practical problem is how to define these curved shapes in the electromagnetic simulation software and perform optimizations?

In commercial simulators like CST and HFSS, in which the author had experience during his thesis, there is an option to construct analytical curves by writing parametric equations in the form $(x(t), y(t))$. With this option, one can define all the necessary curved lines that make up the edges of the 2D shape and fill in the area with a PEC, thus constructing the wanted shape. One only needs to know the parametric functions with which to construct the curved lines of the TE_{11} mode. Unfortunately, this is a huge problem!

The field of the TE_{11} mode is usually written in cylindrical coordinates using Bessel functions; to get parametric functions of the field lines (called “streamlines of vector fields” in mathematics) one would need to convert the field to Cartesian coordinates and solve a series of differential equations

$$\begin{aligned} \frac{dx(t)}{dt} &= E_x(x, y), \\ \frac{dy(t)}{dt} &= E_y(x, y). \end{aligned} \quad (4.8)$$

Needless to say, these differential equations are not analytically solvable. One can always obtain a particular solution numerically, but this is useless for the simulation software where the ability to change any shape on the fly is crucial in optimizing the whole design.

To avoid the problematic of solving (4.8), the author suggests approximating the TE_{11} lines with ellipses for which parametric functions could be found “easily”. The following idea is used in this thesis: There is good similarity between E and H lines in a circular waveguide and equipotential and streamline lines defined by two lines of opposite charges. This is depicted in Figure 104. The difference is that the equipotential and streamline lines are circles and are not curved exactly like E and H lines, thus some “tuning” has to be done.

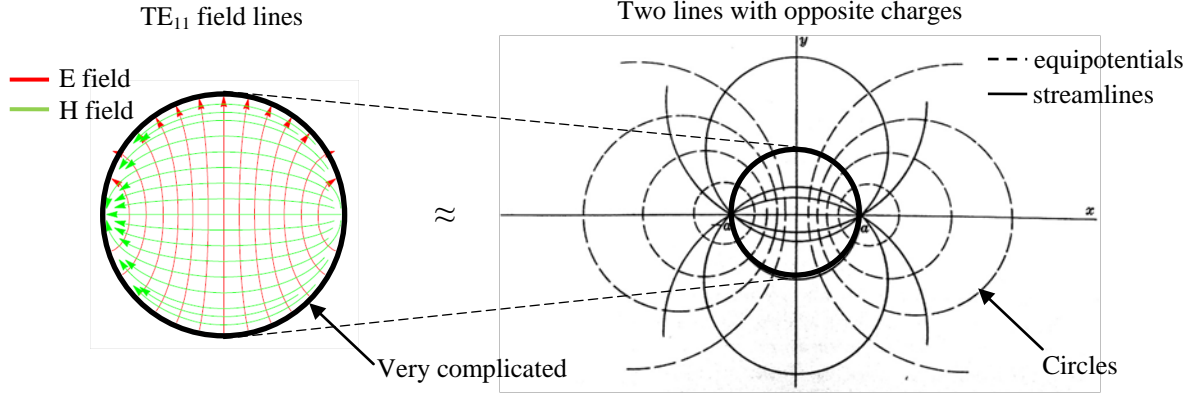


Figure 104 Similarity between the field lines of a TE₁₁ circular mode and the equipotential lines of two line charges. This similarity is exploited to approximate the field lines analytically.

Here we give the procedure to obtain the parametric functions for constructing the metasurface shape. In order to obtain equipotential and streamline lines we are using the method of conformal mapping to find the complex potential due to a source at $z = -a$ and a sink at $z = a$ of equal strengths. Complex potential due to a source $z = -a$ of strength s is usually denoted $s \ln(z + a)$. However, we can use the strength $s = 1$ for simplicity. The complex potential due to a sink at $z = a$ is thus $-\ln(z - a)$. The total complex potential is written as

$$\varphi(z) = \ln(z + a) - \ln(z - a) = \ln\left(\frac{z + a}{z - a}\right). \quad (4.9)$$

Let $z + a = r_1 e^{-j\theta_1}$, $z - a = r_2 e^{-j\theta_2}$. Then we have

$$\varphi(z) = \Phi + j\Psi = \ln\left(\frac{r_1 e^{-j\theta_1}}{r_2 e^{-j\theta_2}}\right) = \ln\left(\frac{r_1}{r_2}\right) + j(\theta_1 - \theta_2) \quad (4.10)$$

So that $\Phi = \ln(r_1/r_2)$, $\Psi = (\theta_1 - \theta_2)$. The equipotential lines and streamlines are given by

$$\begin{aligned} \Phi &= \ln(r_1/r_2) = \alpha, \\ \Psi &= (\theta_1 - \theta_2) = \beta. \end{aligned} \quad (4.11)$$

Using $r_1 = \sqrt{(x + a)^2 + y^2}$, $r_2 = \sqrt{(x - a)^2 + y^2}$, $\theta_1 = \tan^{-1}\{y/(x + a)\}$, $\theta_2 = \tan^{-1}\{y/(x - a)\}$, the equipotential and streamlines are given by

$$\begin{aligned} \Phi &= \frac{(x + a)^2 + y^2}{(x - a)^2 + y^2} = e^{-\alpha}, \\ \Psi &= \tan^{-1}\{y/(x + a)\} - \tan^{-1}\{y/(x - a)\} = \beta \end{aligned} \quad (4.12)$$

This can be rewritten in the form

$$\begin{aligned} \text{Equipotentials: } & [x - a \coth(\alpha)]^2 + y^2 = a^2 \operatorname{csch}^2(\alpha) \\ \text{Streamlines: } & x^2 + [y + a \cot(\beta)]^2 = a^2 \operatorname{csc}^2(\beta) \end{aligned} \quad (4.13)$$

Equipotentials for different values of α are circles having centers at $a \coth(\alpha)$ and radii equal to $a \operatorname{csch}(\alpha)$. Streamlines for different values of β are circles having centers at $-a \cot(\beta)$ and radii $a|\operatorname{csc}(\beta)|$. These circles, which pass through $(-a, 0)$ and $(a, 0)$ are shown in Figure 104.

Remembering the in parametric form a simple circle $x^2 + y^2 = r^2$ is defined by $x = r \sin(t)$, $y = r \cos(t)$, we rewrite (4.13) as

$$\begin{aligned} \text{Equipotentials: } & \begin{cases} x(t) - a \coth(\alpha) = a \operatorname{csch}(\alpha) \sin(t) \\ y(t) = a \operatorname{csch}(\alpha) \cos(t) \end{cases} \\ \text{Streamlines: } & \begin{cases} x(t) = a \operatorname{csc}(\beta) \sin(t) \\ y(t) + a \cot(\beta) = a \operatorname{csc}(\beta) \cos(t) \end{cases} \end{aligned} \quad (4.14)$$

Finally, we want to insert the factors α and β using (4.11) in a way enabling us to specify a point on the x, y axes through which the circles will pass. For equipotentials we choose points $(x_p, y = 0)$ and for streamlines $(x = 0, y_p)$ and write (4.14) in full form as

$$\begin{aligned}
 \text{Equipotentials: } & \begin{cases} x(t) = \frac{a \sin(t)}{\sinh\left(\ln\left(\frac{x_p + a}{x_p - a}\right)\right)} + a \coth\left(\ln\left(\frac{x_p + a}{x_p - a}\right)\right) \\ y(t) = \frac{a \cos(t)}{\sinh\left(\ln\left(\frac{x_p + a}{x_p - a}\right)\right)} \end{cases} \\
 \text{Streamlines: } & \begin{cases} x(t) = \frac{a \sin(t)}{\sin\left(2\tan^{-1}(y_p)\right)} \\ y(t) = \frac{a \cos(t)}{\sin\left(2\tan^{-1}(y_p)\right)} - a \cot\left(2\tan^{-1}(y_p)\right) \end{cases}
 \end{aligned} \tag{4.15}$$

We now introduce a modification to (4.15) in the form of several additional factors to transform the circles into ellipses that better approximate the actual E and H field lines of the TE_{11} mode. These factors are guessed, as they were determined by a visual comparison of the types of lines and not some rigorous method. In the end, the following analytical functions were found to approximate the TE_{11} lines quite well

$$\begin{aligned}
 \text{Approx. E lines: } & \begin{cases} x(t) = \frac{0.96 a \sin(t)}{\sinh\left(\ln\left(\frac{x_p + a}{x_p - a}\right)\right)} + a \coth\left(\ln\left(\frac{x_p + a}{x_p - a}\right)\right) \\ y(t) = \frac{1.35 a \cos(t)}{\sinh\left(\ln\left(\frac{x_p + a}{x_p - a}\right)\right)} \end{cases} \\
 \text{Approx. H lines: } & \begin{cases} x(t) = \frac{1.4 a \sin(t)}{\sin\left(2\tan^{-1}(y_p)\right)} \\ y(t) = \frac{a \cos(t)}{\sin\left(2\tan^{-1}(y_p)\right)} - a \cot\left(2\tan^{-1}(y_p)\right) \end{cases}
 \end{aligned} \tag{4.16}$$

In the design of the metasurface for linear polarization, it is enough to choose one point x_p and the choice of half the radius ($a/2$) was found to be convenient and work well. Points y_p are chosen to break the shape into smaller pieces and points are chosen depending on how many pieces are needed. An example is given in for a 3 piece metasurface is given in Figure 105.

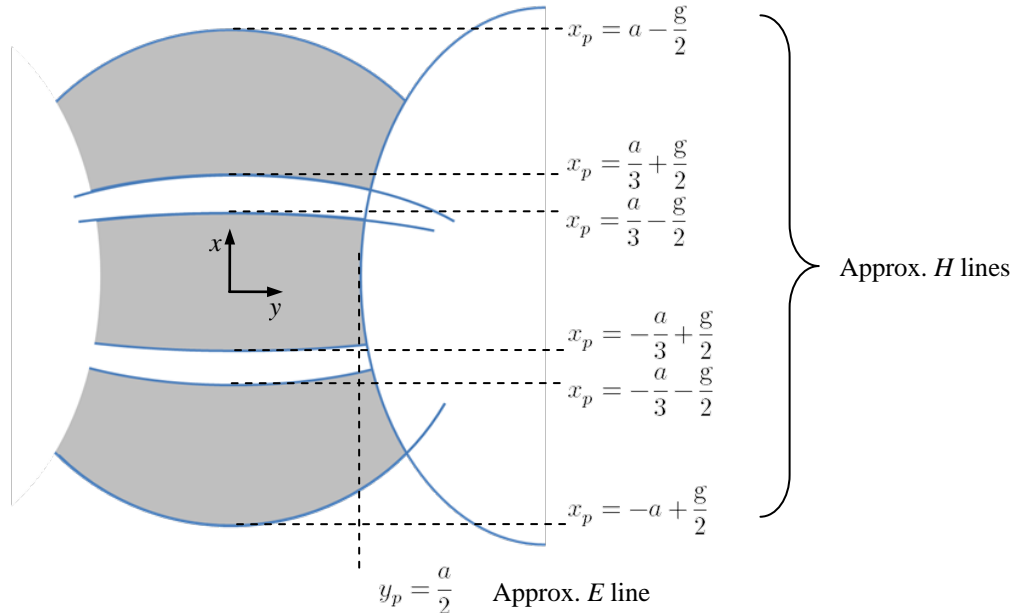


Figure 105 Three element metasurface design for circular geometry. a represents the cavity radius, g is the gap size between the elems.

It was found that the top and bottom H line curve can remain circles if wanted, but other lines should indeed be approximations of the real E and H lines of there is degradation in bandwidth performance.

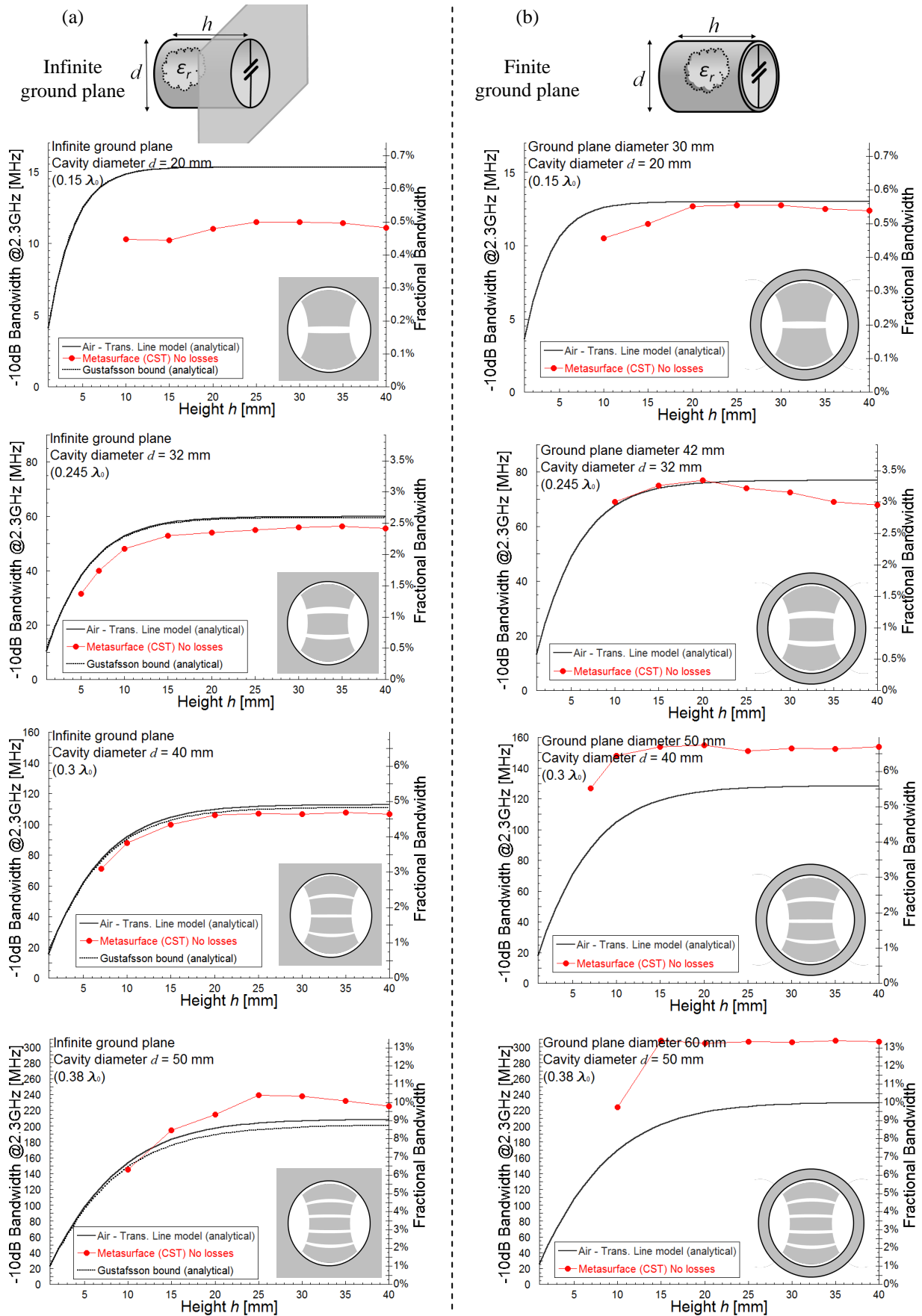


Figure 106 Comparison of simulation results of a metasurface design to analytical predictions from the transmission line model and to the Gustafsson bound on bandwidth (where the polarizability approximation (3.79) is used). (a) infinite ground plane and (b) finite ground plane results.

SIMULATION RESULTS

For the example cavity diameters, bandwidth performance depending on height up to 40 mm ($0.3 \lambda_0$) was investigated in discrete increments of height ($\Delta h = 5$ mm). Full wave simulations using the design shown in Figure 103(a) were carried out using commercial software CST [130]. The multilayer design from Figure 103(b) was used only in the case of the smallest cavity diameter (20mm). The matching condition was optimized for each height by adjusting the gap size between the elements, the coaxial feed position and the length of the tapered transmission line extended from the shield of the coaxial cable. In the simulations we used lossless substrates. With realistic materials, having losses, an increase in bandwidth compared to shown result is expected, with a corresponding decrease in radiation efficiency. The results are shown in Figure 106.

The correct bandwidth behavior is observed for $d/\lambda_0 < 0.35$. In the case of an infinite ground plane, bandwidth curves are close to within a few percent to the predictions the Gustafsson's bound obtained in Chapter 3. Predictions by the transmission line model, introduced in this chapter are added for comparison with Gustafsson's bound. For each cavity size, a schematic is added to the figure to note the number of metasurface elements used in the simulations.

In the case of a finite ground plane predictions are possible only with the transmission line model. These predictions are only approximate due to effect of the finite ground plane size which was taken to be constant in the model, but is in fact changing with height in the simulations (the ground plane is becoming larger with increasing height). Because of this, there is some disagreement between the predictions and simulation data. However, the general bandwidth behavior and bandwidth values are not far apart. The biggest differences are seen in the smallest and largest example size; these differences are addressed below.

Comments on the 20 mm ($0.15 \lambda_0$) cavity diameter:

For this example size, the antenna design shown in Figure 103(b) had to be used to achieve a large enough capacitive effect to bring the antenna resonance to 2.3 GHz. Simulation data shows that the bandwidth of such antenna design is unfortunately below the bound. This difference between theory and simulation results is attributed to the finite thickness of the multilayer metasurface at the aperture. If the capacitor that the metasurface represents is not at the aperture, but has a small portion of a waveguide to the aperture, the transmission line model can correctly predict a reduction in bandwidth. Therefore, when possible, multiple layers should be avoided by using an even higher substrate permittivity which will lead to antennas performing even closer to the bound.

Comments on the 40 ($0.3 \lambda_0$) and 50 mm ($0.38 \lambda_0$) cavity diameter:

The case of $d/\lambda_0 = 0.38$ shows deviation from theory, both in the infinite and finite ground plane case. In the case of $d/\lambda_0 = 0.3$ deviation is seen only in the finite ground plane case. One may be puzzled by the apparent result that the antennas are operating better than the bound, which should be impossible. To explain this, we have to revert back to the starting assumptions. The assumptions in deriving Gustafsson's bound were a high Q factor, while in this case of larger aperture sizes the predicted minimum Q factor is low value, but more importantly, a single resonance antenna is assumed. However, in the simulations a second higher cavity resonance is observed and is affecting the performance of the antenna. In such antennas the S_{11} parameter becomes highly asymmetric around the center frequency of 2.3 GHz. This second cavity resonance is a consequence of the behavior of the aperture admittance at higher frequencies. The link between the Q factor and fractional bandwidth is not clear in the case of multiple resonances. Due to these reasons, we can claim the validity of the theory presented in this thesis up to cavity sizes with $d/\lambda_0 < 0.35$ for the infinite ground plane case. For the finite ground plane case we can claim validity for $d/\lambda_0 < 0.3$. Keep in mind that the predictions for the finite ground plane are only approximate.

This bandwidth broadening effect of the second resonance can be effectively used to design broadband cavity antennas; topic further explored in Chapter 5.

4.3.3. Measurement results

Rectangular prototype:

A prototype of a $32 \times 32 \times 15$ mm ($0.245 \lambda_0 \times 0.245 \lambda_0 \times 0.115 \lambda_0$) cavity has been manufactured at the French-German Research Institute of Saint-Louis. The ground plane was a square block of aluminum $300 \times 300 \times 15$ mm in size with the cavity antenna at the center, shown on Figure 107(a)-(b).

The substrate holding the metallization is Rogers 3010 having permittivity 11.2 (suggested for design in the datasheet) and loss tangent 0.0022, given by the manufacturer. Thickness of the substrate layer was 0.64mm. However, we used 2 layers, one for the upper, metasurface, metallization and one for the bottom, tapered transmission line, metallization. Total substrate thickness was 1.28 mm. Next, the substrate was glued to the cavity wall with a thin layer of glue (≈ 0.2 mm) having approximate permittivity value of 3.5 and loss tangent estimated to be 0.03. Metallization forming the metasurface has the dimensions of width $w = 22$ mm, element

length $l = 9.347$ mm and gap $g = 1.32$ mm. The feeding position is soldered 6.7 mm from the cavity center. Tapered transmission line has the line length $L_t = 2.45$ mm and line width $t = 7$ mm.

Note that the simulation result for this cavity size $0.245 \lambda_0$, shown above on Figure 106(a) assumes no losses anywhere in the antenna and had a bandwidth of about 80 MHz, close to the bound which is also derived for a lossless case. Manufactured antenna has losses of course, thus a simulation including losses was performed, and the result is shown in Figure 107(e). The simulated bandwidth result is 92 MHz. The measurement result, also given on Figure 107(a), is in close agreement with the simulation, resonating at 2.28 GHz, and having 96 MHz of bandwidth.

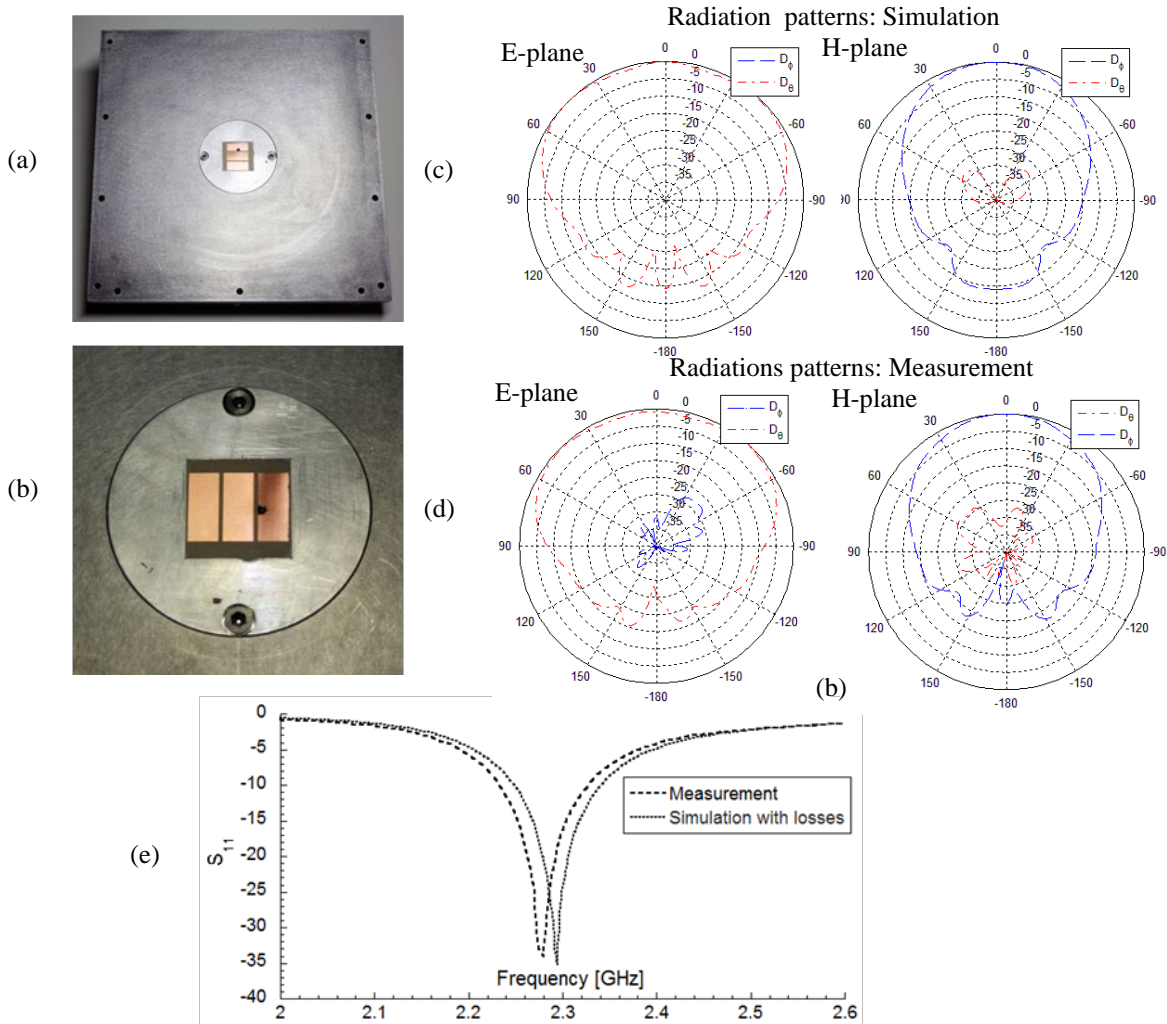


Figure 107 (a) Manufactured prototype of a square cavity antenna in a large ground plane. (b) Close up of the cavity antenna showing the metasurface at the aperture. (c) Simulated radiation pattern in CST. (d) Measured radiation pattern (e) Simulated S_{11} parameter having 92MHz at 2.3 GHz and measured S_{11} parameter showing 96 MHz of bandwidth at 2.28 GHz.

Figure 107(c)-(d) shows a comparison of simulated and measured far field patterns, demonstrating a broadside radiation pattern. Simulated gain was 5.1 dBi at 2.3 GHz with an efficiency of 89%. Measured gain was 4.6 dBi at 2.28 GHz with an efficiency of 85%. The measured half power beam width in the E-plane is 149.5° and in the H-plane 70.5° , in very good agreement with the simulation.

Circular prototype

A finite ground plane circular cavity prototype with aperture diameter of a 32 mm ($0.245 \lambda_0$), cavity height 15 mm ($0.115 \lambda_0$) and wall thickness of 5 mm in all directions has been manufactured at the French-German Research Institute of Saint-Louis. The manufactured cavity antenna is shown on Figure 108(a).

The substrate holding the metallization is Rogers 3010 having permittivity 11.2 and loss tangent 0.0022, given by the manufacturer. Thickness of the substrate layer was 0.64 mm. However, we used 3 layers, two for a multilayered metasurface metallization and one for the bottom, tapered transmission line, metallization. Total substrate thickness was 1.92 mm. Next, the substrate was glued to the cavity wall with a thin layer of glue (≈ 0.2 mm) having approximate permittivity value of 3.5 and loss tangent estimated to be 0.03. Metallization

forming the metasurface has gap $g = 2.05$ mm. The feeding position is soldered 6.6 mm from the cavity center. Tapered transmission line has the line length $L_t = 2.25$ mm and line width $t = 5.6$ mm.

Simulation result for this cavity size $0.245 \lambda_0$, shown above on Figure 106(b) assumes no losses anywhere in the antenna and had a bandwidth of about 75 MHz, close to the bound which is also derived for a lossless case. Manufactured antenna has losses of course, thus a simulation including losses was performed, and the result is shown in Figure 108(c). The simulated bandwidth result is 80 MHz. The measurement result, also given on Figure 108(a), is in close agreement with the simulation, having a bit larger bandwidth of 90 MHz. Probable cause for larger bandwidth are larger losses in reality, compared to the simulation. Importantly, compared to a classical patch antenna in a similar cavity size (achieving about 65 MHz), bandwidth of 90 MHz is an increase by about 40 %.

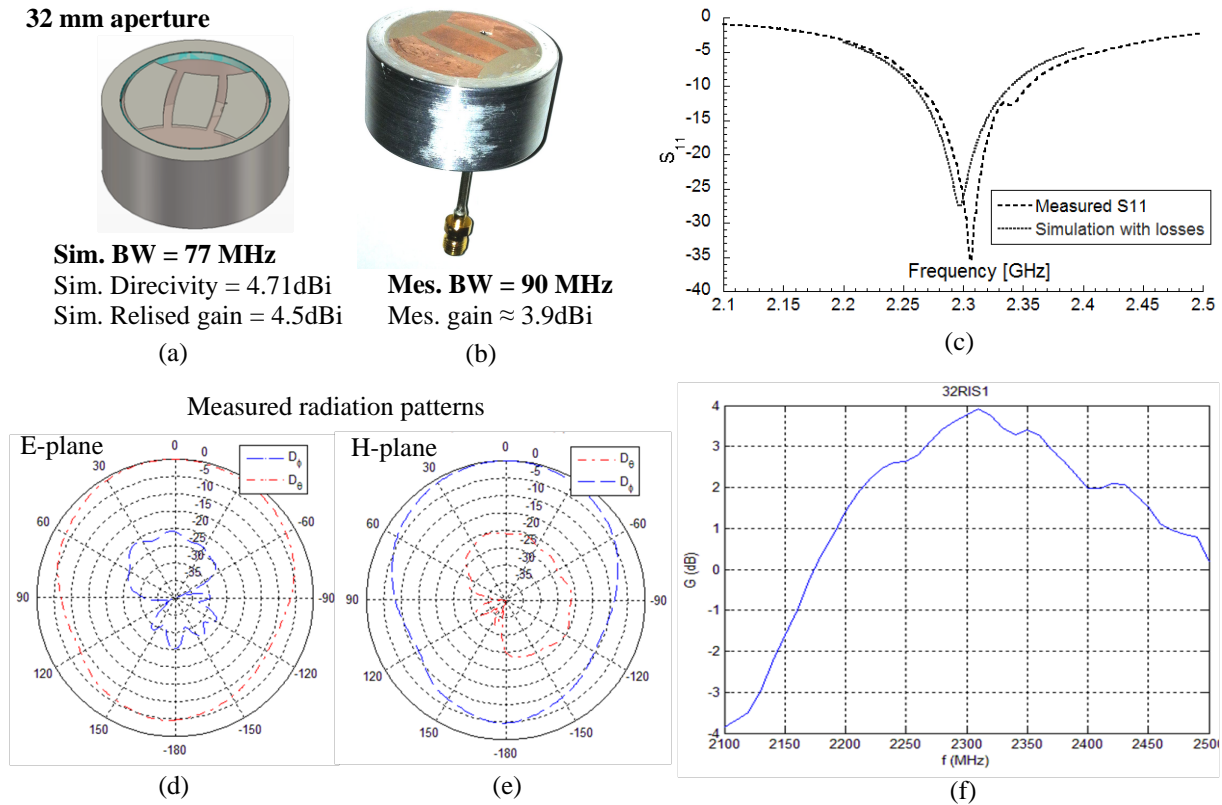


Figure 108 Prototype 32 mm ($0.25\lambda_0$) diameter, metasurface antenna. Cavity volume is filled with $\epsilon_r = 1$ (except for a thin substrate layer holding the metalization with $\epsilon_r = 11.2$). (a) Simulation results and geometry upon which the prototype was built. (b) The manufactured prototype. (c) Comparison of simulated and measured S_{11} parameter. (d) Measured radiation pattern in the E plane and (e) in the H plane. (f) measured gain vs. frequency. ($\approx 50\%$ more than with a patch antenna)

4.4. Achieving circular polarization with cavity antennas

The purpose of this section is not to give a detailed study of circularly polarized cavities, but only to give the basic ideas and a few demonstrative examples.

So far we have always assumed excitation of only the fundamental mode, leading to linear polarization. Here we explore the excitation of the fundamental mode in two orthogonal directions. When the modes are 90 degrees out of phase circular polarization is achieved. There are two possible ways of exciting both modes:

- Using two excitations, one for each mode. The modes are not coupled in any way.
- Using a single excitation while the metasurface at the aperture is anisotropic and couples the two modes together.

In both cases, the metasurface design has to be adjusted to present capacitance for both modes, i.e. in two orthogonal directions. The process of designing an adequate metasurface is depicted in Figure 109 for a square and circular cavity shape.

In the case of rectangular cavity, this process is relatively easy. The surface needs to be broken into parts in both directions, forming an array of small patches, shown in Figure 109(b). A second excitation can be added (by creating a copy of the first excitation and 90° rotation with respect to the antenna center) to excite the orthogonal mode. These two excitations should be 90° out of phase with respect to each other. Dimensions of the small

patches can be adjusted to ensure the same resonance frequency for both modes; this usually makes the patches rectangles instead of squares. Each resonance can have bandwidth close to the bound and circular polarization can be achieved in the whole frequency band.

Alternative option with a square cavity is to use only a single feed while inserting additional slots in the small patches of the metasurface, shown in Figure 109(c). The purpose of these slots is to make the surface anisotropic, i.e. they introduce coupling between the two modes. Operation of this antenna type is drastically different compared to the double feed antenna. As two modes are excited with a single feed, one can observe two closeby resonances in the S_{11} parameter which can lead to a bandwidth broadening effect. Circular polarization is achieved only in the region between the two resonances. As bandwidth is the main concern of this thesis, we shall concentrate more on this type of excitation in example 1 below.

In the case of a circular cavity the situation is more complicated due to the irregular shape of the metasurface. To achieve circular polarization, two separate metasurfaces have to be made; one for each mode i.e. polarization. In order for the two metasurfaces to be decoupled, each metasurface is broken into multiple pieces with vertical lines (E lines) slots shown in Figure 109(e). Next, the metasurfaces can be combined with a 90° rotation between them and each surface can be excited separately. The excitation part is complicated in this case and the best option may be the excitation type that was presented on Figure 100 (c). Again, the two feed should have signals that are 90° out of phase with respect to each other and the expected bandwidth is the same as for a single mode antenna, just with circular polarization.

Alternative option is to introduce slots in the metasurfaces, as depicted on Figure 109(g) and use a single excitation. These additional slots make the surfaces anisotropic and couple energy between the two TE modes. The expected bandwidth can be larger than for a single mode antenna as two resonances can now be used for a bandwidth broadening effect. However, the expected circular polarization bandwidth is narrow, as it occurs only between the two resonances.

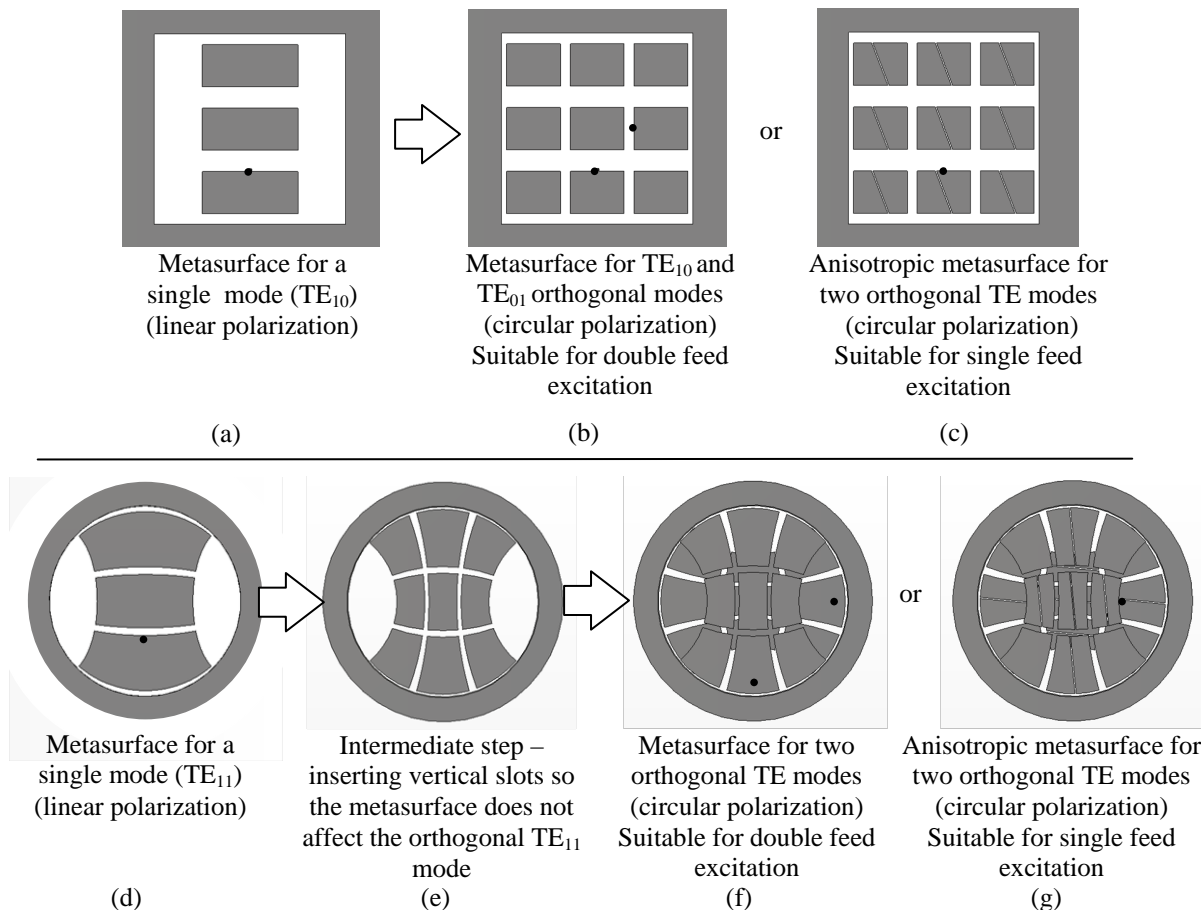


Figure 109 Two forms of achieving circular polarization for a square and a circular cavity shape. (a) Square aperture with a metasurface for linear polarization. (b) Braking the metasurface into an array of patches. The small patches are usually rectangles, not squares, in order to adjust the resonance frequencies for each mode separately. Positions of the excitations are noted with a back dot. (c) Anisotropic metasurface that can be excited with a single source and the energy is coupled into both modes. (d) Circular aperture with a metasurface for linear polarization. (e) Modification of the metasurface to decrease its affect on the orthogonal mode. (f) Introduction of a second, bottom, layer metasurface rotated by 90° to the top layer. Positions of the excitations are noted with a back dot. (g) Anisotropic metasurface that can be excited with a single source and the energy is coupled into both modes.

Below we give two examples of circular polarization with a single feed design. This antenna type is of greater interest in this thesis since it shows the potential to double the antenna bandwidth.

Example 1: Square cavity in an infinite ground plane.

Figure 110 shows an example $32 \times 32 \times 20$ mm cavity with a two layer anisotropic metasurface at the aperture. Cavity volume is filled with air, except for the top part where three 0.64 mm layers of substrate with $\epsilon_r = 10.2$ are used. The bottom layer has the short transmission line metallization and the top two layers have the metasurface metallization. The antenna can exhibit two resonances and was optimized to have a central frequency at 2.3 GHz with one resonance below (corresponding to one polarization direction) and one resonance above (corresponding to an orthogonal polarization direction). Over all bandwidth was found to be 160 MHz, which is a great improvement compared to the linear case, double in value. Circular polarization bandwidth is unfortunately very narrow; only 35 MHz around, determined by the 3 dB axial ratio points in the simulation.

In Chapter 3 the bound for linear polarization was explicitly determined through a derivation of the polarizability. Due to the 90° rotational symmetry of a square cavity, the polarizability in two orthogonal directions is the same. Excitation of both TE_{10} and TE_{01} modes effectively produces two orthogonal magnetic dipole moments at the aperture which are radiating into open space. The total polarizability thus composed of the two polarizabilities in orthogonal directions, making the resulting Q factor half the value compared to linear polarization. Expected bandwidth is should therefore be double compared to linear polarization.

These arguments appear reasonable, but the situation with a single feed exciting two modes is not so clear cut in the opinion of the author. The antenna presented below, in Figure 110, has two closely spaced resonances; however, the link between the Q factor and fractional bandwidth is not clear for such cases. It may be just a coincidence that the author managed to obtain exactly double the bandwidth compared to the linear case. Slightly better result may be possible if the matching between the two resonances is poorer. In any case, the intention is to show that excitation of orthogonal modes can be considered as a bandwidth broadening technique if one is not interested in the polarization. However, a systematic study on the topic of circular polarization bandwidth is outside the scope of this thesis.

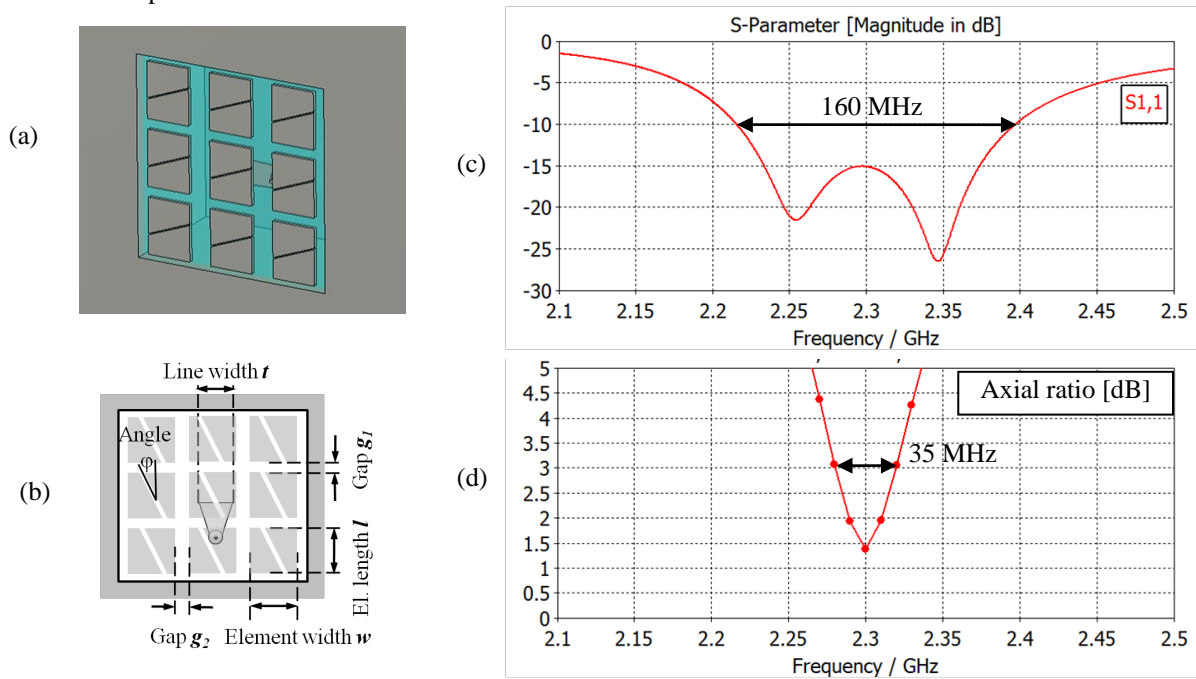


Figure 110 (a) Rectangular $32 \times 32 \times 20$ mm ($0.245 \lambda_0 \times 0.245 \lambda_0 \times 0.15 \lambda_0$) cavity in an infinite ground plane having an anisotropic two layer metasurface at the aperture. (b) Schematic showing dimensions: gap $g_1 = 3.57$ mm, $g_2 = 1.64$ mm, line width $t = 2$ mm, slot angle $\phi = 21^\circ$, slot width = 0.2 mm. Feed position is 6.9 mm from the center. The line length L_s is 5.25 mm (b) Simulated S11 parameter showing a bandwidth broadening effect of two resonances. (c) Simulated axial ratio showing good circular polarization in a narrow frequency band.

Example 2: Circular cavity in a finite ground plane.

Figure 111 shows an example of a 32 mm diameter cavity with 20 mm height having a two layer anisotropic metasurface at the aperture. Cavity volume is filled with air, except for the top part where three 0.64 mm layers of substrate with $\epsilon_r = 10.2$ are used. The bottom layer has the short transmission line metallization and the top two layers have the metasurface metallization. The antenna can exhibit two resonances and was optimized to have a central frequency at 2.3 GHz with one resonance below (corresponding to one polarization direction) and one

resonance above (corresponding to an orthogonal polarization direction). Over all bandwidth was found to be 145 MHz, which is a great improvement compared to the linear case, almost double in value. Circular polarization bandwidth is unfortunately very narrow; only 34 MHz around, determined by the 3 dB axial ratio points in the simulation.

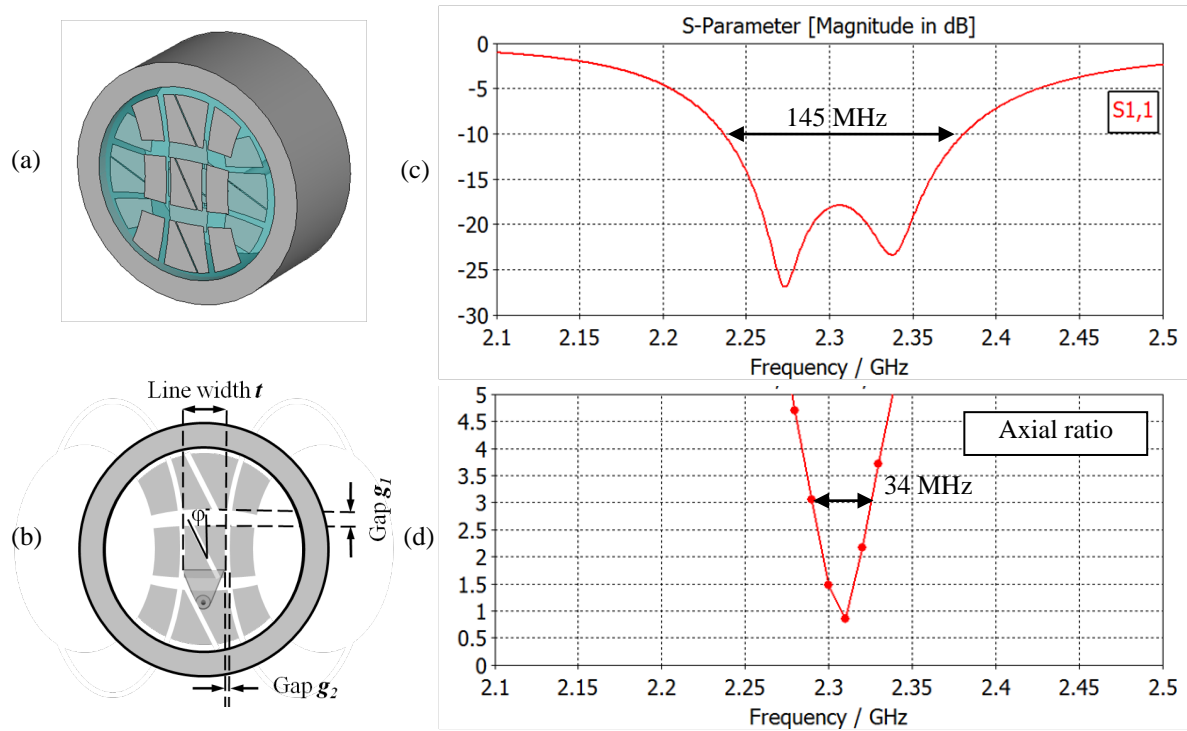


Figure 111 (a) Finite ground plane circular cavity with aperture diameter 32 ($0.245 \lambda_0$) and cavity height 20 mm ($0.15 \lambda_0$) having an anisotropic two layer metasurface at the aperture. Other dimensions are: gap $g_1 = 2.55$ mm, $g_2 = 3.31$ mm, line width $t = 4$ mm, slot angle $\phi = 27^\circ$, slot width is 0.8 mm. Feed position from the center is 7 mm, and line length L_i is 4.05 mm (b) Simulated S_{11} parameter showing a bandwidth broadening effect of two resonances. (c) Simulated axial ratio showing good circular polarization in a narrow frequency band.

The purpose of these two examples was to demonstrate that circular polarization is achievable in both finite and infinite ground plane with both circular and square shapes. The choice between left handed and right handed circular polarization is done through changing the angle of the slots (positive or negative angles). However, the main point is that with a single feed and anisotropic metasurfaces, one can achieve wider overall impedance bandwidth. In some situations where circular polarization is not critical and the receiving antenna is sensitive to both types of polarization, this solution might be desirable.

The added complexity compared to linear antennas is minimal and consists in adding slots and an additional layer in the case of a circular cavity. The square case cavity is simpler and can even be made with a single layer, if desired.

4.5. Conclusion of Chapter 4

In this, central, chapter of the thesis we have presented several important contributions. The abstract, Gustafsson bound was made comprehensible by connecting it to a transmission line mode which is easily understandable. The key novelty is the introduction of a capacitor at the aperture in the model that describes simple, open ended, cavity antennas.

The transmission line model was shown useful in understanding the basic principles behind the operation of antennas that can reach the bound on bandwidth i.e. the resonance condition, bandwidth behavior, the optimum permittivity inside the cavity, and the fact that the capacitor should be a reactive surface, not a lumped element. The transmission line model laid the path to creating the actual antenna with a metasurface at the aperture to approximate the necessary capacitance.

Design of the actual metasurface for the square and circular cavities, along with the proper excitation type is another important achievement presented in this chapter. Numerical simulations were used to show the range of validity of the theory. Manufactured prototypes were described and shown to be in good agreement with the simulations and theory, demonstrating also the feasibility of such antennas in the real world.

Finally, the problematic of circular polarization was presented at the end of the chapter. It was shown that circular polarization can be achieved in the whole band with two excitations. With only one excitation, anisotropic metasurfaces have to be used and circular polarization is achieved in a narrow region between two resonances. However, if one is not interested in polarization, the overall bandwidth can effectively be doubled.

Chapter 5.

Applications and potentials of the new design

In this chapter we explore the benefits of the proposed metasurface design from the last chapter in various applications. Section 5.1 demonstrates the novel possibility of manufacturing electrically small cavity antennas still coming close to the bound on bandwidth. The emphasis is on antennas smaller than previously possible with classical patch antenna design. Section 5.2 briefly explores the other end of the problem; cavity antennas that are not electrically small and the question: how does the new, metasurface design compare to classical designs with increased bandwidth. Section 5.3 is purely theoretical, exploring the potential of magnetic conductors and magnetic materials for improving the bound on Q . Section 5.4 briefly shows the application of small cavity antennas in creating a compact antenna array.

5.1. Applications to projectile design and miniaturization

The challenge in engineering problems is that real world solutions often have to be inexpensive, simple for manufacturing, and have good mechanical properties and on top of all, give the best possible performance. Here we discuss the benefits of the meta-surface design solution in these characteristics compared to the classical patch antennas, used in practice so far.

Benefit of special interest is the ability to manufacture antennas for smaller caliber projectiles for which the patch antenna design is not feasible. Figure 112 gives two such projectiles which are intended to be used with new metasurface antennas.



Figure 112 (a) 40 mm caliber projectile with a drilled cavity of 20 mm in diameter. (b) 30 mm caliber projectile into which a 16 mm diameter cavity can be drilled.

5.1.1. Ability to use lower cost materials

Throughout this thesis, bandwidth results were presented depending on the height of the cavity. I was seen that for optimum bandwidth height of about 15 mm ($0.115 \lambda_0$) or higher is usually sufficient. In simulations with patch antennas, the entire volume was filled with a material of permittivity higher than air. In reality, these high permittivity materials are hard ceramic substrates manufactured by Rogers inc. and are quite expensive. Theoretically, the volume could be filled with a low permittivity material, but high permittivity is needed to miniaturize the patch size it was demonstrated that it can also be beneficial for bandwidth (see “inversed bandwidth-permittivity relation” in Chapter 2).

The most interesting result with the new design, besides enhanced bandwidth performance, is that low permittivity materials are needed. These materials are usually much cheaper. Ideal material in terms of permittivity value is air; it also has almost no losses and is free. However, for mechanical purposes the volume has to be filled with a hard material that can withstand high forces. One material that fits the mechanical requirements and was used in our experiments is polypropylene with $\epsilon_r = 2.26$ and loss tangent $\delta = 0.002$.

In the actual antenna, the metallization is etched on a layer of expensive Rogers material, but the thickness of this layer is small and the rest of the volume is filled with less expensive polypropylene. The total cost of the antennas should thus be less than investigated patch antennas in cavities.

5.1.2. Ability to manufacture smaller cavity antennas

Back in Chapter 2, simulation results of single patch antennas in a circular cavity diameter of 20 mm ($0.15 \lambda_0$) were presented. Now we ask: How feasible are such antennas?

Our simulations used a cavity completely filled with some substrate material, but in reality the cavity and the substrate are manufactured separately. For the two parts to fit, the substrate has to be just slightly smaller than the cavity which leaves a very thin gap between them. This **gap** has to be filled with glue to ensure mechanical stability and, unfortunately, **cannot be ignored** electromagnetically. In small cavities, as the patch size is approximately the size of the cavity aperture, this glue filled gap plays an extremely important role in antenna's performance for the following reasons:

1. Electric fields are very strong between the patch and the wall; therefore also in the gap.
2. The glue's permittivity is different than the substrate's permittivity.
3. The glue material usually has much higher losses than the substrate.

Here we wish to demonstrate a road map for designing very small and feasible cavity antennas through some specific examples. Please note that in our real world experiments we use a lossy glue with $\epsilon_r = 3.5$. However, for the sake of proper comparison of bandwidth, we ignored these additional losses and kept only the permittivity value of 3.5 in the presented examples. However, losses of Rogers 3010 material with $\epsilon_r = 10.2$ are still included.

Example 1: To demonstrate the sensitivity of the patch antenna to the gap, two cases are compared; First case, shown in Figure 113, shows the cavity volume perfectly filled with the substrate material ($\epsilon_r = 10.2$). The simulated bandwidth is 15.5 MHz. Notice that the spacing between the patch and the cavity wall is very narrow.

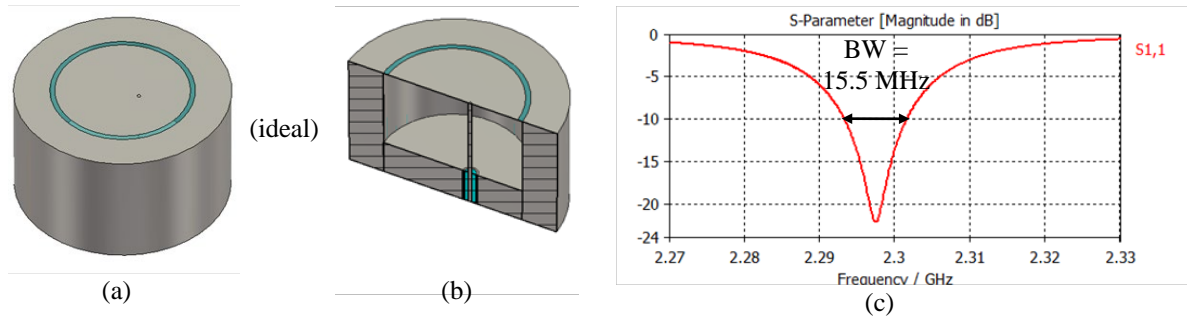


Figure 113 (a) Single patch antenna in a circular cavity of diameter $d = 20$ mm ($0.15 \lambda_0$), height $h = 14$ mm, and substrate relative permittivity $\epsilon_r = 10.2$. (b) Cut plane to show the interior of the antenna. The substrate is transparent. (c) Simulated S_{11} parameter showing 15.5 MHz of bandwidth.

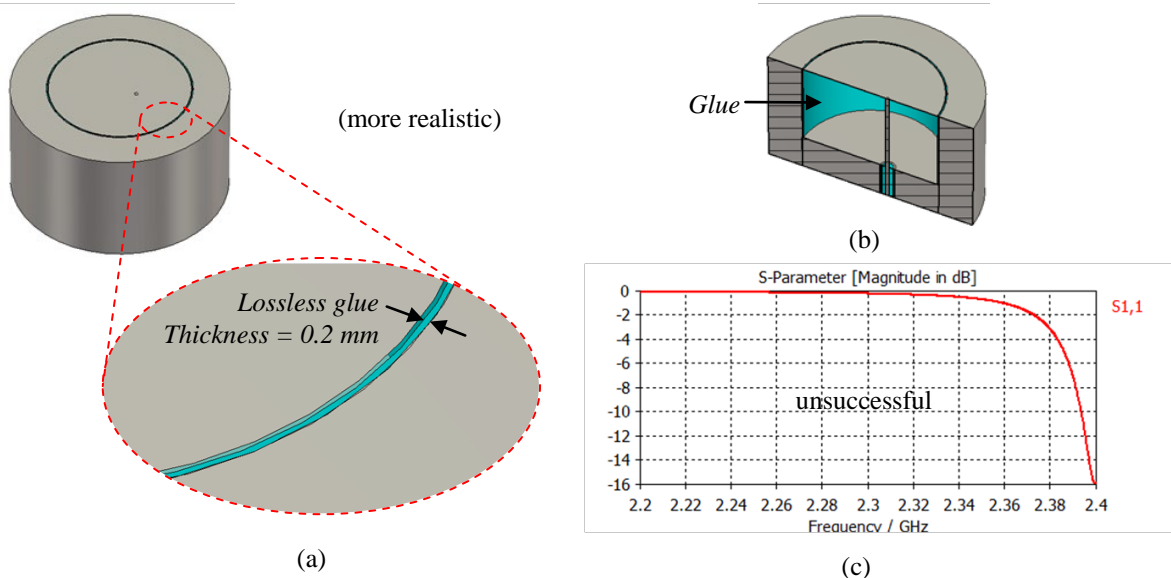


Figure 114 (a) A thin gap with glue, which is a manufacturing necessity, is introduced into the design. (b) Cut plane to show the interior of the antenna. The substrate is transparent and the glue is seen on the cavity walls. (c) Simulated S_{11} parameter showing the resonant frequency is not shifted back to 2.3 GHz even though the patch size has increased to cover almost the entire aperture.

On the other hand, Figure 114 shows a more realistic case by including a thin gap filled with glue. Simulations of this, more realistic design, have shown that the resonance frequency shifts to a higher frequency and cannot be shifted back by increasing the patch size. The patch size can be increased only to cover the entire

area of the substrate material; it cannot cover the glue, as this gap is a consequence of the assembly process. However, the glue’s permittivity inside the thin gap is not enough to shift the resonance frequency down to 2.3 GHz. Theoretically, the antenna could resonate at 2.3 GHz if one could use glue of the same permittivity as the substrate, which was not available to us.

To conclude, we can say that a 20 mm diameter patch antenna inside a cavity is in fact **not** feasible with the manufacturing process we used.

Example 2: Next we will explore a design tweak that can resolve the problem of the antenna’s sensitivity to the glue. We have learned in Chapter 2 that the role of the patch at the aperture is to act as capacitive admittance. For a single patch, the gap between the patch and the wall has to be small to ensure a large enough capacitive effect, but one can imagine that capacitance can be increased by making the patch metallization “thick,” making it a metallic disk. Instead of putting a metallic, the alternative is to stack multiple layers of patches. This effectively increases capacitance to the wall and as a consequence the diameter of the patches is reduced.

Figure 115 presents an example of such an antenna with and without glue. The sensitivity has been reduced and the antenna can be made resonant at 2.3 GHz in both cases, as noted by data from the simulations. It is concluded that this type of antenna is feasible. However, by using such a design we have lost bandwidth performance from 15.5 MHz in the case of a single patch to about 8 MHz in the case of “thick” patch with glue. This is not the desired result.

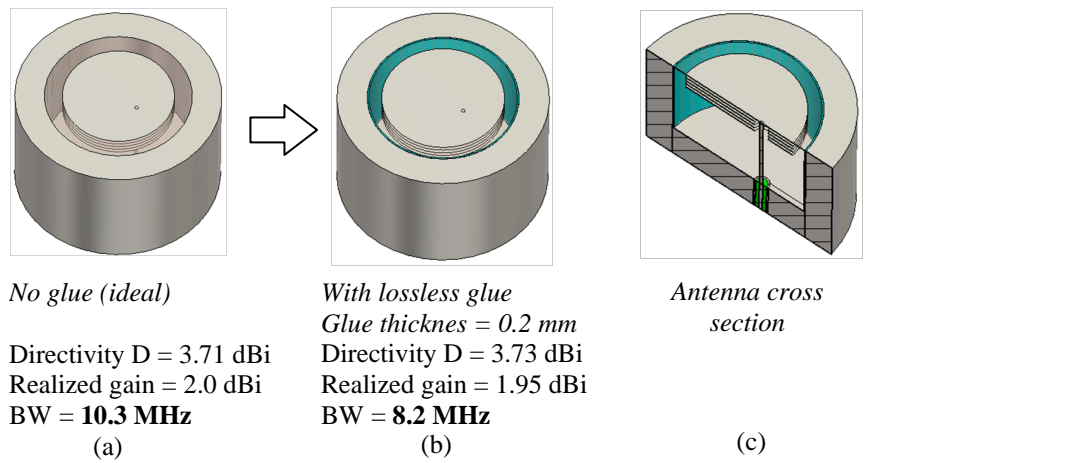


Figure 115 Reduction of patch size in a small cavity by “thickening” the metallization, i.e. stacking multiple thin layers of patches together. In this example, 5 layers with 0.64 mm separation are used. (a) Cavity ideally filled with $\epsilon_r = 10.2$ and a “thick” patch reduced about 23% in diameter compared to a single patch design. (b) Cavity with glue between the substrate and the metal wall. Patch size is now reduced only 16% compared to the single patch design, but the antenna is resonant at 2.3 GHz. (c) Cross section of the antenna in (b).

Example 3: Now we take a look at what is possible with the metasurface design. Figure 116 presents an example of such an antenna with and without glue, with the “thick” design tweak used to ensure higher capacitance. In both cases the antenna can be made resonant at 2.3 GHz, as noted by data from the simulations. We may conclude this antenna type is feasible, but most importantly that bandwidth performance is not severely degraded. In fact, bandwidth remains close to its theoretical maximum value. Probable cause is the distributed capacitance on the metasurface which further minimizes the antennas’ sensitivity to the glue. This is the desired result for small cavity antennas.

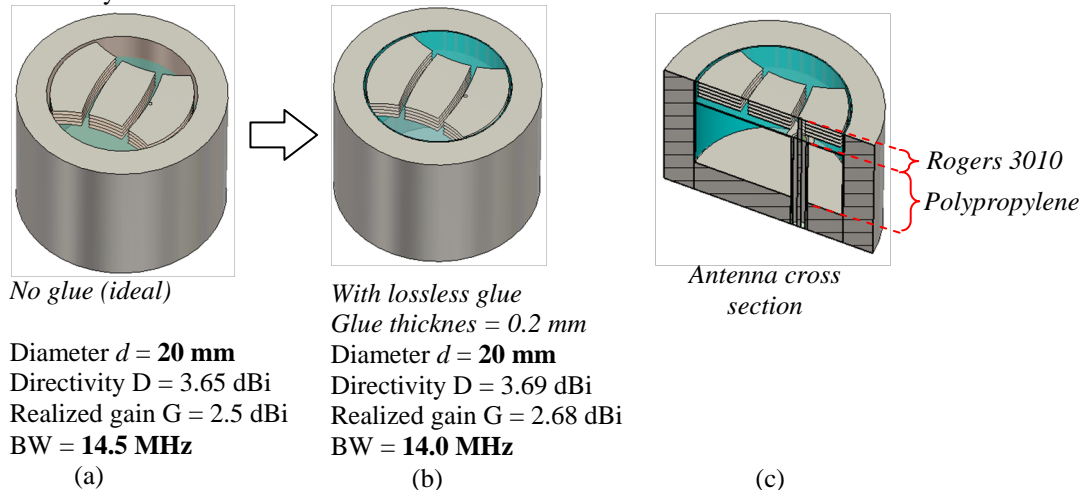


Figure 116 Cavities with a “thick” three element metasurface design. In this example, 6 substrate layers with 0.64 mm thickness and $\epsilon_r = 10.2$ are used. On 5 layers there is the metasurface metallization, while the bottom 6th layer has the small transmission line metallization to which a coaxial shield is connected. The remaining volume is filled with low permittivity polypropylene $\epsilon_r = 2.26$. (a) Cavity ideally filled with substrate materials. (b) Cavity with glue between the substrate and the metal wall. (c) Cross section of the antenna in (b).

Example 4: Finally, now that we demonstrated the benefit of a metasurface design in the last example, we compare examples cavity antennas with a 2 element metasurface giving bandwidth close to the bandwidth bound. Figure 117 shows examples of cavities with aperture radiuses of $a = 10, 9, 8$ mm respectively, which makes $ka < 0.5$ in all cases. Therefore these are truly examples of electrically small (cavity) antennas. The feasibility of these small antennas is shown by the measurement results in the next section.

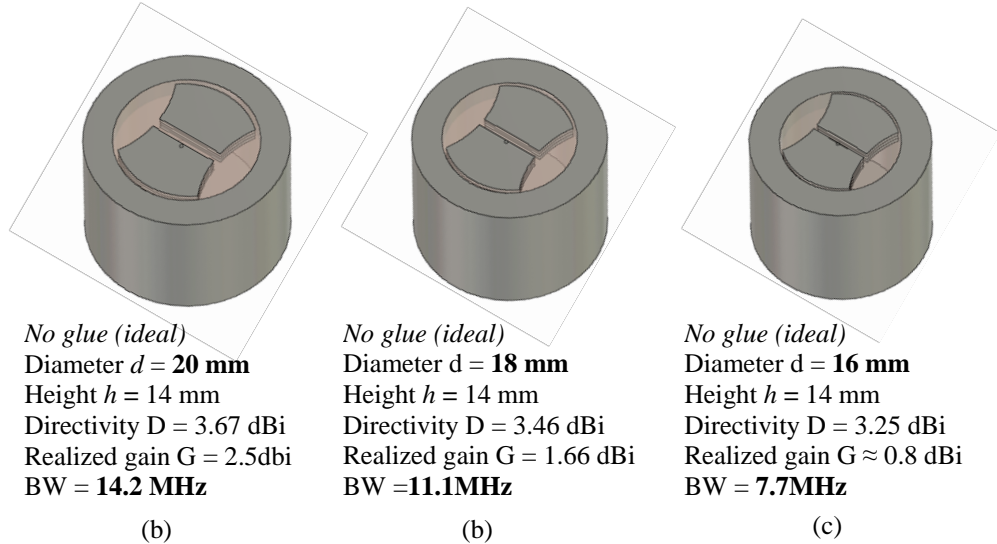


Figure 117 Cavities with a “thick” two element metasurface design. In this example, 5 substrate layers with 0.64 mm thickness and $\epsilon_r = 10.2$ are used. On 4 layers there is the metasurface metallization, while the bottom 5th layer has the small transmission line metallization to which a coaxial shield is connected. The remaining volume is filled with low permittivity polypropylene $\epsilon_r = 2.26$. All cavities are ideally filled with substrate materials. (a) Cavity with aperture radius of 10mm giving $ka = 0.482$. (b) Cavity with aperture radius of 9 mm giving $ka = 0.433$. (c) Cavity with aperture radius of 8 mm giving $ka = 0.385$.

In conclusion, based on all the examples, we can say that new possibilities have been opened with the introduction of the metasurface design. Not only to create cavity antennas with maximum bandwidth but to create really small cavity antennas. Both aspects are a great improvement in comparison to the past designs. In regards to projectiles, this opens up possibilities for smaller caliber projectiles with mounted antennas whose larger bandwidth offers more tolerance in the manufacturing process.

5.1.3. Other characteristics

The metallic cavity and the hard materials used inside the cavity give the antenna excellent mechanical and thermal characteristics. The design is conceived to allow for the antenna to withstand high accelerations and other shocks. In addition, the ability to replace expensive ceramic substrates with cheaper (hard) materials of low permeability can also affect of the mass of the antenna. High permittivity materials usually also have high density so it can be expected that the mass of antennas made with the new metasurface design can be lower (if desired).

5.1.4. Measurement results

Prototype cavity antennas having 20 mm ($0.15 \lambda_0$) and 16 mm ($0.12 \lambda_0$) apertures have been manufactured at the French-German Research Institute of Saint-Louis to confirm the feasibility of these small antennas; the design, along with the measured results are shown in Figure 118 and Figure 119 respectively.

The biggest challenge concerning small antennas in general, besides adjusting the resonance frequency and matching, is low antennas efficiency. Unfortunately, this is also visible in the case of these small cavity antennas. With our prototypes, the main issues are the manufacturing precision and the exact properties of the glue. The glue plays the most important role in the operation of the antenna, due to the high losses, and is the prime reason for reduced efficiency. Detailed descriptions of the antennas are given below.

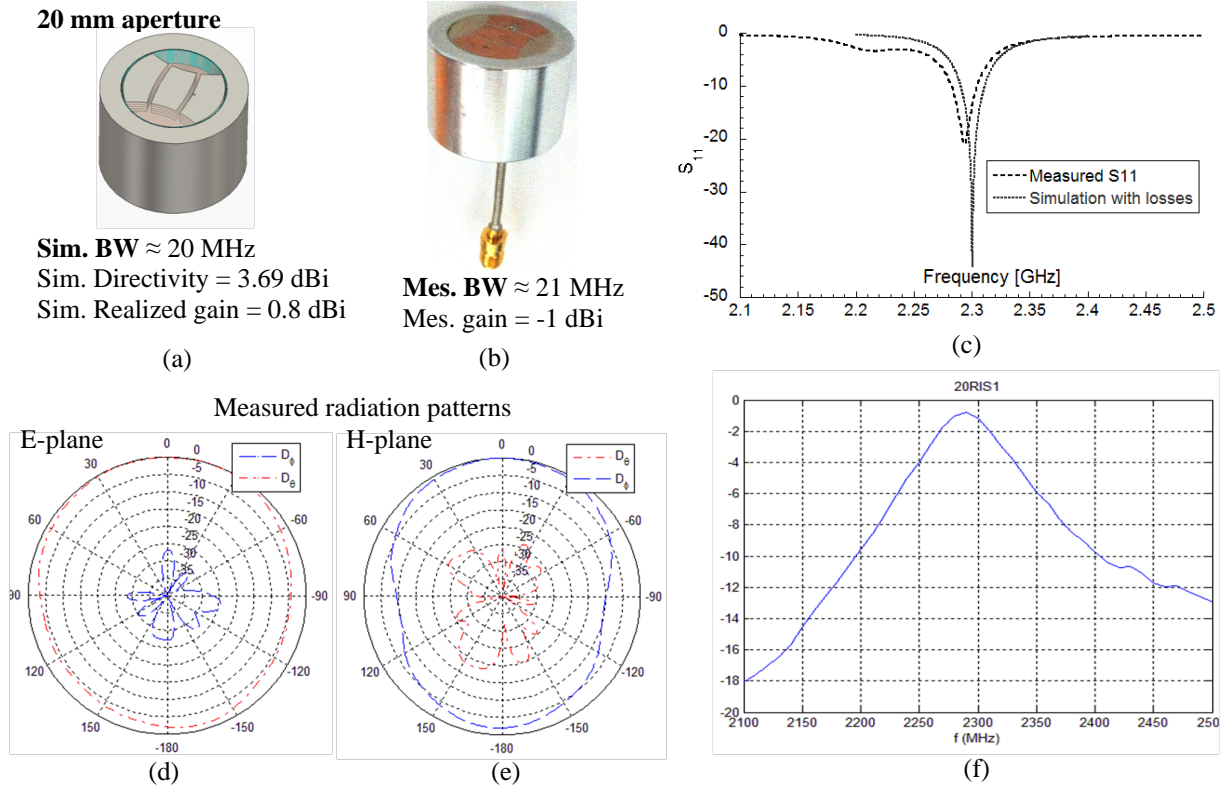


Figure 118 Prototype metasurface antenna with a 20 mm ($0.15\lambda_0$) diameter aperture in a finite ground plane (28 mm in diameter). Cavity volume is filled with polypropylene $\epsilon_r = 2.26$ (except for the 6 substrate layers holding the metalization with $\epsilon_r = 11.2$) (a) Simulation results and geometry upon which the prototype was built. (b) The manufactured prototype. (c) Comparison of simulated and measured S_{11} parameter. (d) Measured radiation pattern in the E plane and (e) in the H plane. (f) Measured gain vs. frequency.

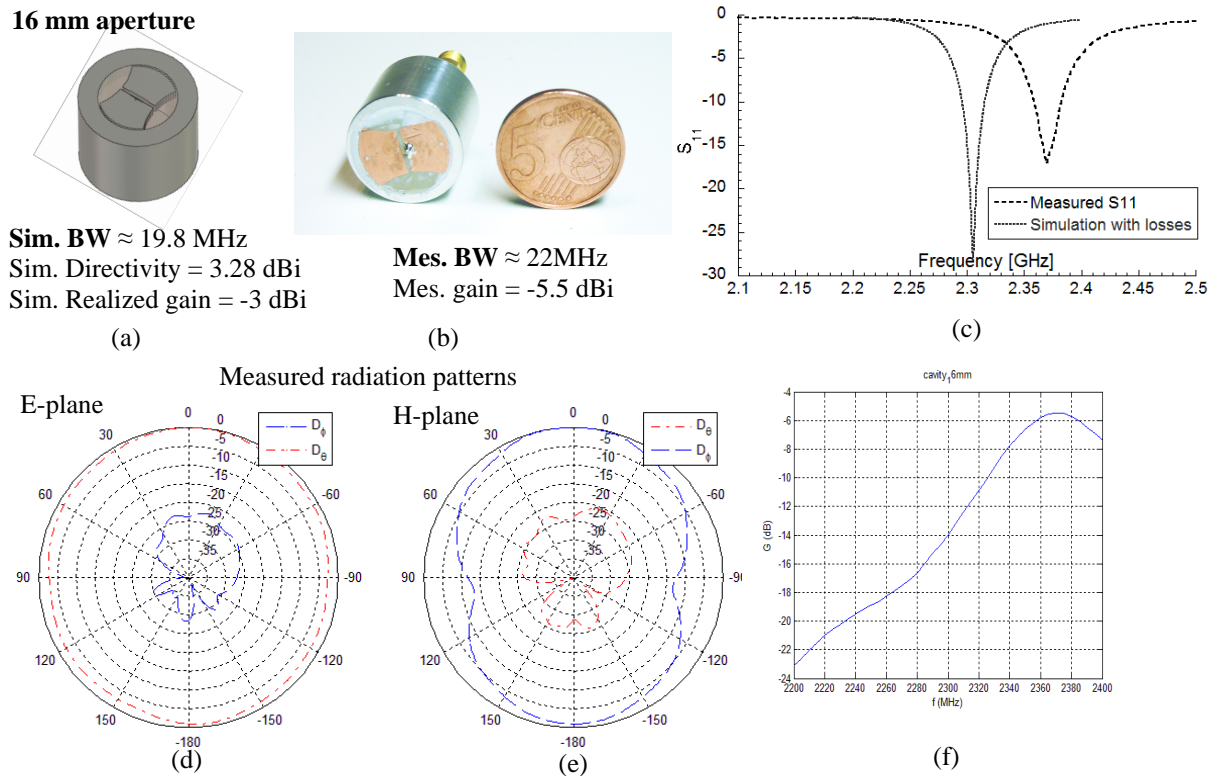


Figure 119 Prototype metasurface antenna with a 16 mm ($0.12\lambda_0$) diameter aperture in a finite ground plane (diameter 20 mm). Cavity volume is filled with polypropylene $\epsilon_r = 2.26$ (except for the 6 substrate layers holding the metalization with $\epsilon_r = 11.2$) (a) Simulation results and geometry upon which the prototype was built. (b) The manufactured prototype. (c) Comparison of simulated and measured S_{11} parameter. (d) Measured radiation pattern in the E plane and (e) in the H plane. (f) Measured gain vs. frequency.

The 20 mm aperture prototype ($ka = 0.482$):

A 20 mm diameter, 14 mm high cavity was drilled into a cylinder of 28 mm diameter of 19 mm height, seen on Figure 118(b). On the bottom of the cavity, a small hole of 2.2 mm diameter was drilled, just enough to insert a coaxial cable of the same diameter through it, thus also ensuring electrical contact between them. Position of this hole i.e., the feed position is 4.1 mm from the center of the cavity. The multilayer metasurface was designed from 6 layers of Rogers 3010 material; five layers with the metasurface and one layer with only the short transmission line to which the cable is soldered. Layers were cut to have a diameter of 19.85 mm which leaves the glue thickness of 0.15 mm. The metasurface was designed with a gap $g = 1.425$ mm; line length of 1.45 mm and line thickness of 4.8 mm.

Measured results have shown the manufactured antenna was well matched close to 2.3 GHz as predicted by the simulation, but had a slightly higher bandwidth and reduced gain, indicating higher losses in the real world compared to the simulation. It is believed that the main cause of losses is the glue. The measured antenna efficiency was 37%. Measured S11 parameter also shows a small dip below 2.3 GHz, which was unexpected. With a closer examination and simulation tests, it was determined that the cause of this dip was a small asymmetry in the antenna. The asymmetry arises if the glue is not distributed evenly in the gap between the substrate and the cavity and as a consequence an orthogonal mode is slightly excited (giving also different polarization). To avoid this, care should be taken to manufacture the antenna as symmetrical as possible.

The 16 mm cavity prototype ($ka = 0.385$):

A 16 mm diameter, 14 mm high cavity was drilled into a cylinder of 20 mm diameter of 19 mm height, seen on Figure 119(b). A small hole of 2.2 mm diameter was drilled on the bottom of the cavity, just enough to insert a coaxial cable of the same diameter through it, ensuring electrical contact between them. Position of this hole i.e., the feed position is 0.6 mm from the center of the cavity. The multilayer metasurface was designed from 6 layers of Rogers 3010 material; five layers with the metasurface and one layer with only the short transmission line to which the cable is soldered. Layers were cut to have a diameter of 15.85 mm which leaves the glue thickness of 0.15 mm. The metasurface was designed with a gap $g = 1.365$ mm; line length of 1.43 mm and line thickness of 4.0 mm.

Measured results have shown the manufactured antenna had resonance up-shifted to 2.37 GHz but was relatively well matched at that frequency. Bandwidth is slightly higher and gain reduced compared to the simulation result, indicating higher losses in the real world compared to the simulation. Again, the main cause of losses is believed to be the glue. The measured antenna efficiency was only 13.4%. However, the fact that such a small antenna can finally be realized is still a great improvement.

5.2. Applications to cavity sizes close to half the wavelength

With a cavity size (diameter) between $0.35 \lambda_0$ and $0.5 \lambda_0$ or larger, antenna performance is no longer restricted to a single resonance. In fact, stacked patches configuration can be effectively used in such cavities to increase bandwidth. At first, it seems as if stacked patches should offer broader bandwidth than the metasurface design because using two closely spaced resonances should approximately double the bandwidth seen for a single patch. This in turn should be larger than the metasurface cavity bandwidth, conceived as a single resonance antenna. In spite of that logic, we saw in the last chapter that metasurface cavities start giving unexpectedly large bandwidth for cavity size exceeding $0.35 \lambda_0$. The reason for this? There is a second cavity resonance at a higher frequency due solely to the cavity size being comparable to $0.5 \lambda_0$. The second resonance is a consequence of the aperture admittance behavior for aperture size above $a/\lambda_0 > 0.5$, where the real part is large and the imaginary part is close to zero. Can the second cavity resonance be effectively used with the metasurface design?

Here we give two brief examples of the possibilities with a metasurface in cavity sizes very close to $0.5 \lambda_0$ at 2.3 GHz. We demonstrate they can be used to create broadband antennas and indeed surpass stacked patches antenna bandwidth, making it a superior design even for larger cavities.

5.2.1. Broadband cavity antennas

We give only a brief example of a rectangular cavity with dimensions $0.49 \times 0.49 \times 0.15 \lambda_0$ at 2.3 GHz demonstrating the possibility of broadband, two resonance, operation with a single metasurface layer. The bound on Q_{min} assumes a single resonance; calculating bandwidth from it is only approximate, especially for low values of Q . For two resonances the link between Q and FBW is not so clear. Thus, it is hard to know the exact maximum bandwidth that can be achieved in this case, and does the shown configuration reach it.

The example antenna geometry is shown in Figure 120(a) with specific dimensions noted in Figure 121. The design is very simple in general. The antenna consists of a single, thin substrate layer with metallization on top, forming the metasurface, and metallization on the bottom, forming a short transmission line to which the coaxial cable is soldered to. On the top layer there is also a small transmission line (see Figure 121(b)) connecting the

feed wire from the coaxial cable and one of the metasurface elements. A small box was added around the feed wire position for soldering purposes if the antenna is to be manufactured. The volume of the cavity is filled with air, or a solid material whose permittivity is close to unity, apart for the top substrate.

By experimenting with the number of metasurface elements, their width and parameters like the position of the coaxial cable and the transmission line length, the author has been able to match the antenna in a region from 2 to 3.4 GHz, giving 52% fractional bandwidth (if the central frequency is taken to be 2.7 GHz).

The radiation pattern remains broadside in the whole frequency band, but shows tilting near 2.9 GHz. It was determined that the position of the coaxial cable has an effect on the radiation pattern and is probably responsible for this tilt in the pattern around 2.9 GHz.

This demonstrates that even with a single metasurface, due to its capacitive effect at the peculiar frequency dependence of the aperture admittance which gives rise to a second resonance, one can have very simple, yet broadband cavity antennas. The benefit is not only in the simplicity, but also in the material saving, since only a single layer of substrate is needed and the rest of the volume can be filled with cheap low permittivity material, reducing the total cost of the antenna.

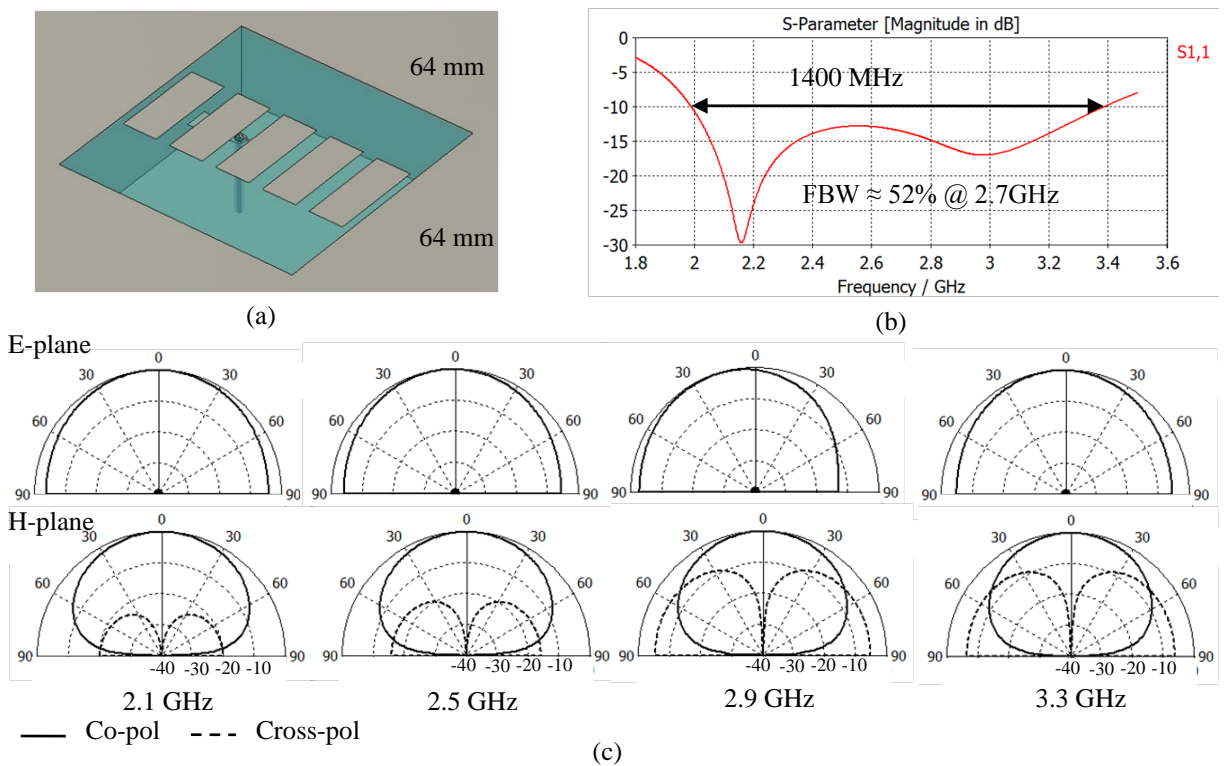


Figure 120 Broadband rectangular cavity antenna in an infinite ground plane of dimensions 64 x 64 x 20 mm or $0.49 \times 0.49 \times 0.15 \lambda_0$ at 2.3 GHz. (a) 5 element metasurface of 24 mm width. Other parameters are given in Figure 121 (b) Simulated S_{11} parameter (c) Simulated radiation pattern for several frequencies.

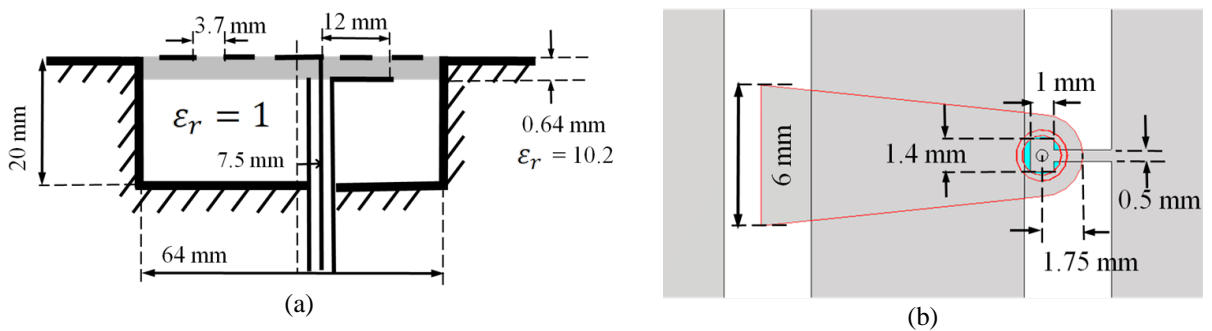


Figure 121 (a) Design of the antenna used in Figure 120. (b) design of the excitation part. The small rectangle around the central wire is mostly intended for soldering purposes.

5.2.2. Comparison with stacked patches

A cavity size $0.475 \times 0.475 \times 0.15 \lambda_0$ at 2.3 GHz has been chosen for the comparison of stacked patches to the metasurface design. On one hand, classical stacked patches configuration is a common choice for bandwidth broadening; on the other hand a single metasurface layer was shown in the last example to offer broadband behavior for cavities close to $0.5 \lambda_0$ in size. The geometries of the two antennas are depicted in Figure 122(a) and (d) with exact dimensions given in Figure 123. It was decided to optimize the geometry to have one resonance below, and one above 2.3 GHz, making 2.3 GHz the central frequency. Results of the simulations are shown in Figure 122(b) and (e). It is clearly visible that the single layer metasurface design offers broader, almost double, bandwidth. In the case of stacked patches, both resonances have narrower compared to the metasurface design, and offer 20.8% fractional bandwidth around 2.3 GHz. For the metasurface design, both resonances offer wider bandwidth, especially the second, higher resonance, offering 37.4% fractional bandwidth in total.

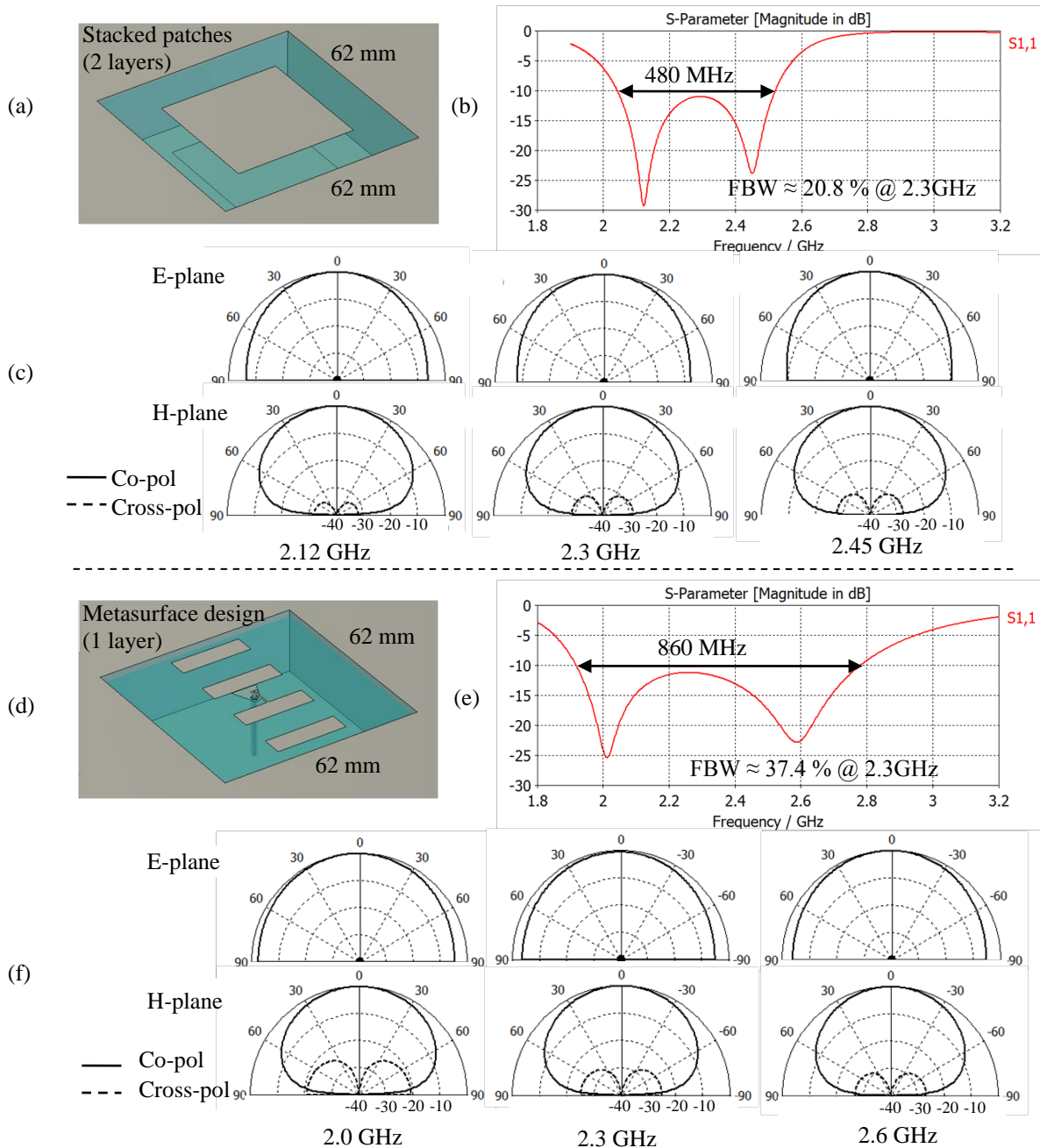


Figure 122 Comparison between stacked patches and metasurface design in a rectangular cavity of dimensions $62 \times 62 \times 20$ mm or $0.475 \times 0.475 \times 0.15 \lambda_0$ at 2.3 GHz embedded in an infinite ground plane. (a) Perspective view of stacked patches. (b) Simulated S_{11} parameter for stacked patches. (c) Simulated radiation patterns for several frequencies. (d) Perspective view of a 4 element metasurface of 24 mm width. (e) Simulated S_{11} parameter for the metasurface design. (f) Simulated radiation pattern for several frequencies.

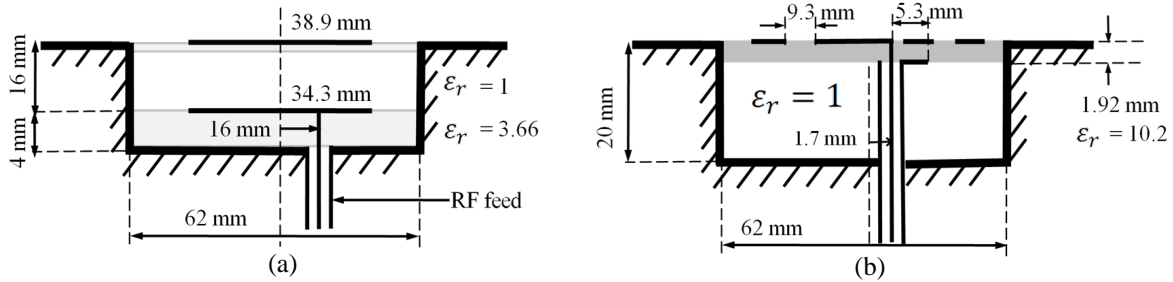


Figure 123 (a) Design with specific dimensions for the stacked patches configuration shown in Figure 122(a). (b) Design with specific dimensions for the metasurface configuration shown in Figure 122(d).

The radiation patterns of the two antennas for several key frequencies are shown in Figure 122(c) and (f). Good broadside patterns are observed in both cases in the whole frequency band.

Finally, we can note that in the case of a finite ground plane, the same general conclusion is expected to hold, i.e. the metasurface design can offer broader bandwidth compared to classical stacked patches. The effect of a finite ground plane should only be to further enlarge the bandwidth because the real part of the aperture admittance increases (as discussed in Chapters 2 and 4).

Circular cavity case:

Regarding circular cavities, a study was made with finite sized cavities using stacked patches, and metasurfaces for various cavity diameters; with results summarized in Table 10. Results of simulations for a single patch and for a metasurface design in the same sized cavity are also added to the table. Values indicated represent the approximate best result obtained for a given size at a height of 20 mm. Some boxes are left blank because the antenna type in the particular cavity size is not feasible, for example, stacked patches configuration is possible only for cavities with 50 mm diameter or larger. Data in the table shows that the metasurface design is superior in all cases to other types of antennas, except for a 50 mm cavity, where stacked patches show better bandwidth performance.

Circular cavity diameter d	70 mm					50 mm			32 mm	20 mm	16 mm	
Bottom sub. permittivity:	3.66	6.15	10.2	6.15	10.2	6.15	10.2	10.2	6.15	10.2	10.2	10.2
Top: sub. permittivity	3.66	3.66	3.66	6.15	6.15	3.66	3.66	6.15	6.15	6.15		
Stacked patches BW [MHz] (CST sim.)	404	494	513	671	521	430	439	423				
Single patch BW [MHz] (CST sim.)	200	200	200	200	200	165	165	165	65	65	8	
Metasurface BW [MHz] (CST sim.)	890	890	890	890	890	307	307	307	80	80	14	7

Table 10 Comparison of various cavity antennas. Numbers are approximate values of the best antenna bandwidth performance at height $h = 20$ mm

In conclusion, we can say that the metasurface design is a better choice than stacked patches design in almost all cases. Bandwidth is superior and the design of the antenna is simpler for it uses only one, thin substrate layer. Material cost can be significantly reduced as low permittivity materials need to be used.

5.3. Potentials of magnetic materials for cavity antennas

Here we expand the presented theory of cavity antennas with the introduction of magnetic materials and magnetic conductors and discuss the potential benefits for bandwidth.

Present day technology offers two types of magnetic materials that can exhibit relative permeability greater than unity ($\mu_r > 1$). First types are natural materials; they rely on quantum mechanics and electron spin, i.e. the inherent magnetic moment of the electron that responds to external magnetic fields. The main ingredient in such materials is usually iron (Fe) and they are usually termed just “ferrites.” They offer very large values of μ_r (up to thousands) but at very low frequencies, usually below 10 MHz. Importantly, at these low frequencies, relative permeability is fairly constant with respect to frequency. At larger frequencies ferrites usually exhibit high losses and lower values of permeability. There is considerable interest in producing high permeability materials operating at high frequencies (above 1 GHz range) as they would have many applications for antennas.

However, to the author's knowledge, current technology can produce only magnetic materials operating below 1 GHz, which are very lossy and have μ_r below 100.

Second types of materials are artificial materials or meta-materials; they rely on man-made metallic inclusions (particles) that respond to external magnetic fields and were introduced in Chapter 1.4. The simplest example of an inclusion that can be used is the split ring resonator (SRR). A volume filled with SRRs can exhibit large permeability values below the resonance frequency of the SRR, and even negative permeability in a narrow frequency band above the resonance. The drawback of meta-materials is the mentioned dependence on the resonance of the inclusion, this makes the effective permeability of the material highly frequency dependant (dispersive).

Magnetic conductors are not found in nature at all, but structures effectively acting as magnetic conductors can also be man-made and are called meta-surfaces, described in Chapter 1.4.3. Meta-surfaces are also highly frequency dependant and act as a magnetic conductor only at the resonant frequency.

In the following analysis, we will first assume an ideal magnetic material or conductor, meaning no frequency dependence and arbitrary values, to get the "best case result" and then discuss if the result is feasible with meta-materials. We will restrict the analysis to rectangular cavities and waveguides due to their simplicity and for brevity.

5.3.1. Modifying the bound with perfect magnetic conductors inside the cavity

In a rectangular waveguide, perfect magnetic conductors (PMC) can be imagined on the two side walls, shown in Figure 124. The TE_{10} mode is no longer the fundamental mode as the boundary conditions have changed and the electric field does not have to be zero on the walls. The fundamental mode in this case is the TEM (plane wave) mode with no cut-off frequency.

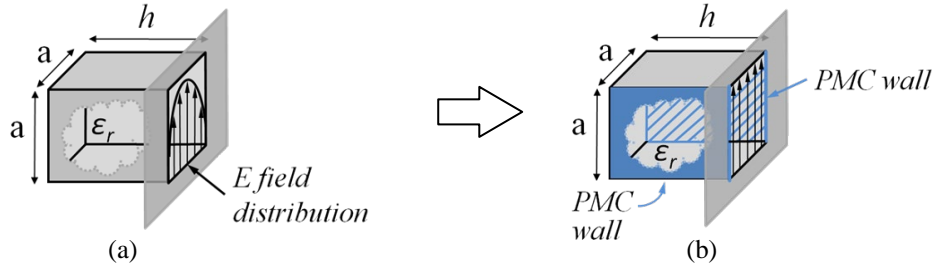


Figure 124 (a) Regular square metallic cavity with a TE_{10} field distribution at the aperture. (b) Square cavity with perfect magnetic conductors on two side walls making the field distribution at the aperture and inside the waveguide uniform.

Propagation inside the waveguide is similar to free space propagating plane wave with the direction parallel to the PMC walls. The propagation constant k_{TE} reduces to $\sqrt{\epsilon_r}k$. To derive the new bound, we start by reducing the waveguide's input admittance to the PMC case as

$$Y^C = -j \frac{k_{TE}}{k\eta_0} \cot(k_{TE}h) \xrightarrow{\text{reduces to}} Y_{uni}^C = -j \frac{\sqrt{\epsilon_r}}{\eta_0} \cot(\sqrt{\epsilon_r}kh). \quad (5.1)$$

For the low frequency limit we use a series expansion around $k = 0$ to get $Y_{uni}^C = 1/(k\eta_0h) + \mathcal{O}(k)$. However, matters are a little more complicated at the aperture side as the PMC makes the field distribution at the aperture is uniform, i.e. $\mathbf{E}(x, y) = \hat{y}E_0^+$. We need to re-calculate all the other steps in the derivation starting from the aperture admittance. Thankfully, the new aperture admittance for a uniform distribution is easily derived (see Balanis [37]) and the result is

$$Y_{uni}^S = \frac{ab}{4\pi^2 k\eta_0} \iint_{\mathbb{R}^2} \frac{k^2 - k_x^2}{\sqrt{k^2 - k_x^2 - k_y^2}} \text{sinc}^2\left(\frac{k_x a}{2}\right) \text{sinc}^2\left(\frac{k_y b}{2}\right) dk_x dk_y \quad (5.2)$$

Where we have used the fact that for a TEM mode in the PMC waveguide the admittance is generally given by $Y_{uni} = 2P_{uni}/(a^2|E_0^+|^2)$. Numerical integration of (5.2) for $a = b$ and curve fitting gives the approximations

$$\begin{aligned} G_{uni} &= 0.011x^2 - 0.0213x^4 + 0.0217x^6 - 0.0131x^8 + 0.00485x^{10} \\ &\quad - 0.001x^{12} + 0.0001x^{14} \\ B_{uni} &= -\frac{0.00745}{x} + 0.0586x - 0.0169x^3 + 0.0239x^5 - 0.0194x^7 \\ &\quad + 0.01x^9 - 0.0035x^{11} + 0.00082x^{13} - 0.00013x^{15} \end{aligned} \quad (5.3)$$

Where $x = a/\lambda_0 = ka/2\pi$. In the low frequency limit we have $Y_{uni}^S = j2\pi b^0/(ka) + \mathcal{O}(k)$, where $b^0 = -0.00745$ from (5.3). Next we have to derive the amplitude of the scattered wave. Using condition (3.14) we can write the equation for the amplitude

$$A \left[\frac{a^2}{2} Y_{uni}^{S*} |E_0^+|^2 + \frac{a^2}{2} Y_{uni}^{C*} |E_0^+|^2 \right] = a^2 |E_0^+|^2 / \eta_0.$$

Which gives

$$A = \frac{2}{\eta_0} \frac{1}{Y_{11}^{S*} + Y_1^{C*}} = \frac{2}{\eta_0} \frac{1}{j \frac{1}{k\eta_0 h} - j \frac{2\pi}{ka} b^0 + \mathcal{O}(k)} = \frac{-j2ka}{\frac{a}{h} - 2\pi b^0 \eta_0} + \mathcal{O}(k^2). \quad (5.4)$$

The electric far field is, according to (3.24) given by

$$\mathbf{E}^S = 2jk \frac{e^{-jkr}}{4\pi r} \hat{\mathbf{z}} \times \int_{-a/2}^{a/2} \int_{-a/2}^{a/2} \hat{\mathbf{x}} A E_0^+ dx dy = \hat{\mathbf{y}} E_0^+ \frac{e^{-jkr}}{4\pi r} jA2ka^2 \quad (5.5)$$

After inserting the amplitude (5.4) and extracting the scattering function, and following (3.3) and (3.4) we finally arrive at the polarizability

$$\gamma = \frac{4a^3}{\frac{a}{h} - 2\pi b^0 \eta_0}, \quad (5.6)$$

The Gustafsson Q factor formula is thus

$$Q \cong \frac{\pi D}{2\eta(ka)^3} \left(\frac{a}{h} - 2\pi b^0 \eta_0 \right) \quad (5.7)$$

What remains is to expand the directivity D in terms of (ka) . **Appendix C** gives the directivity calculation for a regular cavity, which we adapt to the current case of a uniform electric field at the aperture and obtain

$$D = \frac{(ka)^2}{\pi\eta_0 G(k)} = \frac{4\pi}{\eta_0 g^0} - \frac{g^1(ka)^2}{\eta_0 g^0{}^2 \pi} + \mathcal{O}((ka)^4) \quad (5.8)$$

Where g^0 and g^1 are the first and second coefficient of conductance in (5.3) giving $D \cong 3 + 0.149(ka)^2$.

Combining (5.8) with (5.7) and inserting all the numerical values of the coefficients we have the new bound

$$Q \cong \frac{8.4}{(ka)^3} + \frac{4.76}{a^2 h k^3} + \frac{0.41}{(ka)} + \frac{0.23}{hk} \xrightarrow{as \ h \gg} Q \cong \frac{8.4}{(ka)^3} + \frac{0.41}{(ka)}, \quad (5.9)$$

which is considerably lower than the regular square cavity case. In terms of the radius $r = a\sqrt{2}$ we have

$$Q \cong \frac{2.97}{(kr)^3} + \frac{0.29}{(kr)} \text{ for } h \gg. \quad (5.10)$$

5.3.2. On the impossibility of achieving the bound with AMC metasurfaces.

The argument why the bound (5.9) is not achievable with metasurfaces is quite straightforward. The reader is referred back to Figure 60 in Chapter 1.4.2 where the reflection phase behavior of a metasurface is shown depending on the incident angle of the wave. It is demonstrated that for TE polarized waves phase bandwidth reduces as 90° incident angle is approached and is in fact zero at 90° degrees. In other words, when the wave is propagating parallel to the surface (and for TE waves the electric field is also parallel to the surface) the metasurface can no longer operate as an artificial magnetic conductor, except for a single frequency point. Unfortunately, this is exactly the situation that should happen in a waveguide with PMC walls. The wave direction and the electric field inside the waveguide should both be parallel to the PMC walls.

Hypothetically, even if better metasurfaces were designed that are not angle dependant, the second problem is the bandwidth of the metasurface itself. The bound assumes no frequency dependence of the magnetic conductors (as if they were really made of magnetic charges). The bandwidth of the artificial magnetic conductor should be at least as broad as the bound of the cavity itself, which is very large. This brings us to the third problem: volume taken up by the designed metasurface. Bandwidth of the metasurface is directly related to its thickness, i.e volume and any volume taken up by the metasurface would reduce the size of the aperture, which is the most important factor in the bound. Thus, in this hypothetical situation, there would also be a tradeoff between the metasurface and cavity bandwidth.

5.3.3. Modifying the bound with ideal magnetic material inside the cavity

Here we imagine that the cavity volume can be filled with a material having arbitrary relative permeability constant μ_r (in addition to arbitrary relative permittivity ϵ_r), as shown on Figure 125.

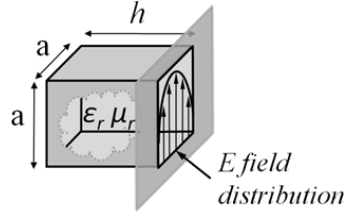


Figure 125 Square metallic cavity with a TE₁₀ field distribution at the aperture filled with a magneto-dielectric material.

To derive the bound we start by writing the input admittance into the cavity as

$$Y^C = -j \frac{\sqrt{\mu_r \epsilon_r k^2 - \left(\frac{\pi}{a}\right)^2}}{\mu_r k \eta_0} \cot \left(\sqrt{\mu_r \epsilon_r k^2 - \left(\frac{\pi}{a}\right)^2} h \right). \quad (5.11)$$

For the low frequency limit (5.11) is expanded around $k = 0$ to get

$$Y^C = -j \frac{1}{ka} \frac{\pi \coth\left(\frac{h\pi}{a}\right)}{\eta_0 \mu_r} + \mathcal{O}(k) \quad (5.12)$$

Which is the same as for the regular cavity except for the μ_r in the denominator. The rest of the derivation is also the same as for the regular cavity because there is no change in the field distribution at the aperture. Therefore we skip to the final result for the polarizability

$$\gamma \cong \frac{32}{\pi^3} \frac{a^3}{-2b_{11}^0 \eta_0 + \frac{\coth\left(\frac{\pi}{a} h\right)}{\mu_r}} \quad (5.13)$$

And the Q factor given by

$$Q \cong \frac{\pi^4 D}{16\eta(ka)^3} \left(\frac{\coth\left(\frac{\pi}{a} h\right)}{\mu_r} - 2b_{11}^0 \eta_0 \right) \quad (5.14)$$

Where it is immediately visible that Q can be minimized if we let $\mu_r \rightarrow \infty$. In this case the effect of the cavity part in the potential antenna would be completely eliminated! Thus theoretically, there is no dependence on h if $\mu_r \gg$ and the cavity can be made very thin.

Using the expansion formula for the directivity (3.50) we have

$$Q \cong \frac{-4\pi^3 b_{11}^0 \eta_0}{\eta g_{11}^0 \eta_0} \left[\frac{1}{(ka)^3} - \frac{g_{11}^1}{4\pi^2 g_{11}^0} \frac{1}{(ka)} \right] \quad \text{for } \mu_r \gg \quad (5.15)$$

and inserting all the numerical values of the coefficients we arrive at the bound

$$Q \cong \frac{22.27}{(ka)^3} + \frac{0.95}{(ka)} \quad \text{for } \mu_r \gg \quad (5.16)$$

Or in terms of the radius $r = a\sqrt{2}$ which makes it comparable to the Chu bound, we have

$$Q \cong \frac{7.87}{(kr)^3} + \frac{0.67}{(kr)} \quad \text{for } \mu_r \gg. \quad (5.17)$$

This bound is much lower than the bound for the regular square cavity, although not as low as for the case of magnetic conductors.

Physical interpretation of this result, depicted in Figure 126 is the following: Electromagnetic energy inside the waveguide (cavity) is evanescent. This decreases the effect of the cavity for larger h . Introducing a magnetic material makes the decay constant bigger and the energy decays faster with increasing h . Additionally, the inductive admittance looking into the waveguide becomes small and ultimately approaches the admittance of an open circuit (zero). In this case the antenna is basically modeled by a parallel resonant circuit for which (from Appendix A) we have $Q = 1/(\omega_0 GL)$, thus larger inductance lowers Q .

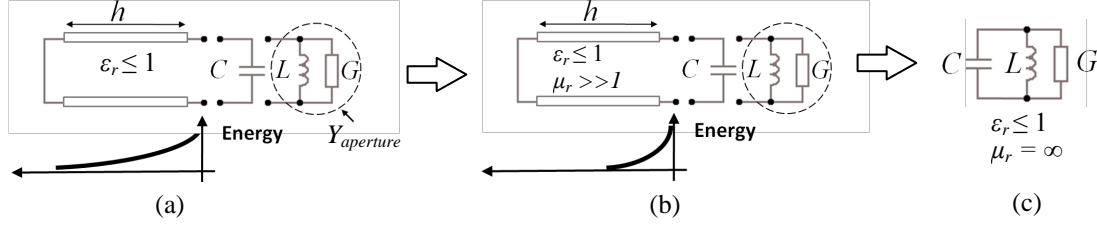


Figure 126 Sketches of a cavity antenna's model showing the decaying energy inside the cavity part for (a) low permittivity dielectric material; (b) for a magnetic material with high permeability; (c) for a material with infinite permeability when the model can be reduced to a simple parallel resonant circuit.

5.3.4. On the impossibility of achieving the bound with SRR type metamaterials

A composite isotropic metamaterial, consisting of an array of split-ring resonators (SRR), can be precisely investigated with an equivalent LCR circuit. The final outcome is a relative scalar permeability

$$\mu_r(k) = 1 + \frac{Fk^2}{k_0^2 - k^2}, \quad (5.18)$$

Where wave-number k is used instead of frequency ω , k_0 is the resonant wave-number, and F is a constant connected with the bandwidth around the resonance. It is important to emphasize that (5.18) can only be used provided that the ring radius is much less than the wavelength and this fits into the concept of a metamaterial as a composite of artificial sub-wavelength “atoms.” The consequence of this assumption is that it permits the conduction current to dominate the displacement current (also known as “quasi-static” approximation).

It is clear that (5.18) does not provide a description of very high-frequency behavior because as $k \rightarrow \infty$ the permeability $\mu_r \rightarrow 1 - F$, while it is $\mu_r \rightarrow 1$ that should be expected physically. There is straightforward physical way to see this by recognizing that the concept of an inductor and capacitor break down at very high frequencies and the quasi-static approximation is incorrect.

On the other hand, in the low frequency limit when $k \rightarrow 0$, the electromotive force driving the current through the ring and producing the magnetic response of the ring tends to zero. Besides that, at low frequencies the capacitive gap of the split-ring resonator prevents any current from flowing and, hence, there can be no magnetic response from the SRR array. This means that the limit $\mu_r \rightarrow 1$ as $k \rightarrow 0$ is the correct one in full accordance with (5.18).

To correctly investigate the effect of a SRR material, we shall need to know not only the behavior of $\mu_r(k)$ as $k \rightarrow 0$ but also its derivatives. Therefore we write

$$\begin{aligned} \mu_r(k) &= 1 + \frac{Fk^2}{k_0^2 - k^2} & \xrightarrow{k=0} \mu_r(0) &= 1 \\ \mu_r'(k) &= \frac{2Fk^3}{(k_0^2 - k^2)^2} + \frac{2Fk}{k_0^2 - k^2} & \xrightarrow{k=0} \mu_r'(0) &= 0 \\ \mu_r''(k) &= \frac{8Fk^4}{(k_0^2 - k^2)^3} + \frac{10Fk^2}{(k_0^2 - k^2)^2} + \frac{2F}{k_0^2 - k^2} & \xrightarrow{k=0} \mu_r''(0) &= \frac{2F}{k_0^2}. \end{aligned} \quad (5.19)$$

We now turn to the calculation of the Q factor. We are not interested in the bound, but in the question: can a cavity filled with SRRs reach the bound set in (5.16)? In that regard, we turn to the method introduced in Chapter 3.5, i.e. we look at the series expansion of

$$Q = \frac{k}{2G(k)} \left| \frac{\partial Y(k)}{\partial k} \right|, \quad (5.20)$$

where we insert the total admittance

$$Y(k) = G(k) + 2 \left(j b_{11}^0 \frac{2\pi}{ka} - j \frac{\sqrt{\varepsilon_r \mu_r(k) k^2 - \left(\frac{\pi}{a}\right)^2}}{\mu_r(k) k \eta_0} \cot \left(\sqrt{\varepsilon_r \mu_r(k) k^2 - \left(\frac{\pi}{a}\right)^2} h \right) \right) \quad (5.21)$$

Upon an expansion around $k = 0$, one arrives at a very complicated expression that is not particularly illuminating. To simplify things and make the result readable and clear, it is good to immediately insert the numerical values of the coefficients and make the limits $h \rightarrow \infty$, and $\varepsilon_r \rightarrow 0$ as this was already shown to lead

to the minimum Q . Additionally, it is useful to insert the value of $\mu_r(0)$ as it is just 1. Finally we can write the result as

$$Q \cong \underbrace{\frac{58.785}{(ka)^3} + \frac{2.52}{(ka)}}_{\text{same as bound for regular square cavity}} + \underbrace{\frac{36.51}{ka^3} \mu_r'(0)^2}_{\text{zero because } \mu_r'(0)=0} + \underbrace{\frac{18.26}{ka^3} \mu_r''(0)}_{\text{positive non zero}}, \quad \text{with } \varepsilon_r = 0, h \gg \quad (5.22)$$

Therefore, the Q factor for a cavity antenna filled with a SRR metamaterial can only have a larger value than the minimum bound due to the last term in (5.22). This is a very interesting result because it shows that although SRR metamaterials can exhibit desired high values of permeability below their resonance, this is completely unimportant. Only the static limit and the frequency dependence are important; where SRRs fail to give beneficial results. This is unfortunate, and it shows that constant high value permeability, which can practically be obtained only with natural materials, should be used to obtain benefits for bandwidth.

5.3.5. Modifying aperture admittance

In the last few sections we discussed changes to the interior, cavity, part of the antenna; here we concentrate on the outside, aperture, part. As sketched in Figure 126, cavity antennas basically operate as parallel LC resonant circuits (with an attached transmission line representing the cavity part). This simplification in thinking and understanding cavity antennas will naturally lead us to the simplest condition for bandwidth enhancement. Remembering the Q factor of a parallel circuit (from Appendix A) as

$$Q^P = \frac{R}{\omega_0 L} = \frac{1}{\omega_0 GL}. \quad \text{for } \frac{1}{LC} = \omega_0^2 = \text{constant} \quad (5.23)$$

Where ω_0 is the desired resonance frequency, we have the following conclusions: There are infinitely many pairs of values of L and C that will give the same ω_0 , but pairs with large L and small C will give lower Q . The way to lower Q , i.e. increase bandwidth is simple: *increase inductance L in any way possible!*

Putting magnetic material inside the cavity will increase inductance on the cavity side of the problem, but increasing inductance of the aperture admittance is perhaps trickier. Aperture admittance depends on the immediate surroundings of the aperture; currents in the ground plane, its shape and material properties. How, exactly, to design the exterior of the cavity does not have a straightforward answer; if the application allows any modifications to the exterior in the first place. However, the author can offer two ideas, depicted in Figure 127. First: by placing a layer of high permeability material around the aperture (see Figure 127(b)). This reduces the current in the ground plane surface and forces it to the edge of the aperture. Second, without any magnetic materials, by reshaping the ground plane so that the current has to follow a meandered path (sketched on Figure 127(c)). Reducing the size of the ground plane will also increase aperture inductance. All these techniques aim to reduce the value of b_{11}^0 coefficient in the bound.

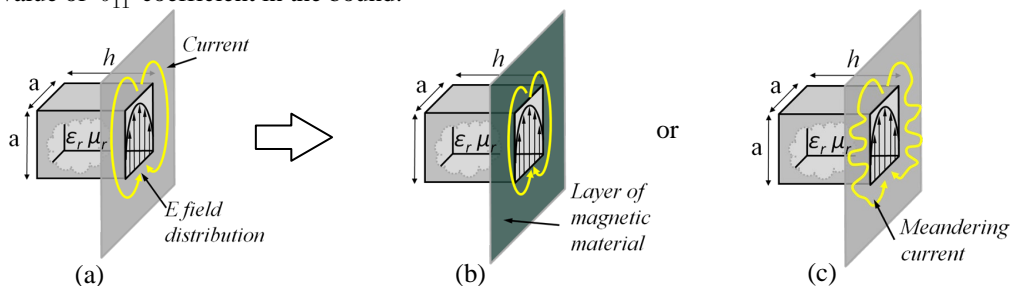


Figure 127 (a) regular cavity antenna with sketched current on the ground plane. (b) Increasing inductance of the aperture admittance by placing a magnetic material around the aperture and (c) by meandering the current path on a normal metallic ground plane.

5.4. Applications for building compact antenna arrays

In connection with antenna arrays, an angle of arrival (AoA), or detection of arrival (DoA) measurement is a method for determining the direction of propagation of a radio-frequency wave incident on the array. AoA determines the direction by measuring the Time Difference of Arrival (TDOA) at individual elements of the array -- from these delays the AoA can be calculated.

Generally this TDOA measurement is made by measuring the difference in received phase at each element in the antenna array. This can be thought of as beam forming in reverse. In beam forming, the signal from each

element is delayed by some weight to "steer" the gain of the antenna array. In AoA, the delay of arrival at each element is measured directly and converted to an AoA measurement.

For example, a two element array spaced apart by one-half the wavelength of an incoming RF wave. If a wave is incident upon the array perpendicularly, it will arrive at each antenna simultaneously. This will yield 0° phase-difference measured between the two antenna elements, equivalent to a 0° AoA. If a wave is incident in parallel to the array orientation, then a 180° phase difference will be measured between the elements, corresponding to a 90° AoA. AoA is generally used to discover the location of pirate radio stations or of any military radio transmitter.

In an effort to create a compact (size $d < \lambda_0/2$) angle of arrival system, an array of four elements was investigated. Here we give a brief example of a possible compact array design. The antenna configuration is given in Figure 128. The ground plane diameter is only $0.46 \lambda_0$ and the four $0.15 \lambda_0$ diameter cavity antennas of the same design as in Section 5.1 are used as elements of the array. In a counter-clockwise fashion, each element is rotated by 90 degrees. Because the elements themselves are linearly polarized this rotation puts nearby elements in orthogonal positions and minimizes the mutual coupling between them. However, elements 1 and 3 on Figure 128(a) are unfortunately oriented in the same way, which leads to relatively high coupling (10 dB), as seen on Figure 128(b). Bandwidth of each element remains almost the same as for the cavity antenna when it is not part of the array (in this case about 14.4 MHz). Additionally, this design is capable of giving circular polarization.

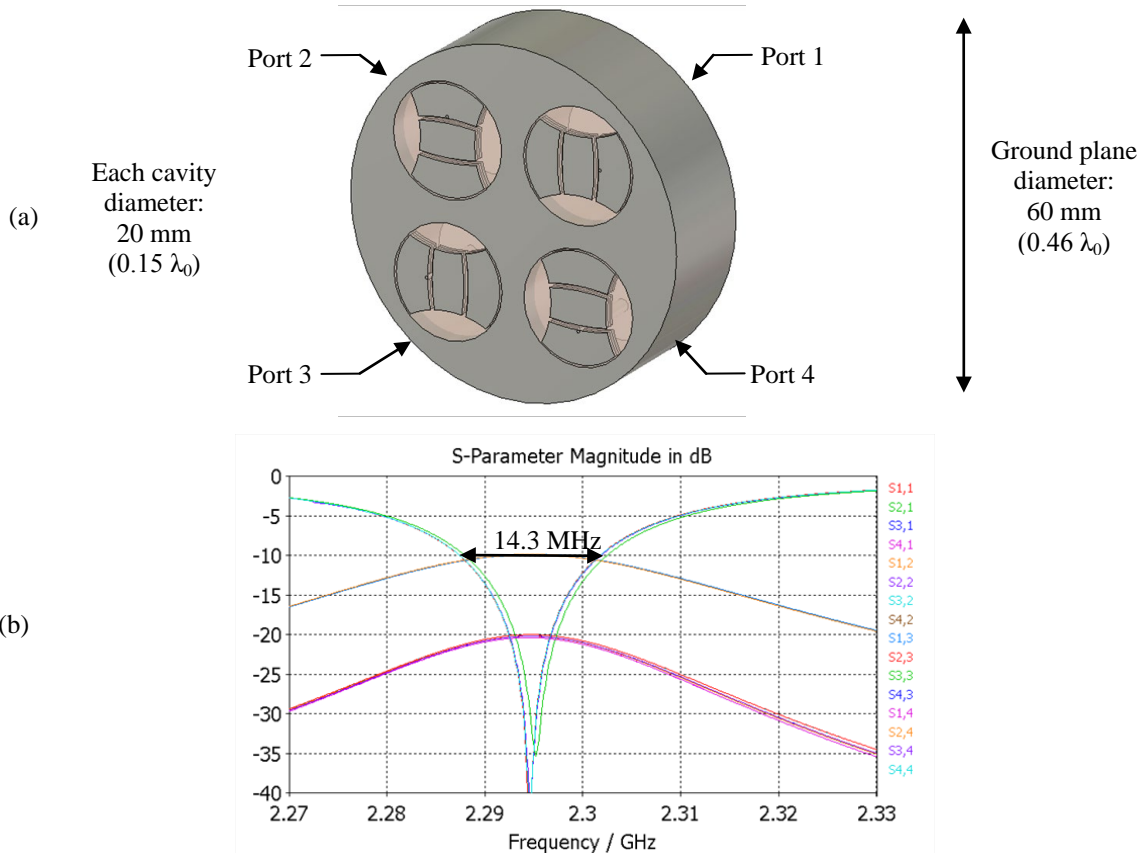


Figure 128 (a) Geometry of the compact antenna array for DOA application. (b) Simulated scattering parameters showing approximate bandwidth of each antenna remains about 14 MHz and coupling between diagonal antennas of -10 dB.

A simple method to reduce the mutual coupling between the antenna elements is recessing the metasurface into the cavity, leaving air or a low permittivity material on the top. This method further isolates each antenna element. However, a significant drawback is loss of bandwidth because the capacitor (i.e. metasurface) is no longer at the aperture. Other methods of element isolation can be used (like modifying the ground plane with holes) but are outside the scope of this work.

5.5. Conclusion of Chapter 5

In this chapter we discussed new possibilities opened up with the introduction of a metasurface design. The possibility to manufacture cavity antennas smaller than ever before is an application of critical importance. It was also one of the central objectives of this thesis to answer the question if this is even possible and how to

achieve it. This chapter demonstrated through simulation data and measurements of several prototypes that smaller cavity antennas are indeed a possibility with the new design. In addition, bandwidth performance is expected to be close to the bound in the ideal, lossless case. The manufactured prototypes were lossy and had increased bandwidth but reduced efficiency.

On the other side of the problem, for cavities that are not electrically small, it was shown that the metasurface design still offers benefits in terms of bandwidth and simplicity compared to classical designs like single and stacked patches.

From a theoretical perspective, this chapter indulged in hypothetical scenarios using ideal magnetic materials and conductors which can significantly improve the bound. In the author's opinion, the analysis is merely an interesting read at the moment, but might become important in the future with further advancements of nanotechnology.

Finally, a demonstration was given of how the ability to design small cavity antennas may be used to construct compact antenna arrays. This topic may be the subject of further research.

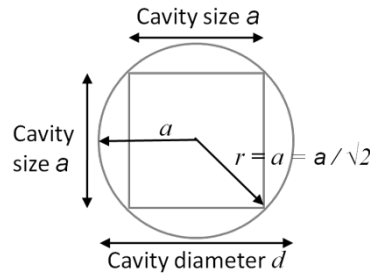
Conclusion

The goal of this work was to study compact, electrically small, cavity antennas. The prevailing question was – is it possible to use metamaterial concepts to develop smaller cavity antennas and at the same time increase their bandwidth performance compared to known cavity antenna types. Luckily, the answer to these questions is in the affirmative. This thesis investigated electrically small cavity antennas in three major ways: theoretically, through rigorous analysis of the bounds for such antennas; numerically, by performing numerous full wave simulations to confirm the theory or to discover new effects; and experimentally, by manufacturing prototypes based on the theory and numerical simulations. In this way, the subject of cavity antennas has been thoroughly explored and was expanded with the introduction of a new type of a cavity antenna. The new antenna type can be labeled “metamaterial inspired” because of its use of a metasurface at the aperture of the cavity and is important in two ways: it is capable of reaching the theoretical bound for Q for small antennas, and it can be made very small in practice; both aspects being a great improvement compared to antenna types used in the literature so far.

The theoretical contributions of this work are seen through the application of a recently introduced “scattering approach,” developed by Gustafsson *et. al.* to determine the bound on Q for specific cavity antennas and through making the connection between the bound and a transmission line model of the antenna, used to completely understand its operation. It was shown that the derived, new, bounds can be directly compared to the well known Chu limit that has been in use for many decades as a crude benchmark for all kinds of small antennas. The new bounds for specific cavity antenna shapes correctly show the dependence of the cavity dimensions and are much stricter than the classic Chu (or Thal) bound. The derivation of the new bounds was shown to be crucial in demonstrating that patch antennas are not the optimal antenna type inside a cavity and in developing a new transmission line model for cavity antennas that reach the bound (by adding a capacitor at the aperture). Analysis of the transmission line model is “easy” compared to the scattering approach, but the scattering approach actually proves that the obtained Q factor is truly the bound. For practical, engineering purposes, it is the transmission line model that needs to be considered and well understood, as it explains why the antenna resonates and what the ideal material inside the cavity volume is. The conclusion of the theoretical analysis was that an ideal capacitor at the aperture had to be designed in order to reach the bound on Q and this conclusion led to a development of a metasurface at the cavity aperture. The theoretical results on bounds of cavity antennas were also expanded with the hypothetical use of magnetic conductors and magnetic materials. Unfortunately, these bounds cannot be reached with metamaterial concepts; only with natural materials which are not available at present. A summary of the theoretical results are given below, in Table 11.

Practical contributions of this work are primarily the design of the metasurface for the rectangular and circular cavity shapes and the proper design of the excitation through a coaxial cable from the bottom of the cavity. Full wave numerical simulations and manufactured prototypes have demonstrated that the proposed design can reach the calculated maximum bandwidth determined through the minimum Q factor. A very important contribution is a demonstration of the possibility to manufacture smaller cavity antennas than previously possible with patch antennas. A summary of practical results concerning this contribution is given below, in Table 12. Additionally, for very large cavities, it was seen that the link between Q and bandwidth is not exact anymore because of a second cavity resonance that effectively broadens the bandwidth. This effect can be effectively used to design broadband cavity antennas with fractional bandwidth larger than 30% using only one layer of a metasurface at the top. Compared to stacked patches configurations used so far in the literature, this also presents great improvements, both in simplicity, bandwidth, and the use of cheaper materials as only low permittivity is needed. The proposed metasurface cavity antenna design thus has benefits for both electrically small cavities and for cavities close to half the operating wavelength in size. The possibility of manufacturing small cavity antennas also introduces the possibility of designing compact antennas arrays. This topic was only briefly touched in this thesis and can be the subject of future work.

Future work on electrically small cavity antennas may include better methods of manufacturing the antennas by using better materials or changing the design of the excitation part. Cavity antennas can also be made in modern “substrate integrated waveguide” (SIW) technology. In very low frequencies (below 10 MHz), where natural magnetic materials are available, the presented concepts can be used in an attempt to manufacture a small and very low profile cavity antennas with a low Q factor.



Q factor comparison	Rectangular cavity	Circular cavity	Comment
Chu bound	$Q = \frac{1}{(kr)^3} + \frac{1}{(kr)}$	$Q = \frac{1}{(ka)^3} + \frac{1}{(ka)}$	For spherical antennas only
Thal Bound	$Q = \frac{3}{(kr)^3} + \frac{3}{(kr)}$	$Q = \frac{3}{(ka)^3} + \frac{3}{(ka)}$	For spherical antennas only
Gustafsson Bound (infinite ground plane)	$Q = \frac{20.78}{(kr)^3} + \frac{1.78}{(kr)}, h \gg$	$Q = \frac{10.88}{(ka)^3} + \frac{1.53}{(ka)}, h \gg$	Achievable using metasurfaces
Approximate bound for finite ground plane	$Q \approx \frac{14.3}{(kr)^3} + \frac{2.4}{(kr)}, h \gg$	$Q \approx \frac{8.25}{(ka)^3} + \frac{2.5}{(ka)}, h \gg$	Achievable using metasurfaces
-with magnetic material (infinite ground plane)	$Q = \frac{7.87}{(kr)^3} + \frac{0.67}{(kr)}, \mu_r \gg$	$Q = \frac{4.28}{(ka)^3} + \frac{0.6}{(ka)}, \mu_r \gg$	Possibly achievable at low frequencies or in the future with advancements in nano-technology
-with magnetic conductor (infinite ground plane)	$Q = \frac{2.97}{(kr)^3} + \frac{0.29}{(kr)}, h \gg$	Not clear	Probably not achievable due to no natural magnetic conductors

Table 11 Summary of the theoretical results

Experimental results for circular cavities in a finite ground plane – achieved bandwidth			
Aperture size	Patch antenna design	Metasurface antenna design	Comment
32 mm	60 MHz	90 MHz	Improvement of 50%
20 mm	Not feasible	21 MHz	Completely new ability
16 mm	Not feasible	22 MHz	

Table 12 Summary and comparison of experimental results concerning circular cavities.

APPENDIX A. DEFINITIONS OF Q FACTOR AND BANDWIDTH

Definition of a tuned antenna

For an antenna with an input impedance $Z(\omega) = R(\omega) + jX(\omega)$ we are defining a “tuned antenna” at the frequency ω_0 as an antenna that has a total input reactance equal to zero at ω_0 . Additionally, the frequency, at which $X(\omega_0) = 0$, defines a *resonant frequency* of the antenna if $X'(\omega_0) > 0$ and an *antiresonant frequency* of the antenna if $X'(\omega_0) < 0$. These definitions of resonance and anti-resonance come from the behavior of the reactance of series and parallel *RLC* circuits, respectively, at their natural frequencies of oscillation. At the “resonant frequency” of a series *RLC* circuit with positive L and C , $X'(\omega_0) > 0$ and at the “anti-resonant frequency” of parallel *RLC* circuit with positive L and C , $X'(\omega_0) < 0$.

Definition of Q

The quality factor Q is a dimensionless parameter that compares the frequency at which a system oscillates to the rate at which it dissipates its energy. In the majority of publications dealing with the determination of the minimum Q of an antenna, the following assumptions are made:

- The antenna is tuned to resonance or anti-resonance using a reactive lossless circuit element.
- There is only one resonance in the considered frequency band
- Under these assumptions the Q factor of the antenna is defined by

$$Q = 2\pi \frac{\text{Energy Stored}}{\text{Energy dissipated per cycle}} = \frac{\omega(W_e + W_m)}{P_R} = \begin{cases} \frac{2\omega W_e}{P_R}, & \text{if } W_e > W_m \\ \frac{2\omega W_m}{P_R}, & \text{if } W_e < W_m \end{cases} \quad (\text{A.1})$$

where W_e is the time averaged stored electric energy density, W_m the corresponding magnetic energy density and P_R the power loss i.e. radiated power. At the resonance frequency, ω_0 , there are equal amounts of stored electric energy and stored magnetic energy, i.e. $W_e = W_m$.

However, with the introduction of metamaterials, i.e. materials with frequency dependent constitutive parameters, a generalization of the definition became necessary. Although it is not impossible for W to have a negative value, and the values of the constitutive parameters may even be negative, it was proven that the internal energy density in lossless antenna material is always greater than or equal to zero [24]. To incorporate these more general materials, a newer, very general definition of $Q(\omega_0)$ for an antenna tuned to have zero reactance at the frequency ω_0 ($X(\omega_0) = 0$) is defined by [23][24]

$$Q = \frac{\omega_0 |W^Q(\omega)|}{P_R}, \quad (\text{A.2})$$

with.

$$W^Q(\omega) = \frac{1}{4} \lim_{r \rightarrow \infty} \left[\int_V \{ \mathbf{E}^* \cdot (\omega \underline{\underline{\epsilon}})' \cdot \mathbf{E} + \mathbf{H}^* \cdot (\omega \underline{\underline{\mu}})' \cdot \mathbf{H} + [\mathbf{E}^* \cdot (\omega \underline{\underline{\tau}})' \cdot \mathbf{H} + \mathbf{H}^* \cdot (\omega \underline{\underline{\nu}})' \cdot \mathbf{E}] \} dV - 2\epsilon_0 r \int_{4\pi} |F|^2 d\Omega \right], \quad (\text{A.3})$$

Where stars (*) denote the complex conjugate, and primes (') denote differentiation with respect to the angular frequency ω . The vectors (\mathbf{E}, \mathbf{D}) and (\mathbf{H}, \mathbf{B}) are the usual time-harmonic ($e^{-j\omega t}$) Maxwellian electric and magnetic fields related by bianisotropic constitutive parameters ($\mathbf{D} = \underline{\underline{\epsilon}} \cdot \mathbf{E} + \underline{\underline{\tau}} \cdot \mathbf{H}$, $\mathbf{B} = \underline{\underline{\mu}} \cdot \mathbf{H} + \underline{\underline{\nu}} \cdot \mathbf{E}$) and \mathbf{F} is the complex far electric-field pattern.

Although the value of W^Q and thus Q can be determined, in principle, by integrating the electric and magnetic fields of the antenna throughout all space, it is however not adequate for the present analysis. This is because the decomposition of the total energy into stored and dissipated parts is a fundamentally difficult task. Therefore, an alternative expression, involving input reactance of the antenna will be given in the next section

Definition of radiation efficiency: The frequency dependent resistance contains both radiation $R_{Rad}(\omega)$ and loss $R_{Loss}(\omega)$ terms from which the antenna’s frequency dependent radiation efficiency η_{eff} is determined using

$$\eta_{eff} = \frac{P_{Rad}}{P_{Ant}} = \frac{P_{Rad}}{P_{Rad} + P_{Loss}}, \quad (\text{A.4})$$

Realistic electrically small antennas behave as either a lossy capacitor (C), a lossy inductor (L), or a combination of both, and its feed point impedance takes the form of a series or parallel RLC circuit. Because it behaves similarly to a lossy circuit element, it is often convenient to describe the properties of the small antenna in terms of circuit equivalent concepts, particularly the quality factor Q , fractional bandwidth FBW, and efficiency (in the case of lossy antennas).

Definition of fractional bandwidth

If the antenna operates at center frequency ω_0 between a lower frequency $\omega_- = \omega_0 - \Delta\omega$ and an upper frequency $\omega_+ = \omega_0 + \Delta\omega$, then the fractional bandwidth FBW is given by

$$FBW = \frac{\omega_+ - \omega_-}{\omega_0} = \frac{2\Delta\omega}{\omega_0}, \quad (\text{A.5})$$

Wideband antennas usually have bandwidth of 20% or more. Antennas with FBW greater than 50% are referred to as ultra-wideband antennas.

Link between Q factor and bandwidth for lumped resonant circuits

The basic series (parallel) resonance circuit consists of series (parallel) connected inductor, capacitor, and resistor, see **Figure 129**. For both types of circuit, the resonance frequency at which the input impedance (admittance) is purely real is $\omega_0^2 = 1/(LC)$.

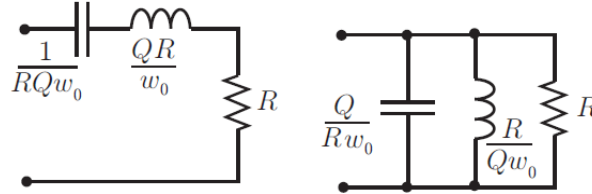


Figure 129. Lumped circuits. a) the series RCL circuit. b) the parallel RCL circuit. Taken from [25].

First we proceed to compute the Q factor by showing two approaches; by direct energy calculation and by derivation of the circuit's reflection coefficient respectively. We start with the energy calculation by writing the power loss and electric and magnetic energies in the circuits as

$$\begin{aligned} P_R^S &= \frac{1}{2}|I|^2 R, & P_R^P &= \frac{1}{2}\frac{|V|^2}{R} \\ W_m^S &= \frac{1}{4}|I|^2 L, & W_m^P &= \frac{1}{4}|I_L|^2 L = \frac{1}{4}\frac{|V|^2}{\omega^2 L} \\ W_e^S &= \frac{1}{4}|V|^2 C = \frac{1}{4}\frac{|I|^2}{\omega^2 C}, & W_e^P &= \frac{1}{4}|V|^2 C \end{aligned} \quad (\text{A.6})$$

Inserting (A.6) directly into (A.1) we can arrive at expressions for Q of a series (parallel) circuit in terms of the values of lumped elements

$$\boxed{Q^S = \frac{\omega_0 L}{R} = \frac{1}{\omega_0 C R}, \quad Q^P = \frac{R}{\omega_0 L} = \omega_0 C R.} \quad (\text{A.7})$$

Alternately, we can show that the Q factor can also be represented using the reflection coefficient Γ from the lumped circuit. For this, using (A.7) we write $L = RQ/\omega_0$ and $C = 1/(RQ\omega_0)$ and $L = R/(Q\omega_0)$ and $C = Q/(R\omega_0)$ in the series and parallel cases, respectively. The reflection coefficient Γ from the circuit is then given by

$$\Gamma = \frac{Z(\omega) - R}{Z(\omega) + R} = \pm \frac{1 - (\omega/\omega_0)^2}{1 - (\omega/\omega_0)^2 + 2j\omega/(Q\omega_0)}, \quad (\text{A.8})$$

where $Z(\omega) = R + jX(\omega)$ denotes the input impedance and R is also assumed as the characteristic impedance of the feeding line. The + and - minus signs correspond to series and parallel circuits, respectively.

Differentiation of the reflection coefficient with respect to ω gives

$$\left. \frac{\partial \Gamma(\omega)}{\partial \omega} \right|_{\omega=\omega_0} = \pm \frac{2j\omega_0 Q(\omega_0^2 + \omega^2)}{(\omega^2 Q - \omega_0^2 Q + 2j\omega_0 \omega)^2} \Big|_{\omega=\omega_0} = \pm j \frac{Q}{\omega_0}, \quad (\text{A.9})$$

and hence $Q = \omega_0 |\Gamma'(\omega)|$.

Written using impedance explicitly we have

$$Q = \omega_0 \left| \frac{\partial \Gamma}{\partial \omega} \right| = \omega_0 \left| \frac{2RZ'(\omega)}{(R+Z(\omega))^2} \right| = \omega_0 \left| \frac{2R(R+jX(\omega))'}{(R+R+jX(\omega))^2} \right| = \frac{\omega_0}{2R} \left| \frac{\partial X(\omega)}{\partial \omega} \right|, \quad (\text{A.10})$$

where the derivatives are evaluated at $\omega = \omega_0$. Equivalently we can arrive at a similar expression using admittances $Q = \omega_0 |B'(\omega)| / (2G)$. To demonstrate the use of (A.10) we show a derivation of Q factor in the case of a series resonant circuit

$$Q^S = \frac{\omega_0}{2R} \left| \frac{\partial}{\partial \omega} \left(j\omega L - j \frac{1}{\omega C} \right) \right| = \frac{\omega_0}{2R} \left(L + \frac{1}{\omega_0^2 C} \right) = \frac{2\omega_0 L}{2R} = \frac{\omega_0 L}{R}, \quad (\text{A.11})$$

Where we have used the fact that the same energy is stored in the inductive part of the circuit as in the capacitive part and have thus used only the inductive part with doubled value. The result of (A.11) coincides with (A.7) for a series circuit.

Second, we proceed to compute the simple case of half-power fractional bandwidth of the resonator. We represent the input impedance or admittance as

$$Z_{in}^S = R + j\omega L \left(1 - \frac{\omega_0^2}{\omega^2} \right), \quad Y_{in}^P = G + j\omega C \left(1 - \frac{\omega_0^2}{\omega^2} \right). \quad (\text{A.12})$$

Half-power (or 3dB) points occur when the magnitude of the impedance is equal to $\sqrt{2}R$. This happens when the real and reactive parts are equal.

$$R = j\omega L \left(\frac{\omega^2 - \omega_0^2}{\omega^2} \right), \quad G = j\omega C \left(\frac{\omega^2 - \omega_0^2}{\omega^2} \right). \quad (\text{A.13})$$

Which leads to a condition

$$\omega^2 - \omega_0^2 = \omega \frac{R}{L}, \quad \omega^2 - \omega_0^2 = \omega \frac{G}{C} \quad (\text{A.14})$$

Where we can now use an approximation $\omega^2 - \omega_0^2 = (\omega - \omega_0)(\omega + \omega_0) = \Delta\omega(2\omega - \Delta\omega) \cong 2\omega\Delta\omega$ if the bandwidth is reasonably small. Introducing this approximation into (A.14), removing ω from the left and right sides, dividing by ω_0 and using the definition of fractional bandwidth $FBW = 2\Delta\omega/\omega_0$ we are led to the same result in both series and parallel circuit case

$$\left. \begin{aligned} FBW^{3dB} &\cong \frac{R}{\omega_0 L} \\ FBW^{3dB} &\cong \frac{G}{\omega_0 C} \end{aligned} \right\} = \frac{1}{Q}. \quad (\text{A.15})$$

This simple result shows that bandwidth and Q are inversely proportional. Note that a crucial assumption here is narrow bandwidth, or high Q , and the link is only an approximation, not an exact relationship.

Although circuits are closed systems and as such amenable to a direct calculation of Q , antennas by their very nature are open systems. From the viewpoint of the antenna, energy that permanently leaves it is the equivalent to energy dissipation in a resistor.

Link between the Q factor and bandwidth for antennas with a general impedance

For many applications it is sufficient to model the antenna as a simple RLC resonance circuit around the resonance frequency. However, the link between Q and fractional bandwidth (FBW) is no trivial matter. As pointed out in the comprehensive paper by Yaghjian and Best [24], the concept of bandwidth has to be refined: they make the distinction between the „**conduction bandwidth**“, defined for a tuned antenna as “*the difference between the two frequencies at which the power accepted by the antenna, excited by a constant voltage V_0 , is a given fraction of the power accepted at the frequency ω_0* ”, and the “**matched VSWR Bandwidth**”, defined as “*the difference for an antenna tuned at frequency ω_0 between two frequencies on either side of ω_0 at which the VSWR equals a constant s* ”

Conduction bandwidth FBW_{cd} and Q factor are closely related under the assumption that the real part of the antenna input impedance $Z(\omega) = R(\omega) + jX(\omega)$ is not changing rapidly with frequency i.e. $R'(\omega_0) \approx 0$. The conductance at a frequency ω of an antenna tuned at the frequency ω_0 can be written as

$$G(\omega) = \text{Re} \left\{ \frac{1}{Z(\omega)} \right\} = \frac{R(\omega)}{R(\omega)^2 + X(\omega)^2}, \quad (\text{A.16})$$

We can immediately point out the problem with using conductance bandwidth, namely, that the derivative of $G(\omega)$ evaluated at ω_0 equals $G'(\omega_0) = R'(\omega_0)/R(\omega_0)$ and thus it is not zero at ω_0 unless $R'(\omega_0) = 0$. This means that in general the conductance will not reach a maximum at the frequency ω_0 . Moreover, in anti-resonant frequency ranges where both the resistance and reactance of the antenna are changing rapidly with frequency, the conductance may not possess a maximum and consequently the conductance bandwidth may not exist in these anti-resonant frequency ranges.

To determine the conductance bandwidth about the shifted frequency $\omega_{cd} = \omega_0 + \Delta\omega_0$ at which $G(\omega)$ actually peaks when the antenna is tuned at ω_0 , we find the two frequencies $\omega_{\pm} = \omega_{cd} + \Delta\omega_{\pm}$ at which the accepted power is $(1 - \alpha)$ times its value at ω_{cd} . Is given from (A.16) as

$$\frac{R(\omega_{\pm})}{R(\omega_{\pm})^2 + X(\omega_{\pm})^2} = (1 - \alpha) \frac{R(\omega_{cd})}{R(\omega_{cd})^2 + X(\omega_{cd})^2}, \quad (\text{A.17})$$

The value of the constant α which lies in the range $0 \leq \alpha \leq 1$ is assumed chosen $\leq 1/2$. Next, all the functions in (A.17) have to be expanded in a Taylor's series about ω_{cd} , and then transformed to involve ω_0 using $\omega_{cd} - \omega_0 = \Delta\omega_0$ and $R'(\omega_0) \ll X'(\omega_0)$ is assumed. After a considerable amount of manipulations the result is found to be [24]

$$\Delta\omega_{\pm} \approx \pm \frac{\sqrt{\beta}R(\omega_0)}{X'(\omega_0)}, \quad \beta = \frac{\alpha}{1 - \alpha} \leq 1 \quad (\text{A.18})$$

Under the additional assumption that the $O[(\Delta\omega_{\pm})^3]$ terms in the Taylor expansion are negligible. An assumption that is generally satisfied if $\Delta\omega_{\pm}/\omega_0 \ll 1$.

The fractional conductance bandwidth FBW_{cd} is therefore given approximately by

$$FBW_{cd}(\omega_0) = \frac{\omega_+ - \omega_-}{\omega_0} = \frac{\Delta\omega_+ - \Delta\omega_-}{\omega_0} \approx \frac{2\sqrt{\beta}R(\omega_0)}{\omega_0|X'(\omega_0)|}. \quad (\text{A.19})$$

We can immediately see that this approximation can be compared with the expression (A.10) for the Q factor of resonant lumped circuits. This is reasonable concerning we assumed the real part of the impedance is not varying with frequency. Combining (A.10) and (A.19) we arrive at

$$FBW_{cd} = \frac{\sqrt{\beta}}{Q}, \quad \beta = \frac{\alpha}{1 - \alpha} \leq 1 \quad (\text{A.20})$$

For the half-power bandwidth $|\Gamma|^2 = 0.5$, (VSWR=5.828) and $\sqrt{\beta} = 1$ is given by $FBW_{cd} = 1/Q$ which is the same as derived in (A.15).

Matched VSWR bandwidth FBW_V and Q are related even for general impedance $Z(\omega) = R(\omega) + jX(\omega)$ where where the real part or the impedance is also frequency dependent. In this case, the reflection coefficient Γ of the antenna is then given by

$$\Gamma = \frac{R(\omega) + jX(\omega) - R(\omega_0)}{R(\omega) + jX(\omega) + R(\omega_0)}, \quad (\text{A.21})$$

where we put the characteristic impedance Z_{ch} of the feed line $Z_{ch} = R(\omega_0)$. We calculate Q the same way as in (A.11) and get.

$$Q = \omega_0 \left| \frac{\partial \Gamma(\omega)}{\partial \omega} \right| = \omega_0 \left| \frac{2R(\omega_0)(R'(\omega) + jX'(\omega))}{(R(\omega_0) + R(\omega) + jX(\omega))^2} \right| \xrightarrow{\omega=\omega_0} \frac{\omega_0 Z'(\omega_0)}{2R(\omega_0)} \quad (\text{A.22})$$

The FBW_V for an antenna tuned at a frequency ω_0 is defined as the difference between the two frequencies on either side of ω_0 with a specific VSWR or, equivalently, at which $|\Gamma(\omega)|^2$ equals $\alpha = (\text{VSWR} - 1)^2 / (\text{VSWR} + 1)^2$ where the constant α is assumed chosen $\leq 1/2$. We thus take the magnitude squared of the reflection coefficient i.e,

$$|\Gamma(\omega)|^2 = \frac{X^2(\omega) + [R(\omega) - R(\omega_0)]^2}{X^2(\omega) + [R(\omega) + R(\omega_0)]^2}, \quad (\text{A.23})$$

Importantly, both $|\Gamma(\omega)|^2$ and its derivative with respect to ω are zero at ω_0 . Consequently, $|\Gamma(\omega)|^2$ has a minimum at ω_0 at which the antenna is tuned ($X(\omega_0) = 0$) and matched to the feed line $Z_{ch} = R(\omega_0)$. This means the matched VSWR bandwidth, $(\omega_+ - \omega_-)$ determined by

$$\frac{X^2(\omega_{\pm}) + [R(\omega_{\pm}) - R(\omega_0)]^2}{X^2(\omega_{\pm}) + [R(\omega_{\pm}) + R(\omega_0)]^2} = \alpha \quad (\text{A.24})$$

unlike the conductance bandwidth, exists at all frequencies (for small enough α), that is, throughout both the antiresonant $X'(\omega_0) < 0$ and resonant $X'(\omega_0) > 0$ frequency ranges. Therefore, the matched VSWR bandwidth is a more fundamental, universally applicable definition of bandwidth for a general antenna than conductance bandwidth.

Bringing the denominator from the left-hand side of (A.24) to the right-hand side and rearranging terms to remove the rapidly varying function $X(\omega)$ from the denominator on the left-hand side of (A.24) produces

$$\frac{X^2(\omega_{\pm}) + [R(\omega_{\pm}) - R(\omega_0)]^2}{R(\omega_{\pm})} = 4\beta R(\omega_0), \quad \beta = \frac{\alpha}{1 - \alpha} \leq 1 \quad (\text{A.25})$$

Expanding the left hand side in a Taylor series about ω_0 we find [YiB]

$$|Z'(\omega_0)|^2 (\Delta\omega_{\pm})^2 \approx 4\beta R^2(\omega_0), \quad (\text{A.26})$$

Under the assumption that the $O[(\Delta\omega_{\pm})^3]$ terms are negligible. The assumption is generally satisfied if $|\Delta\omega_{\pm}/\omega_0| \ll 1$. The solution for $\Delta\omega_{\pm}$ are

$$\Delta\omega_{\pm} = \pm \frac{2\sqrt{\beta}R(\omega_0)}{|Z'(\omega_0)|}, \quad (\text{A.27})$$

So the simplified fractional VSWR bandwidth takes the simple form

$$FBW_V(\omega_0) = \frac{\omega_+ - \omega_-}{\omega_0} = \frac{\Delta\omega_+ - \Delta\omega_-}{\omega_0} \approx \frac{4\sqrt{\beta}R(\omega_0)}{\omega_0|Z'(\omega_0)|}, \quad (\text{A.28})$$

Using the approximate expression (A.28) and comparing it with the exact expression for Q in (A.22) we arrive at

$$\boxed{FBW_V(\omega_0) = \frac{2\sqrt{\beta}}{Q}, \quad \beta = \frac{\alpha}{1 - \alpha} \leq 1} \quad (\text{A.29})$$

The bandwidth of the resonance depends on the threshold level of the reflection coefficient. The relative bandwidth of half power, $|\Gamma|^2 \leq 0.5$, (VSWR=5.828) and $\sqrt{\beta} = 1$ is given by $FBW_V = 2/Q$. Relation (A.29) is circuit and is also a good approximation for single and multiple resonance models if Q is sufficiently large.

Conclusions

Due to the general nature of antenna impedances, the two definitions of bandwidth yield several differences:

- In general, the frequency where the resistive part of the antenna impedance is maximal does not coincide with ω_0 (frequency where the tuned reactance is equal to zero).
- In the case of anti-resonance, the conductance bandwidth may not exist as the conductance of the antenna may not have a maximum.
- Outside the anti-resonant frequency ranges, the matched VSWR bandwidth is equal to twice the conductance bandwidth $FBW_V(\omega_0) \cong 2FBW_{cd}(\omega_0)$
- Consider the VSWR (or equivalently the reflection coefficient) bandwidth rather than the accepted power bandwidth, as it is more fundamental, use the link given by

$$Q(\omega_0) \approx \frac{2 \left(\frac{VSWR - 1}{2\sqrt{VSWR}} \right)}{FBW_V(\omega_0)} \approx \frac{2\sqrt{\frac{\alpha}{1 - \alpha}}}{FBW_V(\omega_0)}, \quad \alpha = |\Gamma|^2 \quad (\text{A.30})$$

- The link is only an approximation, not an exact relationship. A crucial assumption is narrow bandwidth, or $Q \gg 1$. This condition is however always satisfied for electrically small antennas.
- In the cases where the Q factor is near unity, the only conclusion that can be made is that the antenna is potentially broadband but no explicit link between quality factor and bandwidth is made.

APPENDIX B. SCATTERING THEORY USEFUL DEFINITIONS

So called scattering or far field coefficients are the coefficients of e^{-jkr}/r in the far field. Consider the direct scattering problem of a time harmonic plane electromagnetic wave impinging in the forward direction $\hat{\mathbf{k}}$ on a bounded scatterer. The electric field \mathbf{E}^S in the $\hat{\mathbf{k}}$ -direction from an object is expressed by $\mathbf{E}^S(k, \mathbf{r}) = E_0^+ \underline{\mathbf{S}}(k, \hat{\mathbf{k}}) \cdot \hat{\mathbf{p}}_e e^{-jkr}/r$. The bistatic RCS, $\sigma(k, \hat{\mathbf{r}})$ in the $\hat{\mathbf{r}}$ direction, for wavenumber k is defined as

$$\sigma(k, \hat{\mathbf{r}}) = \lim_{r \rightarrow \infty} r^2 \frac{|\mathbf{E}^S(k, \mathbf{r})|^2}{|\mathbf{E}^{\text{inc}}|^2} = |\underline{\mathbf{S}}(k, \hat{\mathbf{k}}) \cdot \hat{\mathbf{p}}_e|^2, \quad (\text{B } 1)$$

Where \mathbf{E}^{inc} denotes the incident electric field, $r = |\mathbf{r}|$ denotes the magnitude of the position vector $\mathbf{r} = r\hat{\mathbf{r}}$. The scattering cross section $\sigma_s(k)$ is the average of the bistatic RCS over all angles, i.e., integration over the unit sphere Ω , namely,

$$\sigma_s(k) = \int_{\Omega} |\underline{\mathbf{S}}(k, \hat{\mathbf{k}}) \cdot \hat{\mathbf{p}}_e|^2 d\Omega, \quad (\text{B } 2)$$

where $d\Omega$ denotes the surface element of the unit sphere. The extinction cross section $\sigma_{ext}(k)$, sometimes designated the total cross section, is defined as $\sigma_{ext}(k) = \sigma_s(k) + \sigma_a(k)$, where $\sigma_a(k)$ is the absorption cross section which measures the power absorbed by the scatterer. The extinction cross section can be determined by measuring the bistatic RCS at all angles and the absorption cross section. However, a more straightforward method is to measure the RCS amplitude in the forward direction, and use the optical theorem to determine $\sigma_{ext}(k)$, through.

$$\sigma_{ext} = 4\pi/k \text{Im}(\hat{\mathbf{p}}_e^* \cdot \underline{\mathbf{S}}(k, \hat{\mathbf{k}}) \cdot \hat{\mathbf{p}}_e). \quad (\text{B } 3)$$

Thus the extinction cross section can also be determined by a measurement of the RCS amplitude in the forward direction.

Optical theorem

Here we will derive only the scalar version of the optical theorem due to the simplicity of the derivation. The optical theorem relates the forward scattering amplitude $S(\theta = 0)$ of a process to the corresponding total or extinction, cross section σ_{ext} . For light waves being scattered off particles, it is usually stated as

$$\sigma_{ext} = \frac{4\pi}{k} \text{Im}(S(\theta = 0)), \quad (\text{B } 4)$$

where $k = \omega/c$ is the (angular) wave number. The fundamental principle behind the optical theorem is the conservation of energy, the optical theorem is a beautiful demonstration of the fact that a handful of deep principles in physics lead to astonishing, far-from-obvious consequences.

Consider an incoming scalar plane wave travelling along the z axis which is scattered by some object at the origin. At a large distance $r \gg \lambda$, the amplitude of the wave can be expanded as

$$\psi(\mathbf{r}) \approx e^{-jkz} + S(\theta) \frac{e^{-jkr}}{r}, \quad (\text{B } 5)$$

where θ is the angle between \mathbf{r} and the z axis and $S(\theta)$ is the scattering amplitude. Close to the z axis ($\theta \ll 1$) we can make the approximation

$$r = \sqrt{x^2 + y^2 + z^2} \approx z + \frac{x^2 + y^2}{2z}. \quad (\text{B } 6)$$

The energy carried by the wave is proportional to the amplitude squared, which is given by

$$\begin{aligned} |\psi(\mathbf{r})|^2 &= 1 + S(\theta) \frac{e^{-jk(r-z)}}{r} + S^*(\theta) \frac{e^{-jk(r-z)}}{r} + \frac{|S(\theta)|^2}{r} \\ &\approx 1 + 2\text{Re} \left(\frac{S(\theta) e^{-jk \frac{(r-z)}{2z}}}{z + \frac{x^2 + y^2}{2z}} \right) \\ &\approx 1 + \frac{2}{z} \text{Re} \left(S(\theta = 0) e^{-jk \frac{x^2 + y^2}{2z}} \right). \end{aligned} \quad (\text{B } 7)$$

Now we consider the total energy absorbed by a screen of area $A = \pi R^2$, which is proportional to

$$\int_A |\psi(\mathbf{r})|^2 dA = \int_0^{2\pi} d\varphi \int_0^R \left[1 + \frac{2}{z} \operatorname{Re}(S(\theta=0)e^{-jk s^2/2z}) \right] s ds, \quad (\text{B } 8)$$

where $s = \sqrt{x^2 + y^2}$. The integration gives

$$\int_A |\psi(\mathbf{r})|^2 dA = \pi R^2 - \frac{4\pi}{k} \operatorname{Im}(S(\theta=0)). \quad (\text{B } 9)$$

We note that this gives the fraction of energy the screen would receive if there were no scattering diminished an amount proportional to $4\pi/k \operatorname{Im}(S(\theta=0))$. The conservation of energy demands that this be equal to the total extinction cross section $\sigma_{ext} = \sigma_s + \sigma_a = 4\pi/k \operatorname{Im}(S(\theta=0))$.

Absolute gain $G(\hat{\mathbf{k}})_\perp$

The absolute gain is the ratio of the radiation intensity in a given direction to the intensity that would be obtained if the power accepted by the antenna was radiated isotropically.

Partial gain $G(\hat{\mathbf{k}}, \hat{\mathbf{p}}_e)$

The partial gain in a give direction is the ratio of the part of the radiation intensity corresponding to a given polarization to the radiation intensity that would be obtained if the power accepted by the antenna was radiated isotropically. The absolute gain is equal to the sum of partial gains for two orthogonal polarizations, i.e. $G(\hat{\mathbf{k}}) = G(\hat{\mathbf{k}}, \hat{\mathbf{p}}_e) + G(\hat{\mathbf{k}}, \hat{\mathbf{p}}_m)$.

Realized gain $G(\hat{\mathbf{k}}, \Gamma)$

The realized gain is the absolute gain of an antenna reduced by the losses due to the impedance mismatch of the antenna, i.e. $G(\hat{\mathbf{k}}, \Gamma) = (1 - |\Gamma|^2)G(\hat{\mathbf{k}})$.

Absolute directivity $D(\hat{\mathbf{k}})$

The absolute directivity is the ratio of the radiation intensity in a given direction to the radiation intensity averaged over all directions. The averaged radiation intensity is equal to the total power radiated divided by 4π .

Partial directivity $D(\hat{\mathbf{k}}, \hat{\mathbf{p}}_e)$

The partial directivity in a given direction is the ratio of that part of the radiation intensity corresponding to a given polarization to the radiation intensity averaged over all directions. The averaged radiation intensity is equal to the total power radiated divided by 4π .

Absorption cross section $\sigma_a(\hat{\mathbf{k}}, \hat{\mathbf{p}}_e, \Gamma)$

The absorption cross section for a given polarization and incident direction is the ratio of the absorbed power in the antenna to the incident power flow density when subject to a plane wave excitation. For a perfectly matched antenna, the absorption cross section coincides with the partial effective area.

Absorption cross section $\sigma_s(\hat{\mathbf{k}}, \hat{\mathbf{p}}_e, \Gamma)$

The absorption cross section for a given polarization and incident direction is the ratio of the scattered power in the antenna to the incident power flow density when subject to a plane wave excitation.

Extinction cross section $\sigma_{ext}(\hat{\mathbf{k}}, \hat{\mathbf{p}}_e, \Gamma)$

The extinction cross section for a given polarization and incident direction is the sum of the absorbed and scattered power of the antenna to the incident power flow density when subject to a plane wave excitation, i.e. $\sigma_{ext}(\hat{\mathbf{k}}, \hat{\mathbf{p}}_e, \Gamma) = \sigma_s(\hat{\mathbf{k}}, \hat{\mathbf{p}}_e, \Gamma) + \sigma_a(\hat{\mathbf{k}}, \hat{\mathbf{p}}_e, \Gamma)$

Absorption efficiency $\eta(\hat{\mathbf{k}}, \hat{\mathbf{p}}_e, \Gamma)$

The absorption efficiency of an antenna for a given polarization and incident direction is the ratio of the absorbed power to the total absorbed and scattered power when subject to a plane wave excitation, i.e. $\eta(\hat{\mathbf{k}}, \hat{\mathbf{p}}_e, \Gamma) = \sigma_s(\hat{\mathbf{k}}, \hat{\mathbf{p}}_e, \Gamma) / \sigma_{ext}(\hat{\mathbf{k}}, \hat{\mathbf{p}}_e, \Gamma)$

APPENDIX C. CALCULATION OF THE APERTURE ADMITTANCE FOR A RECTANGULAR APERTURE.

In this section, using Fourier transform (spectral) techniques, the admittance of an rectangular aperture antenna mounted on an infinite ground plane and radiating into free space will be formulated. The geometrical arrangement of the antenna under consideration a rectangular cavity drilled into a ground plane and filled with some dielectric material of relative permittivity ϵ_r , as shown in Figure 130.

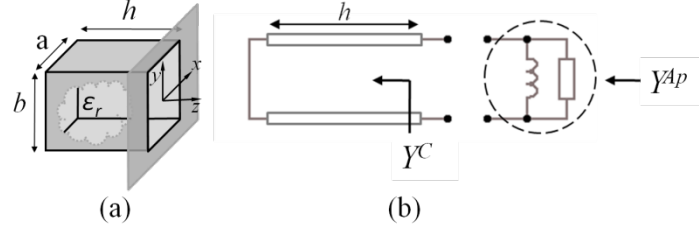


Figure 130 a) A rectangular cavity in an infinite ground plane and (b) the corresponding transmission line model for an electrically small cavity

Aperture field

We will assume that the electric field distribution on the aperture is that given by the TE_{n0} rectangular waveguide mode

$$\mathbf{E}_{y(n)} = \hat{\mathbf{y}}E_0^+ \cos\left(\frac{n\pi}{a}x\right), \quad -\frac{a}{2} \leq x \leq \frac{a}{2}, \quad -\frac{b}{2} \leq y \leq \frac{b}{2}, \quad (C 1)$$

where E_0^+ is a constant, a and b are the dimensions of the aperture.

Power inside the shorted waveguide

Inside the waveguide, the time averaged power transmitted in the TE_{n0} mode can be easily calculated from the Poynting vector

$$\begin{aligned} P_n^C &= \frac{1}{2} \int_A \mathbf{E}_y \times \mathbf{H}_x^* d\mathbf{S} = \frac{1}{2} Y_{wg(n)}^* |E_0^+|^2 \int_{-b/2}^{b/2} dy \int_{-a/2}^{a/2} \cos^2\left(\frac{n\pi}{a}x\right) dx = \\ &= \frac{ab}{4} Y_n^{C*} |E_0^+|^2 \end{aligned} \quad (C 2)$$

From (C 2) we can define the input impedance into the waveguide on FIG (having an electric field imposed at the aperture)

$$Y_n^C = \frac{4 P_{wg(n)}^*}{ab |E_0^+|^2}, \quad (C 3)$$

This formulation will also be suitable to calculate the aperture admittance.

Aperture admittance

It is important to note that unlike in the waveguide, the modes are not orthogonal at the aperture due to different boundary conditions. We thus must also consider the mutual admittance between TE_{0n} and TE_{0m} modes. The complex power flow delivered to the aperture can then be written as

$$Y_{mn}^{Ap} = \frac{4 P_{mn}^{Ap*}}{ab |E_0^+|^2} = G_{mn}^{Ap} + jB_{mn}^{Ap}. \quad (C 4)$$

The complex power transmitted by the aperture can be written as integral is by transforming it to the spectral domain, i.e.:

$$\begin{aligned} P_{mn}^{Ap} &= \frac{1}{2} \int_A \mathbf{E}_{y(n)}(x, y, z=0) \mathbf{H}_{x(m)}^*(x, y, z=0) d\mathbf{S} = \\ &= -\frac{1}{2} \int_A E_{y(n)}(x, y, 0) H_{x(m)}^*(x, y, 0) dx dy \end{aligned} \quad (C 5)$$

An alternate and simpler method in the formulation of the aperture admittance is to use Fourier transforms. By Parseval's theorem

$$\int_{-\infty}^{+\infty} f(x)g^*(x)dx = \frac{1}{2\pi} \int_{-\infty}^{+\infty} F(k_x)G^*(k_x)dk_x, \quad (C 6)$$

We can rewrite (C 5) as

$$P_{mn}^{Ap} = -\frac{1}{8\pi^2} \int_{-\infty}^{+\infty} \int_{-\infty}^{+\infty} E_{y(n)}(k_x, k_y)H_{x(m)}^*(k_x, k_y)dk_x dk_y, \quad (C 7)$$

Where $E_y(k_x, k_y)$ is the Fourier transform of the electric field

$$\begin{aligned} E_{y(n)}(k_x, k_y) &= \int_{-a/2}^{a/2} \int_{-b/2}^{b/2} E_0^+ \cos\left(\frac{n\pi}{a}x\right) e^{j(k_x x + k_y y)} dx dy = \\ &= E_0^+ \int_{-b/2}^{b/2} e^{jk_y y} \cdot \int_{-a/2}^{a/2} \cos\left(\frac{n\pi}{a}x\right) e^{jk_x x} dx, \end{aligned} \quad (C 8)$$

The first integral results in

$$\frac{[e^{jk_y y}]_{-b/2}^{b/2}}{jk_y} = \frac{2j\sin\left(\frac{k_y b}{2}\right)}{jk_y} = b \operatorname{sinc}\left(\frac{k_y b}{2}\right). \quad (C 9)$$

For the second integral we use a complex expansion of the cosine function

$$\begin{aligned} \int_{-a/2}^{a/2} \frac{1}{2} (e^{j\frac{n\pi}{a}x} + e^{-j\frac{n\pi}{a}x}) e^{jk_x x} dx &= \frac{1}{2} \int_{-a/2}^{a/2} e^{j(\frac{n\pi}{a}x + k_x x)} dx + \frac{1}{2} \int_{-a/2}^{a/2} e^{j(-\frac{n\pi}{a}x + k_x x)} dx \\ &= \frac{1}{2} \frac{2j\sin\left[\left(\frac{n\pi}{a} + k_x\right)\frac{a}{2}\right]}{j\left(\frac{n\pi}{a} + k_x\right)} + \frac{1}{2} \frac{2j\sin\left[\left(-\frac{n\pi}{a} + k_x\right)\frac{a}{2}\right]}{j\left(-\frac{n\pi}{a} + k_x\right)} = \\ &= \frac{\left(\frac{n\pi}{a} + k_x\right)\sin\left(\frac{n\pi}{2} + \frac{k_x a}{2}\right) + \left(\frac{n\pi}{a} + k_x\right)\sin\left(-\frac{n\pi}{2} + \frac{k_x a}{2}\right)}{k_x^2 - \left(\frac{n\pi}{a}\right)^2} = \\ &= \frac{\left(-\frac{n\pi}{a} + k_x\right)\cos\left(\frac{k_x a}{2}\right) - \left(\frac{n\pi}{a} + k_x\right)\cos\left(\frac{k_x a}{2}\right)}{k_x^2 - \left(\frac{n\pi}{a}\right)^2} = \\ &= \frac{\frac{2n\pi}{a} \cos\left(\frac{k_x a}{2}\right)}{\left(\frac{n\pi}{a}\right)^2 - k_x^2} = 2n\pi a \frac{\cos\left(\frac{k_x a}{2}\right)}{\frac{(n\pi)^2 - a^2 k_x^2}{a^2}} = \frac{n\pi a}{2} \frac{\cos\left(\frac{k_x a}{2}\right)}{\left(\frac{n\pi}{2}\right)^2 - \left(\frac{k_x a}{2}\right)^2} \end{aligned} \quad (C 10)$$

Combining (C 9) and (C 10) we have

$$E_{y(n)}(k_x, k_y) = \left(\frac{n\pi ab}{2}\right) E_0^+ \frac{\cos\left(\frac{k_x a}{2}\right)}{\left(\frac{\pi}{2}\right)^2 - \left(\frac{k_x a}{2}\right)^2} \operatorname{sinc}\left(\frac{k_y b}{2}\right) \quad (C 11)$$

The transform of the magnetic field can be obtained with the use of two Maxwell's equations written in the spectral domain i.e. $\mathbf{k} \times \mathbf{E} = \omega\mu\mathbf{H}$ and $\mathbf{k} \cdot \mathbf{E} = 0$. We have

$$\mathbf{H}(k_x, k_y) = \frac{1}{k\eta} \mathbf{k} \times \mathbf{E}(k_x, k_y) \Rightarrow H(k_x, k_y) = \frac{1}{k\eta} (E_z k_y - E_y k_z), \quad (C 12)$$

together with

$$E_x k_x + E_y k_y + E_z k_z = 0 \Rightarrow E_z = -\frac{E_x k_x + E_y k_y}{k_z} = -\frac{k_y}{k_z} E_y, \quad (C 13)$$

Which are combined in the expression

$$H_{x(m)} = -\frac{1}{k\eta} \left(k_z + \frac{k_y^2}{k_z}\right) E_{y(m)} = -\frac{1}{k\eta} \frac{k^2 - k_x^2}{k_z} E_{y(m)}, \quad (C 14)$$

where $k_z = \sqrt{k^2 - k_x^2 - k_y^2}$. Combining expression (C 11) for the electric and (C 14) the magnetic field into the power integral (C 7) we arrive at

$$P_{mn}^{Ap} = \frac{mn(ab|E_0^+|^2)}{32 k \eta} \iint_{\mathbb{R}^2} \frac{k^2 - k_x^2}{k_z^*} \frac{\left(\cos\left(\frac{k_x a}{2}\right) \operatorname{sinc}\left(\frac{k_y b}{2}\right) \right)^2}{\left(\left(\frac{n\pi}{2}\right)^2 - \left(\frac{k_x a}{2}\right)^2 \right) \left(\left(\frac{m\pi}{2}\right)^2 - \left(\frac{k_y a}{2}\right)^2 \right)} dk_x dk_y. \quad (\text{C } 15)$$

The aperture admittance differs from the power only by a constant $4/(ab|E_0^+|^2)$ according to definition (C 4) and it is valid for calculating the admittance of a specific TE mode when $n = m$ and mutual admittance between two modes when $n \neq m$. The real part, conductance, is computed by integrating on the interior of the circle $k^2 = k_x^2 + k_y^2$ while the imaginary part, susceptance, by integrating the remaining space, from the circle up to infinity. The integral for the admittance can be made slightly simpler and more suitable for numerical computation by making a variable substitutions $k_x a/2 = X$ and $k_y b/2 = Y$. After the substitution we get

$$Y_{mn}^{Ap} = \frac{1}{ka} \frac{mn}{\eta} \iint_{\mathbb{R}^2} \frac{\left(\frac{ka}{2}\right)^2 - X^2}{\sqrt{\left(\frac{ka}{2}\right)^2 - \left(X^2 + \left(\frac{a}{b}Y\right)^2\right)}} \frac{(\cos(X) \operatorname{sinc}(Y))^2}{\left(\left(\frac{n\pi}{2}\right)^2 - X^2\right) \left(\left(\frac{m\pi}{2}\right)^2 - X^2\right)} dX dY. \quad (\text{C } 16)$$

Furthermore, it is convenient to look at the admittance depending on the size of the aperture compared to the wavelength or a/λ . We can easily replace ka in (C 16) with $2\pi(a/\lambda)$. The resulting integral is

$$Y_{mn}^{Ap} = \frac{mn}{2\pi\eta\left(\frac{a}{\lambda}\right)} \iint_{\mathbb{R}^2} \frac{\pi^2\left(\frac{a}{\lambda}\right)^2 - X^2}{\sqrt{\pi^2\left(\frac{a}{\lambda}\right)^2 - \left(X^2 + \left(\frac{a}{b}Y\right)^2\right)}} \frac{(\cos(X) \operatorname{sinc}(Y))^2}{\left(\left(\frac{n\pi}{2}\right)^2 - X^2\right) \left(\left(\frac{m\pi}{2}\right)^2 - X^2\right)} dX dY. \quad (\text{C } 17)$$

The integral in (C 17) has to be calculated numerically with computer software. As the TE₁₀ mode is of most interest we will plot the numerical result using the *NIntegrate* function in *Mathematica* [126] for the case $n = m = 1$. This resultant function of (a/λ) from 0 to 1 is shown in FIG where the dots represent numerically computed values.

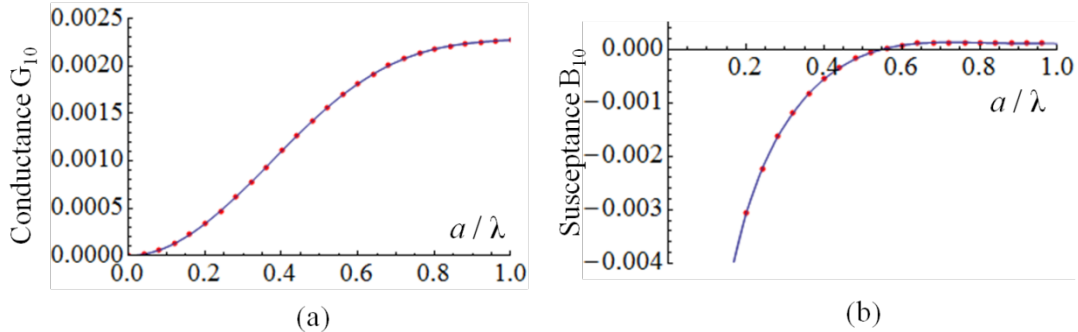


Figure 131 (a) real part of admittance and (b) imaginary part of admittance. Dots represent the numerically computed values and the line is a function approximating the data.

The values obtained numerically were used to create a formula in the form of a polynomial to fit the data. Fitting was also performed in *Mathematica* and the resulting polynomial

$$\begin{aligned} G_{11}^{Ap} &= 0.00897837x^2 - 0.0163648x^4 + 0.0275831x^6 - 0.0668926x^8 + 0.13512x^{10} \\ &\quad - 0.161626x^{12} + 0.101053x^{14} - 0.0255781x^{16} \\ B_{11}^{Ap} &= -\frac{0.00080857}{x} + 0.00537822x - 0.0138123x^3 + 0.0239716x^5 - 0.03366x^7 \\ &\quad + 0.0189707x^9 + 0.0474954x^{11} - 0.109933x^{13} + 0.0881392x^{15} - 0.0256397x^{17} \end{aligned} \quad (\text{C } 18)$$

Where $x = a/\lambda = ka/(2\pi)$. We note here that this polynomial is inspired by Cohens work where he reported the admittance in the same form as (C 18). However, Cohen's coefficients differ slightly from our result. In Cohen's Ph.D. Thesis we find

$$\begin{aligned}
 G_{11}^{Ap} &= 0.00901x^2 - 0.01522x^4 + 0.01436x^6 - 0.00848x^8 + 0.00342x^{10} \\
 &\quad - 0.00101x^{12} + 0.00023x^{14} - 0.00004x^{16} \\
 B_{11}^{Ap} &= -\frac{0.000809}{x} + 0.00537x - 0.01278x^3 + 0.01596x^5 - 0.01161x^7 + 0.00559x^9 \\
 &\quad - 0.00193x^{11} + 0.00049x^{13} - 0.0001x^{15} + 0.00002x^{17}
 \end{aligned} \tag{C 19}$$

The difference in the values of the coefficients in (C 18) and (C 19) can probably be attributed to the method of fitting the curve. Both polynomials will give practically the same admittance, differing only in the third significant number.

Since the low frequency limit $k \rightarrow 0$ is of special importance in this thesis, the first coefficient of the susceptance is the most important. Instead of going through the whole process of approximating the aperture admittance with a polynomial, this particular coefficient b_{mn}^0 for a given mode or for a mutual coupling of modes can be expressed directly. The integral (C 16) can be expanded into a Taylor series around $k = 0$ which will leave for the first term

$$Y_{mn}^{Ap, k \rightarrow 0} = -\frac{1}{ka} \frac{mn}{\eta} \iint_{\mathbb{R}^2} \frac{X^2}{\sqrt{X^2 + \left(\frac{a}{b}Y\right)^2}} \frac{(\cos(X) \operatorname{sinc}(Y))^2}{\left(\left(\frac{n\pi}{2}\right)^2 - (X)^2\right) \left(\left(\frac{m\pi}{2}\right)^2 - (X)^2\right)} dX dY, \tag{C 20}$$

from which we have

$$b_{mn}^0 = -\frac{mn}{2\pi\eta} \iint_{\mathbb{R}^2} \frac{X^2}{\sqrt{X^2 + \left(\frac{a}{b}Y\right)^2}} \frac{(\cos(X) \operatorname{sinc}(Y))^2}{\left(\left(\frac{n\pi}{2}\right)^2 - (X)^2\right) \left(\left(\frac{m\pi}{2}\right)^2 - (X)^2\right)} dX dY. \tag{C 21}$$

Directivity calculation for square ($a = b$) aperture excited by the TE_{10} mode.

Directivity of the aperture antenna is given by

$$D_{max} = 4\pi \frac{U_{max}}{P_{rad}} \tag{C 22}$$

Where P_{rad} is given by the real part of equation (C 15), but since the admittance was explicitly calculated, we can express it using the conductance G as

$$P_{rad} = \frac{a^2 |E_0^+|^2}{4} G_{11}^{Ap}, \tag{C 23}$$

and U_{max} is the farfield power transmitted orthogonal to the aperture. The expression to obtain U_{max} can be found in [38] as:

$$U_{max} = \frac{k^2}{8\pi^2 \eta_0} |\mathbf{E}|_{max}^2 \tag{C 24}$$

Where the electric far field is already given in (C 11), and η_0 is the free space impedance. What remains to be calculated is its maximum value. Since we expect the maximum to occur in the orthogonal \hat{z} direction to the aperture, we can assume $k_x, k_y \rightarrow 0$ in (C 11). This limit gives $E_{max} = E_0^+ 2 a^2 / \pi$. Inserting (C 24) and (C 23) into (C 22) gives

$$D_{max} = \frac{8(ka)^2}{\pi^3 \eta_0 G_{11}^{Ap}}. \tag{C 25}$$

Since the conductance is expressible in a series expansion $G_{11}^{Ap} = g_{11}^0 x^2 + g_{11}^1 x^4 + g_{11}^2 x^6 + \dots$ where $x = ka/(2\pi)$, we can also series expand (C 25) and obtain an approximation for small aperture sizes

$$D_{max} = \frac{32}{\eta_0 g_{11}^0 \pi} - \frac{8g_{11}^1 (ka)^2}{\eta_0 g_{11}^0{}^2 \pi^3} + \mathcal{O}(ka)^4, \tag{C 26}$$

Upon inserting the numerical values of the coefficients the directivity is $D \approx 3 + 0.1283(ka)^2 + \mathcal{O}(ka)^4$. The directivity depending on cavities size is depicted in Figure 132.

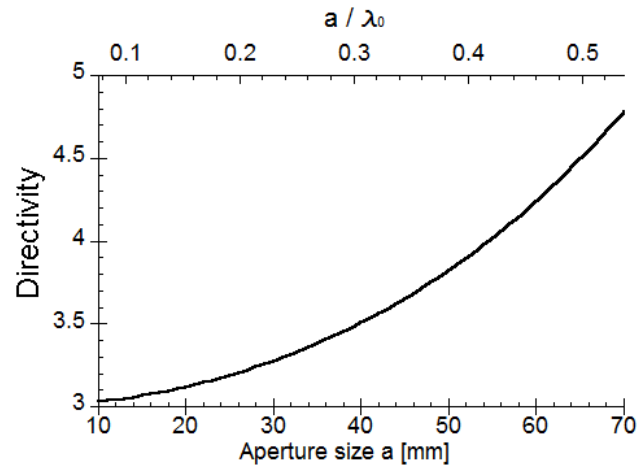


Figure 132 Calculated directivity depending on aperture size.

APPENDIX D. CALCULATION OF THE APERTURE ADMITTANCE FOR A CIRCULAR APERTURE.

In this section, using Fourier transform (spectral) techniques, the admittance of a circular aperture mounted on an infinite ground plane and radiating into free space will be formulated. The geometrical arrangement of the antenna under consideration a rectangular cavity drilled into a ground plane and filled with some dielectric material of relative permittivity ϵ_r , as shown in Figure 133.

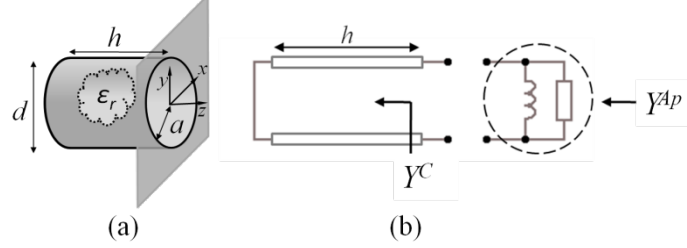


Figure 133 (a) A rectangular cavity in an infinite ground plane and (b) the corresponding transmission line model for an electrically small cavity

Aperture field

We will assume that the electric field distribution on the aperture is that given by the TE_{11} waveguide mode

$$\mathbf{E}(\rho, \phi) = \hat{\rho} E_0^+ \frac{J_1(k_c \rho)}{\rho} \sin(\phi) + \hat{\phi} E_0^+ k_c J_1'(k_c \rho) \cos(\phi), \quad 0 \leq \rho \leq a, 0 \leq \phi \leq 2\pi, \quad (D 10)$$

Higher modes are easily expressible, but the following derivations become extremely difficult. It was shown in the case of the rectangular aperture that the first mode is a good enough approximations. We will thus show here only the derivations involving the fundamental mode in the circular case.

Power inside the cavity

The time averaged power transmitted in the TE_{n0} mode can be easily calculated from the Poynting vector

$$P_n^C = \frac{1}{2} \int_0^a \int_0^{2\pi} \mathbf{E} \times \mathbf{H}^* \cdot \hat{z} \rho d\rho d\phi = \frac{1}{2} \int_0^a \int_0^{2\pi} E_\rho H_\phi^* - E_\phi H_\rho^* \rho d\rho d\phi. \quad (D 11)$$

Using the relations between the magnetic and electric field for TE modes in a circular waveguide, $H_\phi = Y_{TE} E_\rho$ and $H_\rho = -Y_{TE} E_\phi$ we have

$$\begin{aligned} P_n^C &= \frac{1}{2} Y_{TE}^* \int_0^a \int_0^{2\pi} |E_\rho|^2 + |E_\phi|^2 \rho d\rho d\phi \\ &= \frac{1}{2} Y_{TE}^* |E_0^+|^2 \int_0^a \int_0^{2\pi} k_c^2 \left(\frac{J_1(k_c \rho)}{k_c \rho} \right)^2 \sin^2(\phi) + k_c^2 \left(\frac{dJ_1(k_c \rho)}{dk_c \rho} \right)^2 \cos^2(\phi) \rho d\rho d\phi \\ &= \frac{1}{2} Y_{TE}^* |E_0^+|^2 k_c^2 \pi \int_0^a \left(\frac{J_1(k_c \rho)}{k_c \rho} \right)^2 + \left(\frac{dJ_1(k_c \rho)}{dk_c \rho} \right)^2 \rho d\rho \end{aligned} \quad (D 12)$$

At this point we need a known result about Bessel type integrals, taken from (pozar str717) which states

$$\int_0^{p'_{nm}} n^2 \frac{J_n^2(x)}{x^2} + \left(\frac{dJ_n(x)}{dx} \right)^2 x dx = \frac{(p'_{nm})^2}{2} \left(1 - \frac{n^2}{(p'_{nm})^2} \right) J_n^2(p'_{nm}). \quad (D 13)$$

After introducing a variable change $k_c \rho = x$ in (D 12) and using (D 13) we arrive at

$$P_n^C = \frac{\pi}{4} Y_{TE}^* |E_0^+|^2 ((p'_{nm})^2 - 1) J_n^2(p'_{nm}), \quad (D 14)$$

and

$$Y_n^C = \frac{4P_n^{C*}}{\pi |E_0^+|^2 ((p'_{nm})^2 - 1) J_n^2(p'_{nm})}. \quad (D 15)$$

Aperture admittance

We now proceed to finding the Fourier transform of the aperture fields and the aperture admittance. The procedure is significantly more complicated compared to the rectangular case.

$$\begin{aligned}
 \mathbf{E}(k_\rho, \alpha) &= \int_0^a \int_0^{2\pi} E(\rho, \phi) e^{jk_\rho \cos(\phi-\alpha)} \rho d\rho d\phi \\
 &= \int_0^a \frac{J_1(k_c \rho)}{\rho} \rho d\rho \int_0^{2\pi} e^{jk_\rho \cos(\phi-\alpha)} \sin(\phi) d\phi \hat{\boldsymbol{\rho}} \\
 &\quad + \int_0^a k_c J_1'(k_c \rho) \rho d\rho \int_0^{2\pi} e^{jk_\rho \cos(\phi-\alpha)} \cos(\phi) d\phi \hat{\boldsymbol{\phi}}
 \end{aligned} \tag{D 16}$$

The unit vectors $(\hat{\boldsymbol{\rho}}, \hat{\boldsymbol{\phi}})$ also need to be transformed into a new coordinate system where we have $(\hat{\mathbf{k}}_\rho, \hat{\boldsymbol{\alpha}})$.

$$\begin{bmatrix} \hat{\boldsymbol{\rho}} \\ \hat{\boldsymbol{\phi}} \end{bmatrix} = \begin{bmatrix} \cos(\phi - \alpha) & \sin(\phi - \alpha) \\ -\sin(\phi - \alpha) & \cos(\phi - \alpha) \end{bmatrix} \begin{bmatrix} \hat{\mathbf{k}}_\rho \\ \hat{\boldsymbol{\alpha}} \end{bmatrix}, \tag{D 17}$$

We can write intermediate results

$$\int_0^{2\pi} e^{jk_\rho \cos(\phi-\alpha)} \sin(\phi) d\phi \hat{\boldsymbol{\rho}} = \int_0^{2\pi} e^{jk_\rho \cos(\phi-\alpha)} \sin(\phi) (\cos(\phi - \alpha) \hat{\mathbf{k}}_\rho + \sin(\phi - \alpha) \hat{\boldsymbol{\alpha}}) d\phi \tag{D 18}$$

And using a substitution $\phi - \alpha = u$ we can expand (D 18) in the form

$$\begin{aligned}
 &\left\{ \sin(\alpha) \int_{-\alpha}^{2\pi-\alpha} e^{jk_\rho \cos(u)} \cos^2(u) du + \cos(\alpha) \int_{-\alpha}^{2\pi-\alpha} e^{jk_\rho \cos(u)} \sin(u) \cos(u) du \right\} \hat{\mathbf{k}}_\rho + \\
 &+ \left\{ \sin(\alpha) \int_{-\alpha}^{2\pi-\alpha} e^{jk_\rho \cos(u)} \sin(u) \cos(u) du + \cos(\alpha) \int_{-\alpha}^{2\pi-\alpha} e^{jk_\rho \cos(u)} \sin^2(u) du \right\} \hat{\boldsymbol{\alpha}}
 \end{aligned} \tag{D 19}$$

Which can be directly evaluated using known expressions for Bessel functions. The second term of the first bracket and the first term of the second bracket evaluate to zero, and the final result in terms of Bessel functions is

$$2\pi J_1'(k_\rho \rho) \sin(\alpha) \hat{\mathbf{k}}_\rho + 2\pi \frac{J_1(k_\rho \rho)}{k_\rho \rho} \cos(\alpha) \hat{\boldsymbol{\alpha}}. \tag{D 20}$$

Similarly we have

$$\int_0^{2\pi} e^{jk_\rho \cos(\phi-\alpha)} \cos(\phi) d\phi \hat{\boldsymbol{\phi}} = 2\pi J_1'(k_\rho \rho) \cos(\alpha) \hat{\boldsymbol{\alpha}} + 2\pi \frac{J_1(k_\rho \rho)}{k_\rho \rho} \sin(\alpha) \hat{\mathbf{k}}_\rho. \tag{D 21}$$

Inserting (D 18) through (D 21) back into (D 16) we arrive at

$$\begin{aligned}
 \mathbf{E}(k_\rho, \alpha) &= 2\pi \int_0^a \left\{ \left[k_c \frac{J_1(k_c \rho)}{k_c \rho} J_1'(k_\rho \rho) \sin(\alpha) + k_c J_1'(k_c \rho) \frac{J_1(k_\rho \rho)}{k_\rho \rho} \sin(\alpha) \right] \hat{\mathbf{k}}_\rho \right. \\
 &\quad \left. + \left[k_c \frac{J_1(k_c \rho)}{k_c \rho} \frac{J_1(k_\rho \rho)}{k_\rho \rho} \cos(\alpha) + k_c J_1'(k_c \rho) J_1'(k_\rho \rho) \cos(\alpha) \right] \hat{\boldsymbol{\alpha}} \right\} \rho d\rho
 \end{aligned} \tag{D 22}$$

To resolve the integration over the radius ρ we will need to transform the integrating function using several identities for Bessel functions, namely

$$\begin{aligned}
 \frac{n J_n(x)}{x} &= \frac{1}{2} [J_{n-1}(x) + J_{n+1}(x)], \\
 \frac{dJ_n(x)}{dx} &= \frac{1}{2} [J_{n-1}(x) - J_{n+1}(x)], \\
 \frac{dJ_1(x)}{dx} + \frac{J_1(x)}{x} &= J_0(x), \\
 \frac{dJ_1(x)}{dx} - \frac{J_1(x)}{x} &= J_2(x)
 \end{aligned} \tag{D 23}$$

The integral (D 22) can thus be expanded into

$$\begin{aligned}
 \mathbf{E}(k_\rho, \alpha) = 2\pi k_c \int_0^a \rho d\rho \left\{ \left[\frac{1}{2} [J_0(k_c \rho) + J_2(k_c \rho)] J_1'(k_\rho \rho) + \right. \right. \\
 \left. \left. + \frac{1}{2} [J_0(k_c \rho) - J_2(k_c \rho)] \frac{J_1(k_\rho \rho)}{k_\rho \rho} \right] \sin(\alpha) \hat{\mathbf{k}}_\rho \right. \\
 \left. + \left[\frac{1}{2} [J_0(k_c \rho) + J_2(k_c \rho)] \frac{J_1(k_\rho \rho)}{k_\rho \rho} \right. \right. \\
 \left. \left. + \frac{1}{2} [J_0(k_c \rho) - J_2(k_c \rho)] J_1'(k_\rho \rho) \right] \cos(\alpha) \hat{\boldsymbol{\alpha}} \right\}
 \end{aligned} \tag{D 24}$$

That, after a short manipulation, gets reduced to

$$\begin{aligned}
 \mathbf{E}(k_\rho, \alpha) = \pi k_c \int_0^a \rho d\rho \left\{ \left[\underbrace{J_0(k_c \rho) J_0(k_\rho \rho)}_{A_1} - \underbrace{J_2(k_c \rho) J_2(k_\rho \rho)}_{A_2} \right] \sin(\alpha) \hat{\mathbf{k}}_\rho \right. \\
 \left. + \left[\underbrace{J_0(k_c \rho) J_0(k_\rho \rho)}_{A_1} + \underbrace{J_2(k_c \rho) J_2(k_\rho \rho)}_{A_2} \right] \cos(\alpha) \hat{\boldsymbol{\alpha}} \right\}
 \end{aligned} \tag{D 25}$$

To integrate the subparts A_1 and A_2 we use Lommel's integral formulas

$$\int J_n(ax) J_n(bx) x dx = \frac{x}{a^2 - b^2} [b J_{n-1}(bx) J_n(ax) - a J_{n-1}(ax) J_n(bx)], \tag{D 26}$$

Calculating each part of (D 25) separately we have

$$\begin{aligned}
 A_1 &= \int_0^a J_0(k_c \rho) J_0(k_\rho \rho) \rho d\rho = \frac{a}{k_c^2 - k_\rho^2} [k_\rho J_{-1}(k_\rho a) J_0(k_c a) - k_c J_{-1}(k_c a) J_0(k_\rho a)] = \\
 &= \frac{a}{k_c^2 - k_\rho^2} [-k_\rho J_1(k_\rho a) J_0(k_c a) + k_c J_1(k_c a) J_0(k_\rho a)] \\
 A_2 &= \int_0^a J_2(k_c \rho) J_2(k_\rho \rho) \rho d\rho = \frac{a}{k_c^2 - k_\rho^2} [k_\rho J_1(k_\rho a) J_2(k_c a) - k_c J_1(k_c a) J_2(k_\rho a)]
 \end{aligned} \tag{D 27}$$

Where we have used the fact that $J_{-n}(x) = -J_n(x)$. From (D 27) we have

$$\begin{aligned}
 A_1 - A_2 &= \frac{a}{k_c^2 - k_\rho^2} \left[k_c J_1(k_c a) \left[\underbrace{J_0(k_\rho a) + J_2(k_\rho a)}_{\frac{2J_1(k_\rho a)}{k_\rho a}} \right] - k_\rho J_1(k_\rho a) \left[\underbrace{J_0(k_c a) + J_2(k_c a)}_{\frac{2J_1(k_c a)}{k_c a}} \right] \right] =, \\
 &= \frac{2}{k_c^2 - k_\rho^2} \left[\left(\frac{k_c}{k_\rho} - \frac{k_\rho}{k_c} \right) J_1(k_c a) J_1(k_\rho a) \right] = \frac{2}{k_c k_\rho} J_1(k_c a) J_1(k_\rho a)
 \end{aligned} \tag{D 28}$$

and

$$\begin{aligned}
 A_1 + A_2 &= \frac{a}{k_c^2 - k_\rho^2} \left[k_c J_1(k_c a) \left[\underbrace{J_0(k_\rho a) - J_2(k_\rho a)}_{2J_1'(k_\rho a)} \right] - k_\rho J_1(k_\rho a) \left[\underbrace{J_0(k_c a) - J_2(k_c a)}_{2J_1'(k_c a)} \right] \right] = \\
 &= \frac{2a}{k_c^2 - k_\rho^2} [k_c J_1(k_c a) J_1'(k_\rho a)] = \frac{2ak_c}{k_c^2 - k_\rho^2} J_1(k_c a) J_1'(k_\rho a)
 \end{aligned} \tag{D 29}$$

Where we have used again the relations for Bessel functions (D 23). Inserting (D 28) into (D 25) gives finally the Fourier transform of the electric field at the aperture as

$$\mathbf{E}(k_\rho, \alpha) = 2\pi E_0^+ \left[\frac{1}{k_\rho} J_1(k_c a) J_1(k_\rho a) \sin(\alpha) \hat{\mathbf{k}}_\rho + \frac{ak_c^2}{k_c^2 - k_\rho^2} J_1(k_c a) J_1'(k_\rho a) \cos(\alpha) \hat{\boldsymbol{\alpha}} \right], \tag{D 30}$$

The transform of the magnetic field can be obtained with the use of two Maxwell's equations written in the spectral domain i.e. $\mathbf{k} \times \mathbf{E} = \omega\mu\mathbf{H}$ and $\mathbf{k} \cdot \mathbf{E} = 0$. We have $k^2 = k_x^2 + k_y^2 + k_z^2 = k_\rho^2 + k_z^2$ and thus $k_z = \sqrt{k^2 - k_\rho^2}$, so we write

$$\mathbf{k} \cdot \mathbf{E} = (k_\rho \hat{\mathbf{k}}_\rho + k_z \hat{\mathbf{z}}) (E_{k_\rho} \hat{\mathbf{k}}_\rho + E_\alpha \hat{\boldsymbol{\alpha}} + E_z \hat{\mathbf{z}}) = k_\rho E_{k_\rho} + k_z E_z = 0 \Rightarrow E_z = \frac{-k_\rho E_{k_\rho}}{k_z} \quad (\text{D 31})$$

The magnetic field as a rotor of the electric field can then be expressed as

$$\begin{aligned} \mathbf{H} &= \frac{1}{k\eta_0} \mathbf{k} \times \mathbf{E} = \frac{1}{k\eta_0} (k_\rho \hat{\mathbf{k}}_\rho + k_z \hat{\mathbf{z}}) \times (E_{k_\rho} \hat{\mathbf{k}}_\rho + E_\alpha \hat{\boldsymbol{\alpha}} + E_z \hat{\mathbf{z}}) = \\ &= \frac{1}{k\eta_0} [-\hat{\mathbf{k}}_\rho k_z E_\alpha + \hat{\boldsymbol{\alpha}} (k_z E_{k_\rho} - k_\rho E_z) + \hat{\mathbf{z}} k_\rho E_\alpha] \end{aligned} \quad (\text{D 32})$$

Thus the component of the magnetic field are

$$\begin{aligned} H_{k_\rho} &= -\frac{k_z}{k\eta_0} E_\alpha, \\ H_\alpha &= \frac{1}{k\eta_0} (k_z E_{k_\rho} - k_\rho E_z) = \frac{1}{k\eta_0} \left(k_z E_{k_\rho} - \frac{k_\rho^2}{k_z} E_{k_\rho} \right) = \frac{k_\rho^2 + k_z^2}{k\eta_0 k_z} E_{k_\rho} = \frac{k}{k_z \eta_0} E_{k_\rho} \end{aligned} \quad (\text{D 33})$$

We can now write the power integral in spectral domain

$$\begin{aligned} P_{11}^{Ap} &= \frac{1}{2} \int_0^a \int_0^{2\pi} [E_\rho H_\phi^* - E_\phi H_\rho^*] \rho d\rho d\phi = \frac{1}{8\pi^2} \int_0^\infty \int_0^{2\pi} [E_{k_\rho} H_\alpha^* - E_\alpha H_{k_\rho}^*] k_\rho dk_\rho d\alpha = \\ &= \frac{1}{8\pi^2} \int_0^\infty \int_0^{2\pi} \left[\frac{k}{k_z \eta_0} |E_{k_\rho}|^2 + \frac{k_z^*}{k\eta_0} |E_\alpha|^2 \right] k_\rho dk_\rho d\alpha \end{aligned} \quad (\text{D 34})$$

We can use the field components from (D 30)

$$\begin{aligned} P_{11}^{Ap} &= \frac{|E_0^+|^2}{2\eta_0} J_1^2(k_c a) \int_0^\infty \int_0^{2\pi} \left[\frac{k}{k_z^* k_\rho^2} J_1^2(k_\rho a) \sin^2(\alpha) \right. \\ &\quad \left. + \frac{k_z^*}{k} \frac{a^2 k_c^4}{(k_c^2 - k_\rho^2)^2} J_1'^2(k_\rho a) \cos^2(\alpha) \right] k_\rho dk_\rho d\alpha \end{aligned} \quad (\text{D 35})$$

and integrate α from 0 to 2π immediately, we get

$$P_{11}^{Ap} = \frac{J_1^2(k_c a) |E_0^+|^2 \pi}{2\eta_0} \int_0^\infty \left[\frac{k}{k_\rho^2 k_z^*} J_1^2(k_\rho a) + \frac{a^2 k_c^4 k_z^*}{k(k_c^2 - k_\rho^2)^2} J_1'^2(k_\rho a) \right] k_\rho dk_\rho \quad (\text{D 36})$$

From the power expression (D 37) and the definition of circular waveguide admittance (D 15) we can write the aperture admittance

$$Y_{11}^{Ap} = \frac{2}{((p'_{nm})^2 - 1)\eta_0} \int_0^\infty \left[\frac{k}{k_\rho^2 \sqrt{k^2 - k_\rho^2}} J_1^2(k_\rho a) + \frac{a^2 k_c^4 \sqrt{k^2 - k_\rho^2}}{k(k_c^2 - k_\rho^2)^2} J_1'^2(k_\rho a) \right] k_\rho dk_\rho \quad (\text{D 37})$$

Making the change in variables $k_\rho a = X$, $dk_\rho a = dX$ we transform the integral into a slightly more suitable form for numerical computation we have

$$\begin{aligned} Y_{11}^{Ap} &= \frac{2}{((p'_{nm})^2 - 1)\eta_0} \int_0^\infty \left[\frac{ka J_1^2(X)}{X^2 \sqrt{(ka)^2 - X^2}} + \right. \\ &\quad \left. + \frac{(p'_{nm})^4 \sqrt{(ka)^2 - X^2}}{ka((p'_{nm})^2 - X^2)^2} J_1'^2(X) \right] X dX \end{aligned} \quad (\text{D 38})$$

Just as in the rectangular case, it is convenient to work and think with the variable $(a/\lambda) = x$, where a is the radius of the cavity. The final form of the integral, that is numerically computed is

$$Y_{11}^{Ap} = \frac{2}{((p'_{nm})^2 - 1)\eta_0} \int_0^\infty \left[\frac{2\pi x J_1^2(X)}{X^2 \sqrt{(2\pi x)^2 - X^2}} + \frac{(p'_{nm})^4 \sqrt{(2\pi x)^2 - X^2}}{2\pi x ((p'_{nm})^2 - X^2)^2} J_1'^2(X) \right] X dX \quad (D 39)$$

Figure 134 shows the result using the *NIntegrate* function in *Mathematica* [126]. Based on the numerically obtained data, curve fitting was performed to obtain the following polynomial approximation for the circular aperture admittance

$$\begin{aligned} G_{11}^{Ap} &= 0.0292335x^2 - 0.162724x^4 + 0.503821x^6 - 0.967159x^8 + 1.24487x^{10} \\ &\quad - 1.11359x^{12} + 0.662147x^{14} - 0.202231x^{16} \\ B_{11}^{Ap} &= -\frac{0.000504914}{x} + 0.00961453x - 0.0747716x^3 + 0.30591x^5 - 0.737733x^7 \\ &\quad + 1.15816x^9 + 1.27923x^{11} - 1.05773x^{13} + 0.659176x^{15} - 0.243662x^{17} \end{aligned} \quad (D 40)$$

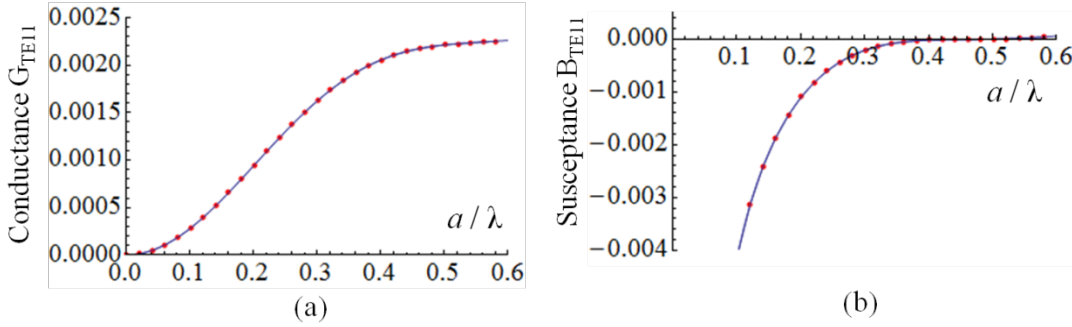


Figure 134 (a) real part of admittance and (b) imaginary part of admittance. Dots represent the numerically computed values and the line is a function approximating the data

Since the low frequency limit $k \rightarrow 0$ is of special importance in this thesis, the first coefficient of the susceptance is the most important. Instead of going through the whole process of approximating the aperture admittance with a polynomial, this particular coefficient $b_{0(mn)}$ for a given mode or for a mutual coupling of modes can be expressed directly. In making the low frequency limit $k \rightarrow 0$, we see that the first term in (D 38) disappears, and only the second term is important. We can thus write

$$Y_{11}^{Ap, k \rightarrow 0} \sim j \frac{2\pi}{ka} \frac{1}{\pi((p'_{nm})^2 - 1)\eta_0} \int_0^\infty \frac{(p'_{nm})^4 X^2 J_1'^2(X)}{((p'_{nm})^2 - X^2)^2} dX + O(k) \quad (D 41)$$

From which we can get the first coefficient as

$$b_{11}^0 = \frac{1}{\pi((p'_{nm})^2 - 1)\eta_0} \int_0^\infty \frac{(p'_{nm})^4 X^2 J_1'^2(X)}{((p'_{nm})^2 - X^2)^2} dX \quad (D 42)$$

That gives values for the amplitudes in the polarizability formula.

Directivity calculation for a circular aperture excited with a TE₁₁ mode

Directivity of the aperture antenna is given by

$$D_{max} = 4\pi \frac{U_{max}}{P_{rad}} \quad (D 43)$$

Where P_{rad} is given by the real part of equation (D 28), but it can be expressed using (D 6) as

$$P_{rad} = \frac{\pi}{4} |E_0^+|^2 ((p'_{11})^2 - 1) J_n^2(p'_{11}) G_{11}^{Ap}, \quad (D 44)$$

and U_{max} is the farfield power transmitted orthogonal to the aperture. The expression to obtain U_{max} can be found in [38] as:

$$U_{max} = \frac{k^2}{8\pi^2 \eta_0} |\mathbf{E}|_{max}^2, \quad (D 45)$$

where the electric far field is already given in (D 22), and η_0 is the free space impedance. What remains to be calculated is its maximum value. Since we expect the maximum to occur in the orthogonal \hat{z} direction to the aperture, we can assume $k_\rho \rightarrow 0$ in (A5).

$$\mathbf{E}(k_\rho, \alpha) \xrightarrow{k_\rho \rightarrow 0} E_0^+ \left[\underbrace{\frac{2\pi}{k_\rho} J_1(k_c a) J_1(k_\rho a) \sin(\alpha)}_{\pi a J_1(k_c a) \sin(\alpha)} \hat{\mathbf{k}}_\rho + \underbrace{\frac{2\pi a k_c^2}{k_c^2 - k_\rho^2} J_1(k_c a) J_1'(k_\rho a) \cos(\alpha)}_{\pi a J_1(k_c a) \cos(\alpha)} \hat{\boldsymbol{\alpha}} \right], \quad (\text{D } 46)$$

Which is easily reduced to

$$\mathbf{E}(k_\rho, \alpha) \xrightarrow{k_\rho \rightarrow 0} \mathbf{E}_{max} = E_0^+ \pi a J_1(k_c a) [\sin(\alpha) \hat{\mathbf{k}}_\rho + \cos(\alpha) \hat{\boldsymbol{\alpha}}] = E_0^+ \pi a J_1(k_c a) \hat{\mathbf{y}}. \quad (\text{D } 47)$$

Remembering that $k_c = p'_{11}/a$ we write in scalar form $E_{max} = E_0^+ \pi a J_1(p'_{11})$. Putting (D 39) and (D 36) into (D 35) gives

$$D_{max} = \frac{2(ka)^2}{\eta_0 G_{11}^{Ap} ((p'_{11})^2 - 1)}. \quad (\text{D } 48)$$

Since the conductance is expressible in a series expansion $G_{11}^{Ap} = g_{11}^0 x^2 + g_{11}^1 x^4 + g_{11}^2 x^6 + \dots$ where $x = ka/(2\pi)$, we can also series expand (D 39) and obtain an approximation for small aperture size

$$D_{max} = \frac{8\pi^2}{\eta_0 g_{11}^0 ((p'_{11})^2 - 1)} - \frac{2g_{11}^1 (ka)^2}{\eta_0 g_{11}^0 ((p'_{11})^2 - 1)} + \mathcal{O}(ka)^4, \quad (\text{D } 49)$$

Inserting the numerical values of the coefficients the directivity is $D \approx 3 + 0.42265(ka)^2 + \mathcal{O}(ka)^4$. The directivity for cavities sizes presented in this paper is presented in Figure 135.

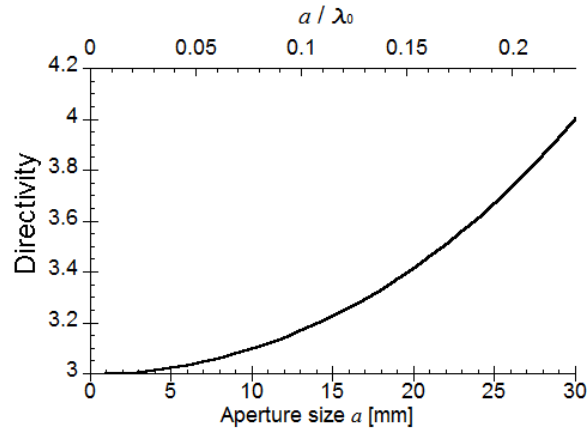


Figure 135 Calculated directivity vs. aperture size.

APPENDIX E. A MORE INTUITIVE INTRODUCTION TO COUNTERINTUITIVE META-MATERIALS

We all heard the world around us is made out of atoms. We see this world by detecting electromagnetic waves on the retina of our eyes. But we don't see the atoms, only materials or textures, which are large groups of atoms, because atoms themselves are much smaller than the visible wavelength of light. We would expect that atoms somehow respond to the electromagnetic waves and are responsible for phenomena like reflection from a mirror or refraction of light in water. These phenomena are in fact an averaged effect of many atoms which are all much smaller than the wavelength of light waves, but as a group affect the propagation of the wave. Today, we are very interested in designing our own types of "atoms", to form materials with reflection or refraction properties that we want, but can't find in nature. These artificially created structures are now called meta-materials and can have some novel and "counterintuitive" properties.

Let us use an analogy to explain the basic principle behind a single meta-material "atom". Imagine you hold a spring with a weight at the bottom like shown in Figure 136. Your hand vibrating is analogous to an incoming wave that forces the weight to move, the movement of the weight on the bottom of the spring is analogous to the "atom's" response to the wave. This system is called a mechanical oscillator, and it can exhibit the phenomenon of **resonance**. When you tune your hands vibration frequency to the resonant frequency, you will notice that a small range of motion of your hand causes the mass to vibrate in a very large range or **amplitude**. Here, one detail is very important, below resonance, when you are vibrating your hand slowly; the weight follows the motion of your hand, showing that the mass and the driving force stay exactly in **phase**. Above resonance, you vigorously vibrate your hand and the weight moves opposite to the motion of your hand, showing that the mass and the driving force stay 180° out of phase. To see this visually, follow the link [127]. That special case of vibration that has a **larger amplitude** than the driving force **AND** it is in **opposite phase** with it, is the key to a meta-material "atom" operation. It is counterintuitive in a sense that when you are pushing the weight down it can be coming back up at you with larger amplitude; you feel it "defying" your force with a vengeance. In a similar sense, one can imagine a material (or a spring as we will see below) that compresses when pulled and stretches when pushed. With electricity this corresponds to electrons (current) "defying" the electric field (voltage), appearing to be repelled by opposite charge instead of attracted (same for magnets). Consequently, effective properties of a material composed of such "atoms" can also be "counterintuitive".

One more important detail, there is a frequency above resonance where the amplitude of the weight will no longer be larger than the amplitude of your forcing hand (see Figure 136(b)) so the "meta-material effect" is **lost**. This depends on the **quality factor** Q of the resonator (low Q = broader frequency range). In practice, the range of frequencies with the desired effect is usually very narrow.

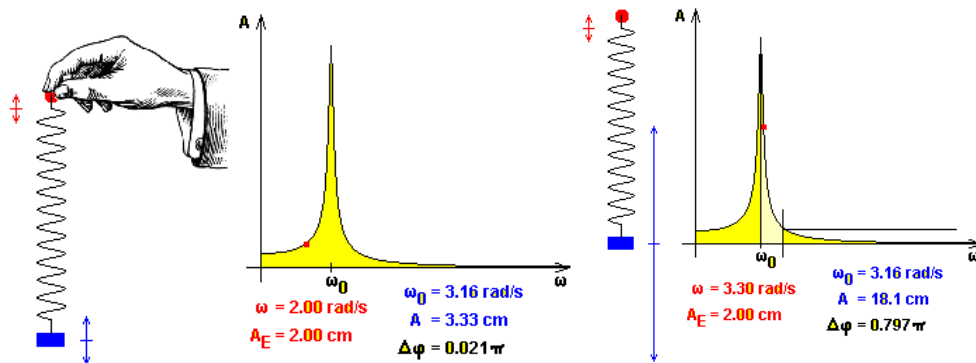


Figure 136 : Mechanical oscillator analogy. (a) oscillating below resonance (b) oscillating near resonance. Only a small brighter region above resonance is interesting for new effects of metamaterials [127].

Next, consider a line of springs and masses made of hollow spheres, a mechanical lattice, shown in Figure 137(a). The hollow spheres can be considered as "atoms" in this case. If we attach a local resonator, a spring and a weight similar to the hand-weight example in Figure 136, this will affect the behavior of the spheres. When we vibrate one end of the line we would expect a wave to travel down the line. In a normal material each "atom" follows the atom before it with a tiny delay and thus a wave travels, but in system like in Figure 137(a) each "atom" has a resonator that can (slightly above its resonance frequency) forcibly oppose the motion of each of its neighbors. Propagation of a wave is not possible in such a case, and the wave "dies out". We describe such a line as having negative effective mass. Very loosely speaking, just above resonance the "atoms" feel like almost "immovable" objects to the mechanical wave.

Now let's look at the spring itself. The stiffness of the spring can be made effectively negative, or "counterintuitive" with a system presented in Figure 137(b). The physical mechanism of negative effective stiffness is that the oscillation of the masses in the vertical direction induces an inertial force in the horizontal

direction, and the vertical resonance effect on the spheres can lead to an expansion of the structure, while loaded under a compressive force. If a line is composed of normal spheres (nothing inside) but with these additional resonators that make the stiffness negative for some frequencies, then again, a wave will not travel down the line at these frequencies. The springs will forcibly oppose the motion of each sphere in this case. Very loosely speaking, just above resonance the “atoms” feel strong, almost “unstoppable” forces between them and motion in every direction is opposed.

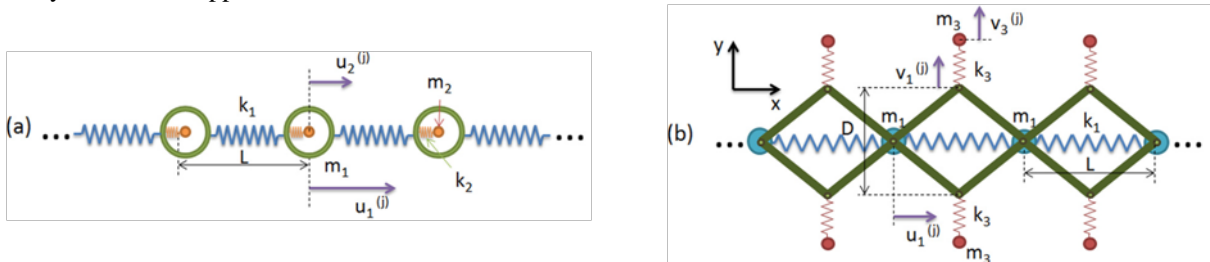


Figure 137 (a) a one dimensional spring—mass line, hollow spheres with local resonators attached to each sphere. (b) a one dimensional spring—mass line with local resonators in attached to each spring [128].

So what happens if at some frequency we combine almost immovable objects with almost unstoppable forces, like in Figure 138? Surprisingly – propagation! One could say that the two negatives cancel each other out, however the propagation one observes is not the usual one. Energy travels down the line just like in a regular spring-mass line with no attached resonators, but if one looks at the waves themselves, they seem to be traveling in towards the source of the oscillation, opposite to what we are expected to see. This phenomena is then called “left-handed propagation” and it is possible only in such double negative systems. However, further explanations of the phenomena that follow from such systems would be out o the scope of this short non-technical introduction.

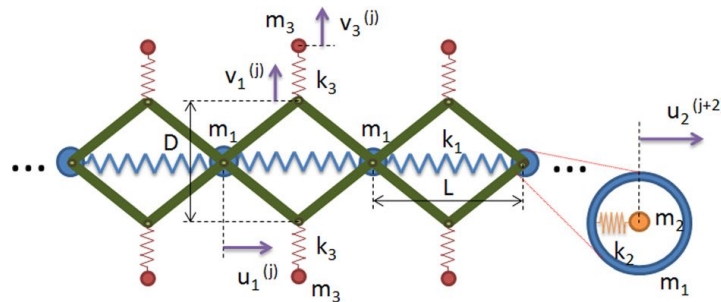


Figure 138 a one dimensional spring—mass line that can ant some frequency have both negative effective mass and negative effective stiffness between the masses [128]

Electromagnetic metamaterials

In electromagnetism, at microwavew frequencies (300 MHz - 300 GHz) metamaterials are designed with metallic structures to manipulate the electric response (**permittivity ϵ**) with wire structures and the magnetic response (**permeability μ**) with ring structures (see Figure 139). Combined, they can have a negative effective index of refraction, negative phase velocity. Just like with the mechanical resonator these structures can be explained as **resonators** composed of inductances (L) and capacitances (C) and behave similar to the mechanical oscillator while the Q factor is determined by the values of L and C .

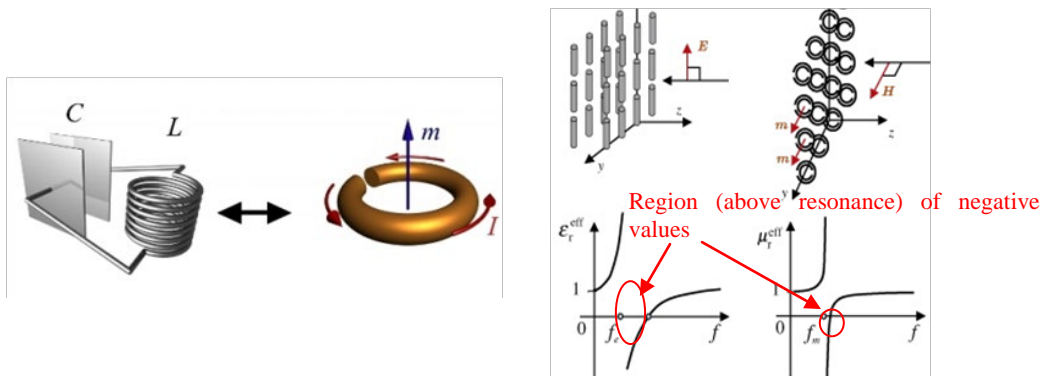


Figure 139 : Cut-wire medium with the frequency dependent effective permittivity and a one layer of Split Ring Resonators with the effective permeability [129].

APPENDIX F. PUBLICATIONS RELATED TO THE THESIS

M. Martinis, K. Mahdjoubi, R. Sauleau, S. Collardey, L. Bernard, "Bandwidth behavior and improvement of miniature cavity Antennas" **accepted with minor revisions** on September 9, 2014 to IEEE Transactions on Antennas and Propag.

M. Martinis, K. Mahdjoubi, R. Sauleau, S. Collardey, L. Bernard, and G. Valerio, "On maximum bandwidth of rectangular cavity antennas," **accepted** on July 31 2014 to IEEE Antennas Wireless Propagation Letters, Volume: PP, Issue: 99 DOI: [10.1109/LAWP.2014.2352274](https://doi.org/10.1109/LAWP.2014.2352274) , Publication Year: 2014

M. Martinis, K. Mahdjoubi, R. Sauleau, S. Collardey, L. Bernard, "Circuit models explaining bandwidth behavior of small circular cavity backed patch antennas," Antennas and Propagation (EUCAP), pp 4256 - 4260, Apr. 2014.

M. Martinis, K. Mahdjoubi, R. Sauleau, S. Collardey, L. Bernard, "Bandwidth behavior of miniature square cavity microstrip antennas," Antennas and Propagation in Wireless Communications (APWC), pp 479 - 482, Sep. 2013.

National conference presentations and posters related to the thesis:

M. Martinis, K. Mahdjoubi, R. Sauleau, S. Collardey, L. Bernard, "Development and characterization of metamaterials in cavities. Applications to the design of compact antennas," Journée des doctorants (Doctorants de l'IETR), Rennes, France, June 14, 2012. (poster)

M. Martinis, K. Mahdjoubi, R. Sauleau, S. Collardey, L. Bernard, "Development and characterization of metamaterials in cavities. Applications to the design of compact antennas," 1st budding science colloquium, ISL, Saint Louis. France, July 04-05, 2012. (oral presentation)

M. Martinis, K. Mahdjoubi, R. Sauleau, S. Collardey, L. Bernard, "Development and characterization of metamaterials in cavities. Applications to the design of compact antennas," Journée des doctorants (Doctorants de l'IETR), Rennes, France, June 20, 2013. (poster)

M. Martinis, K. Mahdjoubi, R. Sauleau, S. Collardey, L. Bernard, "Development and characterization of metamaterials in cavities. Applications to the design of compact antennas," 2nd budding science colloquium, ISL, Saint Louis. France, June 27-28, 2013. (oral presentation)

M. Martinis, K. Mahdjoubi, R. Sauleau, S. Collardey, L. Bernard, "Bandwidth of miniature rectangular cavity antennas," GDR Ondes – Assemblée générale "Interférences d'Ondes," Dijon, France, October 28-30, 2013. (poster)

M. Martinis, K. Mahdjoubi, R. Sauleau, S. Collardey, L. Bernard, "Bandwidth of miniature cavity antennas," JCGE 14 – SEEDS, Saint-Louis, France, June 04-05, 2014. (poster)

M. Martinis, K. Mahdjoubi, R. Sauleau, S. Collardey, L. Bernard, "Development and characterization of metamaterials in cavities. Applications to the design of compact antennas," 3rd budding science colloquium, ISL, Saint Louis. France, October 15-16, 2014. (poster)

References

- [1] L. Bernard, "Numerical and experimental investigations of a new circularly polarized patch antenna with an integrated optical lens," *3rd European Conf. on Antennas and Propag.*, EuCAP 2009, pp 2314 – 2317
- [2] M.E. Cos and F. Las-Heras, "Polypropylene-based dual band CPW-fed monopole antenna," *IEEE Antennas and Propag. Magazine*, vol 55, No. 3, Jun. 2013, pp 264-273
- [3] Rogers Corporation, www.rogerscorp.com
- [4] H. A. Wheeler, "Fundamental limitations of small antennas," *Proc. Of the IRE*, pp. 1479-1484, 1947.
- [5] L. J. Chu, "Physical limitations on omni-directional antennas," *Journal of Applied Physics*, vol 19, pp. 1163-1175, 1948.
- [6] R.E. Collin and S. Rothschild, "Evaluation of antenna Q," *IEEE Trans. on Antennas and Propag.*, vol. 12, pp. 23-27, 1964.
- [7] R.L. Fante, "Quality factor of general ideal antennas", *IEEE Trans. on Antennas and Propag.*, vol. 17, pp 151-155, 1969
- [8] R.M. Fano, "Theoretical limitations on the broadband matching of arbitrary impedances," *J Franklin Inst.* 249, pp. 57-83 see also pp. 139-154, 1950.
- [9] R.E. Collin, "Stored energy Q and frequency sensitivity of planar aperture antennas", *IEEE Trans. on Antennas and Propag.*, vol. 15, pp. 567-568, 1967,
- [10] J.S. Mclean, "A Re-examination of the fundamental limits on the radiation Q of electrically small antennas," *IEEE Trans. on Antennas and Propag.*, vol. AP-44, 1996, pp. 672-676.
- [11] Thal, H. L., JR., "Exact circuit analysis of spherical waves," *IEEE Trans. on Antennas and Propag.*, Vol. 26, pp. 282–287, Mar. 1978.
- [12] Thal, H. L., JR. "New radiation Q limits for spherical wire antennas," *IEEE Trans. on Antennas and Propag.*, Vol. 54, no10, pp. 2757–2763, Oct.2006
- [13] R. C. Hansen and R.E. Collin, "A New Chu Formula for Q," *IEEE Antennas and Propagation Magazine*, vol 51, No. 5, pp. 38-41, Oct 2009.
- [14] R. C. Hansen and R.E. Collin, "Small antenna handbook," *John Wiley & Sons*, 2011.
- [15] S. R. Best, "Low Q electrically small linear and elliptical polarized spherical dipole antennas," *IEEE Trans. on Antennas and Propag.*, vol. 53, pp. 1047-1053, March 2005.
- [16] H. R. Stuart and A. Pidwerbetsky, "Electrically small antenna elements using negative permittivity resonators" *IEEE Trans. on Antennas and Propag.*, vol. 54, no. 6, pp. 1644–1653, Jun. 2006.
- [17] Steven R. Best, "A Low Q electrically small magnetic (TE Mode) dipole," *IEEE Ant. and Wireless Propag. Lett.*, Vol. 8, pp 572-575, 2009
- [18] H. R. Stuart and A. D. Yaghjian, "Approaching the lower bounds on Q for electrically small electric-dipole antennas using high permeability shells," *IEEE Trans. on Antennas and Propag.*, vol. 58, no. 12, pp. 3865–3872, Dec. 2010.
- [19] R.F. Harrington, "On the Gain and Bandwidth of directional Antennas," *IRE Transactions on Antennas and Propagation*, vol. AP-&, 1958, pp. 219-225.
- [20] D. M. Pozar, "New results for minimum q, maximum gain, and polarization properties of electrically small arbitrary antennas," *3rd European Conf. on Antennas and Propag.*, EuCAP 2009, pp. 1993-1996, Mar. 2009.
- [21] A. D. Yaghjian, "Internal Energy, Q energy, Poynting's theorem and stress dyadic in dispersive material," *IEEE Trans. On Antennas and Propag.*, vol. 55, pp 1495-1505, 2007,
- [22] S. R. Best and A.D. Yaghjian, "The lower bound on Q for lossy electric and magnetic dipole antennas," *IEEE Antennas and Wireless propagation Letters*, vol. 3, 2004, pp 314-316.
- [23] A.D. Yaghjian, "Improved formulas for the Q of antennas with highly lossy dispersive materials," *IEEE Antennas Wireless Propagation Lett.*, vol.5, Online, August 2006.
- [24] A. D. Yaghjian and S. R. Best, "Impedance, bandwidth, and Q of antennas," *IEEE Trans. on Antennas and Propag.*, vol. 53, no. 4, pp. 1298-1324, Apr. 2005.

- [25] M. Gustafsson and S. Nordebo, "Bandwidth, Q factor, and resonance models of antennas," LUTEDX/(TEAT-7138)/1-16/(2005)
- [26] M. Gustafsson, C. Sohl, and G. Kristensson, "Physical limitations on antennas of arbitrary shape," *Proc. R. Soc. A*, vol. 463, pp. 2589-2607, 2007.
- [27] M. Gustafsson, C. Sohl, and G. Kristensson, "Illustrations of New Physical Bounds on Linearly Polarized Antennas," *IEEE Trans. Antennas Propag.*, vol 57, pp. 1319-1327, May 2009.
- [28] M. Gustafsson, M. Cismasu, and S. Nordebo, "Absorption efficiency and physical bounds on antennas," Technical report LUTEDX/(TEAT-7200)/1-20/2010.
- [29] C. Larsson, M. Gustafsson, and G. Kristensson, "Wideband microwave measurements of the extinction cross section—experimental techniques," Technical report LUTEDX/(TEAT-7182)/1-22/(2009)
- [30] C. Sohl, and M. Gustafsson, "Physical limitations on broadband scattering by heterogenous obstacles," *J. Phys. A: Math. Theor.*, vol 40, pp. 11165-11182, 2007.
- [31] J. L. Volakis and Thomas F. Eibert, "Antenna Engineering Handbook Fourth_Edition," *McGraw-Hill*, 2007
- [32] L. Jofre, M. Martinez-Vazquez, R. Serrano, and G. Roqueta, "Handbook on small antennas," 1st ed. EurAAP 2012. Ch 1. Fundamental limitations (edited by A. K. Skrivervik and M. Gustafsson)
- [33] R. F. Harrington, "Time-Harmonic Electromagnetic Fields," Wiley-IEEE Press; 2nd edition, 2001.
- [34] R. E. Kleinman and T. B. A. Senior, "Rayleigh scattering," in V. K. Varadan and V. V. Varadan editors, "Low and high frequency asymptotics," chapter 1, pp. 1-70. Elsevier Science Publishers, Amsterdam, 1986.
- [35] L. Tsang, J. A. Kong, K. H. Ding, "Scattering of electromagnetic waves: Theories and applications" *John Wiley & Sons, Inc.* 2000.
- [36] J. L. Volakis, C. C. Chen, K. Fujimoto, "Small Antennas: Miniaturization techniques & Applications," *McGraw Hill*, 2010.
- [37] C. A. Balanis, "Antenna theory analysis and design," 3rd ed. New York: *Wiley*, 1997, Ch. 12. Aperture antennas.
- [38] Sophocles J. Orfanidis "Electromagnetic waves and antennas," free internet edition, *Rutgers University*, 2010.
- [39] Hao Xu, D. R. Jackson,, J. T. Williams, "Comparison of models for the probe inductance for a parallel-plate waveguide and a microstrip patch," *IEEE Trans. on Antennas and Propag.*, vol. 53, no. 10, Oct. 2005.
- [40] K.C. gupta, R. Garg, I. Bahl, P. Bhartia, "Microstrip lines and slotlines," Artech House, 2nd ed. 1996.
- [41] D. M. Pozar, "Microwave engineering," 4th ed. *John Wiley & Sons, Inc.* 2011. ch 6. Microwave Resonators
- [42] K. L. Wong, "Compact and Broadband Microstrip Antennas," *John Wiley & Sons, Inc.*, 2002.
- [43] K. L. Wong and S. C. Pan, "Compact triangular microstrip antenna," *Electron. Lett.* 33, 433–434, March 13, 1997
- [44] K. L. Wong, C. L. Tang, and H. T. Chen, "A compact meandered circular microstrip antenna with a shorting pin," *Microwave Opt. Technol. Lett.* 15, 147–149, June 20, 1997
- [45] J. S. Kuo and K. L. Wong, "A compact microstrip antenna with meandering slots in the ground plane," *Microwave Opt. Technol. Lett.* 29, 95–97, April 20, 2001
- [46] C. L. Tang, Studies of compact circular microstrip antennas, M.S. thesis, Department of Electrical Engineering, National Sun Yat-Sen University, Kaohsiung, Taiwan, 1998
- [47] C. K. Wu and K. L. Wong, "Broadband microstrip antenna with directly coupled and gap-coupled parasitic patches," *Microwave Opt. Technol. Lett.* 22, 348–349, Sept. 5, 1999
- [48] N. Herscovici, "A wide-band single-layer patch antenna," *IEEE Trans. Antennas Propagat.* 46, 471–473, April 1998.
- [49] T. Huynh and K. F. Lee, "Single-layer single-patch wideband microstrip antenna," *Electron.Lett.* 31, 1310–1311, Aug. 3, 1995
- [50] K. L. Wong and W. H. Hsu, "A broadband rectangular patch antenna with a pair of wide slits," *IEEE Trans. on Antennas and Propagat.* 49, 1345–1347, Sept. 2001
- [51] J. Y. Jan and K. L. Wong, "A broadband circular microstrip antenna with two open-ring slots," *Microwave Opt. Technol. Lett.* 23, 205–207, Nov. 1999.
- [52] K. L. Wong and J. Y. Jan, "Broadband circular microstrip antenna with embedded reactive loading," *Electron. Lett.* 34, 1804–1805, Sept. 17, 1998.

- [53] M. H. Cohen, "The normal modes of cavity antennas," Ph.D. Thesis, Antenna Laboratory, Department of Electrical Engineering, Ohio State University Research Foundation, 1952.
- [54] M. H. Cohen, "On the band width of cavity antennas," *Journal of Applied Physics*, vol.25, issue 5, pp. 582-587, May 1954.
- [55] V. A. Counter, "Miniature Cavity Antennas," Quarterly Reports Nos. 2-6, Microwave Laboratory, Stanford University 1948-1950.
- [56] A. Kummar, and H. D. Hristov, "Microwave Cavity Antenna." Norwood, MA: *Artech House*, 1989.
- [57] N. C. Karmakar And Mukesh Singh, "Investigations Into A Circular Patch Antenna In A Cylindrical Cavity Enclosure," *Singapore ICCS'94. Conference proceedings*, Vol 2, pp 446-450, Nov. 1994.
- [58] N. C. Karmakar, "Investigations into a cavity-backed circular-patch antenna," *IEEE Trans. on Antennas and Propag.*, vol. 50, no. 12, Dec. 2002.
- [59] J. M. Baracco and P. Brachat, "Shielded microstrip subarrays with large bandwidth and low cross polarization," *IEEE AP-S Int.Symp.*, Chicago, IL, pp. 293–296, July 1992.
- [60] J. A. Navarro and K. Chang, "A Ka-band cavity-enclosed aperture-coupled circular patch antenna and array for millimeter-wave circuit integration," *IEEE AP-S Int. Symp. Dig.*, 1992, pp. 313–316, 1992.
- [61] J. T. Aberle, "On the use of metallized cavities backing microstrip antennas," *IEEE AP-S Int. Symp. Dig.*, 1993, pp. 60–63, 1993.
- [62] M. Lye, R. B. Waterhouse, D. Novak, F. Zavosh, and J. T. Aberle, "Design and development of printed antenna remote units for optically distributed mobile communications," *IEEE Microwave Guided Wave Lett.*, vol. 8, pp. 432–434, Dec. 1998.
- [63] F. Zavosh and J. T. Aberle, "Infinite phased arrays of cavity-backed patches," *IEEE Trans. on Antennas and Propag.*, vol. 42, no. 3, Mar. 1994.
- [64] F. Zavosh and J. T. Aberle, "Improving the performance of microstrip patch antennas," *IEEE Antennas Propagat. Mag.*, vol. 38, pp. 7–12, Aug. 1996.
- [65] F. Zavosh and J. T. Aberle, "Design of high gain microstrip antennas," *Microwave J.*, vol. 42, no. 9, pp. 138–148, Sept. 1999.
- [66] M. A. Gonzalez, J. A. Encinar, and J. Zapata, "Radiation pattern computation of cavity-backed and probe-fed stacked microstrip patch arrays," *IEEE Trans. on Antennas and Propag.*, vol. 48, pp. 502–509, Apr. 2000.
- [67] M. A. Gonzalez, J. Zapata, and J. A. Encinar, "Broad-band cavity-backed and capacitively probe-fed microstrip patch arrays," *IEEE Trans. on Antennas and Propag.*, vol. 48, pp. 784–789, Apr. 2000.
- [68] M. J. Tsai and B. Rulf, "A simple double-slot radiator for E-plane beam control," presented at the Proc. 2000 Int. Union of Radio Science (URSI), Salt Lake City, UT, July 2000.
- [69] F. Zavosh and J. T. Aberle: "Single and stacked circular microstrip patch antennas backed by a circular cavity," *IEEE Trans. on Antennas and Propag.*, vol. 43, no. 7, Jul. 1995.
- [70] A. Boag, Y. Shimony, A. Boag, and R. Mittra, "Dual band cavity-backed quarter-wave patch antenna," *IEEE Antennas and Propagation Int. Symp. Dig.*, Newport Beach, CA, June 1995, pp. 2124–2127, 1995
- [71] S. Noghanian and L. Shafai, "Control of microstrip antenna radiation characteristics by ground plane size and shape," *Proc. Inst. Elect. Eng. Microwave Antennas Propagat.*, vol. 145, no. 3, pp. 207–212, June 1998.
- [72] J. L. Volakis and J. M. Jin, "A scheme to lower the resonant frequency of the microstrip patch antenna," *IEEE Microwave Guided Wave Lett.*, vol. 2, pp. 292–293, July 1992.
- [73] R. B. Waterhouse, "Small printed antenna easily integrated into a mobile handset terminal," *Elect. Lett.*, vol. 34, no. 17, pp. 1629–1631, Aug. 20, 1998.
- [74] M. Zheng, Q. Chen, P. S. Hall, and V. F. Fusco, "Oscillator noise reduction in cavity-backed active microstrip patch antenna," *Elect. Lett.*, vol.33, no. 15, pp. 1276–1277, July 17, 1997.
- [75] M. W. Nurnberger, M. A. Abdelmoneum, and J. K. Volakis, "New techniques for extremely broadband planar slot spiral antennas," *IEEE Antennas Propagation. Symp.*, Orlando, FL., July 1999, pp.2690–2693, 1999
- [76] C. I. Coman, I. E. Lager, L. P. Ligthart, "Unitary approach to the design of cavity-backed probe-fed antennas," *Wireless Technology Conference*, pp 431-434, Oct. 2005.
- [77] M. H. Awida, S. H. Suleiman, A. E. Fathy, "Substrate-integrated cavity-backed patch arrays: a low-cost approach for bandwidth enhancement," *IEEE Trans. on Antennas and Propag.*, vol. 59, pp 1155-1163, Apr. 2011.
- [78] D. Guha and J. Y. Siddiqui, "Effect of a cavity enclosure on the resonant frequency of inverted microstrip circular patch antenna," *IEEE Trans. on Antennas and Propag.*, Vol 52, no 8, pp 2177-2181, Aug. 2004

- [79] M. Biswas, J. Y. Siddiqui, D. Guha, Yahia M. M. Antar, "Effect of a cylindrical cavity on the resonance of a circular microstrip patch with variable air-gap," *IEEE Antennas And Wireless Propagation Letters*, Vol. 5, 2006.
- [80] C. Caloz and T. Itoh, "Electromagnetic Metamaterials: Transmission line theory and microwave applications," Hoboken, NJ: *John Wiley & Sons*, 2006.
- [81] S. Anantha Ramakrishna, Tomasz M. Grzegorzczak, "Physics and applications of negative refractive indeks materials," Bellingham, Washington USA, *CRC Press*, 2009.
- [82] S. Tretyakov, "Analytical Modeling in Applied Electromagnetics," *Artech House*, 2003.
- [83] N. Engheta and R.W. Ziolkowski, Eds., "Metamaterials: physics and engineering explorations," Hoboken, NJ: *John Wiley & Sons*, 2006.
- [84] G. V. Eleftheriades and K.G. Balmain, Eds., "Negative-refraction metamaterials: fundamental principles and applications," Hoboken, NJ: *John Wiley & Sons*, 2005.
- [85] R. Marques, F. Martin, and M. Sorolla, "Metamaterials with negative parameters: theory, design and microwave applications," Hoboken, NJ: *John Wiley & Sons*, 2007.
- [86] F. Capolino: "Theory and phenomena of metamaterials," *CRC Press*, 2009.
- [87] J. B. Pendry, A. J. Holden, D.J. Robbins, and W. J. Stewart, "Magnetism from Conductors, and Enhanced Non-Linear Phenomena," *IEEE Transactions on Microwave Theory and Techniques*, Volume 47, Page 2075, 1999.
- [88] V. Veselago, "The electrodynamics of substances with simultaneously negative values of μ and ϵ ," *Soviet Physics Uspekhi*, vol. 10, no. 4, pp509-514, Jan., Feb. 1968.
- [89] R. A. Shelby, D. R. Smith, S. Schultz, "Experimental verification of a negative index of refraction," *Science*, Vol. 292 no. 5514 pp. 77-79, Apr. 2001.
- [90] R. W. Ziolkowski, P. Jin, C. Lin, "Metamaterial-Inspired Engineering of Antennas," *Proceedings of the IEEE*, Volume:99, Issue 10, Oct 2011.
- [91] Y. Rahmat-Samii and H. Mosallaei, "Electromagnetic band-gap structures: classification, characterization and applications," *IEE-ICAP Symposium* (April 2001): 560–564
- [92] A. Grbic, G. V. Eleftheriades, "A backward-wave antenna based on negative refractive index LC networks," *IEEE Antennas and Propagation Society International Symposium*, vol 4, pp 340-343, 2002.
- [93] C. Caloz, T. Itoh, and A. Rennings, "CRLH traveling-wave and resonant metamaterial antennas," *IEEE Antennas Propag. Mag.*, vol. 50, no. 5, pp. 25–39, Oct. 2008.
- [94] A. Sanada, K. Murakami, I. Awai, H. Kubo, C. Caloz, and T. Itoh, "A planar zeroth-order resonator antenna using a left-handed transmission line," in *Proc. 34th Eur. Microw. Conf.*, Amsterdam, The Netherlands, Oct. 2004, pp. 1341–1344
- [95] C. Caloz and A. Rennings, "Overview of Resonant Metamaterial Antennas," EuCAP 2009.
- [96] S. Otto, A. Rennings, C. Caloz, P. Waldow, "Dual mode zeroth order ring resonator with tuning capability and selective mode excitation," *European Microwave Conference*, vol.1, Oct. 2005
- [97] A. Lai, K. Leong, and T. Itoh, "Infinite wavelength resonant antennas with monopolar radiation pattern based on periodic structures," *IEEE Trans. Antennas Propag.*, vol. 55, no. 3, pp. 868–876, Mar. 2007.
- [98] Y. Dong and T. Itoh, "Miniaturized substrate integrated waveguide slot antennas based on negative order resonance," *IEEE Trans. on Antennas and Propag.*, vol. 58, no. 12, pp. 3856–3864, Dec. 2010.
- [99] T. Jang, J. Choi, and S. Lim, "Compact coplanar waveguide (CPW)-fed zeroth-order resonant antennas with extended bandwidth and high efficiency on vialess single layer," *IEEE Trans. on Antennas and Propag.*, vol. 59, no. 2, pp. 363–372, Feb. 2011.
- [100] Y. Dong, H. Toyao, and T. Itoh, "Compact circularly-polarized patch antenna loaded with metamaterial structures," *IEEE Trans. on Antennas and Propag.*, vol. 59, no. 11, pp. 4329–4333, Nov. 2011.
- [101] A. Alù, "Metamaterials for Radiating Setups, Planar and Conformal Antennas," Ph.D. Thesis, Roma, February 2007.
- [102] A. Alu, F. Bilotti, N. Engheta, and L. Vegni, "Subwavelength, compact, resonant patch antennas loaded with metamaterials," *IEEE Trans. on Antennas and Propag.*, vol. 55, no. 1, pp. 13–25, Jan. 2007.

- [103] R. W. Ziolkowski and A. Erentok, "Metamaterial-based efficient electrically small antennas," *IEEE Trans. on Antennas and Propag.*, vol. 54, no. 7, pp. 2113–2130, Jul. 2006.
- [104] A. Ahmadi, S. Saadat, and H. Mosallaei, "Resonance and Q performance of ellipsoidal ENG subwavelength radiators," *IEEE Trans. on Antennas and Propag.*, vol. 59, no. 3, pp. 706–713, Mar. 2011.
- [105] A. Erentok and R. W. Ziolkowski, "Metamaterial-inspired efficient electrically small antennas," *IEEE Trans. on Antennas and Propag.*, vol. 56, no. 3, pp. 691–707, Mar. 2008.
- [106] G. Mumcu, K. Sertel, and J. L. Volakis, "Miniature antenna using printed coupled lines emulating degenerate band edge crystals," *IEEE Trans. on Antennas and Propag.*, vol. 57, no. 6, pp. 1618–1624, Jun. 2009.
- [107] J. L. Volakis and K. Sertel, "Narrowband and wideband metamaterial antennas based on degenerate band edge and magnetic photonic crystals," *Proc. IEEE*, vol. 99, no. 10, pp. 1732–1745, Oct. 2011.
- [108] H. Mosallaei and K. Sarabandi, "Antenna miniaturization and bandwidth enhancement using a reactive impedance substrate," *IEEE Trans. on Antennas and Propag.*, vol. 52, no. 9, pp. 2403–2414, Sep. 2004."
- [109] F. Yang and Y. Rahmat-Samii, "Reflection phase characterizations of the EBG ground plane for low profile wire antenna applications," *IEEE Trans. on Antennas and Propag.*, vol. 51, no. 10, pp. 2691–2703, Oct. 2003.
- [110] Y. Zhang, J. von Hagen, M. Younis, C. Fischer, and W. Wiesbeck, "Planar artificial magnetic conductors and patch antennas," *IEEE Trans. on Antennas and Propag.*, vol. 51, no. 10, pp. 2704–2712, Oct. 2003.
- [111] L. Bernard, G. Chertier, and R. Sauleau, "Wideband circularly polarized patch antennas on reactive impedance substrates," *IEEE Ant. Wireless Propag. Letters*, vol. 10, 2011, pp 1015- 1018
- [112] A. P. Feresidis, G. Goussetis, S. Wang, and J. C. Vardaxoglou, "Artificial magnetic conductor surfaces and their application to low-profile high-gain planar antennas," *IEEE Trans. on Antennas and Propag.*, vol. 53, no. 1, pp. 209–215, Jan. 2005.
- [113] Y. Dong, H. Toyao, and T. Itoh, "Miniaturized zeroth order resonance antenna over a reactive impedance surface," in *Proc. Int. Workshop Antenna Technol.*, Mar. 2011, pp. 58–61.
- [114] M. Antoniadou and G. V. Eleftheriades, "A folded-monopole model for electrically small NRI-TL metamaterial antennas," *IEEE Antennas Wireless Propag. Lett.*, vol. 7, pp. 425–428, 2008.
- [115] J. H. Park, Y. H. Ryu, and J. H. Lee, "Mu-zero resonance antenna," *IEEE Trans. on Antennas and Propag.*, vol. 58, no. 6, pp. 1865–1875, Jun. 2010.
- [116] O. S. Kim and O. Breinbjerg, "Miniaturised self-resonant split-ring resonator antenna," *Electron. Lett.*, vol. 45, no. 4, pp. 196–197, Feb. 2009.
- [117] K. B. Alici and E. Ozbay, "Electrically small split ring resonator antennas," *J. Appl. Phys.*, vol. 101, pp. 083104-1–083104-4, 2007.
- [118] Y. Dong, H. Toyao, and T. Itoh, "Design and characterization of miniaturized patch antennas loaded with complementary split-ring resonators," *IEEE Trans. on Antennas and Propag.*, vol. 60, no. 2, pt. 2, pp. 772–785, Feb. 2012.
- [119] R.C. Hansen and M. Burke, "Antennas with magneto-dielectrics," *Microwave and Optical Technology Letters*, Vol. 26, No.2, July 2000.
- [120] Hossein Mosallaei, and Kamal Sarabandi, "Magneto-dielectrics in electromagnetics: concept and applications," *IEEE Trans. on Antennas and Propag.*, vol. 52, no. 6, pp 1558- 1567, Jun. 2004.
- [121] Hossein Mosallaei, and Kamal Sarabandi, "Design and modeling of patch antenna printed on magneto-dielectric embedded-circuit metasubstrate," *IEEE Trans. on Antennas and Propag.*, vol. 55, no. 1, pp. 45- 52, Jan 2007.
- [122] P. M. T. Ikonen and S. A. Tretyakov, "Comments on 'Design and modeling of patch antenna printed on magneto-dielectric embedded-circuit metasubstrate,'" *IEEE Trans. Antennas Propag.*, vol. 55, pp. 2935–2936, Oct. 2007.
- [123] O. S. Kim, "Low-Q electrically small spherical magnetic dipole antenna," *IEEE Trans. on Antennas and Propag.*, vol. 58, no. 7, pp. 2010–2217, Jul. 2010.
- [124] Y. Dong, T. Yang, and T. Itoh, "substrate integrated waveguide loaded by complementary split-ring resonators and its applications to miniaturized waveguide filters," *IEEE Trans. Microw. Theory Tech.*, vol. 57, no. 9, pp. 2211–2223, Sep. 2009.
- [125] R. F. Harrington, "Resonant behavior of a small aperture backed by a conducting body," *IEEE Trans. on Antennas and Propag.*, vol. 30, no.2, pp. 205-212. Mar. 1982

- [126] Wolfram Mathematica. Available: www.wolfram.com, version Mathematica 8.
- [127] <http://www.walter-fendt.de/ph14e/resonance.htm>
- [128] H. H. Huang and C. T. Sun, "Anomalous wave propagation in a one-dimensional acoustic metamaterial having simultaneously negative mass density and Young's modulus," *J. Acoust. Soc. Am.* 132(4), Pt.2, Oct. 2012
- [129] "Nanostructured Metamaterials" European Commission, Directorate-General for Research, Editor: Anne F. de Baas
- [130] CST Microwave studio. Available: <http://www.cst.com/>, version 2011.